Dissertation

Non-restrictive Methods for Inertial Sensor Fusion in Human Motion Analysis

Daniel Laidig

Berlin 2023

Non-restrictive Methods for Inertial Sensor Fusion in Human Motion Analysis

vorgelegt von
M.Sc.
Daniel Laidig
ORCID: 0000-0003-2928-2446

an der Fakultät IV – Elektrotechnik und Informatik
der Technischen Universität Berlin
zur Erlangung des akademischen Grades

Doktor der Ingenieurwissenschaften
– Dr.-Ing. –

genehmigte Dissertation

Promotionsausschuss:

Vorsitzender:	Prof. Dr.-Ing. Clemens Gühmann
Gutachter:	Prof. Dr.-Ing. Jörg Raisch
Gutachterin:	Prof. Dr.-Ing. Thomas Seel
Gutachter:	Prof. Dr. Manon Kok
Gutachter:	Prof. Dr. Bertram Taetz

Tag der wissenschaftlichen Aussprache: 20. September 2023

Berlin 2023

Abstract

The miniaturization of MEMS-based inertial measurement units (IMUs) facilitates their widespread use in a growing number of application domains. IMUs measure angular rate, specific force, and often the magnetic field strength, each as a 3D vector in a local coordinate system. Those measurements are processed via sensor fusion methods to estimate motion parameters of interest. In human motion analysis, IMUs have the potential to overcome the need for expensive stationary motion capture labs and to enable long-term monitoring in unsupervised settings. In practice, adoption is limited by the fact that most existing methods are restrictive: They only yield precise estimates after careful parameter tuning, require the subjects to perform tedious calibration motions, and rely on a homogeneous magnetic field that is rarely found in indoor environments. This thesis aims at developing a modular set of methods for non-restrictive inertial motion analysis that overcome those limitations.

As a fundamental building block for inertial motion analysis, a versatile orientation estimation algorithm is introduced. This algorithm simultaneously estimates the 6D and 9D sensor orientation and includes extensions for gyroscope bias estimation and for magnetic disturbance rejection. The new method is evaluated with a specifically designed, extensive benchmark dataset. A comparison with eight literature methods shows that the proposed method provides unprecedented out-of-the-box accuracy.

In order to overcome the need for precise sensor attachment or tedious precise calibration motions, methods for automatic anatomical calibration are developed. The methods exploit kinematic constraints of 2-DoF joints and work with arbitrary joint motions. The experimental evaluation on the elbow joint shows that joint axes can be estimated from only ten seconds of motion, and joint angles can be obtained with similar accuracy as conventional methods while being less restrictive.

The same kinematic constraints are then used to recover the missing relative heading information for long-term stable magnetometer-free motion tracking. A robust window-based optimization approach for hinge joints and 2-DoF joints is developed. It detects rest phases and phases in which the constraints become singular. The experimental evaluation shows that the methods achieve long-term stable tracking in mechanical and finger joints.

Those methods are complemented by a set of non-restrictive methods for gait assessment with foot-worn IMUs. They support the detection of a comprehensive set of gait phases, spatiotemporal parameters, and foot position and angle trajectories. The methods are extensively validated using data recorded with healthy subjects and subjects with diverse gait pathologies. A pressure-based system and optical motion capture are used as reference. In contrast to most existing methods, the proposed methods reliably work on patients in addition to healthy subjects and still produce accurate results.

In summary, the modular set of developed methods addresses the current limitations in IMU-based human motion analysis. This work contributes toward realizing the full potential of body-worn IMUs as a measurement technology and enabling non-restrictive plug-and-play motion tracking in biomedical research, rehabilitation, and other health-related applications.

Zusammenfassung

Die Miniaturisierung von MEMS-basierten Inertialsensoren ermöglicht ihre weitverbreitete Verwendung in einer wachsenden Zahl von Anwendungsgebieten. Inertialsensoren messen die Winkelgeschwindigkeit, die Beschleunigung und oft auch die magnetische Feldstärke, jeweils als 3D-Vektor in einem lokalen Koordinatensystem. Diese Messwerte werden mittels Sensorfusion verarbeitet, um Bewegungsparameter zu schätzen. Bei der Analyse menschlicher Bewegungen haben Inertialsensoren das Potenzial, teure stationäre Bewegungslabore zu ersetzen und ein unbeaufsichtigtes Langzeitmonitoring zu ermöglichen. In der Praxis wird die Verbreitung inertialer Bewegungsanalyse dadurch eingeschränkt, dass die meisten bestehenden Methoden restriktiv sind: Sie liefern nur nach sorgfältigem Parametertuning genaue Schätzungen, erfordern mühsame Kalibrierbewegungen von den Probanden und sind auf ein homogenes Magnetfeld angewiesen. Ziel dieser Dissertation ist es, einen modularen Satz an Methoden zur nicht-restriktiven inertialen Bewegungsanalyse zu entwickeln, der diese Einschränkungen überwindet.

Als grundlegender Baustein der inertialen Bewegungsanalyse wird ein vielseitiger Algorithmus zur Orientierungsschätzung vorgestellt. Dieser schätzt gleichzeitig die 6D- und 9D-Sensororientierung und enthält Erweiterungen für die Gyroskop-Bias-Schätzung und für die Unterdrückung magnetischer Störungen. Diese neue Methode wird mittels eines speziell entwickelten, umfangreichen Benchmark-Datensatzes evaluiert. Ein Vergleich mit acht Literaturmethoden zeigt, dass die vorgeschlagene Methode eine bisher unerreichte Out-of-the-Box-Genauigkeit liefert.

Um auf eine präzise Sensoranbringung oder mühsame präzise Kalibrierbewegungen verzichten zu können, werden Methoden zur automatischen anatomischen Kalibrierung entwickelt. Die Methoden basieren auf kinematischen Zwangsbedingungen von Gelenken mit zwei Freiheitsgraden und setzen keine bestimmten Gelenkbewegungen voraus. Die experimentelle Auswertung am Ellbogengelenk zeigt, dass Gelenkachsen aus nur zehn Sekunden Bewegung geschätzt werden können und dass die vorgeschlagenen Methoden Gelenkwinkel mit ähnlicher Genauigkeit wie konventionelle Methoden liefern, dabei aber weniger restriktiv sind.

Dieselben kinematischen Zwangsbedingungen werden anschließend verwendet, um die fehlende relative Heading-Information zu schätzen und damit auch ohne Magnetometer eine langzeitstabile Bewegungserfassung zu ermöglichen. Dazu wird ein robuster fensterbasierter Optimierungsansatz für Scharniergelenke und Gelenke mit zwei Freiheitsgraden entwickelt. Dieser erkennt Ruhephasen und Phasen, in denen die Zwangsbedingungen singulär werden. Die experimentelle Auswertung zeigt, dass die Methoden bei mechanischen Gelenken und Fingergelenken eine langzeitstabile Bewegungserfassung ermöglichen.

Schließlich wird eine Reihe von nicht-restriktiven Methoden zur Ganganalyse mittels am Fuß angebrachten Inertialsensoren entwickelt. Diese erkennen einen umfassenden Satz an Gangphasen, Gangparametern sowie Fußwinkel- und Positionstrajektorien. Die Methoden werden umfassend anhand von Daten gesunder Probanden und Probanden mit verschiedenen Gangpathologien validiert. Als Referenz werden dabei Daten von einem druckbasierten System und optischer Bewegungserfassung verwendet. Im Gegensatz zu den meisten bestehenden Methoden liefern die vorgeschlagenen Methoden auch bei Patienten mit Gangpathologien zuverlässig genaue Ergebnisse.

Zusammenfassend bietet der modulare Satz an entwickelten Methoden eine Lösung für einige der derzeitigen Einschränkungen in der Bewegungsanalyse mit Inertialsensoren. Die Ergebnisse dieser Dissertation tragen dazu bei, das Potenzial von am Körper getragenen Inertialsensoren als Messtechnologie voll auszuschöpfen und eine nicht-restriktive Plug-and-Play-Bewegungsanalyse in vielen medizinischen, rehabilitativen und anderen gesundheitsbezogenen Anwendungen zu ermöglichen.

Acknowledgements

First and foremost, I am sincerely grateful to Prof. Dr.-Ing. Jörg Raisch and Prof. Dr.-Ing. Thomas Seel for giving me the opportunity to work in such an interesting field of research and for strongly and continuously supporting me and my work. When I was looking for a Bachelor thesis topic almost ten years ago and Thomas introduced me to inertial sensors, I would never have imagined that this was only the beginning of a long journey. Thank you, Thomas, for always being approachable and for always being interested and willing to jump in and provide input on what was needed at the moment, from discussing big ideas to grammatical nitpicking. I am furthermore indebted to Prof. Dr. Manon Kok and Prof. Dr. Bertram Taetz for agreeing to be part of my doctoral committee and to Prof. Dr.-Ing. Clemens Gühmann for chairing the committee. Your opinion on my work is highly appreciated. Beyond that, I would like to thank several people who contributed to the presented results and the related publications.

The BROAD dataset introduced in Chapter 3 was created with the highly valuable support of Kai Brands. Many thanks go to Andrea Cereatti and Marco Caruso for the fruitful collaboration on IOE accuracy evaluation. I am also grateful to Ive Weygers for his contributions toward making VQF more visible in the scientific community.

Sincere thanks go to Philipp Müller for laying the foundation upon which my work on automatic anatomical calibration in Chapter 4 is built. Further, I thank Johanna Carstensen and Lars Nienerowski for their skillful support in conducting the experiments and processing the experimental data used for the evaluation of the methods.

Dustin Lehmann greatly contributed to the methods and results presented in Chapter 5, both as part of his exceptional Master thesis and afterward as a colleague. He deserves credit for designing highly professional 3D-printed joints, conducting experiments, and implementing the heading tracking methods. Sincere thanks also go to Christina Salchow-Hömmen and Markus Valtin for creating the hand sensor system used in the experimental evaluation and to Bo Yang for his contribution toward making sure that an implementation of the method and many other useful things are available in the open-source toolbox *qmt*.

The evaluation of the gait analysis methods in Chapter 6 would not have been possible without the invaluable help of Andreas Jocham, who worked hard to record an impressive dataset and contributed his insight on clinical gait analysis. My gratitude also goes to all colleagues at FH Joanneum Graz, NTK Kapfenberg, and Rehabilitation Center Kitzbühel that helped with the extensive data collection, and to Andrew Cote and Eva Kastenbauer for their skillful support in algorithm development and evaluation.

I would also like to thank all my colleagues from the Control Systems Group at TU Berlin, especially Thomas Schauer, Benjamin Riebold, and Constantin Wiesener, for many discussions and support during my research. I am grateful to Dustin Lehmann, Ive Weygers, and Patrick Seiler for proofreading parts of this thesis. My thanks furthermore go to the volunteers who supported this work by participating in experimental trials.

Finally, I am grateful to my family and friends for their support and for always believing in me. My deepest thanks go to Xiangnan for her constant encouragement and patience, and for giving the guy in Figures 1.1 and 3.1 proper hair and eyes.

Daniel Laidig
Berlin, April 2023

Table of Contents

List of Figures

List of Tables

Abbreviations

6D sensor fusion with gyroscope and accelerometer data 9, 12, 45

9D sensor fusion with gyroscope, accelerometer, and magnetometer data 9, 12, 45

AMR anisotropic magnetoresistance 12

BasicVQF basic version of VQF (IOE algorithm) 46

BROAD Berlin Robust Orientation Estimation Assessment Dataset 33

DIP distal interphalangeal joint 119

DoF degrees of freedom 71, 74

EKF extended Kalman filter 27

ENU east-north-up 9, 45

FE flexion and extension 75

FES functional electrical stimulation 2

FKF Guo's Fast Kalman Filter (IOE algorithm) 28

HDF5 Hierarchical Data Format, version 5 41

IIR infinite impulse response 194

IMU inertial measurement unit 1, 10

IOE inertial orientation estimation 12, 23

ISB International Society of Biomechanics 20

ITOP individual trial-optimized performance 40

KOK Kok's complementary filter (IOE algorithm) 29

MAD Madgwick's complementary filter (IOE algorithm) 28

MAD mean of the absolute difference 149

MAH Mahony's complementary filter (IOE algorithm) 28

MAV micro aerial vehicle 32

MCID minimal clinically important difference 159

MCP metacarpophalangeal joint 72, 119

MEMS microelectromechanical systems 1, 10

MKF Matlab's Kalman filter (IOE algorithm) 29

OfflineVQF offline version of VQF (IOE algorithm) 46

OMC optical motion capture 1

$\mathbf{OMC_{IMU}}$ ground truth derived from optical markers attached to the IMU 154

$\mathbf{OMC_{SHOE}}$ ground truth derived from optical markers attached to the shoe 154

PIP proximal interphalangeal joint 119

PS pronation and supination 75

RIANN Robust IMU-based Attitude Neural Network (IOE algorithm) 29

RMS root mean square 35

RMSE root mean square error 36

SDC smallest detectable change 159

SEL Seel's complementary filter (IOE algorithm) 29

TAGP trial-agnostic generalized performance 40

$\mathbf{TAGP_x}$ extended trial-agnostic generalized performance 60

VAC Valenti's complementary filter (IOE algorithm) 28

VQF Versatile Quaternion-based Filter (IOE algorithm) 46

Symbols

$\mathbf{a}$ Accelerometer measurement, 3D vector in $\mathrm{m/s^2}$ 9
a_{th} Threshold for acceleration norm 137
$a_{\mathrm{th,min}}$ Lower bound for a_{th} 138, 148

$\mathbf{b}$ Gyroscope bias 54
$\hat{\mathbf{b}}$ Gyroscope bias estimate 54

c Cadence 141

$\mathbf{e}$ Error vector 81
e Total orientation error (Chapter 3) 39
e Kinematic constraint error (Chapter 4) 80
e_{h} Heading error 40
e_{i} Inclination error 40
e_{relori} Error of relative orientation 121
$e_{w,k}$ weighted constraint error of sample k of window w 115

f_{c} Cutoff frequency 48
f_{s} Sampling rate, inverse of the sampling time 80

h_a Hysteresis factor for acceleration 137, 148
h_ω Hysteresis factor for angular rate 137, 148

i Sensor index (used as subscript), for joints: 1 for the proximal segment, 2 for the distal segment 9
i Stride index (Chapter 6) 136

$\mathbf{J}$ Jacobian 81
$\mathbf{j}$ Jerk 140
$\mathbf{j}_1$ First joint axis, fixed in the coordinates of $\mathcal{B}_1$ 76
$\mathbf{j}_2$ Second joint axis, fixed in the coordinates of $\mathcal{B}_2$ 76
j_{th} Relative threshold for jerk norm 141, 148
j_{win} Ratio of the window to look for initial contact 140, 148

k Sampling index 9

L Stride length 143
l Iteration index 81, 138

M Number of samples used for joint axis estimation (Chapter 4) 80
M Number of strides (Chapter 6) 136

$\mathbf{m}$ Magnetometer measurement, 3D vector in µT 9

N Number of samples 9

$\mathbf{p}$ Position 142
p_{lift} Vertical lift of foot 144
p_{shift} Lateral shift of foot 144

$\mathbf{q}$ Quaternion 15
${}^{\mathcal{S}_i}_{\mathcal{E}_i}\mathbf{q}$ 6D orientation quaternion, orientation of IMU $\mathcal{S}_i$ relative to $\mathcal{E}_i$ 45
${}^{\mathcal{S}_i}_{\mathcal{E}}\mathbf{q}$ 9D orientation quaternion, orientation of IMU $\mathcal{S}_i$ relative to $\mathcal{E}$ 45
q_w scalar w-component of a quaternion 15
q_x x-component of a quaternion 15
q_y y-component of a quaternion 15
q_z z-component of a quaternion 15

$\mathbf{R}$ Rotation matrix 17
r Sample rating (Chapter 5) 106, 114
r Combined rest signal (Chapter 6) 138
r_a Accelerometer-based rest signal 137
r_ω Gyroscope-based rest signal 138
r_w Window rating 116

$T_{0,\mathrm{min}}$ Minimum duration of zero-phase 137, 148
$T_{1,\mathrm{min}}$ Minimum duration of one-phase 137, 148
T_{est} Estimation time instants 114
t_{fc} Time instant of full contact 136
t_{hr} Time instant of heel rise 136
t_{ic} Time instant of initial contact 136
t_k Sampling time instant at sampling index k 9
t_{rest} Time instant at the middle of the foot flat phase 136
T_{s} Sampling time, inverse of the sampling rate 9
T_{stance} Stance duration 141
T_{stride} Stride duration 141
T_{swing} Swing duration 141
t_{to} Time instant of toe-off 136
T_{win} Window duration 115
$t_{w,k}$ Time of sample k of window w 115

$\mathbf{v}$ Velocity 142
v Walking speed 143

$\mathbf{v}_{\mathrm{df}}$ Drift-free velocity 142

w Index of estimation window 85, 115
w_a Factor for a_{th} auto-tuning 138, 148
w_ω Factor for ω_{th} auto-tuning 139, 148

$\mathcal{B}$ Coordinate system of a (human) body segment ("body") 9
$\mathcal{B}_1$ Coordinate system of the proximal body segment of a joint 76
$\mathcal{B}_2$ Coordinate system of the distal body segment of a joint 76
$\mathcal{B}_i$ Coordinate system of the (human) body segment ("body") with index i 9
$\mathcal{E}$ Reference frame ("earth") with z-axis pointing up and y-axis pointing north (ENU) 9
$\mathcal{E}_i$ Reference frame ("earth") of IMU i with z-axis pointing up and arbitrary slowly-drifting heading 9
$\mathcal{M}$ Reference frame of the OMC system, defined during calibration of the OMC system 37
$\mathcal{F}$ Foot coordinate system 143
$\mathcal{I}_i$ Almost-inertial frame of IMU i used in IOE, slowly drifting due to errors in gyroscope strapdown integration 45
$\mathcal{S}$ Coordinate system of the IMU ("sensor") 9
$\mathcal{S}_1$ Coordinate system of the IMU attached to the proximal body segment of a joint 75
$\mathcal{S}_2$ Coordinate system of the IMU attached to the distal body segment of a joint 75
$\mathcal{S}_i$ Coordinate system of the IMU ("sensor") with index i 9

(α, β, γ) Euler angles 19
α Misalignment angle of the joint axis estimates 86
β_0 Fixed second Euler angle of a 2-DoF joint, elbow: carrying angle 76
δ Heading offset 78
$\hat{\delta}$ Estimate of the heading offset 113
δ_{f} Filtered heading offset 106
δ_i Heading offset of IMU i 45
$\delta_{\mathrm{progression}}$ Heading of the line of progression of gait 144
δ_{ref} Ground truth for heading offset 121
ε_w Variability angle of window w 86
Γ Tilt rate 139
$\boldsymbol{\omega}$ Gyroscope measurement, 3D vector in rad/s 9
ω_{th} Threshold for angular rate norm 137
$\omega_{\mathrm{th,min}}$ 148
$\boldsymbol{\Phi}$ Parameter vector 81
φ_i First spherical coordinate of joint axis $\mathbf{j}_i$ 80
τ_{acc} Time constant for accelerometer correction 51
τ_{mag} Time constant for magnetometer correction 51
θ_i Second spherical coordinate of joint axis $\mathbf{j}_i$ 80

1

Introduction

1.1 Scientific Background and Motivation

Human motion analysis is an essential tool in countless applications, for example, in the fields of rehabilitation [1, 2], sports [3], and entertainment [4]. While various technologies can facilitate motion tracking, marker-based optical motion capture (OMC) is commonly considered the gold standard [5, 6]. A promising alternative that has seen growing popularity in recent years is the use of inertial measurement units (IMUs) based on microelectromechanical systems (MEMS) [7]. Modern battery-powered wireless IMUs are affordable, small, and lightweight [8], and IMU-based measurement is not restricted to stationary lab environments. There is no line-of-sight requirement, and the subject's clothing does not interfere with the measurement. Those advantages make motion analysis with IMUs far less cost-intensive and less restrictive than motion analysis with OMC.

IMUs measure angular rate, specific force (also called proper acceleration), and often the magnetic field strength, each as a time-dependent 3D vector in an intrinsic sensor coordinate system [9]. Those measurements are processed to determine the motion parameters of interest, e.g., the orientation of an object to which the sensor is attached, the object's velocity or position, or other application-specific motion parameters [9, 10]. Figure 1.1 illustrates the typical steps of IMU-based motion analysis in kinematic chains:

1. The orientation of each sensor is estimated by sensor fusion of the gyroscope measurements with the accelerometer measurements and, sometimes, with the magnetometer measurements.
2. The attachment orientation of the sensor on the body segment is determined in a step called anatomical calibration or sensor-to-segment calibration.
3. If magnetometer measurements are not employed, the missing relative heading information has to be recovered by other means.
4. The resulting segment orientations can be used to calculate joint angles or for 3D visualization.
5. Additional motion parameters are obtained by application-specific algorithms.

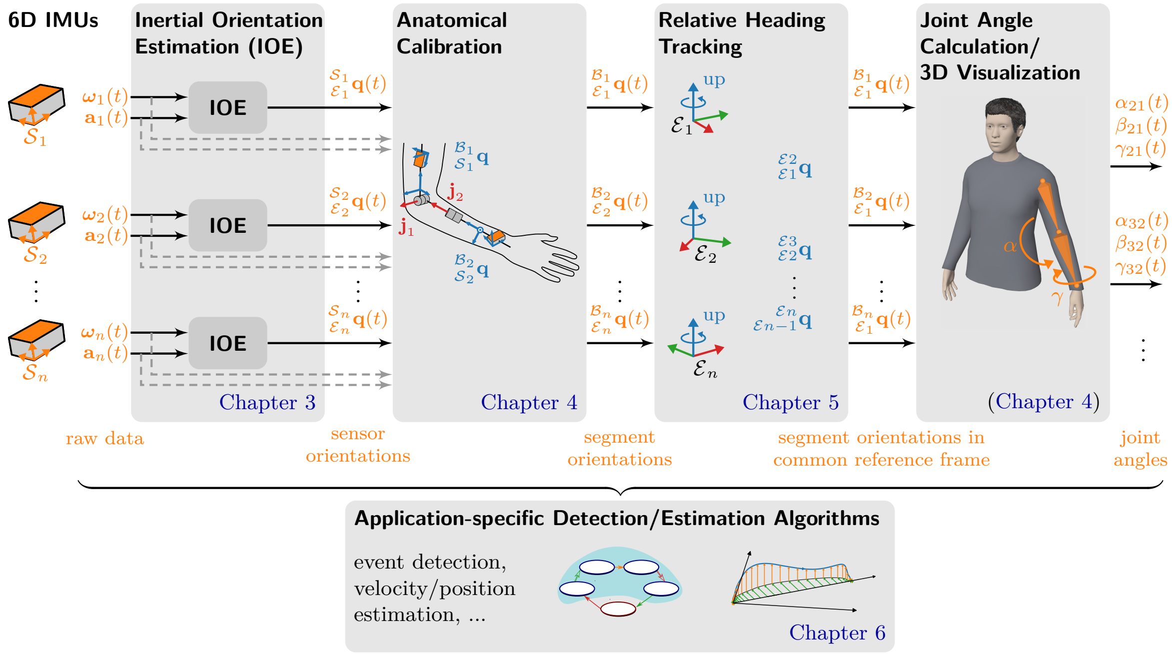

Figure 1.1: Typical steps of inertial motion tracking in kinematic chains. An IMU is attached to each motion segment of interest. From the raw data of each IMU, its orientation is estimated. Then, anatomical calibration determines the relative orientation between the sensor and the anatomical segment coordinate system. If magnetometers are not used, the relative heading information is recovered, for example, by exploiting kinematic constraints. The resulting orientations can be used for joint angle calculation and 3D visualization. Furthermore, application-specific motion parameters are derived from the raw data and the estimated orientations.

IMUs have been employed for motion analysis in many application domains, e.g., in medicine and rehabilitation [11]. In these fields, IMUs often serve as a measurement tool, e.g., for objective outcome measurement [12, 13, 14], rehabilitation monitoring [15], or gait analysis [16, 17]. Alternatively, they are used to provide immediate feedback in interactive applications, e.g., in rehabilitation training games for children with cerebral palsy [18] or training systems based on rehabilitation robotics [19], or to trigger functional electrical stimulation (FES) in drop foot stimulators [20] or in neuroprosthetic systems that allow people with paraplegia to perform swimming exercises [21]. Other application domains include sports, such as baseball [22], kayaking [23], and beach volleyball [24], as well as entertainment [4] and indoor pedestrian navigation [25]. Beyond human motion analysis, similar IMU-based approaches facilitate motion tracking in robotic or mechanical applications, such as autonomous vehicles [26], aerial vehicles [27], or kites [28]. Comprehensive reviews on IMUs-based motion analysis can be found in [1, 2, 5, 6, 29], and Chapters 3 to 6 include summaries of the state of the art in the field covered in the respective chapter.

Despite the promise of using IMUs in unsupervised long-term daily-life assessment scenarios, the actual use of IMUs for motion analysis is mostly still limited to carefully designed experiments performed by trained personnel in controlled lab environments. Several challenges and limitations in the state of the art impede the widespread adoption of IMU-based motion analysis:

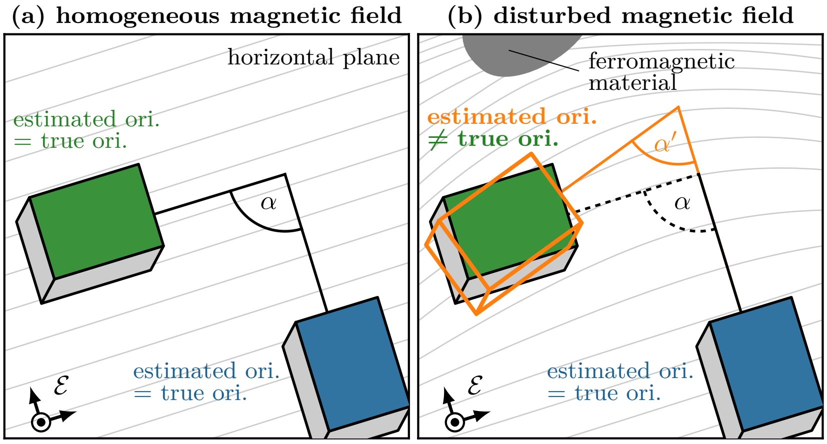

Figure 1.2: The orientation of two bodies is estimated **(a)** in a homogeneous magnetic field and **(b)** in a magnetic field disturbed by ferromagnetic material. The magnetic disturbance causes the estimated relative orientation of the two bodies to be corrupted, i.e., we obtain wrong joint angles.

- There is a need for sensor fusion algorithms to estimate the orientation, and current methods only provide high accuracy in certain situations and require careful application-specific parameter tuning.
- There is a need to know in which orientation the sensors are attached to the body segments, which is often solved by careful manual sensor placement or by performing dedicated calibration movements, both of which are time-consuming and error-prone.
- Most applications require heading information and, thus, the use of magnetometers. However, in indoor environments, the magnetic field is often severely disturbed, leading to large errors in the obtained motion parameters, as illustrated in Figure 1.2. There is a need for robust and long-term stable magnetometer-free motion tracking methods.
- Often, advanced estimation tasks are tackled by complex monolithic application-specific algorithms that solve several problems at once and are therefore hard to reuse.

As summarized in [30], in recent years, many researchers have contributed to overcoming those limitations. This thesis aims to make a contribution toward this important development by proposing a modular set of methods, following the structure introduced in Figure 1.1, that help overcome the challenges mentioned above and facilitate non-restrictive magnetometer-free motion tracking in kinematic chains.

1.2 Contributions to the State of the Art

The main contributions of this thesis to the state of the art in IMU-based motion analysis are:

1. A modular approach for magnetometer-free IMU-based motion analysis based on the separation of heading and inclination information.
2. A comprehensive publicly available benchmark dataset for the evaluation of inertial orientation estimation algorithms.

3. A highly accurate IMU orientation estimation algorithm that supports online gyroscope bias estimation and magnetic disturbance rejection and that does not require application-specific parameter tuning.
4. A set of methods for automatic anatomical calibration for 2-DoF joints that work on arbitrary motions.
5. A set of methods for magnetometer-free motion tracking in kinematic chains that consist of hinge joints and 2-DoF joints.
6. A set of methods for gait assessment by foot-worn IMUs that allows for the calculation of spatiotemporal parameters (such as gait phase durations, stride length, and cadence), as well as 3D position and angle trajectories, and that is extensively validated on data recorded with healthy subjects and subjects with various gait pathologies.

The value and impact of those contributions will be discussed in Chapter 7.

1.3 Outline

Following the introduction, this thesis consists of six further chapters. Chapter 2 introduces fundamental concepts relevant to the understanding of the subsequent chapters. In Chapter 3, the extensive BROAD dataset for orientation estimation is presented, the VQF orientation estimation algorithm is introduced, and its accuracy is validated on a diverse collection of experimental data. Chapter 4 presents methods for automatic anatomical calibration that allow for the estimation of the sensor-to-segment orientation by exploiting kinematic joint constraints without using magnetometer measurements and without requiring the subject to perform specific and precise calibration movements. The same constraints are used in Chapter 5 to recover the relative heading of body segments in kinematic chains in order to facilitate long-term stable magnetometer-free motion tracking. Chapter 6 presents methods for non-restrictive gait assessment via foot-worn IMUs and evaluates the accuracy on a large number of trials with healthy subjects and subjects with diverse gait pathologies, using a pressure-based system and optical motion capture as reference. Finally, Chapter 7 provides general conclusions and an outlook.

1.4 Related Publications by the Author

This thesis is based in part on the publications listed below. A detailed statement regarding the relation between those publications and the content of this thesis is given at the beginning of Chapters 3 to 6.

[135] D. Laidig, T. Schauer, and T. Seel. “Exploiting Kinematic Constraints to Compensate Magnetic Disturbances When Calculating Joint Angles of Approximate Hinge Joints from Orientation Estimates of Inertial Sensors”. In: *2017 International Conference on Rehabilitation Robotics (ICORR)*. London, UK, July 17–20, 2017, pp. 971–976. DOI: 10.1109/ICORR.2017.8009375.

[91] D. Laidig, P. Müller, and T. Seel. “Automatic Anatomical Calibration for IMU-based Elbow Angle Measurement in Disturbed Magnetic Fields”. In: *Current Directions in Biomedical Engineering* 3.2 (2017), pp. 167–170. DOI: 10.1515/cdbme-2017-0035.

[137] D. Laidig, D. Lehmann, M.-A. Bégin, and T. Seel. “Magnetometer-Free Realtime Inertial Motion Tracking by Exploitation of Kinematic Constraints in 2-DoF Joints”. In: *2019 41st Annual International Conference of the IEEE Engineering in Medicine and Biology Society (EMBC)*. Berlin, Germany, July 23–27, 2019, pp. 1233–1238. DOI: 10.1109/EMBC.2019.8857535.

[136] D. Lehmann, D. Laidig, and T. Seel. “Magnetometer-Free Motion Tracking of One-Dimensional Joints by Exploiting Kinematic Constraints”. In: *Proceedings on Automation in Medical Engineering* 1.1 (Feb. 16, 2020), Article 027. URL: https://www.journals.infinite-science.de/index.php/automed/article/view/335.

[50] D. Laidig, M. Caruso, A. Cereatti, and T. Seel. “BROAD—A Benchmark for Robust Inertial Orientation Estimation”. In: *Data* 6.7 (7 July 2021), Article 72. DOI: 10.3390/data6070072.

[159] D. Laidig, A. J. Jocham, B. Guggenberger, K. Adamer, M. Fischer, and T. Seel. “Calibration-Free Gait Assessment by Foot-Worn Inertial Sensors”. In: *Frontiers in Digital Health* 3 (2021), Article 147. ISSN: 2673-253X. DOI: 10.3389/fdgth.2021.736418.

[51] D. Laidig, I. Weygers, S. Bachhuber, and T. Seel. “VQF: A Milestone in Accuracy and Versatility of 6D and 9D Inertial Orientation Estimation”. In: *2022 25th International Conference on Information Fusion (FUSION)*. Linköping, Sweden, July 4–7, 2022, pp. 1–6. DOI: 10.23919/FUSION49751.2022.9841356.

[52] D. Laidig and T. Seel. “VQF: Highly Accurate IMU Orientation Estimation with Bias Estimation and Magnetic Disturbance Rejection”. In: *Information Fusion* 91 (Mar. 1, 2023), pp. 187–204. ISSN: 1566-2535. DOI: 10.1016/j.inffus.2022.10.014.

[92] D. Laidig, I. Weygers, and T. Seel. “Self-Calibrating Magnetometer-Free Inertial Motion Tracking of 2-DoF Joints”. In: *Sensors* 22.24 (24 Dec. 2022), Article 9850. ISSN: 1424-8220. DOI: 10.3390/s22249850.

[160] A. J. Jocham, D. Laidig, B. Guggenberger, and T. Seel. “Measuring Highly Accurate Foot Position and Angle Trajectories with Foot-Mounted IMUs in Clinical Practice”. [Manuscript submitted for publication]. 2023.

Furthermore, the author of this thesis authored or co-authored the following publications that do not directly constitute part of this thesis but are related to the field of inertial motion tracking.

[201] D. Laidig, T. Seel, and T. Schauer. “Entwicklung einer inertialsensorbasierten Eversionswinkelregelung für einen Peroneus-Stimulator [Development of an Inertial Sensor-Based Eversion Angle Control System for a Peroneal Stimulator]”. In: *7th International Symposium on Automatic Control*. Wismar, Germany, 2014, pp. 1–12.

[20] T. Seel, D. Laidig, M. Valtin, C. Werner, J. Raisch, and T. Schauer. “Feedback Control of Foot Eversion in the Adaptive Peroneal Stimulator”. In: *22nd Mediterranean Conference on Control and Automation*. Palermo, Italy, June 16–19, 2014, pp. 1482–1487. DOI: 10.1109/MED.2014.6961585.

[247] D. Laidig, S. Trimpe, and T. Seel. “Event-Based Sampling for Reducing Communication Load in Realtime Human Motion Analysis by Wireless Inertial Sensor Networks”. In: *Current Directions in Biomedical Engineering* 2.1 (2016), pp. 711–714. DOI: 10.1515/cdbme-2016-0154.

[158] M. Valtin, C. Salchow, T. Seel, D. Laidig, and T. Schauer. “Modular Finger and Hand Motion Capturing System Based on Inertial and Magnetic Sensors”. In: *Current Directions in Biomedical Engineering* 3.1 (2017), pp. 19–23. DOI: 10.1515/cdbme-2017-0005.

[139] D. Laidig and T. Seel. “Deriving Kinematic Quantities from Accelerometer Readings for Assessment of Functional Upper Limb Motions”. In: *Current Directions in Biomedical Engineering* 3.2 (2017), pp. 573–576. DOI: 10.1515/cdbme-2017-0119.

[138] C. Salchow-Hömmen, L. Callies, D. Laidig, M. Valtin, T. Schauer, and T. Seel. “A Tangible Solution for Hand Motion Tracking in Clinical Applications”. In: *Sensors* 19.1 (Jan. 2019), Article 208. DOI: 10.3390/s19010208.

[248] T. Zhang, D. Laidig, and T. Seel. “Stop Repeating Yourself: Exploitation of Repetitive Signal Patterns to Reduce Communication Load in Sensor Networks”. In: *2019 18th European Control Conference (ECC)*. Naples, Italy, June 25–28, 2019, pp. 2893–2898. DOI: 10.23919/ECC.2019.8796022.

[14] M. Dechenaud, D. Laidig, T. Seel, H. B. Gilbert, and N. A. Kuznetsov. “Development of Adapted Guitar to Improve Motor Function after Stroke: Feasibility Study in Young Adults”. In: *2019 41st Annual International Conference of the IEEE Engineering in Medicine and Biology Society (EMBC)*. Berlin, Germany, July 23–27, 2019, pp. 5488–5493. DOI: 10.1109/EMBC.2019.8856651.

[157] D. Lehmann, D. Laidig, R. Deimel, and T. Seel. “Magnetometer-Free Inertial Motion Tracking of Arbitrary Joints with Range of Motion Constraints”. In: *IFAC-PapersOnLine*. 21st IFAC World Congress 53.2 (Jan. 1, 2020), pp. 16016–16022. ISSN: 2405-8963. DOI: 10.1016/j.ifacol.2020.12.401.

[54] M. Caruso, A. M. Sabatini, D. Laidig, T. Seel, M. Knaflitz, U. Della Croce, and A. Cereatti. “Analysis of the Accuracy of Ten Algorithms for Orientation Estimation Using Inertial and Magnetic Sensing under Optimal Conditions: One Size Does Not Fit All”. In: *Sensors* 21.7 (7 Jan. 2021), Article 2543. DOI: 10.3390/s21072543.

1.5 Related Theses Supervised by the Author

Many of the results that are presented in this thesis have been obtained with the invaluable support of several students whose Bachelor thesis or Master thesis the author supervised or co-supervised.

[Th-1] Lars Nienerowski. “Experimentelle Weiterentwicklung und Validierung von Methoden zur selbstkalibrierenden inertialen Bewegungsanalyse am Arm”. Master Thesis, Hochschule Stralsund, Germany, 2018.

[Th-2] Eva Kastenbauer. “Data-based Development and Validation of Inertial Foot Motion Tracking and 3D Visualisation for Clinical Gait Analysis”. Bachelor Thesis, TU Berlin, Germany, 2019.

[Th-3] Dustin Lehmann. “Magnetometer-free Inertial Motion Tracking in Truncated Kinematic Chains”. Master Thesis, TU Berlin, Germany, 2019.

[Th-4] Kai Brands. “Development and Validation of Long-Time Stable Magnetometer-Free Inertial Lower-Body Motion Tracking”. Master Thesis, TU Berlin, Germany, 2020.

[Th-5] Ricardo Martínez García. “Motion Tracking For Autonomous Search And Rescue Drones”. Master Thesis, TU Berlin, Germany, 2020.

[Th-6] Carlos Tiana Gómez. “Gait Analysis Methods’ Review, Extension and Validation using Magnetometer-free Inertial Data”. Master Thesis, TU Berlin, Germany, 2020.

[Th-7] Bo Yang. “Full-body Motion Capture by Magnetometer-Free Inertial Sensor Fusion”. Master Thesis, TU Berlin, Germany, 2021.

2

Fundamentals

In this chapter, we will take a brief look at fundamental concepts that are relevant to the understanding of the subsequent chapters and introduce the notation used throughout this thesis.

2.1 Notation

First, we briefly summarize the notation employed in this thesis. Note that many aspects are explained in more detail in the subsequent sections of this chapter. The main aspects are also illustrated in Figure 2.1.

When dealing with sampled signals, we use a sampling index $k \in \{1, 2, \ldots, N\}$ to define the sampling time instants $t_k = kT_\mathrm{s}$, with the sampling time $T_\mathrm{s} \in \mathbb{R}_{>0}$. The raw IMU measurements are denoted $\boldsymbol{\omega}(t_k) \in \mathbb{R}^3$ for the gyroscope, $\mathbf{a}(t_k) \in \mathbb{R}^3$ for the accelerometer, and $\mathbf{m}(t_k) \in \mathbb{R}^3$ for the magnetometer. In the following, we use the term 9D to refer to sensor fusion with gyroscopes, accelerometers, and magnetometers, while 6D refers to magnetometer-free sensor fusion from gyroscopes and accelerometers.

We use unit quaternions in vector notation to represent rotations and orientations, which will be introduced in Section 2.4. We denote quaternion multiplication by $\otimes$ and, in this context, implicitly regard 3D vectors as pure quaternions. Quaternions that represent the rotation of an angle $\alpha \in \mathbb{R}$ around an axis $\mathbf{v} \in \mathbb{R}^3$ are written as $(\alpha \,@\, \mathbf{v}) := \begin{bmatrix} \cos\frac{\alpha}{2} & \frac{\mathbf{v}^\intercal}{\|\mathbf{v}\|} \sin\frac{\alpha}{2} \end{bmatrix}^\intercal$. Coordinate systems are denoted by calligraphic letters, the most common being $\mathcal{S}$ for IMUs *(sensor)*, $\mathcal{B}$ for (human) body segments *(body)*, and $\mathcal{E}$ for reference frames *(Earth)*. A sensor index i is used to distinguish sensor-specific coordinate systems. In particular, $\mathcal{E}$ refers to the common east-north-up (ENU) reference frame, in contrast to sensor-specific reference frames $\mathcal{E}_i$ that are used in 6D orientation estimation and have a vertical z-axis and an undefined heading.

For quaternions, the coordinate systems are specified in left upper and lower indices. For example, ${}^{\mathcal{S}_i(t_k)}_{\mathcal{E}}\mathbf{q}$ is the orientation of IMU i at time t_k, relative to the ENU reference frame $\mathcal{E}$, and ${}^{\mathcal{S}_i(t_k)}_{\mathcal{S}_i(t_{k-1})}\mathbf{q}$ is the rotation of IMU i from time t_{k-1} to t_k. For vectors, we use

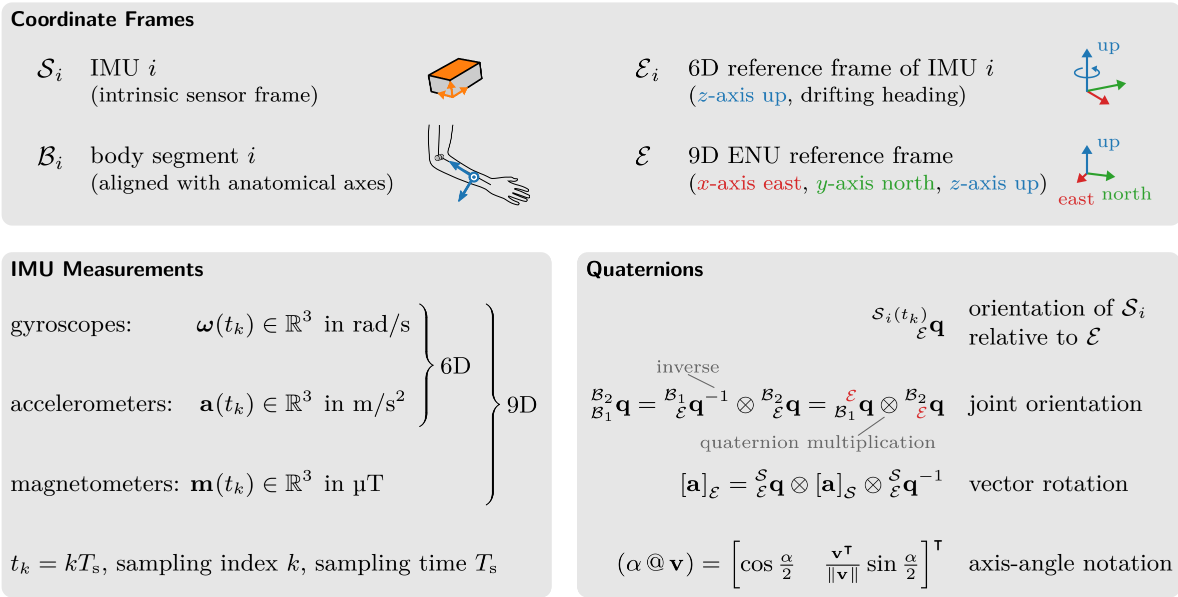

Figure 2.1: Overview of the notation employed in this thesis. Calligraphic letters are used for coordinate systems, the IMU measurements are $\boldsymbol{\omega}(t_k)$, $\mathbf{a}(t_k)$, and $\mathbf{m}(t_k)$, and left upper and lower indices are used to indicate coordinate frames of rotation and orientation quaternions.

square brackets to specify the coordinate system in which a vector is expressed. For example, $[\mathbf{a}]_{\mathcal{E}} = {}^{\mathcal{S}}_{\mathcal{E}}\mathbf{q} \otimes \mathbf{a} \otimes {}^{\mathcal{S}}_{\mathcal{E}}\mathbf{q}^{-1}$ is the accelerometer measurement transformed into frame $\mathcal{E}$.

Furthermore, $\mathbf{v}^\intercal$ denotes the transpose of the vector $\mathbf{v}$, and $\|\cdot\|$ refers to the Euclidean norm. Scalars are typeset in italics, while bold letters are used for vectors and matrices. The operators $\times$ and $\cdot$ are used for cross and dot products, respectively. The two-argument arctangent, which calculates the argument to the complex number $x + jy$, is denoted $\operatorname{atan2}(y, x)$.

2.2 Inertial Sensors

An inertial measurement unit (IMU), sometimes also just called inertial sensor, consists of a three-axis gyroscope, a three-axis accelerometer, and, often, a three-axis magnetometer. It measures angular rates, specific force (also called proper acceleration), and magnetic field strength. The measurements are 3D vectors in a local coordinate system that rotates with the IMU. In the following, we briefly examine the measurement principles and the main properties of miniaturized IMUs realized as microelectromechanical systems (MEMS).

2.2.1 Accelerometers

Accelerometers measure specific force [9], which includes both acceleration due to gravity and acceleration due to change in velocity and is commonly reported in m/s^2 or g (i.e., multiples of Earth's gravity). Note that gravity is sensed as a vector pointing in upward direction (with a length of approximately 9.81 m/s^2), which becomes clear when considering the displacement of the mass due to gravity in Figure 2.2a.

This figure illustrates the basic working principle of a MEMS accelerometer, which in the following is summarized based on the detailed description given in [7]: A mass m is suspended on the sensor frame via springs to allow for movement in the sensing direction. Due to inertia, an acceleration $\mathbf{a}(t)$ in sensing direction causes a displacement $\Delta x(t)$ of the mass (proportional

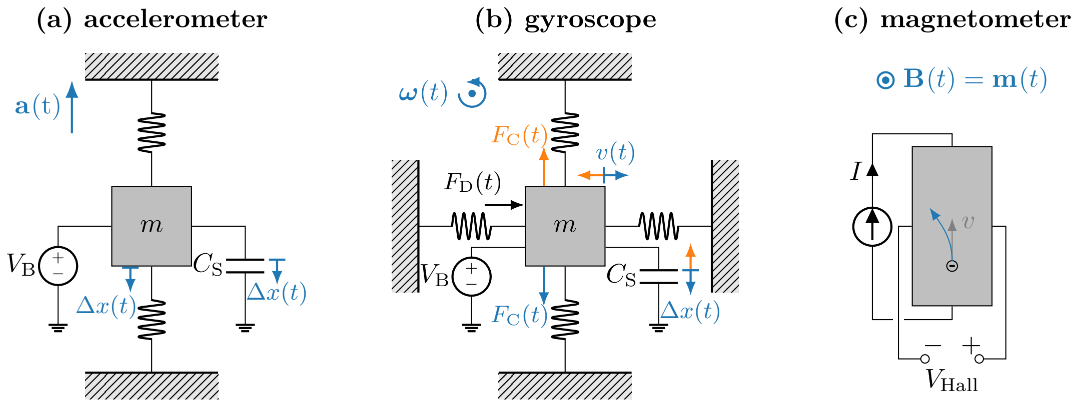

Figure 2.2: Illustration of the working principles of gyroscopes, accelerometers, and magnetometers. **(a)** An accelerometer can be realized via a MEMS spring-mass system. Acceleration causes displacement of a mass m, which causes a change in the sensing capacity C_S. [7] **(b)** MEMS gyroscopes induce a vibration of a mass m in driving direction (horizontal). The Coriolis force F_C, orthogonal to both rotation direction and the velocity v in driving direction, causes a displacement and, therefore, a change in the sensing capacity C_S [7]. **(c)** Magnetic fields can, for example, be measured via the Hall effect [31].

to the acceleration, the mass, and the spring constant). This displacement causes a change in the sensing capacity C_S and, due to the constant bias voltage V_B, a change in the charge of this capacity, which can be measured and converted to a digital acceleration value.

2.2.2 Gyroscopes

Gyroscopes measure the angular velocity, also called angular rate, of the sensor frame with respect to any inertial frame [9], i.e., a frame that is neither rotating nor accelerating. Note that, due to Earth's rotation, an IMU that is stationary on Earth's surface measures a rotation of approximately 15 °/h or 0.004 °/s. Often, this rotation is neglected, and the Earth-fixed reference frame $\mathcal{E}$ is assumed to be an inertial frame of reference.

MEMS-based vibratory rate gyroscopes make use of the Coriolis force $\mathbf{F}_C(t) = -2m(\boldsymbol{\omega}(t) \times \mathbf{v}(t))$, i.e., the inertial force that acts on objects of mass m that are moving at velocity $\mathbf{v}(t)$ in a reference frame that is rotated with angular velocity $\boldsymbol{\omega}(t)$. The basic working principle is illustrated in Figure 2.2b and in the following summarized based on the detailed description given in [7]: A mass m is suspended on the sensor frame via springs to allow for movement in two orthogonal directions: a driving direction and a sensing direction. A driving force $F_D(t)$ is applied to induce a known sinusoidal velocity $v(t)$ (which, like the sensing capacities, can be realized via MEMS capacities with a variable gap distance). An angular rate orthogonal to the driving and the sensing direction experiences a Coriolis force, which can be measured via the sensing capacity C_S.

2.2.3 Magnetometers

Magnetometers measure the magnetic field strength (strictly speaking, the magnetic flux density) and often report values in µT or in arbitrary units. As further detailed in Section 2.3, the magnetic field observed by the sensor is a combination of Earth's magnetic field, influences from ferromagnetic material and electric devices in the environment, as well as influences from ferromagnetic material and electric circuits that are rigidly attached to the sensor.

Magnetometers can be realized with various different approaches, for example, based on the Hall effect or anisotropic magnetoresistance (AMR) [31]. The Hall effect is illustrated in Figure 2.2c. In an electric field $\mathbf{E}(t)$ and a magnetic field $\mathbf{B}(t)$, a particle with charge q and velocity $\mathbf{v}$ experiences the Lorentz force $\mathbf{F}_\mathrm{L} = q\mathbf{E} + q\mathbf{v} \times \mathbf{B}$. When a current flows through a (semi)conductor, the Lorentz force redirects the charged particles in a direction that is orthogonal to both the magnetic field and the direction of the current. The resulting voltage between the sides of the conductor is called the Hall voltage V_Hall and is proportional to the magnetic field strength.

2.2.4 Error Characteristics

In the following, we take a brief look at the main errors of IMUs and their characteristics.

The measurements of each sensor axis can be subject to a constant offset, scaling errors, as well as nonlinearities. Furthermore, the axes of the three sensors of each kind are usually not perfectly orthogonal *(non-orthogonality)*, and the coordinate systems of the gyroscope, accelerometer, and magnetometer triads are not perfectly aligned *(misalignment)*. Those errors can be eliminated via calibration and are therefore collectively called calibration errors [10]. For magnetometers, the calibration errors additionally include soft and hard iron effects caused by material rigidly attached to the sensor, which we will consider in more detail in Section 2.3. Even after calibration, some of the errors remain, either due to imperfect calibration, missing or incomplete compensation of temperature effects, or slow changes in the calibration errors over time. In practice, the slow change in errors is especially relevant for sensor biases.

For properly calibrated gyroscopes and accelerometers, Gaussian noise and a slowly changing bias are the main errors of concern [9]. For strapdown integration of gyroscopes, the angular error due to bias grows linearly with time, while for the angle random walk due to noise, the standard deviation of the angular error grows with the square root of time [10]. With current MEMS gyroscopes, the effect of bias on the error is much larger than the effect of random walk due to noise. Consider a realistic value of angle random walk of $0.4\,^\circ/\sqrt{\mathrm{h}}$ (Section 3.4.1) and a very small residual gyroscope bias of $0.05\,^\circ/\mathrm{s}$. Random walk leads to a standard deviation of the error of $\sqrt{10\,\mathrm{s}}\;0.4\,^\circ/\sqrt{\mathrm{h}} = 0.02^\circ$ in ten seconds and 0.4° in one hour, while the drift due to bias is 0.5° after ten seconds and 180° after one hour.

Inertial sensor errors are often characterized by the Allan variance [9, 10, 32]. Two particularly useful metrics that can be derived from the Allan variance are the random walk, corresponding to the Allan deviation for an observation time of 1 s, and the bias instability, corresponding to the minimum Allan deviation [10].

2.2.5 Inertial Orientation Estimation

Inertial orientation estimation (IOE) is the estimation of the sensor orientation with respect to a reference frame. This is achieved by sensor fusion of the gyroscope measurements with the accelerometer and magnetometer measurements. If only gyroscopes and accelerometers are employed, we use the term 6D IOE, while 9D IOE refers to IOE with the use of magnetometers. In both cases, strapdown integration of the angular rates is used to track changes in the orientation, which is only accurate for short time spans, and the fact that the accelerometer measurements contain information about the vertical direction is used to correct long-term drift. In 9D IOE, a further drift correction step exploits the fact that the magnetometer measurements provide information on the direction of the local magnetic field. Therefore, 9D IOE yields the sensor orientation with respect to a fixed reference frame, typically using the ENU convention. Note that, due to the rotation of the Earth, this reference frame is not an inertial frame in the strict sense. In 6D IOE, there is no horizontal reference, and the resulting orientations are provided with respect to a reference frame that has one vertical axis, typically the z-axis, but slowly drifts around this axis.

2.3 Indoor Magnetic Fields

Many IMU-based motion analysis protocols rely on a homogeneous magnetic field since the direction of the magnetic field is used as a reference for the heading. However, in indoor environments, the magnetic field is often inhomogeneous, which can cause large errors in the estimated motion parameters. In the following, we take a closer look at the characteristics of Earth's magnetic field, magnetic disturbances, indoor magnetic fields, and the implications for IMU-based motion analysis.

The fundamental idea of using the magnetic field as a common reference to align the heading of multiple IMUs is based on the assumption that Earth's magnetic field is homogeneous, at least when considering distances relevant for human motion tracking. In the context of IOE, the two fundamental properties to describe Earth's magnetic field are the magnitude and the dip angle (also called magnetic dip or inclination). The dip angle is commonly defined so that a positive angle indicates that the magnetic field points downward (typically in the northern hemisphere) and a negative angle indicates that the magnetic field points upward (typically in the southern hemisphere) [33]. For example, in Berlin, Earth's magnetic field has a total magnitude of 49.9 µT and a dip angle of 68.0° [34]. This implies that the magnitude of the horizontal component is 18.7 µT.

This magnetic field is influenced by hard and soft iron effects due to nearby ferromagnetic material and electric devices. Hard iron effects are the result of permanent magnetization of ferromagnetic material [35]. Soft iron effects are caused by the response of materials to external magnetic fields (e.g., Earth's magnetic field) [35].

If the source of the hard and soft iron effects is rigidly attached to the IMU (i.e., if it is part of the IMU itself or a device onto which the IMU is attached), hard iron effects cause a constant bias and soft iron effects cause a combination of scaling and rotation of the measured magnetic field [35]. The influence of those effects can be eliminated by magnetometer calibration [35]. Note that, due to changes in magnetization, frequent recalibration is necessary.

If the sources of magnetic disturbances are part of the environment, i.e., not rigidly attached to the IMU, their influence on the magnetometer measurements depends on the orientation and distance between the IMU and the source of the disturbance. Thus, magnetometer calibration cannot eliminate those effects.

Abundant studies have shown that in indoor environments, severe magnetic disturbances are common and that the local magnetic fields are inhomogeneous, e.g., [36, 37, 38, 39, 40]. One illustrative example from [36] is shown in Figure 2.3. The consequence in the context of 9D IOE is that the assumption of a common reference frame that is shared by all IMUs

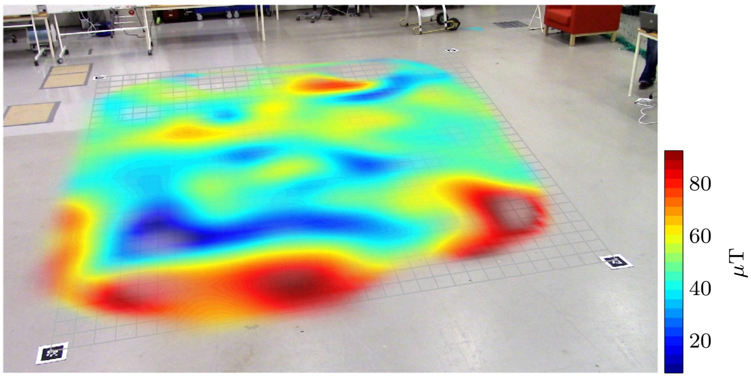

Figure 2.3: Magnitude of the magnetic field in a lab environment. In indoor environments, the magnetic field is often severely disturbed, which limits the usefulness of magnetometers as a heading reference. Image from [36], © 2018 IEEE.

does not hold anymore. This leads to errors when calculating relative orientations and joint angles, as illustrated in Figure 1.2. Consider three distinct disturbance scenarios that may occur when using inertial sensors indoors.

1. A magnetic disturbance might be temporary, i.e., in an otherwise homogeneous magnetic field, the sensor comes close to a ferromagnetic object for a short time (or a ferromagnetic object moves near the sensor). This type of disturbance can often be detected, for example, based on the magnetic field strength and the dip angle.

2. If a sensor moves near a large ferromagnetic object and stays there (e.g., the hand rests on a desk with a ferromagnetic frame), the magnetic field is disturbed permanently or for long time spans.

3. Indoors, the magnetic field may be different from Earth's magnetic field but almost homogeneous in a person's movement area. When the person moves to a different location or leaves the building, the magnetic field can also be locally homogeneous but with different strength and direction.

Different approaches exist in inertial sensor fusion to deal with magnetic disturbances, which are detailed in the following.

The standard approach is to employ 9D sensor fusion, always relying on the magnetic field to determine the heading. This method is affected by magnetic disturbances. The only way to reduce the influence of magnetic disturbances is to use large time constants for the fusion of the magnetometer readings. This reduces the errors caused by very short disturbances. However, the choice of the fusion weights is limited by the expected gyroscope drift that is supposed to be corrected by the magnetic field measurements.

A better solution to deal with short disturbances is gating of the sensor fusion weights, i.e., detecting that the magnetic field is disturbed and not employing the magnetic field readings in that case. Therefore, 9D sensor fusion with proper gating is not influenced by temporary disturbances. However, while the gating is active, gyroscope bias on the global vertical axis is not corrected, and the heading of the estimated orientations will slowly drift. This limits the maximum duration that disturbances can be tolerated.

A different approach is to use 6D sensor fusion, i.e., to not rely on the magnetic field at all. In this case, the heading of each sensor's orientation is unknown and slowly drifts due to gyroscope bias. However, knowledge of at least the relative heading between the different IMUs is necessary to calculate many kinematic quantities, such as joint angles. Therefore, approaches for magnetometer-free motion tracking either focus on quantities that can be calculated without heading information or on estimating the missing heading information from other sources.

2.4 Representing Rotations and Orientations

There is a large variety of mathematical representations for rotations in three-dimensional space, the most common being unit quaternions, rotation matrices, and Euler angles. For many applications, unit quaternions are the most suitable choice due to the efficient representation and the lack of singularities. The following is a concise introduction with a focus on the knowledge needed to employ unit quaternions for representing rotations and orientations. Comprehensive references that include further information and more mathematical background include [41, 42, 43].

2.4.1 Quaternions

Quaternions, first described by William Rowan Hamilton in 1843, are often described as an extension of complex numbers. In contrast to complex numbers $a + jb \in \mathbb{C}$ with two components $a, b \in \mathbb{R}$ and the imaginary unit $j^2 = -1$, quaternions consist of four components, with the three imaginary units i, j, and k defined by

$$i^2 = j^2 = k^2 = ijk = -1. \tag{2.1}$$

For simplicity, we use the vector notation and represent quaternions by four-dimensional vectors, i.e., we write the quaternion $\mathbf{q} = q_w + iq_x + jq_y + kq_z$, with $q_w, q_x, q_y, q_z \in \mathbb{R}$, as

$$\mathbf{q} = \begin{bmatrix} q_w & q_x & q_y & q_z \end{bmatrix}^\intercal \in \mathbb{R}^4. \tag{2.2}$$

The component q_w is called the scalar part, and $[\, q_x \;\; q_y \;\; q_z \,]^\intercal$ is called the vector part of the quaternion $\mathbf{q}$. A quaternion with $q_w = 0$ is called *pure*.

When adding two quaternions, their corresponding components are added, i.e., for $\mathbf{q}_1 =: [\, q_{1w} \;\; q_{1x} \;\; q_{1y} \;\; q_{1z} \,]^\intercal$ and $\mathbf{q}_2 =: [\, q_{2w} \;\; q_{2x} \;\; q_{2y} \;\; q_{2z} \,]^\intercal$,

$$\mathbf{q}_1 + \mathbf{q}_2 = [\, q_{1w} + q_{2w} \;\; q_{1x} + q_{2x} \;\; q_{1y} + q_{2y} \;\; q_{1z} + q_{2z} \,]^\intercal. \tag{2.3}$$

When multiplying a quaternion with a scalar, each element of the quaternion is multiplied with the scalar, i.e., for $\mathbf{q} =: [\, q_w \;\; q_x \;\; q_y \;\; q_z \,]^\intercal$ and $s \in \mathbb{R}$,

$$s\mathbf{q} = [\, sq_w \;\; sq_x \;\; sq_y \;\; sq_z \,]^\intercal. \tag{2.4}$$

Multiplication of two quaternions $\mathbf{q}_1 =: [\, q_{1w} \;\; q_{1x} \;\; q_{1y} \;\; q_{1z} \,]^\intercal$ and $\mathbf{q}_2 =: [\, q_{2w} \;\; q_{2x} \;\; q_{2y} \;\; q_{2z} \,]^\intercal$ directly follows from expanding $(q_{1w} + iq_{1x} + jq_{1y} + kq_{1z})(q_{2w} + iq_{2x} + jq_{2y} + kq_{2z})$ and applying

(2.1). We use the symbol $\otimes$ to denote quaternion multiplication and obtain

$$\mathbf{q}_1 \otimes \mathbf{q}_2 = \begin{bmatrix} q_{1w}q_{2w} - q_{1x}q_{2x} - q_{1y}q_{2y} - q_{1z}q_{2z} \\ q_{1w}q_{2x} + q_{1x}q_{2w} + q_{1y}q_{2z} - q_{1z}q_{2y} \\ q_{1w}q_{2y} - q_{1x}q_{2z} + q_{1y}q_{2w} + q_{1z}q_{2x} \\ q_{1w}q_{2z} + q_{1x}q_{2y} - q_{1y}q_{2x} + q_{1z}q_{2w} \end{bmatrix}. \tag{2.5}$$

The quaternion $[1\ 0\ 0\ 0]^\intercal$ is the multiplicative identity, i.e., $[1\ 0\ 0\ 0]^\intercal \otimes \mathbf{q} = \mathbf{q} \otimes [1\ 0\ 0\ 0]^\intercal = \mathbf{q}$ for all quaternions $\mathbf{q}$. Note that in general, like matrix multiplication, quaternion multiplication is not commutative.

The conjugate $\mathbf{q}^*$ of a quaternion $\mathbf{q} =: [\,q_w\ \ q_x\ \ q_y\ \ q_z\,]^\intercal$ is

$$\mathbf{q}^* := \begin{bmatrix} q_w & -q_x & -q_y & -q_z \end{bmatrix}^\intercal, \tag{2.6}$$

and the norm $\|\mathbf{q}\|$ is

$$\|\mathbf{q}\| := \sqrt{q_w^2 + q_x^2 + q_y^2 + q_z^2}. \tag{2.7}$$

The quaternion norm is multiplicative, i.e., $\|\mathbf{q}_1 \otimes \mathbf{q}_2\| = \|\mathbf{q}_1\|\,\|\mathbf{q}_2\|$, and a unit quaternion, i.e., a quaternion with norm 1, can be obtained by dividing a quaternion $\mathbf{q}$ by its norm.

For every quaternion $\mathbf{q}$, there is an inverse quaternion $\mathbf{q}^{-1}$ so that $\mathbf{q} \otimes \mathbf{q}^{-1} = \mathbf{q}^{-1} \otimes \mathbf{q} = [1\ 0\ 0\ 0]^\intercal$, given by

$$\mathbf{q}^{-1} := \frac{\mathbf{q}^*}{\|\mathbf{q}\|^2}. \tag{2.8}$$

Note that for unit quaternions, the inverse and the conjugate are identical.

2.4.2 Representing Rotations and Orientations with Unit Quaternions

Euler's rotation theorem states that any sequence of rotations can be expressed as a single rotation. This rotation can be specified by a rotation angle $\alpha \in \mathbb{R}$ and an axis $\mathbf{v} \in \mathbb{R}^3$. The same information can be represented as a unit quaternion. This quaternion $\mathbf{q}$, in the following denoted $(\alpha\,@\,\mathbf{v})$, is given as

$$\mathbf{q} = (\alpha\,@\,\mathbf{v}) := \begin{bmatrix} \cos\frac{\alpha}{2} \\ \frac{\mathbf{v}}{\|\mathbf{v}\|}\sin\frac{\alpha}{2} \end{bmatrix}. \tag{2.9}$$

Note that, without restricting the values of α or $\mathbf{v}$, a given axis-angle representation of a rotation is not unique. For example, rotating 90° around the x-axis has the same effect as rotating 270° around the negative x-axis. For unit quaternions, there are two different representations of each rotation since $\mathbf{q}$ and $-\mathbf{q}$ represent the same rotation (the rotation angle of $-\mathbf{q}$ is $2\pi - \alpha$, and the rotation axis is $-\mathbf{v}$).

The rotation angle of a quaternion $\mathbf{q} =: [\,q_w\ \ q_x\ \ q_y\ \ q_z\,]^\intercal$ can be recovered by $\alpha = 2\arccos q_w$ or, more numerically stable, by $\alpha = 2\,\mathrm{atan2}(\sqrt{q_x^2 + q_y^2 + q_z^2}, q_w)$ (both returning an angle in the interval $[0, 2\pi]$). The rotation axis can be recovered by normalizing the vector part of the quaternion (and choosing an arbitrary axis if the quaternion is $[\pm 1\ 0\ 0\ 0]^\intercal$).

The rotation matrix equivalent to a rotation expressed as a unit quaternion $\mathbf{q} =: [\,q_w \;\; q_x \;\; q_y \;\; q_z\,]^\intercal$ is

$$\mathbf{R} = \begin{bmatrix} 1-2q_y^2-2q_z^2 & 2(q_xq_y-q_zq_w) & 2(q_xq_z+q_yq_w) \\ 2(q_xq_y+q_zq_w) & 1-2q_x^2-2q_z^2 & 2(q_yq_z-q_xq_w) \\ 2(q_xq_z-q_yq_w) & 2(q_yq_z+q_xq_w) & 1-2q_x^2-2q_y^2 \end{bmatrix}. \tag{2.10}$$

The conversion from rotation matrices to unit quaternions is possible via various algorithms with different numerical properties (see [43] for one example).

The *orientation* of an object is specified relative to a reference frame and represented using the imaginary rotation between the coordinate system of the reference frame and the coordinate system of the object. Note that analogously, a position in 3D space is represented via the translation from the origin of a reference frame to the origin of the object's coordinate system. In the following, we use left upper and lower indices to denote the object's coordinate system and the reference frame, respectively. For example, we write the orientation of an IMU $\mathcal{S}$ *(sensor)* at time t, relative to the time-invariant ENU reference frame $\mathcal{E}$ *(earth)*, as ${}^{\mathcal{S}(t)}_{\mathcal{E}}\mathbf{q}$.

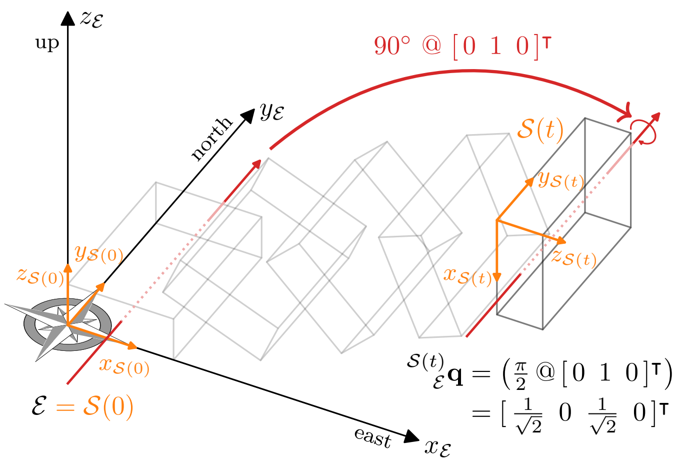

Figure 2.4: Example orientation of an IMU coordinate system $\mathcal{S}$ at time t, relative to an ENU reference frame $\mathcal{E}$. The orientation is specified via the rotation from a hypothetical time $t = 0$, in which reference frame and IMU coordinate system were aligned, to the current orientation at time t. In the given example, this is a rotation of 90° around the y-axis. Note that the translation is for illustration purposes only and does not affect the orientation.

Figure 2.4 illustrates this orientation and the relation to a rotation for a simple example. In this example, we assume that the reference frame $\mathcal{E}$ and the IMU coordinate system $\mathcal{S}$ are initially aligned, i.e., ${}^{\mathcal{S}(t=0)}_{\mathcal{E}}\mathbf{q} = [\,1 \;\; 0 \;\; 0 \;\; 0\,]^\intercal$. The orientation of the IMU at time t, i.e., ${}^{\mathcal{S}(t)}_{\mathcal{E}}\mathbf{q}$, is represented by the imaginary rotation from $\mathcal{E} = \mathcal{S}(t=0)$ to $\mathcal{S}(t)$, i.e., a rotation of 90° around the y-axis. Therefore,

$${}^{\mathcal{S}(t)}_{\mathcal{E}}\mathbf{q} = {}^{\mathcal{S}(t)}_{\mathcal{S}(0)}\mathbf{q} = \left(\tfrac{\pi}{2} @ [\,0 \;\; 1 \;\; 0\,]^\intercal\right) = \begin{bmatrix} \frac{1}{\sqrt{2}} & 0 & \frac{1}{\sqrt{2}} & 0 \end{bmatrix}^\intercal. \tag{2.11}$$

Orientations can also uniquely be defined by two linearly independent vector observations. In the given example, this means that in order to define ${}^{\mathcal{S}(t)}_{\mathcal{E}}\mathbf{q}$, we could use two axes of $\mathcal{E}$ expressed in $\mathcal{S}(t)$ coordinates or vice versa. The general task of determining the rotation between two reference frames from vector observations is known as Wahba's problem [44, 45].

2.4.3 Common Operations with Rotations and Orientations

Multiple rotations can be concatenated using quaternion multiplication (in the same way that rotations can be concatenated by matrix multiplication of their rotation matrices). Assume that an IMU $\mathcal{S}$ is rigidly attached to a body segment with coordinate system $\mathcal{B}$ and that we know the IMU orientation ${}^{\mathcal{S}}_{\mathcal{E}}\mathbf{q}$ and the orientation in which the IMU is attached to the body segment, i.e., ${}^{\mathcal{B}}_{\mathcal{S}}\mathbf{q}$. In this case, we can obtain the orientation of the segment relative to the reference frame $\mathcal{E}$ as

$$ {}^{\mathcal{B}}_{\mathcal{E}}\mathbf{q} = {}^{\mathcal{S}}_{\mathcal{E}}\mathbf{q} \otimes {}^{\mathcal{B}}_{\mathcal{S}}\mathbf{q}. \tag{2.12} $$

Note how, with the introduced notation, coordinate system indices – here $\mathcal{S}$ – cancel out in "backslash" direction.

In the context of chaining rotations, the terms *intrinsic* and *extrinsic rotation* are sometimes used. An intrinsic rotation is specified in the rotated coordinate system and corresponds to multiplying a quaternion on the right side. For example, in (2.12), ${}^{\mathcal{B}}_{\mathcal{S}}\mathbf{q}$ is an intrinsic rotation that is applied to the IMU orientation ${}^{\mathcal{S}}_{\mathcal{E}}\mathbf{q}$. For extrinsic rotations, the rotation axis is specified in the reference frame, which corresponds to multiplying a quaternion on the left side.

The inverse of a rotation and orientation is obtained by inverting the quaternion[1], which effectively multiplies the rotation axis with -1. With the introduced notation, this swaps the upper and lower index, i.e., ${}^{\mathcal{S}}_{\mathcal{E}}\mathbf{q}^{-1} = {}^{\mathcal{E}}_{\mathcal{S}}\mathbf{q}$. In combination with quaternion multiplication, the inverse allows us to obtain relative orientations. Assume that we know the orientations ${}^{\mathcal{S}_1}_{\mathcal{E}}\mathbf{q}$ and ${}^{\mathcal{S}_2}_{\mathcal{E}}\mathbf{q}$ of two IMUs $\mathcal{S}_1$ and $\mathcal{S}_2$. Their relative orientation ${}^{\mathcal{S}_2}_{\mathcal{S}_1}\mathbf{q}$ is given by

$$ {}^{\mathcal{S}_1}_{\mathcal{E}}\mathbf{q}^{-1} \otimes {}^{\mathcal{S}_2}_{\mathcal{E}}\mathbf{q} = {}^{\mathcal{E}}_{\mathcal{S}_1}\mathbf{q} \otimes {}^{\mathcal{S}_2}_{\mathcal{E}}\mathbf{q} = {}^{\mathcal{S}_2}_{\mathcal{S}_1}\mathbf{q}. \tag{2.13} $$

When applying the rotation given by the quaternion $\mathbf{q}$ to a vector $\mathbf{v} \in \mathbb{R}^3$, the rotated vector $\mathbf{v}_{\text{rot}}$ is given by

$$ \begin{bmatrix} 0 \\ \mathbf{v}_{\text{rot}} \end{bmatrix} = \mathbf{q} \otimes \begin{bmatrix} 0 \\ \mathbf{v} \end{bmatrix} \otimes \mathbf{q}^{-1}, \tag{2.14} $$

which is equivalent to the matrix-vector product of the corresponding rotation matrix $\mathbf{R}$ and the vector $\mathbf{v}$, i.e., $\mathbf{v}_{\text{rot}} = \mathbf{R}\mathbf{v}$. Note that the operation $\mathbf{q} \otimes \cdot \otimes \mathbf{q}^{-1}$ preserves the scalar component (in this case, zero) and the norm of the vector part. For a compact notation, we implicitly regard 3D vectors as their corresponding pure quaternions and write

$$ \mathbf{v}_{\text{rot}} = \mathbf{q} \otimes \mathbf{v} \otimes \mathbf{q}^{-1}. \tag{2.15} $$

We use square brackets to specify the coordinate system in which a vector is expressed. With the introduced quaternion notation, the rotation operation transforms vectors from the coordinate system specified in the upper index into the coordinate system specified in the lower index of the quaternion. This means that rotation with a sensor orientation ${}^{\mathcal{S}(t)}_{\mathcal{E}}\mathbf{q}$ transforms a vector expressed in sensor coordinates $[\mathbf{v}]_{\mathcal{S}(t)}$ into a vector $[\mathbf{v}]_{\mathcal{E}}$ expressed in $\mathcal{E}$ coordinates:

$$ [\mathbf{v}]_{\mathcal{E}} = {}^{\mathcal{S}(t)}_{\mathcal{E}}\mathbf{q} \otimes [\mathbf{v}]_{\mathcal{S}(t)} \otimes {}^{\mathcal{S}(t)}_{\mathcal{E}}\mathbf{q}^{-1} \tag{2.16} $$

[1] Remember that for unit quaternions, the norm and the conjugate are the same. We still write $\mathbf{q}^{-1}$ rather than $\mathbf{q}^*$ to emphasize the effect on the rotation rather than the mathematical operation.

As an example, consider Figure 2.4 and a local measurement in sensor coordinates of $[\mathbf{v}]_{\mathcal{S}(t)} = [1\ 0\ 0]^\intercal$. As can be seen in the figure, $x_{\mathcal{S}(t)}$ points down, and the same vector expressed in global coordinates is $[\mathbf{v}]_{\mathcal{E}} = [0\ 0\ -1]^\intercal$. The vector $[0\ 0\ -1]^\intercal$ is obtained by rotating $[1\ 0\ 0]^\intercal$ by an angle of 90° around the y-axis, i.e., by rotating with the sensor orientation ${}^{\mathcal{S}(t)}_{\mathcal{E}}\mathbf{q}$.

The operation $\mathbf{q} \otimes \cdot \otimes \mathbf{q}^{-1}$ can also be used to transform the reference frame of rotations and orientations. In this case, the operation rotates the rotation axis of the quaternion while the scalar part and therefore the rotation angle do not change. For example, when we consider the relative sensor orientation ${}^{\mathcal{S}_2}_{\mathcal{S}_1}\mathbf{q} = {}^{\mathcal{S}_1}_{\mathcal{E}}\mathbf{q}^{-1} \otimes {}^{\mathcal{S}_2}_{\mathcal{E}}\mathbf{q}$, the rotation axis of this quaternion is expressed in the coordinate systems of $\mathcal{S}_1$ and $\mathcal{S}_2$.[2] Rotating this axis using ${}^{\mathcal{S}_1}_{\mathcal{E}}\mathbf{q}$ expresses the relative sensor orientation as a rotation in the reference frame $\mathcal{E}$:

$$\left[{}^{\mathcal{S}_2}_{\mathcal{S}_1}\mathbf{q}\right]_{\mathcal{E}} = {}^{\mathcal{S}_1}_{\mathcal{E}}\mathbf{q} \otimes {}^{\mathcal{S}_2}_{\mathcal{S}_1}\mathbf{q} \otimes {}^{\mathcal{S}_1}_{\mathcal{E}}\mathbf{q}^{-1} = {}^{\mathcal{S}_2}_{\mathcal{E}}\mathbf{q} \otimes {}^{\mathcal{S}_1}_{\mathcal{E}}\mathbf{q}^{-1}. \tag{2.17}$$

Note that the same result is obtained when using ${}^{\mathcal{S}_2}_{\mathcal{E}}\mathbf{q}$ instead of ${}^{\mathcal{S}_1}_{\mathcal{E}}\mathbf{q}$, since $\left[{}^{\mathcal{S}_2}_{\mathcal{S}_1}\mathbf{q}\right]_{\mathcal{E}} = {}^{\mathcal{S}_2}_{\mathcal{E}}\mathbf{q} \otimes {}^{\mathcal{S}_2}_{\mathcal{S}_1}\mathbf{q} \otimes {}^{\mathcal{S}_2}_{\mathcal{E}}\mathbf{q}^{-1} = {}^{\mathcal{S}_2}_{\mathcal{E}}\mathbf{q} \otimes {}^{\mathcal{S}_2}_{\mathcal{S}_1}\mathbf{q} \otimes {}^{\mathcal{E}}_{\mathcal{S}_2}\mathbf{q} = {}^{\mathcal{S}_2}_{\mathcal{E}}\mathbf{q} \otimes {}^{\mathcal{S}_1}_{\mathcal{E}}\mathbf{q}^{-1}$.

2.4.4 Euler Angles

Rotations and orientations can also be described by Euler angles, which are a sequence of three rotation angles. Those three angles specify a chained rotation sequence around coordinate axes. When using Euler angles, it is necessary to specify

1. if extrinsic or intrinsic rotations are used (i.e., if the rotation axes stay fixed in the original coordinate system or if they move with each rotation),
2. which of the 12 possible sequences of rotation axes is used.

When given Euler angles (α, β, γ), a corresponding quaternion can easily be obtained by concatenating the corresponding rotations. For extrinsic z-x-y Euler angles, for example, the corresponding quaternion is

$$\mathbf{q}_{\text{ext}} = (\gamma\,@\,[0\ 1\ 0]^\intercal) \otimes (\beta\,@\,[1\ 0\ 0]^\intercal) \otimes (\alpha\,@\,[0\ 0\ 1]^\intercal)\,, \tag{2.18}$$

and for intrinsic z-x'-y'' Euler angles (where $'$ and $''$ indicate that the axes are rotated), the corresponding quaternion is

$$\mathbf{q}_{\text{int}} = (\alpha\,@\,[0\ 0\ 1]^\intercal) \otimes (\beta\,@\,[1\ 0\ 0]^\intercal) \otimes (\gamma\,@\,[0\ 1\ 0]^\intercal)\,. \tag{2.19}$$

Any unit quaternion can be decomposed into Euler angles. For example, for a quaternion $[q_w\ q_x\ q_y\ q_z]^\intercal$, the intrinsic z-x'-y'' Euler angles (α, β, γ) can be calculated as

$$\alpha = \operatorname{atan2}(2q_wq_z - 2q_xq_y, q_w^2 - q_x^2 + q_y^2 - q_z^2), \tag{2.20}$$
$$\beta = \arcsin(2q_wq_x + 2q_yq_z), \tag{2.21}$$
$$\gamma = \operatorname{atan2}(2q_wq_y - 2q_xq_z, q_w^2 - q_x^2 - q_y^2 + q_z^2). \tag{2.22}$$

[2] Note that rotations do not change the coordinates of the rotation axis vector. Therefore, the coordinates of the rotation axis are the same in $\mathcal{S}_1$ and $\mathcal{S}_2$.

Similar equations can be derived for all other possible sequences of rotation axes.

Euler angles are subject to a singularity, often called gimbal lock, that causes two of the three angles to not be well-defined for certain orientations.[3] Even close to this singularity, a small change in the orientation can lead to a large change in the corresponding Euler angles. Still, Euler angles are widely used for reporting joint angles, and the recommendations by the International Society of Biomechanics (ISB) for the reporting of human joint motion [46, 47] directly translate to intrinsic Euler angles.

2.4.5 Decomposition into Rotation Around Axis and Residual (Projection)

Any given rotation $\mathbf{q}$ can be decomposed into a "main" rotation around a given axis $\mathbf{v}$ such that the residual rotation $\mathbf{q}_{\text{res}}$ is as small as possible, i.e.,

$$\mathbf{q} = (\alpha \,@\, \mathbf{v}) \otimes \mathbf{q}_{\text{res}}, \tag{2.23}$$

where α and $\mathbf{q}_{\text{res}}$ are to be determined. Since this operation is similar to vector projection, in which a vector is decomposed into a vector in a specified direction and the shortest possible residual vector, we call this method quaternion projection and note two useful properties:

1. The rotation axis of $\mathbf{q}_{\text{res}}$ is always orthogonal to $\mathbf{v}$.
2. When changing the order of the rotations, i.e., $\mathbf{q} = \tilde{\mathbf{q}}_{\text{res}} \otimes (\alpha \,@\, \mathbf{v})$, we obtain the same projection angle α, and the residual rotation $\tilde{\mathbf{q}}_{\text{res}}$ has the same angle (but, in general, a different axis).

In the field of motion planning in robotics, this decomposition is known as the swing-twist decomposition [48] and is used to decompose a given rotation of a robotic arm into a rotation around the longitudinal axis *(twist)* and an orthogonal rotation *(swing)*.

To derive an efficient way of calculating the projection angle, we minimize the rotation angle of the residual quaternion $\mathbf{q}_{\text{res}} = (\alpha \,@ -\mathbf{v}) \otimes \mathbf{q}$. With $\mathbf{q} =: [\, q_w \;\; q_x \;\; q_y \;\; q_z \,]^\intercal$, $\mathbf{v} =: [\, v_x \;\; v_y \;\; v_z \,]^\intercal$ and $\|\mathbf{v}\| = 1$, the w-component w_{res} of $\mathbf{q}_{\text{res}}$ is

$$\begin{aligned} w_{\text{res}} &= q_w \cos\frac{\alpha}{2} + (q_x v_x + q_y v_y + q_z v_z) \sin\frac{\alpha}{2} \\ &= \sqrt{q_w^2 + [\, q_x \;\; q_y \;\; q_z \,]\mathbf{v}} \cos\left(\frac{\alpha}{2} - \operatorname{atan2}([\, q_x \;\; q_y \;\; q_z \,]\mathbf{v}, q_w)\right) \end{aligned} \tag{2.24}$$

and has a maximum (corresponding to the smallest possible rotation angle) at

$$\alpha = 2 \operatorname{atan2}([\, q_x \;\; q_y \;\; q_z \,]\mathbf{v}, q_w). \tag{2.25}$$

The angle of the residual quaternion can be derived from the value of the w-component at this maximum and is $2 \arccos \sqrt{q_w^2 + [\, q_x \;\; q_y \;\; q_z \,]\mathbf{v}}$.

[3] This happens when the second angle is ±90° for *Tait-Bryan angles* (for which the first and third axes are different, e.g., z-x'-y'') and when the second angle is 0° or 180° for *proper Euler angles* (for which the first and third axes are the same, e.g., z-x'-z'').

2.5 Heading and Inclination

Different definitions of heading and inclination have been used in the literature. In the following, we introduce a definition that is particularly useful for magnetometer-free motion tracking and avoids the use of Euler angles.

Inclination, also called attitude, is the orientation with respect to the vertical axis (or, equivalently, the horizontal plane) and can be determined from accelerometer measurements during rest. Heading, also called azimuth or yaw, is a rotation around the vertical axis and is commonly defined via the direction of magnetic north.

Often, the heading is defined to be the first angle of z-y'-x'' or z-x'-y'' Euler angles, while the other two Euler angles (pitch and roll) are defined to be the inclination [9, 49]. With this definition, the inclination is a concatenation of two rotations, and, in general, the rotation axis of the inclination quaternion is not horizontal. Furthermore, the specific value of the heading angle depends on the arbitrary choice of the Euler rotation sequence. Close to gimbal lock, small rotations around a horizontal axis can cause large deviations in the observed heading angle.

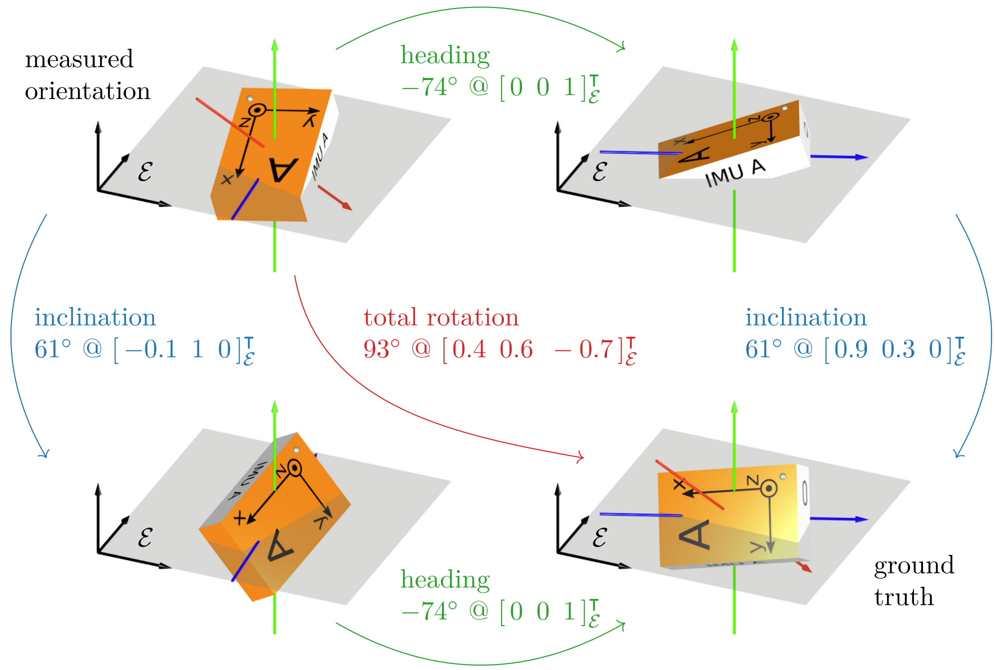

Figure 2.5: Decomposition of an exemplary orientation difference into heading and inclination. Heading is a rotation around the vertical axis, and inclination is a rotation around a horizontal axis. Note that in contrast to other decompositions that are used in literature, the angles commute.

To avoid those disadvantages, we instead decompose a given rotation quaternion into a rotation around the vertical z-axis, called heading, and a rotation around a horizontal axis, called inclination, as illustrated in Figure 2.5. Mathematically, we achieve this by employing the quaternion projection method from Section 2.4.5, with the projection axis being $[0\ \ 0\ \ 1]^\intercal$. For a given quaternion $\mathbf{q} = \mathbf{q}_\mathrm{h} \otimes \mathbf{q}_\mathrm{i} =: [\, q_w\ \ q_x\ \ q_y\ \ q_z \,]^\intercal$, the heading δ is the projection angle, i.e.,

$$\mathbf{q}_\mathrm{h} = (\delta \,@\, [0\ \ 0\ \ 1]^\intercal)\,, \text{ with } \delta = \operatorname{atan2}(q_z, q_w), \tag{2.26}$$

and the inclination is the residual quaternion

$$\mathbf{q}_\mathrm{i} = \mathbf{q}_\mathrm{h}^{-1} \otimes \mathbf{q}, \tag{2.27}$$

which has a rotation angle of $2\arccos\sqrt{q_w^2 + q_z^2}$. Note that the heading angle and the inclination angle do not uniquely define the orientation. However, the decomposition can easily be extended to be reversible by adding a third angle that describes the direction of the inclination rotation axis in the horizontal plane.

This decomposition into heading and inclination is only valid if the rotation axis of the quaternion is expressed in a reference frame with vertical z-axis. When using the notation introduced in Section 2.4, this means that one of the two indices has to be $\mathcal{E}$ or $\mathcal{E}_i$. If this is not the case, the rotation has to be transformed into the reference frame (see Section 2.4.3). As an example, consider the estimate of a sensor orientation ${}^{\mathcal{S}}_{\mathcal{E}}\mathbf{q}$ and a given ground truth for this orientation ${}^{\mathcal{S}_\mathrm{true}}_{\mathcal{E}}\mathbf{q}$. The relative orientation ${}^{\mathcal{S}}_{\mathcal{S}_\mathrm{true}}\mathbf{q} = {}^{\mathcal{S}_\mathrm{true}}_{\mathcal{E}}\mathbf{q}^{-1} \otimes {}^{\mathcal{S}}_{\mathcal{E}}\mathbf{q}$, describing the estimation error, is expressed in local sensor coordinates. To decompose this estimation error into heading and orientation, we first transform the relative orientation into the reference frame $\mathcal{E}$, i.e.,

$$\begin{aligned} \left[{}^{\mathcal{S}}_{\mathcal{S}_\mathrm{true}}\mathbf{q}\right]_{\mathcal{E}} &= {}^{\mathcal{S}}_{\mathcal{E}}\mathbf{q} \otimes \left({}^{\mathcal{S}_\mathrm{true}}_{\mathcal{E}}\mathbf{q}^{-1} \otimes {}^{\mathcal{S}}_{\mathcal{E}}\mathbf{q}\right) \otimes {}^{\mathcal{S}}_{\mathcal{E}}\mathbf{q}^{-1} \\ &= {}^{\mathcal{S}}_{\mathcal{E}}\mathbf{q} \otimes {}^{\mathcal{S}_\mathrm{true}}_{\mathcal{E}}\mathbf{q}^{-1}, \end{aligned} \tag{2.28}$$

and then decompose this quaternion into heading and inclination.

3

Versatile Inertial Orientation Estimation Algorithm

Inertial orientation estimation (IOE) is the fusion of gyroscope measurements with accelerometer and magnetometer measurements to estimate the orientation of a single IMU. It is the most fundamental task in inertial sensor fusion and a central building block in most advanced applications of IMUs. This chapter introduces a robust and versatile open-source IOE algorithm. It can perform simultaneous 6D and 9D sensor fusion and includes optional extensions for gyroscope bias estimation and magnetic disturbance rejection. An extensive benchmark dataset, specifically designed for robust IOE validation, is introduced. Together with existing publicly available datasets, it is used to evaluate the accuracy of the proposed method.

Text, figures, and tables found in this chapter have been previously published, with slight modifications, in the following works:

- [50] D. Laidig, M. Caruso, A. Cereatti, and T. Seel. "BROAD—A Benchmark for Robust Inertial Orientation Estimation". In: *Data* 6.7 (7 July 2021), Article 72. DOI: `10.3390/data6070072`.
- [51] D. Laidig, I. Weygers, S. Bachhuber, and T. Seel. "VQF: A Milestone in Accuracy and Versatility of 6D and 9D Inertial Orientation Estimation". In: *2022 25th International Conference on Information Fusion (FUSION)*. Linköping, Sweden, July 4–7, 2022, pp. 1–6. DOI: `10.23919/FUSION49751.2022.9841356`.
- [52] D. Laidig and T. Seel. "VQF: Highly Accurate IMU Orientation Estimation with Bias Estimation and Magnetic Disturbance Rejection". In: *Information Fusion* 91 (Mar. 1, 2023), pp. 187–204. ISSN: 1566-2535. DOI: `10.1016/j.inffus.2022.10.014`.

Sections 3.3, 3.4, and 3.5 have been previously published in [50]. Sections 3.6 and 3.7 have been previously published in [52] (except for Figure 3.14, which was published in [51]). Sections 3.1 and 3.8 include content from both [50] and [52]. Section 3.2 was added in this thesis and extends the information found in [51] and [52].

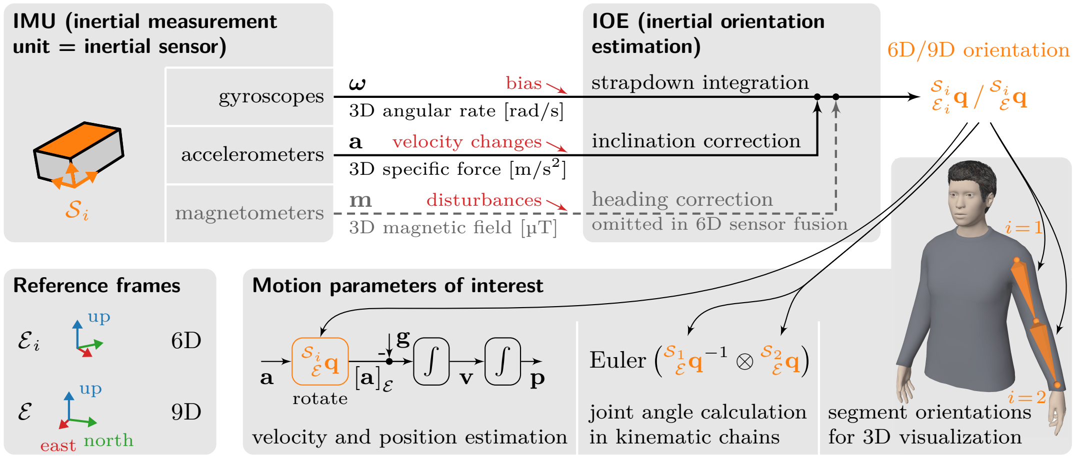

Figure 3.1: Inertial orientation estimation (IOE) is achieved by sensor fusion of the gyroscope measurements with the accelerometer measurements and, in 9D sensor fusion, the magnetometer measurements. Obtaining an accurate orientation estimate is the prerequisite for fundamental further steps in inertial motion tracking, including velocity and position estimation, joint angle calculation, and 3D visualization.

3.1 Introduction

In applications that employ IMUs for motion tracking, the raw measurements (angular rate, specific force, and magnetic field strength) are processed to determine the motion parameters of interest, e.g., the orientation of an object to which the sensor is attached, the object's velocity or position, or other application-specific motion parameters [9, 10]. As shown in Figure 3.1, determining such motion parameters generally requires the prior estimation of the orientation of the sensor with respect to an inertial frame of reference, a procedure called *inertial orientation estimation (IOE)*.

Since IOE is such a fundamental step in IMU-based motion analysis and the accuracy of all further parameters of interest depends on the accuracy of the orientation estimate, it is not surprising that abundant prior research has aimed at solving this task. This research is briefly reviewed in Section 3.2.

As illustrated in Figure 3.2, there is a general need for robust IOE algorithms that provide accurate orientation estimates and perform well for a broad range of motions without the need to manually adjust tuning parameters for each type of motion [53]. When it comes to assessing the performance of IOE algorithms, a vast number of contributions evaluate specific algorithms in specific application contexts, but few papers investigate the ability of IOE algorithms to perform across different types of motion and environmental conditions. To the best of the author's knowledge, only Caruso et al. [54] provide a systematic evaluation of multiple algorithms with respect to three different movement speeds, and Fan et al. [55] investigate the influence of magnetic disturbances on the inclination and heading estimates. However, there are no studies providing a systematic and comprehensive evaluation of the impact of different magnetic disturbances, the difference between translational and rotational motions, and different movement speeds on various IOE algorithms.

As will be detailed in Section 3.3, a thorough algorithm comparison is limited by the lack of an extensive and openly available benchmark that includes a large number of trials comprising a diverse set of movement types and environmental conditions and therefore allows

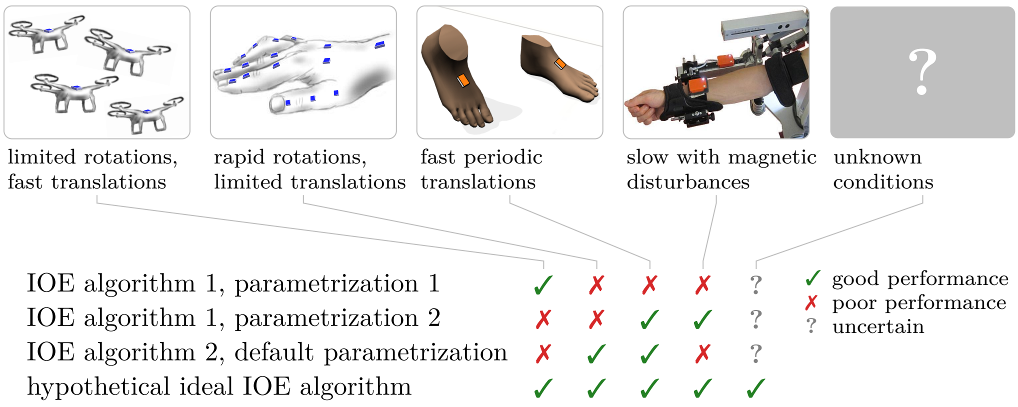

Figure 3.2: The accuracy of IOE depends on the employed algorithm, the chosen algorithm parametrization, and the specific application scenario. There is a lack of datasets and methods for systematic evaluation of IOE algorithm performance across a broad range of motion characteristics and environmental conditions.

for a truly comprehensive evaluation and assessment of IOE solutions. Such a heterogeneous set of trials with either only rotation, only translation, or combined movements at different speeds and with different durations is important for two reasons. First, in order to assess the robustness of an IOE algorithm for a wide variety of motions and environmental conditions, those motions and conditions must be included in the dataset. Second, comparing the errors for different trials yields insight into how algorithm performance or the choice of optimal parameters depends on the characteristics of the motion. As magnetic disturbances represent a major challenge in orientation estimation, it is crucial to not only consider homogeneous magnetic fields but to also include a broad range of magnetic disturbances.

In an attempt to fill this gap, this chapter introduces a benchmark dataset that is particularly useful for the objective assessment and further development of IOE algorithms. In contrast to existing publicly available datasets, this benchmark dataset

1. includes a broad range of different motions at various speeds,
2. contains separate trials with various deliberate magnetic disturbances,
3. contains separate trials with disturbances that affect the measured accelerations,
4. is already time-synchronized and contains ground truth data that requires no further preprocessing.

Furthermore, error metrics that separately consider heading, inclination, and the total orientation error are introduced, well-defined benchmark metrics that can be used to assess and compare IOE algorithm performance are specified, and example code to calculate those metrics is provided.

In previous literature that proposes new IOE algorithms, validation is almost only performed with non-public datasets, and therefore the reported performance figures cannot be compared directly. This lack of common datasets and suitable benchmarks has recently been addressed by the publication of the Sassari dataset [53] and the benchmark dataset introduced in this chapter. Newly proposed algorithms should be validated using such publicly available datasets in comparison with other state-of-the-art algorithms [56].

The few existing comparative studies show that the out-of-the-box performance of most algorithms is poor and that application-specific algorithm selection, as well as laborious parameter tuning, are necessary to achieve good results [54], which represents a severe limitation of the state of the art. Even with optimized parameters, the root-mean-square errors achieved by the best IOE algorithms are in the range of 1° to 3° for slow and smooth motions and as much as 5° to 15° for fast and challenging motions [54]. Further improving this accuracy seems highly desirable in view of the numerous applications.

In summary, while there is ample work on various IOE algorithms, evaluation of the proposed methods is often limited and cannot be compared across publications. Recent comparative reviews and benchmarks show that there is no one-size-fits-all solution that works out of the box and yields high accuracy for a wide variety of application scenarios. Furthermore, the widespread adoption of novel IOE algorithms is not only driven by accuracy but also depends on the availability of an easy-to-use implementation. In combination, this demonstrates that there is a need for an algorithm that is validated on a very large and diverse set of experimental data, provides accurate out-of-the-box orientation estimates without tuning, and is easy to use and to integrate into existing code projects.

To fill this gap, this chapter introduces a new feature-rich quaternion-based orientation estimation algorithm and then performs an extensive validation to demonstrate the exceptionally high accuracy that is achieved by this algorithm. The key differences of the proposed algorithm with respect to the state of the art are best expressed by the following five features:

1. As a novel approach to sensor fusion of gyroscopes and accelerometers, the accelerometer information is low-pass filtered in an almost-inertial frame, which yields robust rejection of accelerations that are caused by velocity changes.

2. Magnetometer-based heading correction is performed in a modular decoupled step, which eliminates the influence of magnetic disturbances on the inclination and facilitates simultaneous 6D and 9D estimation.

3. The algorithm includes extensions for online gyroscope bias estimation during rest and motion and an optional magnetic disturbance rejection strategy.

4. In contrast to the vast majority of previous approaches, an acausal offline version is available, which further increases the accuracy in situations in which real-time capability is not required.

5. Easy-to-use open-source implementations of the proposed algorithms are provided in C++, Python, and Matlab.

The main contributions and results of the extensive accuracy evaluation are:

1. In contrast to most previous work, the proposed method is extensively evaluated using a large collection of publicly available data, and in comparison with eight existing IOE algorithms.

2. The results show that the proposed method outperforms all evaluated existing methods, providing a 1.8-fold to 5-fold increase in orientation estimation accuracy.

3. For a large variety of motions, speeds, and disturbed environments, the proposed method works out of the box, and application-specific parameter tuning is not necessary.

3.2 State of the Art in Inertial Orientation Estimation

Because IOE is a fundamental step in inertial motion analysis and the accuracy of all further parameters of interest depends on the accuracy of the orientation estimate, it is not surprising that there is a large amount of previous work for solving this task. Comprehensive reviews that classify and compare the existing solution approaches are found in [54, 56]. In the following, we take a brief look at the main properties of existing IOE algorithms.

Mainly, IOE algorithms are categorized into Kalman filters, complementary filters, and, more recently, neural networks [57, 58]. In Kalman filters [59, 60], the estimate of the state of a system is updated based on a system model, a measurement model of the system outputs, and the assumption of Gaussian process and measurement noise. Since Kalman filters are widely used in state estimation and sensor fusion, it is natural that they are also employed for IOE. Due to the nonlinearity of orientation representations (Section 2.4), nonlinear Kalman filter variants such as the extended Kalman filter (EKF) [61, 62, 63, 64] or error-state Kalman filters [65, 66, 67] are often used. However, aiming to reduce computational complexity, several algorithms also use the original linear Kalman filter formulation [68, 69, 70, 71, 72].

Complementary filters [73] fuse sensor information with different noise characteristics, typically from a sensor with high-frequency disturbances and a second sensor with low-frequency disturbances. Applied to IOE, gyroscopes provide an orientation estimate that is disturbed by slow (i.e., low-frequency) drift, while the orientation estimate from accelerometers and magnetometers does not drift but exhibits severe high-frequency disturbances. IOE algorithms based on complementary filters, e.g., [73, 74, 75, 76], are popular due to their low computational complexity.

Besides estimating the sensor orientations, several IOE algorithms include additional features, the most common one being gyroscope bias estimation. In IOE algorithms based on Kalman filters, gyroscope bias is commonly modeled as a constant state with non-zero process noise [66, 67]. In complementary filters, gyroscope bias is often estimated via integral action, i.e., bias is estimated via feedback from the accelerometer and magnetometer correction step [73, 74, 76]. An alternative is to detect phases in which the IMU is at rest and bias can be estimated directly via low-pass filtering of the gyroscope measurements [75].

It is a well-known fact that the amount of information and certainty that is contained in each measurement signal varies depending on the performed motion and environmental factors such as the presence of vibrations and magnetic disturbances [58, 77]. In a fast and jerky motion, the accelerometer must be used much more carefully than during a smooth and slow motion. The magnetometer measurements are known to be highly susceptible to the presence of ferromagnetic material and electronic devices [38] (cf. Section 2.3). Previous research has led to adaptive algorithms that try to compensate such variations and disturbances. Approaches range from adapting the gain used for accelerometer correction based on the norm of the measured accelerations [75] to employing finite state machines [78] or decision trees [67] to govern how accelerometer and magnetometer information is used. In [79], magnetic

Table 3.1: Overview of selected state-of-the-art inertial orientation estimation algorithms.

Algorithm		6D	9D	Bias	Implementation
MAH	Mahony et al. [73]	✓	✓	✓	`https://x-io.co.uk/open-source-imu-and-ahrs-algorithms/`
MAD	Madgwick [74]	✓	✓	✗	`https://x-io.co.uk/open-source-imu-and-ahrs-algorithms/`
VAC	Valenti et al. [75]	✓	✓	✓	`https://wiki.ros.org/imu_complementary_filter`
FKF	Guo et al. [71]	✗	✓	✗	`https://github.com/zarathustr/FKF`
SEL	Seel et al. [76]	✓	✓	✓	`https://github.com/dlaidig/qmt`, qmt.oriEstIMU
MKF	Matlab	✓	✓	✓	Matlab R2021b (The MathWorks Inc., Natick, MA, USA), imufilter/ahrsfilter
KOK	Kok et al. [81]	✗	✓	✓	`https://github.com/manonkok/fastRobustOriEst`
RIANN	Weber et al. [57]	✓	✗	✗	`https://github.com/daniel-om-weber/riann`
VQF	proposed method	✓	✓	✓	`https://github.com/dlaidig/vqf`

disturbances are detected based on norm and dip angle. This information is used to weigh between a 6D and a 9D estimate. An alternative is to employ a model-based approach to estimate and compensate the current magnetic disturbances [80].

Anticipating the need to compare the performance of the proposed IOE algorithm with state-of-the-art literature methods, we now take a closer look at eight existing methods. The algorithms were chosen based on popularity and based on whether an official implementation from the authors (or, in some cases, another widespread implementation) is available. Table 3.1 lists those algorithms, in order of publication, along with the novel method VQF that is introduced later in this chapter. This table also shows whether the algorithm can be used for 6D and 9D orientation estimation, whether it supports gyroscope bias estimation, and where the implementation is available. Further details on each algorithm are provided in the following.

MAH is a complementary filter by Mahony et al. [73], popular due to the low computational complexity and the easy-to-use open-source implementation by Sebastian Madgwick. Gyroscope bias is estimated via integral action.

MAD is a complementary filter by Madgwick [74] based on a gradient-descent approach and popular due to the low computational complexity and the easy-to-use open-source implementation by Sebastian Madgwick. Gyroscope bias is estimated via integral action. (Note that there is also a second variant [82] of this algorithm that does not include gyroscope bias estimation.)

VAC is a complementary filter by Valenti et al. [75]. It ensures that magnetic disturbances do not influence the inclination estimates and estimates gyroscope bias with an approach based on rest detection. The algorithm is included in ROS (`http://www.ros.org/`).

FKF ("Fast Kalman Filter") is a computationally efficient IOE algorithm based on a Kalman filter by Guo et al. [71].

SEL is a complementary filter by Seel et al. [76] that ensures that magnetic disturbances do not influence the inclination estimates. It supports gyroscope bias estimation based on integral action and easy tuning via half-error time constants for the accelerometer and magnetometer correction.

MKF is the proprietary EKF-based algorithm included in the Sensor Fusion and Tracking Toolbox of Matlab.

KOK is a complementary filter by Kok et al. [81] that is influenced by MAD but further reduces the computational complexity by one third.

RIANN is a recent neural network for 6D orientation estimation by Weber et al. [57].

3.3 Brief Review of Existing Datasets for IOE Validation

Objective assessment of the accuracy of an IOE algorithm requires a highly reliable and accurate ground truth measurement. The most widely accepted gold standard measurement for the orientation of a moving object is to derive its orientation from the position measurements of active or reflective optical markers that are tracked by a set of cameras, a technique that is known as stereophotogrammetry or optical motion capture (OMC). In the past two decades, a number of studies have been performed in which an IMU and optical markers are attached to moving objects, including human body segments, aerial vehicles, and robotic systems. While many of the datasets used in these studies would be suitable for accuracy evaluation of IOE algorithms, the data is often not openly available or only available upon request to the authors, often due to privacy or ethical concerns. Furthermore, there is a lack of systematic benchmarking approaches for IOE accuracy evaluation. Despite this general lack of datasets and methods for evaluation, a few datasets have been made publicly available and are briefly reviewed in the following. Some of these datasets are created for general IOE validation, and some are provided for evaluation in specific application contexts.

In total, a literature search yielded five publicly available datasets that contain optical and inertial data from a moving object in a way that allows for accuracy evaluation of IOE algorithms. An overview of key features of the found datasets and the proposed dataset is given in Table 3.2.

In order to allow for evaluation of different aspects of an IOE algorithm, a useful universal benchmark dataset should fulfill a number of requirements. First and foremost, it should contain a large number of trials and a wide range of movements – including isolated translation and rotation movements – conducted at different speeds. To evaluate the robustness against magnetic disturbances, it is crucial to include both data recorded in a magnetically undisturbed environment and recordings with deliberate magnetic disturbances.

Furthermore, the quality of both the recorded IMU data as well as the ground truth OMC data is essential. In order to evaluate the performance in state-of-the-art applications, a state-of-the-art IMU with a sufficiently high sampling rate should be employed. Also, care should be taken to avoid artifacts due to errors in the reference system or in the recording of the IMU data. Figure 3.3 shows four examples of artifacts found in the publicly available datasets. The effects of such issues in the recorded data can often dominate the overall estimation error.

Table 3.2: Overview of key features of available datasets and the proposed benchmark dataset.

Dataset	Sensor	Sampling rate	Number of trials	Isolated translations	Isolated rotations	Different velocities	Short and long motion phases	Accelerometer disturbances	Disturbed magnetic fields	Initial rest phase	GT includes position	GT is synchronized	GT coordinate frames aligned	Reproducible error metrics defined
RepoIMU T-stick [83]	Xsens MTi	100 Hz	29	✓	✓	✓	✗	✗	✗	✗	✗	✓	✗	✗
RepoIMU Pendulum [83]	custom [84]	90-166 Hz[a]	22	✗	✗	✓	✗	✗	✗	✗	✗	✓	✗	✗
Sassari [53]	3 models	100 Hz	3	✗	✓	✓	✗	✗	✗	✓	✓	✓	✗[b]	✓
OxIOD [85]	iPhone	100 Hz	132	✗	✗	✓	✗	✗	✗	✓	✓	✓	✗	✗
EuRoC MAV [86]	ADIS16448	200 Hz	6[c]	✗	✗	✓	✗	✓	✗	✗	✓	✓	✓	✗
TUM VI [87]	BMI160	200 Hz	6[d]	✗	✗	✗	✗	✗	✗	✗	✓	✓	✓	✗
BROAD	myon aktos-t	286 Hz	39	✓	✓	✓	✓	✓	✓	✓	✓	✓	✓	✓

[a]effective rate much lower, see description
[b]local frames aligned by precise placement, reference frames not aligned, see description
[c]only counting the *Vicon room* trials with full OMC ground truth (GT)
[d]only counting the *room* trials with full OMC ground truth

In the best case, this makes the resulting observations less distinct, and in the worst case, it could lead to wrong conclusions. Therefore, measurement data should be carefully checked before it is used for evaluation.

As can be seen in Table 3.2, each of the previously published datasets covers some of the mentioned aspects, but none of them fulfill all previously mentioned requirements for a universal IOE benchmarking dataset. In the following, we will discuss each dataset in detail.

3.3.1 RepoIMU Dataset (T-stick Trials)

Of the five public datasets, RepoIMU [83] is the only dataset specifically aimed at IOE evaluation and published in a dedicated publication. The dataset consists of two distinct sets of trials, recorded with a *T-stick* and a *pendulum*.

The *T-stick* data consists of 29 trials with a duration of approximately 90 s each. As the name implies, the IMU is attached to a T-shaped stick equipped with six reflective markers. Each trial consists of either slow or fast rotation around one primary sensor axis or translation along one primary sensor axis. Data from an XSens MTi IMU and a Vicon Nexus OMC system is synchronized and provided at 100 Hz.

The authors explicitly state that the coordinate systems of IMU and ground truth are not aligned and propose a method to compensate one of the two required rotations (cf. Section 3.4.4) by a method based on quaternion averaging. Unfortunately, some of the trials contain gyroscope clipping (Figure 3.3a) and artifacts in the ground truth orientation (Figure 3.3c) that have a

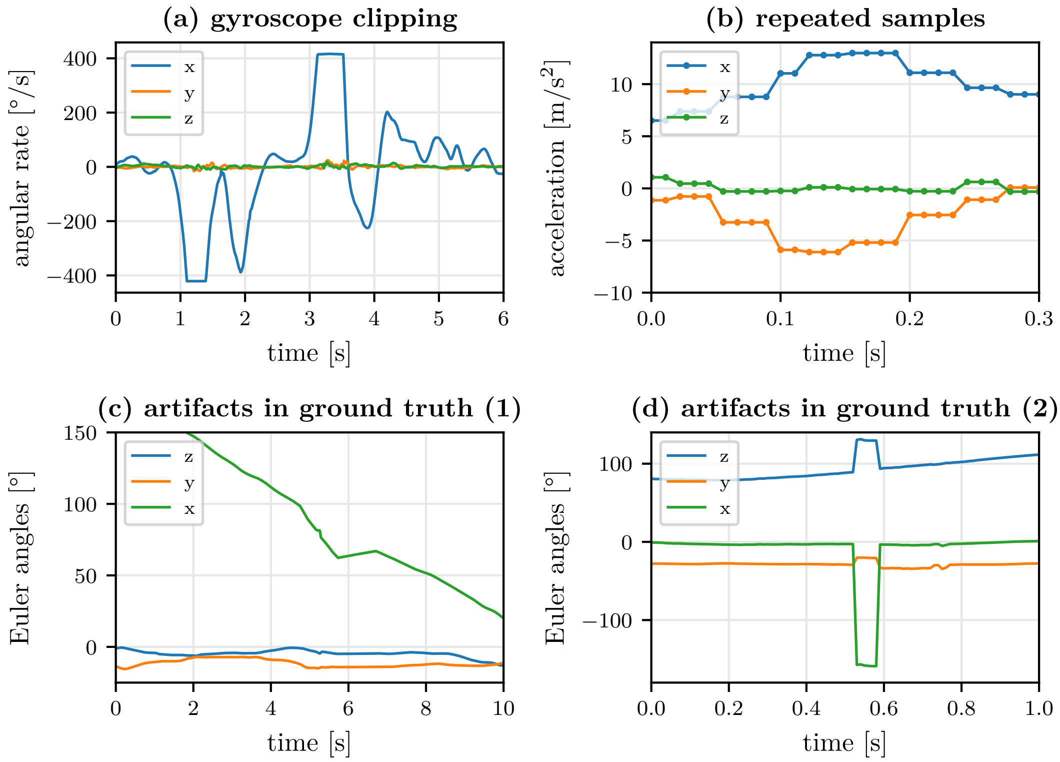

Figure 3.3: Examples of artifacts found in existing datasets. **(a)** Gyroscope clipping leading to large errors in angular rate strapdown integration. **(b)** Repeated samples in IMU data, leading to a very low effective sampling rate. **(c, d)** Two examples of artifacts found in the OMC ground truth orientations, potentially caused by interpolation of gaps and swapped markers.

substantial effect on the obtained errors. Therefore, careful preprocessing and exclusion of some trials should be considered when using the dataset for IOE accuracy evaluation.

3.3.2 RepoIMU Dataset (Pendulum Trials)

The second part of the RepoIMU dataset consists of data from a triple pendulum on which IMUs are mounted. The measurement data is provided at 90 Hz or 166 Hz. However, the IMU data frequently contains repeated samples, as shown in Figure 3.3b. This is typically a result of artificial upsampling or transmission problems where lost samples get replaced by copying the last received sample and effectively reduces the sampling rate. The sampling rate that is obtained when repeated samples are discarded is around 25 Hz for the accelerometer data and 48 Hz for the gyroscope data. Due to this fact, using the *pendulum* trials should be avoided for high-precision IOE accuracy evaluation.

3.3.3 Sassari Dataset

The dataset published in [53] is targeted at the validation of a parameter-tuning approach based on the orientation difference of two IMUs of the same model. To facilitate this, six IMUs from three manufacturers (Xsens, APDM, Shimmer) are placed on one wooden board. Rotation around specific axes and free rotation around all axes are repeated at three different speeds. The data is synchronized and provided at 100 Hz. The local coordinate frames are aligned by precise manual placement. The authors clearly describe how they calculate the obtained error metrics, including a method of using the initial orientation to align the reference frames.

This makes the dataset valuable for validating IOE accuracy. The inclusion of different speeds and multiple IMU types increases the value of this dataset. However, all motions are performed in a homogeneous magnetic field, and purely translational movements are not included. The total movement duration of all three trials is 168 s, with the longest movement phase lasting 30 s.

3.3.4 OxIOD Dataset

The Oxford Inertial Odometry Dataset (OxIOD) [85] is an extensive collection of inertial data recorded by smartphones (primarily an iPhone 7 Plus) at 100 Hz, consisting of 158 trials and covering a distance of over 42 km. An OMC ground truth is available for 132 trials. Being targeted for inertial odometry, it does not include isolated rotation and translation movements, which are useful for systematic assessment of IOE performance in various conditions, but instead covers a broad range of everyday motions.

Due to that different focus, some information (e.g., the alignment of the coordinate frames) is not described in detail. Furthermore, the ground truth orientation contains frequent irregularities (e.g., spikes in the orientation that are not accompanied by similar jumps in the IMU data, see Figure 3.3d for one example). In order to use this dataset for IOE assessment, careful preprocessing should be considered.

3.3.5 EuRoC MAV Dataset

The EuRoC MAV dataset [86] features indoor flight data of a micro aerial vehicle (MAV) and is aimed at visual-inertial 3D environment reconstruction. The six *Vicon room* trials offer a synchronized and aligned OMC-based ground truth and are suitable for IOE accuracy evaluation. Note that camera images and 3D point cloud data are also included, which are not relevant in the context of IOE.

Magnetometer data is not included, which limits the evaluation to the inclination component (cf. Section 3.5). It is noteworthy that due to the nature of the data, the motion mostly consists of horizontal translation and rotation around the vertical axis, and the inclination does not vary substantially throughout the trials. As the vibrations due to the flight are clearly visible in the raw accelerometer data, the EuRoC MAV dataset provides a unique test case for orientation estimation with disturbed accelerometer data.

Note that there is a similar but older dataset of the same research group [88]. However, the data files for this dataset do not seem to be available anymore (checked on June 22, 2021).

3.3.6 TUM VI Dataset

The TUM VI dataset [87] for visual-inertial odometry consists of 28 trials with a handheld object equipped with a camera and an IMU. Due to this application focus, most trials only include OMC ground truth data at the beginning and at the end of the trial. However, the six *room* trials include full OMC data and are suitable for IOE accuracy assessment.

Time synchronization is straightforward using provided time stamps, and the local and global coordinate systems of the OMC ground truth are aligned to the IMU frame (cf. Section 3.4.4). Similar to the EuRoC MAV data, the motion mostly consists of horizontal translation and rotation around the vertical axis, and magnetometer data is not included.

3.3.7 Summary

All reviewed datasets have in common that inertial measurements have been recorded alongside an optical ground truth. While some datasets [53, 83] are specifically recorded for evaluating the accuracy of IOE algorithms, others [85, 86, 87] are recorded with a different focus but still contain the data necessary for this purpose. The datasets [83] and [53] contain recordings with isolated rotation and translation movements at different speeds, but the number of trials and the length of the movement duration are limited. As discussed above, trials with magnetic disturbances are crucial for objective performance evaluation of high-end IOE algorithms. However, none of the datasets contain recordings performed in deliberately and realistically disturbed magnetic fields.

Due to the described lack of a universal benchmark dataset, publications proposing new IOE algorithms commonly use data for evaluation that is only available to the respective authors (see, e.g., [63, 82]), and the errors reported in different publications cannot be compared. This leads to the conclusion that there is a considerable need for an extensive benchmarking dataset for IOE accuracy assessment.

3.4 Proposed Benchmark Dataset for IOE Validation

This section introduces the Berlin Robust Orientation Estimation Assessment Dataset (BROAD). This benchmark dataset for orientation estimation consists of a diverse collection of trials, covering different movement types, speeds, and both undisturbed motions as well as motions with deliberate accelerometer disturbances and motions performed in the presence of magnetic disturbances. The dataset is publicly available at `https://dx.doi.org/10.14279/depositonce-12033` and `https://github.com/dlaidig/broad` under the terms of the CC-BY 4.0 license.

3.4.1 Hardware Setup

IMU data was recorded at a sampling rate of 286 Hz using a commercially available 9-axis inertial sensor (myon aktos-t, myon AG, Switzerland). Ground truth data at 120 Hz was obtained via an Optitrack OMC system (NaturalPoint, Inc., USA) consisting of eight Flex13 cameras.

In order to ensure a highly precise ground truth orientation, the IMU and five reflective optical markers were placed on a rigid but lightweight 3D-printed structure, which is shown in Figure 3.4, with a minimum distance of 187 mm between any two corner markers. At those marker distances, the mean position accuracy of 0.6 mm of the optical system corresponds to an angular orientation accuracy of approximately 0.2°.

The IMU input ranges were set to ±2000 °/s, ±16 g, and ±1 mT. In the recorded trials, turn-on gyroscope bias was found to be 0.17 °/s on average (per sensor axis), with 0.50 °/s

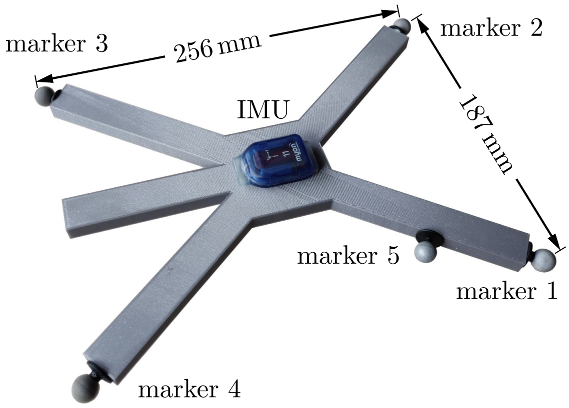

Figure 3.4: Custom 3D-printed rigid body used in the experiments. The IMU is attached to the center of the board using tape. Four reflective optical markers are attached to the ends of the X-shaped structure to increase the distance between markers. A fifth marker is used to ensure that the orientation can uniquely be determined from the marker positions.

being the maximum value. To create realistic conditions, this gyroscope bias is contained in the recorded data files. Further sensor characteristics were determined from a 49 min recording of the IMU being at rest. The noise standard deviations in x, y, and z direction were found to be 0.10 °/s, 0.09 °/s, and 0.12 °/s for the gyroscope, 0.044 m/s^2, 0.050 m/s^2, and 0.074 m/s^2 for the accelerometer, and 0.71 µT, 0.70 µT, and 0.68 µT for the magnetometer. The gyroscope random walk was 0.36 °/$\sqrt{\text{h}}$, 0.30 °/$\sqrt{\text{h}}$, and 0.41 °/$\sqrt{\text{h}}$ (Allan deviation for observation time of 1 s), and the bias instability was 6.5 °/h, 4.0 °/h, and 4.3 °/h (minimum Allan deviation).

3.4.2 Trials

The proposed benchmark dataset consists of 39 trials. We can distinguish the performed trials based on different criteria:

- the type of motion: *rotation*, *translation*, and *combined* (rotational and translational motions),
- the speed at which the motion was performed: *slow* and *fast*,
- whether the trial consists of one uninterrupted continuous motion or of several segments with short breaks in between: *no breaks* and *with breaks*,
- whether there are deliberate disturbances that affect the accelerometer measurements: *undisturbed*, *tapping*, and *vibrating smartphone*,
- the magnetic environment in which the motion takes place: *undisturbed* (homogeneous indoor magnetic field), *stationary magnet*, *attached magnet*, and *office environment*.

An overview of the performed trials can be found in Table 3.3. The considered disturbances are as follows. In the *tapping* trials, the IMU was repeatedly tapped using a finger, leading to spikes in the measured accelerations. In two trials, a *vibrating smartphone* was placed on the 3D-printed rigid body, causing substantial high-frequency disturbances in the accelerometer measurements while at the same time disturbing the magnetometer measurements. In the *stationary magnet* trials, a small neodymium magnet was placed in the vicinity of the resting

Table 3.3: Overview of the 39 trials included in the proposed benchmark dataset.

undisturbed	slow	fast
rotation	1, 2, 3, 4*, 5*	6, 7, 8*, 9*
translation	10, 11, 12, 13*, 14*	15, 16, 17*, 18*
combined	19, 20	21, 22, 23
disturbed (medium speed)		
tapping		24, 25
vibrating smartphone		26, 27
stationary magnet		28, 29, 30*, 31*
attached magnet (1–5 cm)		32, 33, 34, 35, 36
office environment		37, 38
mixed (disturbed and undisturbed)		39*

* trial consists of several motion phases with short breaks in between

place, and part of the motion was deliberately performed close to the magnet. In the *attached magnet* trials, the magnet was placed on the rigid body at distances of 1, 2, 3, 4, and 5 cm. The *office environment* (Figure 3.5) consists of various types of ferromagnetic material and electronic devices chosen to represent a typical indoor workplace environment. The *mixed* trial consists of various short challenging motion phases, both disturbed and undisturbed.

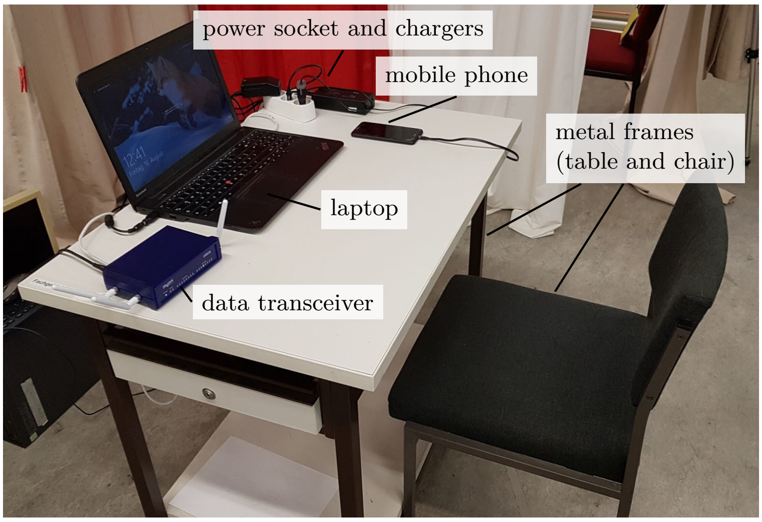

Figure 3.5: Office environment used to provide a realistic indoor scenario with magnetic disturbances.

All trials contain a rest phase of approximately 30 s at the beginning and at the end, during which the rigid body with the IMU is resting on a table. A separate annotation signal in the provided data files shows whether the IMU is at rest or in motion. This annotation was performed manually based on plots of the measurement data.

The 39 trials have a total duration of 8478 s when considering rest and motion phases and 5274 s when only considering phases with movement. The duration of a single motion phase ranges from 15 to 358 s. For the 39 trials, the root mean square (RMS) value of the angular velocity norm during motion ranges from 22 to 490 °/s (slow trials: 22 to 124 °/s, fast trials: 151 to 490 °/s) with peak values (99th percentile) of up to 1116 °/s. The RMS value of the acceleration norm (with 9.81 $\mathrm{m/s^2}$ removed) ranges from 0.5 to 23 $\mathrm{m/s^2}$ (slow trials: 0.5 to 1.6 $\mathrm{m/s^2}$, fast trials: 1.6 to 23 $\mathrm{m/s^2}$) with peak values (99th percentile) of up to 67 $\mathrm{m/s^2}$. The

RMS values of all trials are shown in Figure 3.6 and cover a wider range than the publicly available datasets.

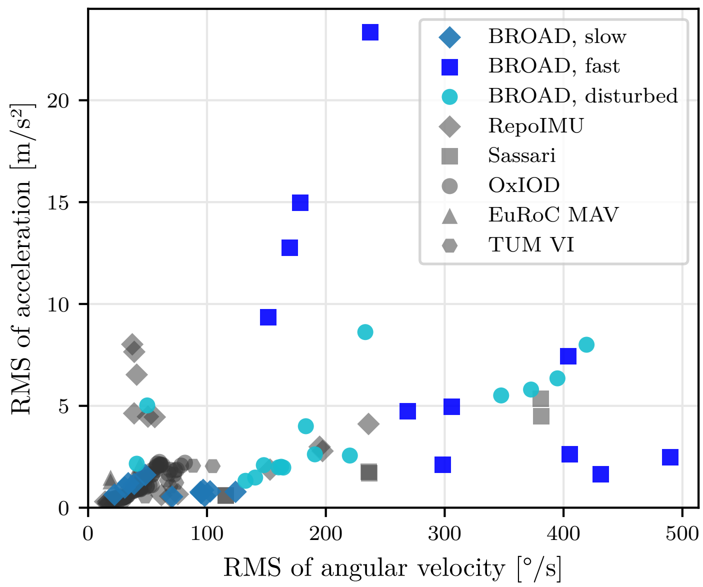

Figure 3.6: RMS values of the angular velocity and accelerometer norm for the undisturbed slow, undisturbed fast, and disturbed trials of the proposed dataset in comparison to the publicly available datasets (only considering trials suitable for IOE accuracy evaluation, cf. Section 3.3). The BROAD dataset covers a wider range of motions than the publicly available datasets.

3.4.3 Time Synchronization

Highly precise time synchronization of the IMU and OMC data streams is crucial because even very short time delays can have a substantial effect on the observed orientation estimation errors. Synchronization was performed via optimization based on the norm of the angular velocity measured by the IMU and the norm of the angular velocity derived from the OMC orientations. In addition to a time offset, a clock drift correction factor was determined in order to account for small deviations from the nominal sampling frequencies of both measurement systems. The resulting parameters were used to interpolate the OMC ground truth data to the exact sampling time instants of the IMU data.

In detail, this time synchronization is performed by the following procedure:

Denote the sampling time of the IMU as T_s and the sampling time of the OMC system as $T_\mathrm{s,OMC}$. First, we derive an *optical angular velocity* $\boldsymbol{\omega}_\mathrm{OMC}(t_k)$ from the optical orientation ${}^{\mathcal{B}}_{\mathcal{M}}\mathbf{q}(t_k)$ (cf. Figure 3.7):

$$[\, q_w \;\; q_x \;\; q_y \;\; q_z \,]^\intercal := {}^{\mathcal{B}}_{\mathcal{M}}\mathbf{q}(t_{k-1})^{-1} \otimes {}^{\mathcal{B}}_{\mathcal{M}}\mathbf{q}(t_k), \tag{3.1}$$

$$\boldsymbol{\omega}_\mathrm{OMC}(t_k) := \frac{2 \arccos q_w}{T_\mathrm{s,OMC}} \frac{[\, q_x \;\; q_y \;\; q_z \,]^\intercal}{\|[\, q_x \;\; q_y \;\; q_z \,]^\intercal\|}. \tag{3.2}$$

We then low-pass filter each component of the inertial angular velocity $\boldsymbol{\omega}(t_k)$ and the optical angular velocity with a cutoff frequency of 10 Hz.

By nonlinear least-squares optimization, we determine the time offset t_0 and the scaling factor s of the nominal OMC sampling rate that minimize the root mean square error (RMSE) between the norms of both angular rates, i.e.,

$$e := \sqrt{\frac{1}{N}\sum_{k=1}^{N}(\|\boldsymbol{\omega}(t_k)\| - \|\boldsymbol{\omega}_{\mathrm{OMC}}(t'_k)\|)^2}, \tag{3.3}$$

with

$$t'_k := s\frac{T_{\mathrm{s,OMC}}}{T_{\mathrm{s}}} + t_0. \tag{3.4}$$

To ensure robust convergence, we first determine an initial estimate of the time offset by evaluating this cost function with linearly spaced time offsets. In a second step, we parametrize the influence of clock drift via additional time offsets at the beginning and at the end of the measurement.

As the final step, we use the obtained time shift and OMC sampling rate to resample the measured OMC data to the IMU sampling instants.

3.4.4 Coordinate System Alignment

In order to obtain an accurate ground truth for the IMU orientation, the different local and global coordinate frames of both measurement systems have to be aligned [89]. See Figure 3.7 for an illustration of the different coordinate systems. The local coordinate systems of the IMU $\mathcal{S}$ (determined by sensor manufacturing and calibration) and the rigid body $\mathcal{B}$ (determined by the placement of optical markers) can agree well ($< 1°$) when care is taken to ensure precise placement, but even this small deviation might affect the results. The IMU reference frame $\mathcal{E}$ is determined by gravity and the horizontal projection of the local magnetic field. In contrast, OMC systems provide marker position measurements in a different reference frame $\mathcal{M}$ that is defined by a calibration procedure.

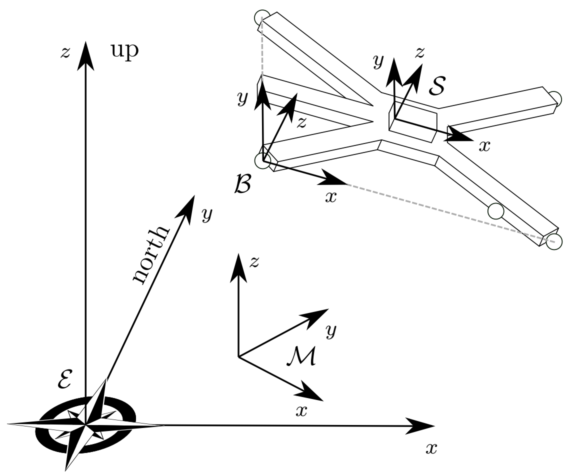

Figure 3.7: Illustration of the different local coordinate systems and reference frames. IOE algorithms estimate the orientation of the sensor frame $\mathcal{S}$ with respect to a frame of reference $\mathcal{E}$, defined by gravity and the local magnetic field. The OMC reference system tracks the orientation of a rigid body $\mathcal{B}$, defined by reflective markers, relative to a reference frame $\mathcal{M}$ that is defined during calibration and, in general, does not coincide with $\mathcal{E}$.

For a precise evaluation of the actual IOE errors, the constant offsets between $\mathcal{S}$ and $\mathcal{B}$ and between $\mathcal{E}$ and $\mathcal{M}$ must be determined [89]. This is done by minimizing the disagreement between the IMU measurements and the corresponding quantities derived from the OMC measurement data. This alignment is performed using a separate alignment recording that was created on each measurement day. In those recordings, the IMU and the board are carefully and slowly rotated in all directions in order to ensure a sufficiently rich motion. The obtained alignment parameters are then used to calculate ground truth orientations from the OMC measurements of the 39 motion trials.

Note that the rotation between the $\mathcal{S}$ frame and the $\mathcal{B}$ frame ${}^{\mathcal{S}}_{\mathcal{B}}\mathbf{q}$ and the rotation between the $\mathcal{M}$ frame and the $\mathcal{E}$ frame ${}^{\mathcal{M}}_{\mathcal{E}}\mathbf{q}$ are constant throughout the entire duration of the motion. They only depend on the installation of the markers, the calibration of the optical ground truth system, the local magnetic field inside the room, and the attachment of the IMU on the rigid body.

In detail, those two rotations are determined from the alignment recording via the following procedure.

Assume that the inertial and optical data is already synchronized by the method described in Section 3.4.3. During this synchronization, we deliberately only considered the norm of the optical angular velocity $\boldsymbol{\omega}_{\mathrm{OMC}}(t_k)$ and the gyroscope measurements $\boldsymbol{\omega}(t_k)$ because the 3D vectors are given in the local coordinate systems $\mathcal{B}$ and $\mathcal{S}$, respectively. We can exploit the direction of those vectors to determine the relative orientation ${}^{\mathcal{S}}_{\mathcal{B}}\mathbf{q}$. When also considering a fixed gyroscope bias $\mathbf{b}_\omega \in \mathbb{R}^3$, it can be expected that the correct rotation ${}^{\mathcal{S}}_{\mathcal{B}}\mathbf{q}$ minimizes the following cost function:

$$e_{\mathrm{gyr}} := \sqrt{\frac{1}{N}\sum_{k=1}^{N} \boldsymbol{\omega}(t_k) - \mathbf{b}_\omega - {}^{\mathcal{S}}_{\mathcal{B}}\mathbf{q}^{-1} \otimes \boldsymbol{\omega}_{\mathrm{OMC}}(t_k) \otimes {}^{\mathcal{S}}_{\mathcal{B}}\mathbf{q}}. \tag{3.5}$$

Using the central second-order finite difference, we derive an optical acceleration signal $\mathbf{a}_{\mathrm{OMC}}(t_k)$ from the OMC position measurements. In order to make this measurement agree with the IMU accelerometer measurements, knowledge of both ${}^{\mathcal{S}}_{\mathcal{B}}\mathbf{q}$ and ${}^{\mathcal{B}}_{\mathcal{M}}\mathbf{q}$ is needed. In the $\mathcal{M}$ frame, the measured gravitational acceleration is $[\mathbf{g}]_{\mathcal{M}} = {}^{\mathcal{M}}_{\mathcal{E}}\mathbf{q}^{-1} \otimes [0 \;\; 0 \;\; g]^\intercal \otimes {}^{\mathcal{M}}_{\mathcal{E}}\mathbf{q}$, with a fixed but unknown $g \approx 9.8\,\mathrm{m/s^2}$. We express the IMU accelerometer measurements in the $\mathcal{M}$ frame using the OMC orientation ${}^{\mathcal{B}}_{\mathcal{M}}\mathbf{q}_{\mathrm{OMC}}(t_k)$:

$$[\mathbf{a}]_{\mathcal{M}}(t_k) = {}^{\mathcal{B}}_{\mathcal{M}}\mathbf{q}_{\mathrm{OMC}}(t_k) \otimes {}^{\mathcal{S}}_{\mathcal{B}}\mathbf{q} \otimes (\mathbf{a}(t_k) - \mathbf{b}_{\mathrm{a}}) \otimes ({}^{\mathcal{B}}_{\mathcal{M}}\mathbf{q}_{\mathrm{OMC}}(t_k) \otimes {}^{\mathcal{S}}_{\mathcal{B}}\mathbf{q})^{-1}. \tag{3.6}$$

The vector $\mathbf{b}_{\mathrm{a}} \in \mathbb{R}^3$ denotes an unknown but constant accelerometer bias. Using those quantities, we define the following cost function:

$$e_{\mathrm{acc}} := \sqrt{\frac{1}{N}\sum_{k=1}^{N} \left\| \mathbf{a}_{\mathrm{OMC}}(t_k) + [\mathbf{g}]_{\mathcal{M}} - [\mathbf{a}]_{\mathcal{M}}(t_k) \right\|^2}. \tag{3.7}$$

We then determine the parameters ${}^{\mathcal{S}}_{\mathcal{B}}\mathbf{q}$, ${}^{\mathcal{M}}_{\mathcal{E}}\mathbf{q}$, $\mathbf{b}_\omega$, $\mathbf{b}_{\mathrm{a}}$, and g that minimize the sum of both cost functions, i.e., $e := e_{\mathrm{gyr}} + e_{\mathrm{acc}}$. This problem can be solved by standard nonlinear optimization methods. It is generally well-behaved, and the solution is straightforward to find. Note that for a unique solution, we set the z-component of ${}^{\mathcal{M}}_{\mathcal{E}}\mathbf{q}$ to zero, which ensures a consistent heading. To increase robustness, we low-pass filter the optical and inertial measurements with a cutoff frequency of 10 Hz.

The heading component of ${}^{\mathcal{M}}_{\mathcal{E}}\mathbf{q}$ is determined in a second step: We transform the magnetometer measurements into the $\mathcal{E}$ frame using the OMC orientation and the results from the previous step and, for each sample, calculate the angle of the measurement in the horizontal plane. Finally, the mean of the obtained heading angles is used to determine the heading of ${}^{\mathcal{M}}_{\mathcal{E}}\mathbf{q}$.

3.4.5 Metrics for Orientation Accuracy

For any of the performed motions, the orientation estimated by an IMU-based algorithm can be compared with the corresponding optical ground truth measurement. Along with the dataset, example code to obtain the proposed metrics is provided.

The disagreement between two unit quaternions representing orientations is well described by the shortest angular distance e between both orientations. As detailed in Section 2.4, for any estimated sensor orientation ${}^{\mathcal{S}}_{\mathcal{E}}\mathbf{q}(t)$ and corresponding ground-truth orientation ${}^{\mathcal{S}}_{\mathcal{E}}\mathbf{q}_{\mathrm{OMC}}(t)$ this error is

$$\mathbf{q}_{\mathrm{e}}(t) = {}^{\mathcal{S}}_{\mathcal{E}}\mathbf{q}^{-1}_{\mathrm{OMC}}(t) \otimes {}^{\mathcal{S}}_{\mathcal{E}}\mathbf{q}(t) =: [\, q_w \;\; q_x \;\; q_y \;\; q_z \,]^\intercal, \tag{3.8}$$

$$e(t) := 2 \arccos |q_w|. \tag{3.9}$$

This angular performance parameter well describes the overall accuracy of the estimated orientation, and root-mean-square values can be used to quantify the performance of a motion interval of interest.

It is important to note that the error e yields only very limited insight into the potential cause of estimation errors. It is highly desirable to distinguish between the portion of the error that results from inaccurate heading estimation and the portion that results from inaccurate inclination estimation. While the accuracy of the former primarily depends on the sensor fusion between gyroscopes and magnetometers, the accuracy of the latter primarily depends on the fusion between gyroscopes and accelerometers. In magnetically disturbed environments, the heading component of the error might easily be ten times larger than the inclination component of the orientation error.

While different definitions of heading have been used in literature, we use the decomposition into heading and inclination defined in Section 2.5, which is particularly useful for the current purpose. To implement this decomposition, the following two steps are carried out. First, we express the orientation error in the global frame $\mathcal{E}$ as follows.

$$\begin{aligned}[\mathbf{q}_{\mathrm{e}}]_{\mathcal{E}}(t) &:= {}^{\mathcal{S}}_{\mathcal{E}}\mathbf{q}(t) \otimes \left({}^{\mathcal{S}}_{\mathcal{E}}\mathbf{q}^{-1}_{\mathrm{OMC}}(t) \otimes {}^{\mathcal{S}}_{\mathcal{E}}\mathbf{q}(t)\right) \otimes {}^{\mathcal{S}}_{\mathcal{E}}\mathbf{q}^{-1}(t) \\ &= {}^{\mathcal{S}}_{\mathcal{E}}\mathbf{q}(t) \otimes {}^{\mathcal{S}}_{\mathcal{E}}\mathbf{q}^{-1}_{\mathrm{OMC}}(t).\end{aligned} \tag{3.10}$$

We then decompose the orientation error $[\mathbf{q}_{\mathrm{e}}]_{\mathcal{E}}(t) =: [\, q_w \;\; q_x \;\; q_y \;\; q_z \,]^\intercal$ into a rotation around the vertical z-axis and the shortest possible residual rotation. The absolute rotation angle of the former is called the heading error e_{h}, and the absolute rotation angle of the latter is called the inclination error e_i. They are determined mathematically by

$$e_\mathrm{h}(t) := 2 \arctan \left| \frac{q_z}{q_w} \right|, \tag{3.11}$$

$$e_\mathrm{i}(t) := 2 \arccos \sqrt{q_w^2 + q_z^2}. \tag{3.12}$$

The proposed decomposition facilitates the interpretation of the overall estimation error with respect to potential sources of inaccuracy when comparing the orientations obtained by an IOE algorithm to the OMC ground truth. In general, large inclination errors $e_\mathrm{i}(t)$ indicate non-ideal fusion of accelerometer with gyroscope measurements, while large heading errors $e_\mathrm{h}(t)$ are mostly caused by magnetic disturbances. The error $e(t)$ is a suitable metric for the overall orientation estimation error. The sum of both error portions is always larger or equal to the overall orientation error, while each portion for itself is smaller than that overall error.

Note that for 6D IOE, absolute heading information is not available. While, in this case, the heading error $e_\mathrm{h}(t)$ has a large offset and exhibits a slow drift, the inclination error $e_\mathrm{i}(t)$ is a suitable metric for assessing the accuracy of magnetometer-free IOE algorithms.

We can use the previously defined error metrics $e(t)$, $e_\mathrm{h}(t)$, and $e_\mathrm{i}(t)$, which are defined for each time instant, to assess the performance of a given IOE algorithm in different scenarios. In order to assess the overall performance for one trial, we use the RMSE of the respective metric while only considering the motion phases (as labeled in the data files). When considering a set of trials, we report the mean of the RMSE values obtained for each trial as a metric for the overall accuracy. In both cases, small RMSE values indicate good performance.

3.4.6 Benchmark Metrics

In order to allow for a simple and well-defined performance comparison between different IOE algorithms, we define two benchmark metrics that can be obtained from the BROAD dataset for any given IOE algorithm: the trial-agnostic generalized performance (TAGP) and the individual trial-optimized performance (ITOP). Both metrics are based on the average RMSE that is obtained as follows:

1. Run the IOE algorithm on all 39 trials with a given parameter setting.
2. For each trial, calculate the orientation RMSE (i.e., the RMS of $e(t)$) while only considering the labeled motion phases.
3. Average all 39 RMSE values.

The **TAGP** is the smallest achievable average RMSE over all 39 trials that can be obtained with a *common parameter setting* for all trials.

The **ITOP** is the smallest achievable average RMSE over all 39 trials that can be obtained with *individual parameter tuning* for each trial.

Section 3.5 will demonstrate how to obtain those metrics and how to use the proposed benchmark for further in-depth evaluation.

3.4.7 File Format

The benchmark dataset consists of the 39 trials as presented in Table 3.3. Each trial is stored in a separate file, and the filename indicates the trial number and the type of trial (e.g., "01_undisturbed_slow_rotation_A"). A machine-readable "trials.json" file is included, which can be used to automatically find and filter all trials.

The measurement data is provided both as an HDF5 data file and a Matlab data file (.mat) with identical content. Each file contains the following variables:

imu_gyr IMU gyroscope measurements in rad/s

imu_acc IMU accelerometer measurements in m/s^2

imu_mag IMU magnetometer measurements in µT

opt_quat OMC ground truth orientation as a unit quaternion (w component first, ENU reference frame)

opt_pos OMC ground truth position in m

movement Boolean array (0/1) indicating movement phases

sampling_rate sampling rate of the measurements in Hz ($2000/7\,\mathrm{Hz} \approx 286\,\mathrm{Hz}$, HDF5: stored as an attribute)

info short description of the file contents (HDF5: stored as an attribute)

The data is already synchronized and aligned as described in Section 3.4.3 and Section 3.4.4. In order to obtain comparable results, orientation estimation algorithms should be run over the whole trial data but when calculating errors, the *movement* array should be used to exclude the rest phases.

3.4.8 Example Code

In addition to the measurement data, example code written in Python is provided. The code implements the evaluation and benchmark metrics described in Section 3.4.5 and Section 3.4.6, respectively, and re-creates Figures 3.8 and 3.9 from the case study in Section 3.5. Please refer to the information provided in the "README.md" file for instructions on how to run the code.

3.5 Case Study on the Proposed Benchmark Dataset

The following exemplary case study demonstrates the usefulness of the proposed benchmark and shows how it can be employed to achieve an objective and broad assessment and comparison of IOE algorithms under different conditions by answering several exemplary research questions. To this end, we evaluate the performance of two popular orientation estimation algorithms, the complementary filters proposed in [82] (Algorithm A) and [73] (Algorithm B). For both filters, we employ the commonly used C implementation by Sebastian Madgwick[1].

[1] https://x-io.co.uk/open-source-imu-and-ahrs-algorithms/

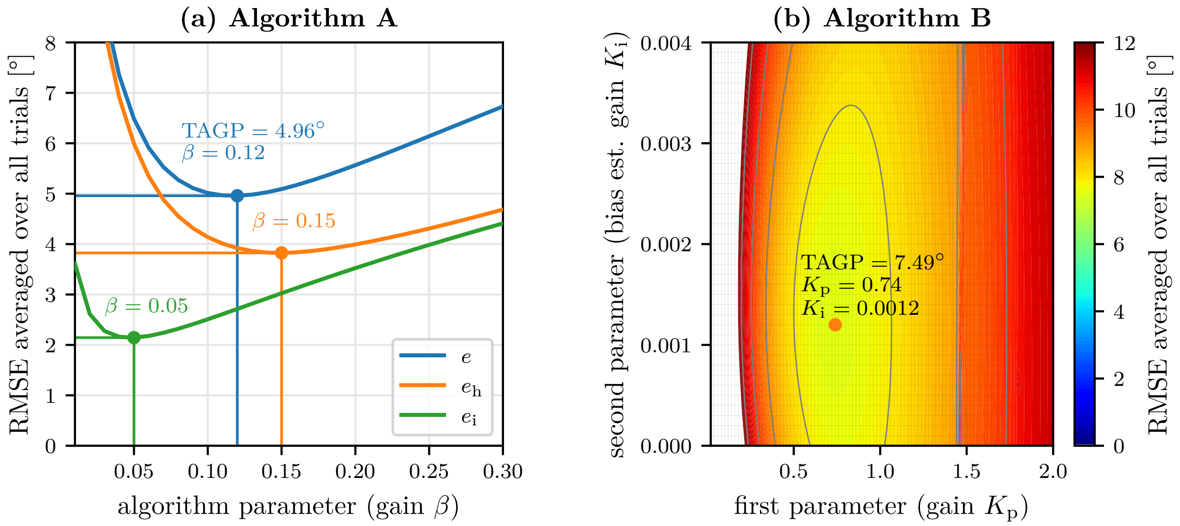

Figure 3.8: Orientation estimation RMSE (averaged over all trials) obtained with Algorithms A [82] and B [73] for different values of the tuning parameters. For various motions at different speeds, a parameter choice of $\beta = 0.12$ yields the lowest overall errors for Algorithm A. For Algorithm B, the parameter combination $K_\mathrm{p} = 0.74$, $K_\mathrm{i} = 0.0012$ yields the lowest overall errors.

Consider orientation estimation in an application setting in which we *do not* have knowledge regarding the speed and type of motions and in which we cannot guarantee an undisturbed environment. Our aim is to find robust parameter settings for Algorithms A and B that minimize the average error over all possible scenarios. This specific research question is equivalent to finding the parameter settings associated with the TAGP. In order to determine this value, we calculate the average RMSE as defined in Section 3.4.6 for many different parameter values. For Algorithm A, we use linearly spaced values of the single tuning parameter β (0.01 to 0.3 in steps of 0.01).[2] Since Algorithm B has two tuning parameters, a fusion weight K_p (similar to β) and a parameter for gyroscope bias estimation K_i, we search a linearly spaced grid of parameter values (K_p: 0.02 to 2.0 in steps of 0.02, K_i: 0 to 0.004 in steps of 0.0001). The result is shown in Figure 3.8. We can see that, for this broad range of motions, a value of $\beta = 0.12$ yields the lowest overall errors for Algorithm A and that for Algorithm B, the lowest overall error is obtained for the parameter combination $K_\mathrm{p} = 0.74$, $K_\mathrm{i} = 0.0012$.

Besides this research question, the details presented in Figure 3.8a can be used to answer various minor research questions: Consider an application for which only the inclination error is relevant and therefore should be minimized. As can be seen in Figure 3.8a, $\beta = 0.05$ should be used in this case. Analogously, we see that accurate heading estimation requires larger values for β, with the optimum being at $\beta = 0.15$. The line plot representation also allows us to answer the question of how non-ideal values for β influence the error: We can see that the error gradient is much steeper when β is too small than when it is too large, i.e., if in doubt, larger values for β should be chosen.

[2] Note that two slightly different versions of Madgwick's algorithm exist. For illustration purposes, we now use the version from [82] with a single parameter, while the version found in [74] and used in Section 3.7 supports gyroscope bias estimation and has two parameters.

In order to take an in-depth look at the strengths and weaknesses of a given IOE algorithm, we pose the following research question: How does the estimation accuracy of Algorithms A and B depend on the type of motion and environmental conditions? Unlike previous datasets, the BROAD benchmark is well suited for answering this question. This can be achieved for example as follows. We calculate the average inclination, heading, and total RMSE for the groups of trials as defined in Table 3.3 with the TAGP parametrization. Furthermore, we determine the minimum achievable error when using different parameters for each trial. In Figure 3.9, the TAGP performance is shown with bars, and the minimum achievable error is indicated with black dots.

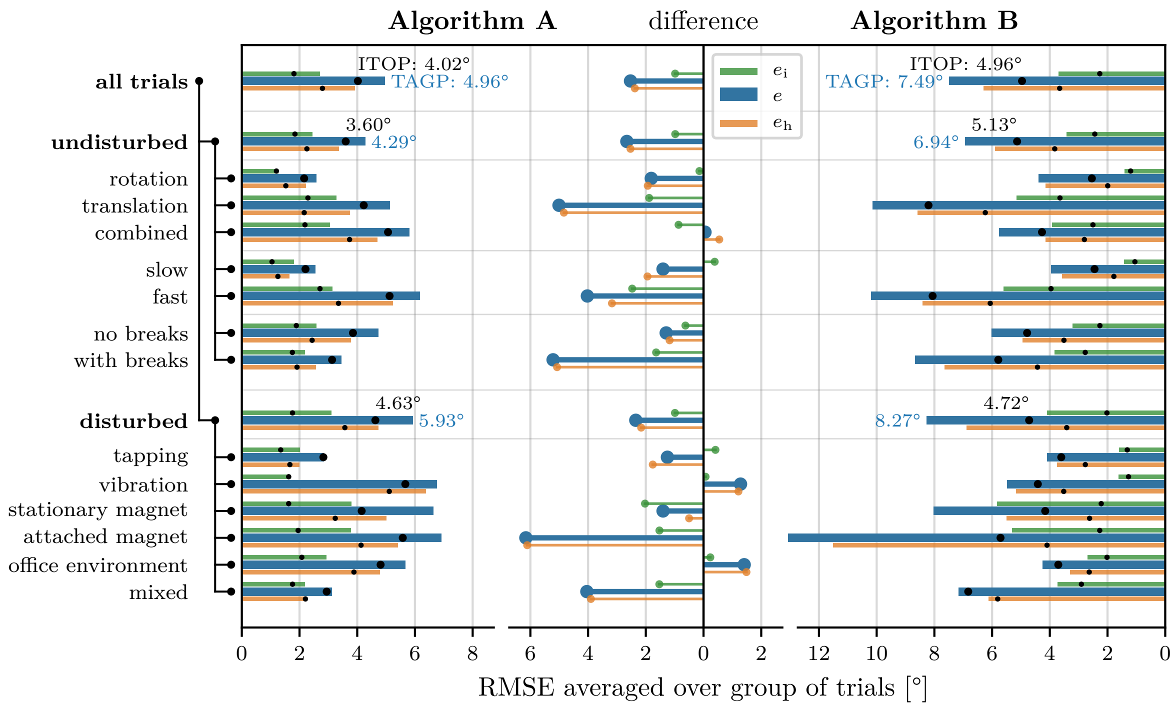

Figure 3.9: Averaged RMSE values for Algorithms A [82] and B [73] for various groups of trials. The bars show errors with the trial-agnostic parameters, and the black dots indicate the minimum error achievable with individual parameters for each trial. The lines originating from the center show the difference between the errors obtained with Algorithm A and B. It can be seen that for most groups of trials, Algorithm A yields smaller errors.

We see that for the TAGP benchmark metric, Algorithm A reaches a score of 4.96°, and Algorithm B reaches a score of 7.49°, i.e., Algorithm A yields a better overall performance. Furthermore, the breakdown into trial groups allows for a detailed evaluation of the estimation accuracy in various scenarios. For example, we can see that, for both algorithms, pure rotational movements yield lower errors than translational movements. For Algorithm A, the error for combined motions is larger than for translational movements, while for Algorithm B, the error obtained for combined motions is smaller than for pure translational movements. Unsurprisingly, faster movements lead to larger errors with both algorithms. As can be seen in Figure 3.9, the estimation errors do not show any notable difference between long continuous movement phases and short phases with breaks in between. The decomposition into heading and inclination error, in combination with the magnetic disturbances included in the dataset, allows for insight into potential sources of errors. In the undisturbed trials, heading and inclination contribute to the total error almost equally. In contrast, for the *attached-magnet* trials and Algorithm B, the heading error is twice as large as the inclination error.

Comparing the results of the two algorithms in Figure 3.9 enables us to easily answer another research question: Which of the algorithms provides the best overall accuracy, and which algorithm is more accurate for any given motion scenario? To facilitate the comparison of algorithm performance, we plot the error difference for each group of trials as lines originating from the center of Figure 3.9. We see that when using the common robust parameter settings, the performance of Algorithm A is better than the performance of Algorithm B when considering the average performance of all trials. Algorithm A also yields lower or almost equal errors for most trial groups except for the vibration and office environment trials, where the performance of Algorithm B is better.

The differences between TAGP and ITOP performance allow us to answer another research question: How well do algorithms A and B generalize, i.e., can they provide near-optimum performance for a wide variety of motions with a single common parameter choice? The ability to generalize is a desirable property since individual parameter tuning depending on the expected motion is often not possible in practice [53]. In Figure 3.9, we see that for Algorithm B, the ITOP errors are much smaller than the TAGP errors, whereas for Algorithm A, the difference between individual tuning and a common parameter choice is much smaller. This shows that there is more potential for parameter tuning with Algorithm B while Algorithm A generalizes better.

As a final research question, we aim to determine how well the two considered IOE algorithms perform compared to other state-of-the-art algorithms. Since Algorithm A and B are complementary filters, we choose two algorithms based on Kalman filters for which an implementation is available in [54]: the method proposed by Ligorio et al. [69] (Algorithm C, *LIG* in [54]) that yielded the best performance in [54] and the computationally efficient *Fast Kalman Filter* proposed by Guo et al. [71] (Algorithm D, *GUO* in [54], *FKF* in Section 3.7). To answer this question, we determine the benchmark metric TAGP for all algorithms.

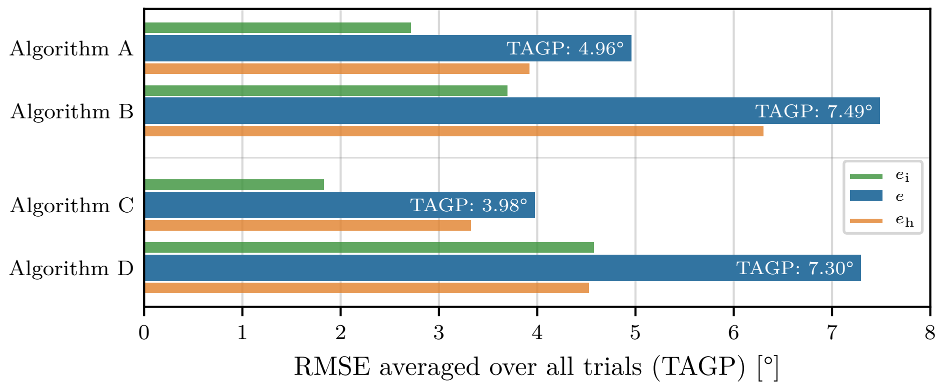

Figure 3.10: TAGP for Algorithms A [82], B [73], C [69], and D [71]. The overall performance of Algorithm D is comparable to the performance of Algorithm B, while Algorithm C slightly outperforms Algorithm A.

The results are shown in Figure 3.10. As can be seen, Algorithm D yields an overall performance that is very similar to the performance of Algorithm B. With a TAGP of 3.98°, Algorithm C provides the best overall performance and outperforms Algorithm A by around

1°. The breakdown of the TAGP into heading and inclination components shows that, while the errors are lower for both heading and inclination, a larger part of the overall improvement of Algorithm C can be attributed to more accurate inclination estimates.

3.6 Proposed Orientation Estimation Algorithm

The following section introduces a modular method for simultaneous 6D and 9D orientation estimation.

3.6.1 Terminology and Notation

As illustrated in Figure 3.1, the following measurements are available in inertial orientation estimation (IOE): gyroscope readings $\boldsymbol{\omega}(t_k) \in \mathbb{R}^3$, accelerometer readings $\mathbf{a}(t_k) \in \mathbb{R}^3$, and magnetometer readings $\mathbf{m}(t_k) \in \mathbb{R}^3$, sampled at times $t_k = kT_\mathrm{s}$, $k \in \{1, 2, \dots, N\}$, $T_\mathrm{s} \in \mathbb{R}_{>0}$.

If only gyroscopes and accelerometers are employed, we use the term 6D IOE, while 9D IOE additionally uses magnetometers. Therefore, 9D IOE yields the sensor orientation with respect to a fixed inertial reference frame, typically using the east-north-up (ENU) convention (i.e., z is pointing up, and y is pointing north). In contrast, only vertical reference information is available in 6D IOE, and the resulting orientations are thus provided with respect to an almost-inertial reference frame, which has one vertical axis and slowly drifts around this axis (at a rate determined by the gyroscope bias, i.e., typically $\leq 1\,°/\mathrm{s}$).

We denote the moving sensor frame, i.e., the coordinate system in which the sensor readings are provided, by $\mathcal{S}_i(t_k)$. The ENU inertial reference frame used in 9D IOE is denoted $\mathcal{E}$, and the sensor-specific almost-inertial reference frame used in 6D IOE is denoted $\mathcal{E}_i(t_k)$. Anticipating the common application scenario with multiple IMUs on different segments of a kinematic chain, a sensor index i is used for sensor-specific quantities.

3.6.2 A Modular Estimation Approach

The most fundamental state of any IOE algorithm is the current orientation estimate, which is commonly represented by a single orientation quaternion. For the proposed method, we use a more modular approach and represent the 6D estimate ${}^{\mathcal{S}_i(t_k)}_{\mathcal{E}_i(t_k)}\mathbf{q}$ as the concatenation of an inclination correction quaternion ${}^{\mathcal{I}_i(t_k)}_{\mathcal{E}_i(t_k)}\mathbf{q}$ with a gyroscope strapdown integration quaternion ${}^{\mathcal{S}_i(t_k)}_{\mathcal{I}_i(t_k)}\mathbf{q}$. Furthermore, the 9D estimate ${}^{\mathcal{S}_i(t_k)}_{\mathcal{E}}\mathbf{q}$ is the concatenation of a heading correction rotation ${}^{\mathcal{E}_i(t_k)}_{\mathcal{E}}\mathbf{q}$, represented by the scalar heading offset $\delta_i(t_k)$, with the 6D estimate, i.e.,

$$\underbrace{{}^{\mathcal{S}_i(t_k)}_{\mathcal{E}}\mathbf{q}}_{\text{9D estimate}} = \underbrace{\overbrace{(\delta_i(t_k) @ [0\ \ 0\ \ 1]^\intercal)}^{\substack{\text{magnetometer}\\ \text{correction}}}}_{{}^{\mathcal{E}_i(t_k)}_{\mathcal{E}}\mathbf{q}} \otimes \underbrace{\overbrace{{}^{\mathcal{I}_i(t_k)}_{\mathcal{E}_i(t_k)}\mathbf{q}}^{\substack{\text{accelerometer}\\ \text{correction}}} \otimes \overbrace{{}^{\mathcal{S}_i(t_k)}_{\mathcal{I}_i(t_k)}\mathbf{q}}^{\substack{\text{strapdown}\\ \text{integration}}}}_{\text{6D estimate}}. \tag{3.13}$$

The introduced auxiliary coordinate system $\mathcal{I}_i(t_k)$, with $\mathcal{I}_i(t_0) = \mathcal{S}_i(t_0)$, is an almost-inertial frame that slowly drifts around arbitrary axes due to errors in gyroscope strapdown integration. See Figure 3.11 for an illustration of the four distinct coordinate systems that are used in (3.13).

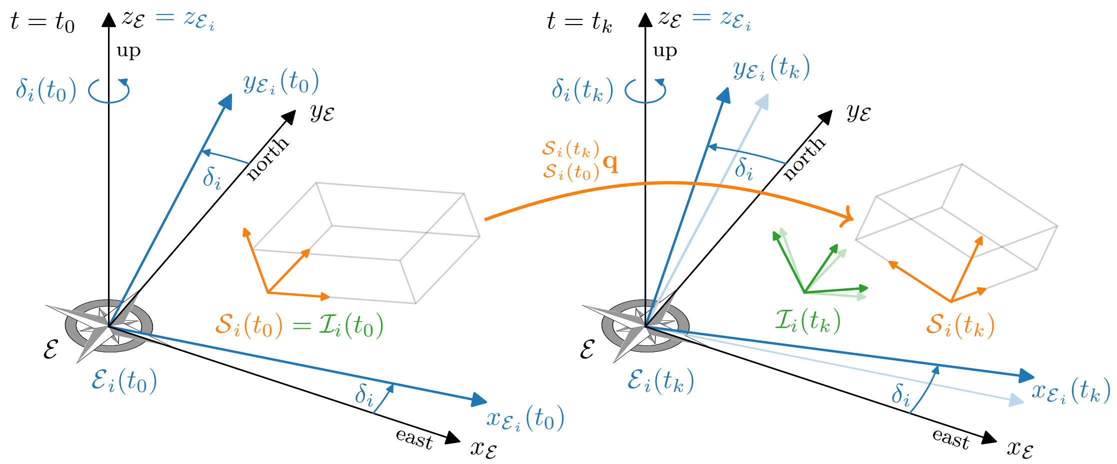

Figure 3.11: Illustration of the different coordinate systems used by the proposed method. The aim of IOE is to determine the orientation of the sensor $\mathcal{S}_i$ relative to an ENU reference frame $\mathcal{E}$ (in 9D sensor fusion) or relative to a reference frame $\mathcal{E}_i$ with vertical z-axis (in 6D sensor fusion). The angle δ_i describes the slowly drifting heading offset between $\mathcal{E}$ and $\mathcal{E}_i$. Internally, the auxiliary $\mathcal{I}_i$ frame is used to represent the orientation obtained by pure gyroscope strapdown integration and slowly drifts due to the integration of gyroscope bias.

As demonstrated in [76], a drawback of many existing methods is that magnetic disturbances can severely impact the inclination estimates. While previous methods [75, 76] have already ensured that the magnetometer correction can only influence the heading but not the inclination, the proposed modular state representation makes this property very explicit by representing the heading offset with a scalar variable $\delta_i(t_k)$. Furthermore, this state representation facilitates simultaneous 6D and 9D orientation estimation.

The chosen approach of separating strapdown integration, inclination correction, and heading correction in the state is also represented in the filter structure as shown in Figure 3.12. Unlike conventional methods, the correction steps are decoupled from the previous steps, i.e., there is no feedback loop from the heading correction to the strapdown integration and, therefore, neither to the inclination correction.

This basic filter structure is extended by an optional gyroscope bias estimation algorithm and an algorithm for magnetic disturbance detection and rejection. The bias estimation algorithm includes a rest detection algorithm and automatically adjusts to whether the IMU is at rest or in motion. The extended filter structure is shown in Figure 3.13. Note that it is also possible, and supported by the reference implementation (Section 3.6.8), to independently enable or disable rest bias estimation, motion bias estimation, and magnetic disturbance rejection.

In the following, we call the extended algorithm *VQF* (Versatile Quaternion-based Filter) and the basic version *BasicVQF*. Furthermore, we introduce an acausal implementation called *OfflineVQF* in Section 3.6.7.

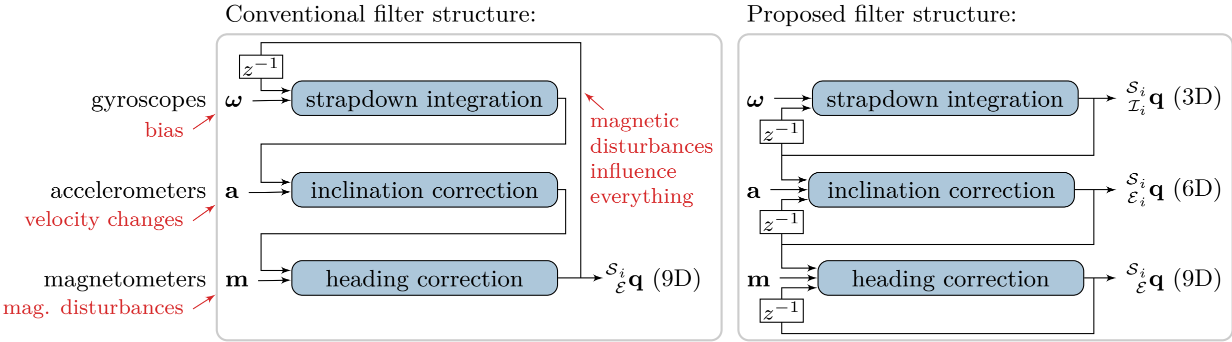

Figure 3.12: Illustration of conventional and proposed filter structures (z^{-1} denotes the unit delay). The proposed filter structure avoids the feedback of the 9D estimate on the strapdown integration. It thereby enables simultaneous 6D and 9D orientation estimation and ensures that the inclination cannot be influenced by magnetic disturbances.

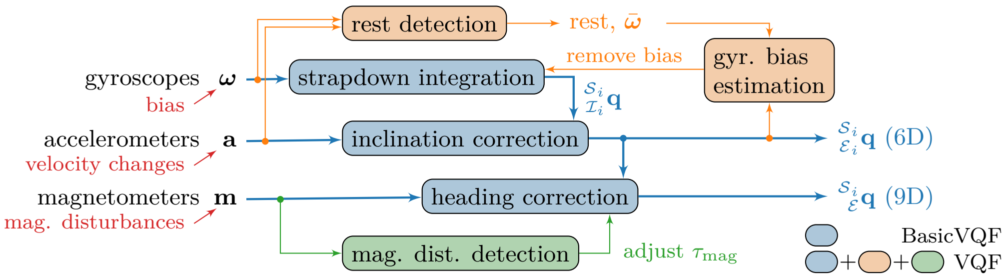

Figure 3.13: Variants of the proposed algorithm. *BasicVQF* consists of strapdown integration, inclination correction, and heading correction. The full version *VQF* additionally includes rest detection, gyroscope bias estimation, and magnetic disturbance rejection (which can be enabled or disabled independently).

3.6.3 Fusion of Gyroscope, Accelerometer, and Magnetometer Measurements

The basic filter update consists of gyroscope-based prediction, followed by accelerometer correction and, in 9D IOE, by magnetometer correction. The algorithm is given in Algorithm 1 and illustrated as a block diagram in Figure 3.14.

Gyroscope prediction is performed via strapdown integration of the measured angular rate. Errors due to gyroscope bias, noise, and other measurement errors lead to slow drift of the $\mathcal{I}_i$ frame.

To obtain a vertical reference, we transform the measured accelerations into the almost-inertial frame $\mathcal{I}_i$ and then apply a second-order Butterworth low-pass filter to each component. This low-pass filter effectively averages the accelerometer measurements and allows for short-term acceleration and deceleration to cancel out. The inclination of the orientation estimate is then corrected so that the filtered acceleration points in upward direction. Conventional IOE algorithms typically regard each single accelerometer sample as a 3D vector and perform a nonlinear correction step based on the comparison of this vector to a vertical reference vector. Compared to those approaches, the use of a linear low-pass filter in the $\mathcal{I}_i$ frame more effectively and robustly separates the gravitational acceleration component from the acceleration caused by velocity changes.

If magnetometer measurements are provided, a heading offset is derived from the projection of the magnetic field vector into the horizontal plane and tracked via an exponential filter.

Algorithm 1 BasicVQF

procedure InitializeFilter
  ${}^{\mathcal{S}_i}_{\mathcal{I}_i}\mathbf{q} \leftarrow [1\ 0\ 0\ 0]^\intercal$ ▷ Gyroscope strapdown integration quaternion
  ${}^{\mathcal{I}_i}_{\mathcal{E}_i}\mathbf{q} \leftarrow [1\ 0\ 0\ 0]^\intercal$ ▷ Accelerometer correction quaternion
  $\delta_i \leftarrow 0$ ▷ Magnetometer correction angle
  initialize low-pass filter state
end procedure
procedure FilterUpdate($\boldsymbol{\omega} = \boldsymbol{\omega}(t_k), \mathbf{a} = \mathbf{a}(t_k), \mathbf{m} = \mathbf{m}(t_k), f_{\mathrm{c,acc}}, k_{\mathrm{mag}}, T_{\mathrm{s}}$)
  ${}^{\mathcal{S}_i}_{\mathcal{I}_i}\mathbf{q} \leftarrow {}^{\mathcal{S}_i}_{\mathcal{I}_i}\mathbf{q} \otimes (T_{\mathrm{s}}\,\|\boldsymbol{\omega}\| \,@\, \boldsymbol{\omega})$ ▷ Perform gyroscope strapdown integration
  $[\mathbf{a}]_{\mathcal{I}_i} \leftarrow {}^{\mathcal{S}_i}_{\mathcal{I}_i}\mathbf{q} \otimes \mathbf{a} \otimes {}^{\mathcal{S}_i}_{\mathcal{I}_i}\mathbf{q}^{-1}$ ▷ Transform acceleration into $\mathcal{I}_i$ frame
  $[\mathbf{a}_{\mathrm{LP}}]_{\mathcal{I}_i} \leftarrow \mathrm{lpfStep}([\mathbf{a}]_{\mathcal{I}_i}, f_{\mathrm{c}} = f_{\mathrm{c,acc}})$ ▷ Apply low-pass filter
  $[\mathbf{a}_{\mathrm{LP}}]_{\mathcal{E}_i} \leftarrow {}^{\mathcal{I}_i}_{\mathcal{E}_i}\mathbf{q} \otimes [\mathbf{a}_{\mathrm{LP}}]_{\mathcal{I}_i} \otimes {}^{\mathcal{I}_i}_{\mathcal{E}_i}\mathbf{q}^{-1}$ ▷ Transform into $\mathcal{E}_i$ frame
  $[\,a_x\ \ a_y\ \ a_z\,]^\intercal \leftarrow \frac{[\mathbf{a}_{\mathrm{LP}}]_{\mathcal{E}_i}}{\left\|[\mathbf{a}_{\mathrm{LP}}]_{\mathcal{E}_i}\right\|}$ ▷ Normalize
  $q_w \leftarrow \sqrt{\frac{a_z+1}{2}}$
  ${}^{\mathcal{I}_i}_{\mathcal{E}_i}\mathbf{q} \leftarrow [\,q_w\ \ \frac{a_y}{2q_w}\ \ \frac{-a_x}{2q_w}\ \ 0\,]^\intercal \otimes {}^{\mathcal{I}_i}_{\mathcal{E}_i}\mathbf{q}$ ▷ Update correction quaternion
  ${}^{\mathcal{S}_i}_{\mathcal{E}_i}\mathbf{q} \leftarrow {}^{\mathcal{I}_i}_{\mathcal{E}_i}\mathbf{q} \otimes {}^{\mathcal{S}_i}_{\mathcal{I}_i}\mathbf{q}$ ▷ Calculate 6D orientation estimate
  if m is given **then**
    $[\,m_x\ \ m_y\ \ m_z\,]^\intercal \leftarrow {}^{\mathcal{S}_i}_{\mathcal{E}_i}\mathbf{q} \otimes \mathbf{m} \otimes {}^{\mathcal{S}_i}_{\mathcal{E}_i}\mathbf{q}^{-1}$ ▷ Transform magnetometer sample into $\mathcal{E}_i$ frame
    $\delta_{\mathrm{mag}} \leftarrow \mathrm{atan2}(m_x, m_y)$ ▷ Calculate heading offset from mag. sample
    $\delta_i \leftarrow \delta_i + k_{\mathrm{mag}}\,\mathrm{wrapToPi}(\delta_{\mathrm{mag}} - \delta_i)$ ▷ Update correction angle
  end if
  ${}^{\mathcal{S}_i}_{\mathcal{E}}\mathbf{q} \leftarrow [\,\cos\frac{\delta_i}{2}\ \ 0\ \ 0\ \ \sin\frac{\delta_i}{2}\,]^\intercal \otimes {}^{\mathcal{S}_i}_{\mathcal{E}_i}\mathbf{q}$ ▷ Calculate 9D orientation estimate
  return ${}^{\mathcal{S}_i}_{\mathcal{E}_i}\mathbf{q}$, ${}^{\mathcal{S}_i}_{\mathcal{E}}\mathbf{q}$ ▷ Provide 6D and 9D orientation estimate
end procedure

lpfStep: update step of second-order Butterworth low-pass filter with cutoff frequency f_{c}
wrapToPi: bring angle into the interval $[-\pi, \pi]$ by adding integer multiples of 2π

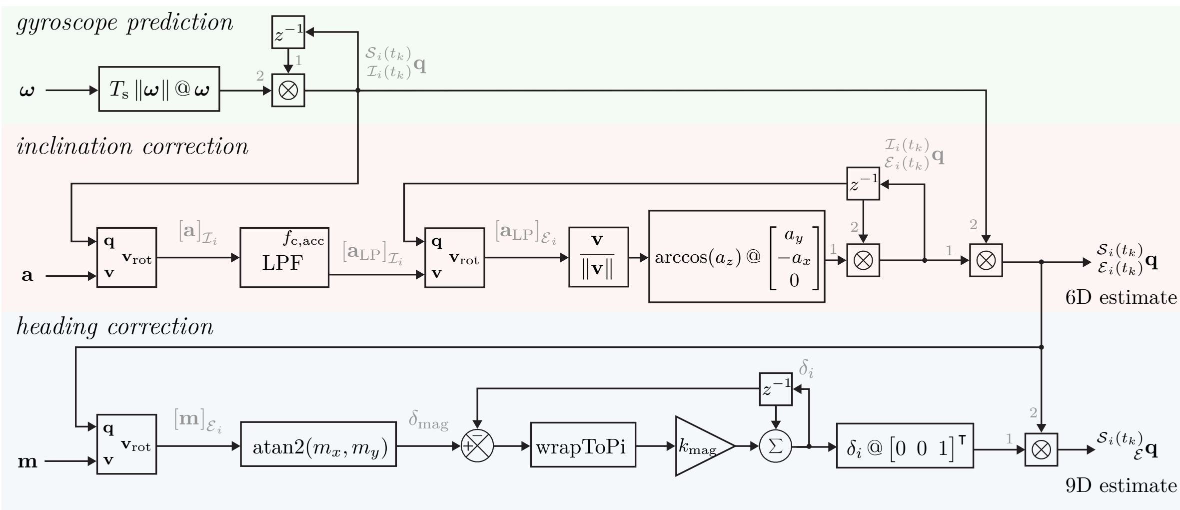

Figure 3.14: Block diagram of the proposed BasicVQF algorithm. The filter performs simultaneous 6D and 9D orientation estimation, and there is no feedback loop from the correction steps to the previous filter steps. For quaternion multiplication, the small numbers indicate the operand order ($\mathbf{q}_1 \otimes \mathbf{q}_2$).

In the following, the update steps are described in more detail.

3.6.3.1 Gyroscope Prediction

Gyroscope prediction via strapdown integration is performed by multiplying the previous estimate with a quaternion based on the norm and direction of the measured angular rate:

$$ {}^{\mathcal{S}_i(t_k)}_{\mathcal{I}_i(t_k)}\mathbf{q} = {}^{\mathcal{S}_i(t_{k-1})}_{\mathcal{I}_i(t_{k-1})}\mathbf{q} \otimes (T_\mathrm{s}\|\boldsymbol{\omega}\| \,@\, \boldsymbol{\omega})\,. \tag{3.14} $$

The rotation due to the gyroscope measurement is composed of the true change of sensor orientation and an error, due to gyroscope bias, noise, and other measurement errors (e.g., scaling errors, nonlinearity, misalignment, and clipping). This error can be regarded as a small drift in the $\mathcal{I}_i$ frame, i.e., as ${}^{\mathcal{I}_i(t_{k-1})}_{\mathcal{I}_i(t_k)}\mathbf{q}$, which can be shown via quaternion algebra (cf. Appendix A.1).

3.6.3.2 Accelerometer Correction

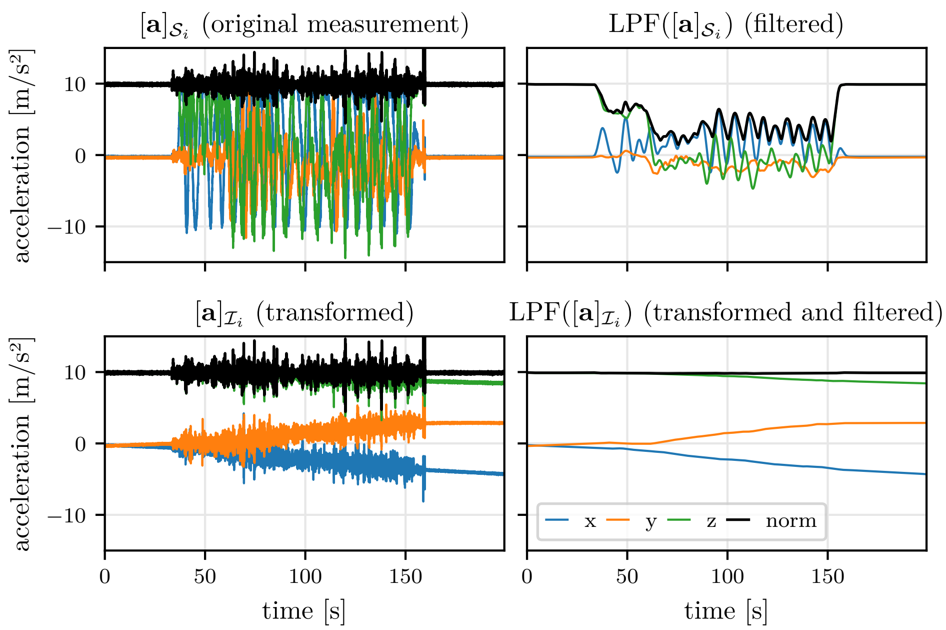

Figure 3.15: Example of unfiltered and low-pass filtered accelerations in the original sensor frame $\mathcal{S}_i$ and the almost-inertial frame $\mathcal{I}_i$. Applying a low-pass filter with a low cutoff frequency to each component in the sensor frame does not give a meaningful output. In the $\mathcal{I}_i$ frame, low-pass filtering each component of the acceleration effectively averages the measurement, allowing for acceleration and deceleration to cancel out, and the result shows the drift of the $\mathcal{I}_i$ frame due to errors in gyroscope integration.

The accelerometer measurements consist of the gravitational acceleration, change of velocity, as well as noise, bias, and other measurement errors. Most existing methods [73, 74, 76] interpret each single accelerometer sample as a 3D vector and use the angle between this vector and the expected vertical direction to derive the correction step. In contrast, to better separate the gravitational acceleration from the other components of the measurement, we transform the measured accelerations into the almost-inertial frame $\mathcal{I}_i$ and then apply a linear low-pass filter to each component. The resulting signal provides a vertical reference in the $\mathcal{I}_i$

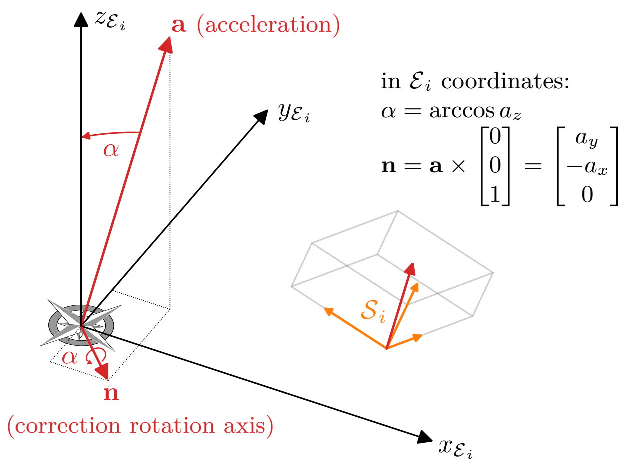

Figure 3.16: Illustration of the inclination correction step based on the filtered accelerometer measurement. In $\mathcal{E}_i$ coordinates, the filtered and normalized acceleration $\mathbf{a} = [\,a_x \;\; a_y \;\; a_z\,]^\intercal$ is expected to point in positive z-direction. This can be achieved by a correction rotation with angle $\arccos a_z$ and axis $[\,a_y \quad -a_x \;\; 0\,]^\intercal$.

frame, which slowly drifts due to errors in gyroscope integration, as shown in Figure 3.15. As a low-pass filter, we use a second-order Butterworth filter. The cutoff frequency $f_{\mathrm{c,acc}}$ of this filter defines the weight between gyroscope prediction and accelerometer correction. To ensure a fast and robust convergence when the algorithm is initialized, we calculate the arithmetic mean for the first few samples instead of using the Butterworth filter. Then, the filter state is initialized based on this mean value.

As illustrated in Figure 3.16, we can use this vertical reference to correct the inclination estimate. If $[\,a_x \;\; a_y \;\; a_z\,]^\intercal$ denotes the filtered and normalized acceleration measurement in the $\mathcal{E}_i$ frame, the shortest rotation for inclination correction has an angle of $\arccos a_z$ around the axis $[\,a_x \;\; a_y \;\; a_z\,]^\intercal \times [\,0 \;\; 0 \;\; 1\,]^\intercal = [\,a_y \quad -a_x \;\; 0\,]^\intercal$. The quaternion $\mathbf{q}_{\mathrm{corr}}$ that corresponds to this rotation can be expressed without trigonometric functions as

$$q_w = \cos\left(\frac{\arccos a_z}{2}\right) = \sqrt{\frac{a_z+1}{2}}, \tag{3.15}$$

$$\mathbf{q}_{\mathrm{corr}} = \begin{bmatrix} q_w & \frac{a_y}{2q_w} & \frac{-a_x}{2q_w} & 0 \end{bmatrix}^\intercal. \tag{3.16}$$

This quaternion is used to correct the estimate of the quaternion ${}^{\mathcal{I}_i}_{\mathcal{E}_i}\mathbf{q}$, i.e.,

$${}^{\mathcal{I}_i(t_k)}_{\mathcal{E}_i(t_k)}\mathbf{q} = \mathbf{q}_{\mathrm{corr}}(t_k) \otimes {}^{\mathcal{I}_i(t_{k-1})}_{\mathcal{E}_i(t_{k-1})}\mathbf{q}. \tag{3.17}$$

After the correction step, the low-pass filtered acceleration will perfectly point in upward direction, i.e., in z-direction of the $\mathcal{E}_i$ and $\mathcal{E}$ frames.

3.6.3.3 Magnetometer Correction

If magnetometer measurements are given, we use them to correct the heading estimate. As shown in (3.13), the heading is tracked via a scalar state $\delta_i(t_k)$ that represents the vertical rotation from the global $\mathcal{E}$ frame (with the y-axis pointing north) to the $\mathcal{E}_i$ frame. As illustrated in Figure 3.17, we can use the current magnetometer sample to derive a measurement $\delta_{\mathrm{mag}}(t_k)$ for this state by projecting the magnetic field vector into the horizontal plane. The state is

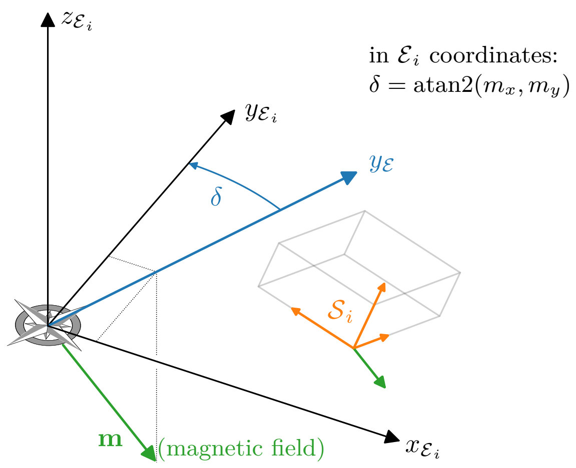

Figure 3.17: Illustration of the heading correction step based on the magnetometer measurement. In many parts of the world, Earth's magnetic field is dominated by the vertical component, e.g., in Berlin, the magnetic field is pointing down with a dip angle of 68°. An estimate of the magnetic north direction can be obtained by projecting the measured magnetic field into the horizontal plane.

then corrected by a fixed fraction k_{mag} of the deviation between state and measurement. This corresponds to a first-order low-pass filter with exponential convergence.

The parameter k_{mag} defines the fusion weight between gyroscope prediction and magnetometer correction. To ensure robust and fast convergence when the filter is initialized with the default value $\delta_i(t_0) = 0$, we average the first measurements by choosing the filter weight k_{mag} as $1, \frac{1}{2}, \frac{1}{3}, \ldots$ during the first $\frac{1}{k_{\text{mag}}}$ steps.

3.6.4 Definition of Intuitive Fusion Weights

As it is common in IOE algorithms, the behavior can be influenced by fusion weights that balance between rejecting gyroscope drift and rejecting disturbances in the accelerometer and magnetometer measurements. In Algorithm 1, those parameters are the cutoff frequency $f_{\text{c,acc}}$ and the magnetometer correction gain k_{mag}. Like for many existing methods, the meaning of the values assigned to those parameters is hard to interpret, depends on the sampling time (for k_{mag}), and does not allow for a comparison between the trust assigned to the accelerometer and the trust assigned to the magnetometer. To provide a more intuitive parametrization, we replace those parameters with time constants τ_{acc} and τ_{mag} that can be changed by the user to influence the algorithm behavior. Small time constants lead to fast correction and indicate high trust in the accelerometer or magnetometer measurements, while large time constants indicate trust in the gyroscope measurements.

Those time constants map to the internal values $f_{\text{c,acc}}$ and k_{mag} as follows.

In order to specify the gain k_{mag} of the first-order exponential filter for magnetometer correction, we use the time constant $\tau = \frac{1}{2\pi f_{\text{c}}}$ that is commonly used to characterize first-order systems. This time constant corresponds to the time needed for the step response to reach $1 - e^{-1} \approx 63.2\,\%$ of its final value. The filter weight for the proportional update can be derived from it as

$$k_{\text{mag}} = 1 - \exp\left(-\frac{T_{\text{s}}}{\tau_{\text{mag}}}\right). \tag{3.18}$$

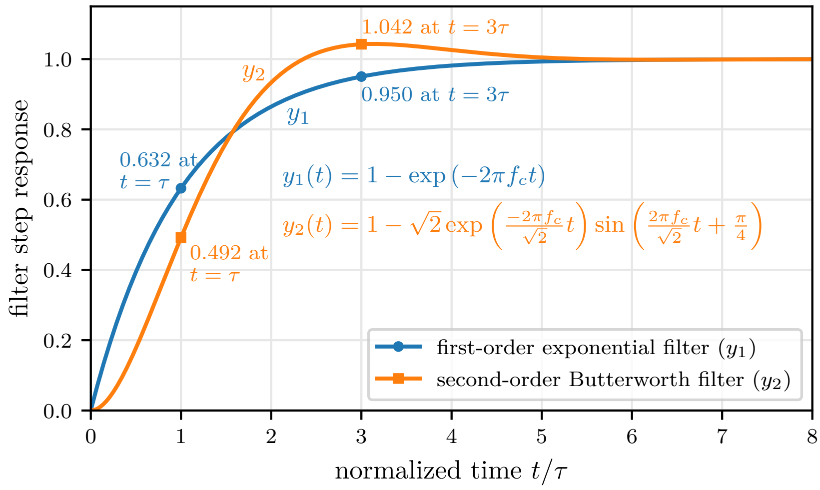

Figure 3.18: Step response for first- and second-order low-pass filters. The time axis is normalized, i.e., divided by the time constant τ of the proposed parametrization. Both filter outputs are roughly close to 0.5 at $t = \tau$ and converge up to a deviation of $\leq 5\,\%$ at $t = 3\tau$.

The second-order Butterworth filter used for accelerometer correction is characterized by the cutoff frequency $f_{\mathrm{c,acc}}$. In order to obtain a parametrization that is similar to the parametrization of the magnetometer correction, we use a time constant that corresponds to the undampened part of the step response, i.e., $\tau_{\mathrm{acc}} = \frac{\sqrt{2}}{2\pi f_{\mathrm{c,acc}}}$. The cutoff frequency used to determine the Butterworth filter coefficients is then given as

$$f_{\mathrm{c,acc}} = \frac{\sqrt{2}}{2\pi\tau_{\mathrm{acc}}}. \tag{3.19}$$

See Figure 3.18 for a comparison of the step responses of both filter types in relation to the time constant τ.

This mapping is used to derive the internal parameters $f_{\mathrm{c,acc}}$ and k_{mag} from the user-specified time constants τ_{acc} and τ_{mag}. The same parametrization via time constants is also used for the other first-order and second-order filters introduced in the following subsections. Note that we will later determine default values for τ_{acc} and τ_{mag} that yield excellent out-of-the-box accuracy for a large range of application scenarios, and manual tuning by adjusting these time constants is therefore only required in rare edge cases.

3.6.5 Gyroscope Bias Estimation

To ensure high accuracy in the presence of gyroscope bias, we extend the BasicVQF algorithm from Section 3.6.3 by a method to estimate and compensate such bias. This method is given in Algorithm 2. In existing IOE algorithms, bias estimation is commonly realized by integral action [73, 74, 76]. However, this approach requires feedback of both accelerometer and magnetometer correction [74], making the gyroscope bias estimate susceptible to magnetic disturbances. To prevent this, the proposed method for gyroscope bias estimation avoids using any information from the magnetometer correction step. Instead, during motion, the bias is estimated solely from the disagreement between strapdown integration and accelerometer measurements.

Algorithm 2 Gyroscope Bias Estimation

procedure RestDetection($\boldsymbol{\omega}, \mathbf{a}$)
  $T_{\text{rest}} \leftarrow T_{\text{rest}} + T_{\text{s}}$
  $\boldsymbol{\omega}_{\text{LP}} \leftarrow$ low-pass filter $\boldsymbol{\omega}$ with $\tau = 0.5\,\text{s}$
  $\mathbf{a}_{\text{LP}} \leftarrow$ low-pass filter $\mathbf{a}$ with $\tau = 0.5\,\text{s}$
  if $\|\boldsymbol{\omega} - \boldsymbol{\omega}_{\text{LP}}\| \geq 2\,°/\text{s}$ or $\|\mathbf{a} - \mathbf{a}_{\text{LP}}\| \geq 0.5\,\text{m/s}^2$ **then**
    $T_{\text{rest}} \leftarrow 0$
  end if
  if $T_{\text{rest}} \geq 1.5\,\text{s}$ **then**
    rest detected
  else
    movement detected
  end if
end procedure
procedure InitializeKalmanFilter
  $\hat{\mathbf{b}} \leftarrow [0\ \ 0\ \ 0]^\intercal$ ▷ Gyroscope bias estimate
  $\mathbf{P} \leftarrow (0.5\,°/\text{s})^2 \mathbf{I}_{3\times 3}$ ▷ Covariance matrix
  $v \leftarrow (0.1\,°/\text{s})^2 T_{\text{s}} (100\,\text{s})^{-1}$ ▷ System noise
  $w_{\text{motion}} \leftarrow (0.1\,°/\text{s})^4 v^{-1} + (0.1\,°/\text{s})^2$ ▷ Motion update variance
  $w_{\text{rest}} \leftarrow (0.03\,°/\text{s})^4 v^{-1} + (0.03\,°/\text{s})^2$ ▷ Rest update variance
end procedure
procedure BiasEstimationStep(${}^{\mathcal{I}_i}_{\mathcal{E}_i}\mathbf{q}, a_x, a_y, a_z$)
  $\mathbf{R} \leftarrow$ rotation matrix corresponding to ${}^{\mathcal{I}_i}_{\mathcal{E}_i}\mathbf{q}$
  $\mathbf{R}_{\text{LP}} \leftarrow$ low-pass filter $\mathbf{R}$ with $\tau = \tau_{\text{acc}}$
  $\hat{\mathbf{b}}_{\mathcal{E}_i,\text{LP}} \leftarrow$ low-pass filter $\mathbf{R}\hat{\mathbf{b}}$ with $\tau = \tau_{\text{acc}}$
  if rest detected **then**
    $\mathbf{y} \leftarrow \hat{\mathbf{b}}$
    $\mathbf{C} \leftarrow \mathbf{I}_{3\times 3}$
    $\mathbf{W} \leftarrow w_{\text{rest}} [1\ \ 1\ \ 1]^\intercal$
  else
    $\mathbf{y} \leftarrow T_{\text{s}}^{-1} [a_y\ \ -a_x\ \ 0]^\intercal + \text{diag}(1, 1, 0)\hat{\mathbf{b}}_{\mathcal{E}_i,\text{LP}}$
    $\mathbf{C} \leftarrow \mathbf{R}_{\text{LP}}$
    $\mathbf{W} \leftarrow w_{\text{motion}} [1\ \ 1\ \ \frac{1}{0.0001}]^\intercal$
  end if
  $\mathbf{P} \leftarrow \mathbf{P} + v[1\ \ 1\ \ 1]^\intercal$ ▷ Kalman filter update
  $\mathbf{K} \leftarrow \mathbf{P}\mathbf{C}^\intercal(\mathbf{W} + \mathbf{C}\mathbf{P}\mathbf{C}^\intercal)^{-1}$
  $\hat{\mathbf{b}} \leftarrow \hat{\mathbf{b}} + \mathbf{K}\,\text{clip}(\mathbf{y} - \mathbf{C}\hat{\mathbf{b}}, -2\,°/\text{s}, 2\,°/\text{s})$ ▷ Limit disagreement to $2\,°/\text{s}$
  $\mathbf{P} \leftarrow \mathbf{P} - \mathbf{K}\mathbf{C}\mathbf{P}$
  $\hat{\mathbf{b}} \leftarrow \text{clip}(\hat{\mathbf{b}}, -2\,°/\text{s}, 2\,°/\text{s})$ ▷ Limit bias estimate to $2\,°/\text{s}$
end procedure

Moreover, note that in many application scenarios, the IMU will occasionally be at rest for several seconds, and those phases can be detected reliably. The proposed bias estimation algorithm leverages this and determines the bias directly from low-pass-filtered gyroscope measurements whenever it detects a period of rest.

To detect whether the IMU is at rest (procedure RestDetection in Algorithm 2), we first filter each component of the gyroscope and accelerometer measurements with a second-order Butterworth filter and a time constant of $\tau = 0.5\,\mathrm{s}$. Note that, unlike the low-pass filter for the acceleration used for inclination correction, we apply the filter directly in the sensor frame. We then calculate the Euclidean norm of the deviation between the current measurement and the filtered measurement. Rest is detected if, in the last $1.5\,\mathrm{s}$, the gyroscope and accelerometer deviations are always less than $2\,°/\mathrm{s}$ and $0.5\,\mathrm{m/s^2}$, respectively. Note that we deliberately do not use magnetometer measurements for rest detection since the rest detection was found to be very reliable when only using gyroscope and accelerometer measurements, whereas using magnetometers did not provide additional value.

To estimate the gyroscope bias during rest and motion, we employ a Kalman filter [59, 60], with the gyroscope bias as state and a time-dependent output matrix:

$$\mathbf{b}(t_k) = \mathbf{b}(t_{k-1}) + \mathbf{v}(t_k), \qquad \mathbf{v}(t_k) \sim \mathcal{N}(0, \mathbf{V}), \tag{3.20}$$

$$\mathbf{y}(t_k) = \mathbf{C}(t_k)\mathbf{b}(t_k) + \mathbf{w}(t_k), \qquad \mathbf{w}(t_k) \sim \mathcal{N}(0, \mathbf{W}(t_k)). \tag{3.21}$$

During rest, we use the low-pass filtered gyroscope readings $\boldsymbol{\omega}_{\mathrm{LP}}$ (which we calculated in the rest detection procedure) as a direct measurement of the bias, i.e., $\mathbf{C}(t_k) = \mathbf{I}_{3\times 3}$ and $\mathbf{y}(t_k) = \boldsymbol{\omega}_{\mathrm{LP}}(t_k)$. Because the IMU is at rest and gyroscope readings are already filtered, we can assign a comparatively large weight (i.e., a small covariance) to this measurement update and achieve fast convergence for the bias estimate $\hat{\mathbf{b}}(t_k)$.

During motion, we estimate the gyroscope bias from the inclination correction steps. At every time step, the new error due to gyroscope bias is a local rotation (i.e., in $\mathcal{S}_i$) with the rotation vector $T_{\mathrm{s}}(\mathbf{b} - \hat{\mathbf{b}})$, and the inclination correction is a global rotation (i.e., in $\mathcal{E}_i$) with a horizontal rotation vector $\mathbf{c} = [\,c_x \;\; c_y \;\; 0\,]^\intercal$. In ideal conditions (i.e., in a steady state and without noise or other errors), the correction rotation will exactly compensate the inclination portion of the bias rotation. As illustrated in Figure 3.19, in this case, the correction is the inverse of the horizontal projection of the bias rotation.

With $\mathbf{R}$ being the rotation matrix corresponding to ${}^{\mathcal{S}_i}_{\mathcal{E}_i}\mathbf{q}$, we can express this as

$$\mathbf{R}(\mathbf{b} - \hat{\mathbf{b}}) = -\frac{1}{T_{\mathrm{s}}}\begin{bmatrix} c_x \\ c_y \\ * \end{bmatrix}, \tag{3.22}$$

where the star indicates that the gyroscope bias in the current vertical direction is not observable by accelerometer measurements.

To achieve slow forgetting of the bias for the special case in which the same axis is vertical for a long time, we set the corresponding measurement to zero, with a substantially larger variance to slow down convergence.

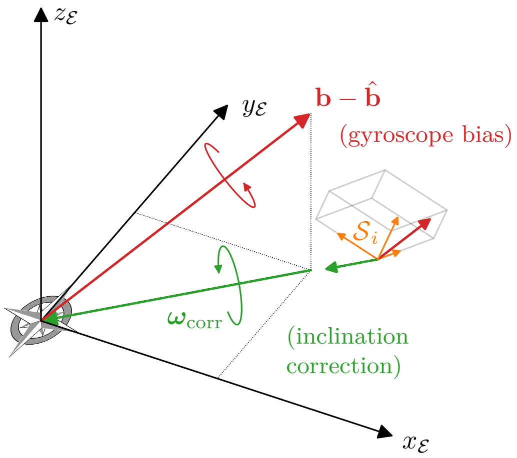

Figure 3.19: Illustration of the principle behind gyroscope bias estimation from the inclination correction step. In the steady state, the correction angular rate $\boldsymbol{\omega}_\mathrm{corr}$ that corresponds to the accelerometer-based correction is the (negative) horizontal projection of the remaining gyroscope bias $\mathbf{b} - \hat{\mathbf{b}}$.

With an output matrix of $\mathbf{C}_k = \mathbf{R} =: (r_{ij})$ and the correction vector $[a_y \quad -a_x \quad 0]^\intercal$, we obtain the following measurement equation:

$$\mathbf{y}_k = \begin{bmatrix} -\frac{1}{T_\mathrm{s}} a_y + r_{11}\hat{b}_x + r_{12}\hat{b}_y + r_{13}\hat{b}_z \\ \frac{1}{T_\mathrm{s}} a_x + r_{21}\hat{b}_x + r_{22}\hat{b}_y + r_{23}\hat{b}_z \\ 0 \end{bmatrix}. \tag{3.23}$$

This measurement equation does not take into account that the measured accelerations are low-pass filtered in the $\mathcal{I}_i$ frame. In order to substantially improve the accuracy and robustness of the bias estimation, we low-pass filter the components of $\mathbf{R}$ and $\mathbf{R}\hat{\mathbf{b}}$ with the same filter used for the accelerometer measurements in the $\mathcal{I}_i$ frame. See Appendix A.2 for a detailed derivation of this full measurement equation.

The tuning parameters of a Kalman filter are the initial covariance, the covariance of the process noise, and the covariance of the measurement noise. Since the real values of those covariances are hard to obtain and would furthermore depend on the sampling rate, we employ a parametrization that ensures the following properties:

1. The initial estimation uncertainty is $\sigma_\mathrm{init} = 0.5\,°/\mathrm{s}$.

2. During motion, the uncertainty converges to $\sigma_\mathrm{motion} = 0.1\,°/\mathrm{s}$ (for the non-vertical axes).

3. During rest, the uncertainty converges to $\sigma_\mathrm{rest} = 0.03\,°/\mathrm{s}$.

4. Without updates, the estimation uncertainty increases from 0 to $0.1\,°/\mathrm{s}$ in the forgetting time $t_\mathrm{forget} = 100\,\mathrm{s}$.

How those parameters translate to the covariances internally used by the Kalman filter is specified in Algorithm 2 and further explained in Appendix A.3. Note that the absolute values of the provided parameters are arbitrary and chosen to facilitate an intuitive understanding of the estimation uncertainty. For the behavior of the Kalman filter, only the relation between the parameters is relevant.

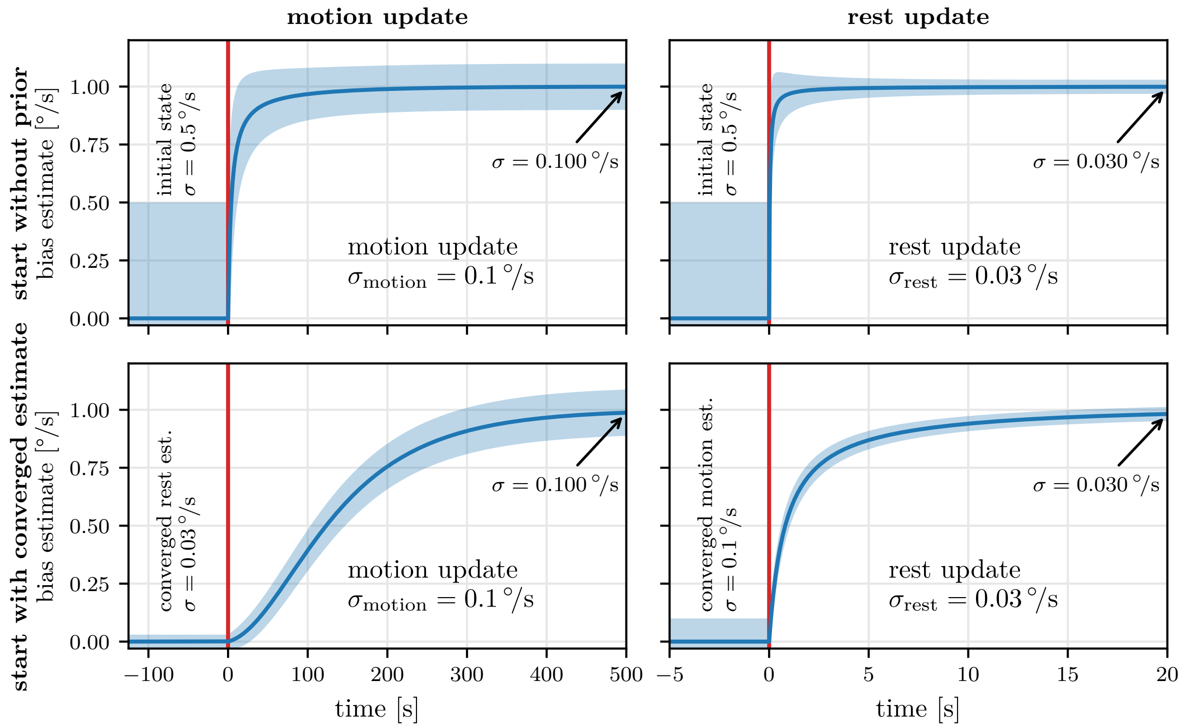

Figure 3.20: Step response for the Kalman filter with the proposed parametrization. The blue bands show the standard deviation σ of the estimate. At $t = 0$, the Kalman filter either starts in the initial state ($\sigma = 0.5\,°/\text{s}$) or in a converged state of either the motion or rest update with an estimate of $0\,°/\text{s}$. At $t = 0$, the measurement changes to $1\,°/\text{s}$. Directly after initialization, the filter converges much faster than in cases where a (contradictory) previous estimate was already obtained. In general, the motion update converges much slower than the rest update.

Figure 3.20 shows how the Kalman filter behaves with the proposed parametrization. The relation between the uncertainty of the measurement (large during motion, small during rest) and the uncertainty of the current estimate determines how fast the bias estimation converges. After initialization without prior knowledge, the estimation uncertainty is large, which leads to fast convergence. From a converged estimate during motion (i.e., with medium uncertainty), a contradicting but much more reliable observation during rest is adopted within several seconds. From a converged rest estimate, a contradicting observation during motion is adopted much slower due to the larger uncertainty of the measurement.

3.6.6 Magnetic Disturbance Rejection

We extend the proposed IOE algorithm with a set of methods that enable adaptive filtering of the magnetometer measurements with the aim of reducing the influence of temporary magnetic disturbances. The employed strategy is composed of three parts: magnetic disturbance *detection*, magnetic disturbance *rejection*, and new magnetic field *acceptance*. The full algorithm is given in Algorithm 3.

The magnetic disturbance *detection* uses a user-defined or automatically determined reference for the norm and dip angle of the local magnetic field. The magnetometer measurements are considered to be undisturbed only if they have been close to the reference for at least 0.5 s – and disturbed otherwise. Whenever the magnetic field is considered to be

Algorithm 3 Magnetic Disturbance Rejection

procedure MagDistDetection($\mathbf{m}, {}^{\mathcal{S}_i}_{\mathcal{E}_i}\mathbf{q}$)
  $n \leftarrow \|\mathbf{m}\|$ ▷ Norm of magnetic field
  $\theta \leftarrow -\arcsin\left(\begin{bmatrix}0 & 0 & 1\end{bmatrix}\left({}^{\mathcal{S}_i}_{\mathcal{E}_i}\mathbf{q} \otimes \mathbf{m} \otimes {}^{\mathcal{S}_i}_{\mathcal{E}_i}\mathbf{q}^{-1}\right) n^{-1}\right)$ ▷ Dip angle
  low-pass filter n and θ with $\tau = 0.05\,\mathrm{s}$
  if $|n - n_{\mathrm{ref}}| < 0.1 n_{\mathrm{ref}}$ and $|\theta - \theta_{\mathrm{ref}}| < 10°$ **then**
    $T_{\mathrm{undist}} \leftarrow T_{\mathrm{undist}} + T_{\mathrm{s}}$
    if $T_{\mathrm{undist}} \geq 0.5\,\mathrm{s}$ **then**
      disturbed $\leftarrow$ false
      $n_{\mathrm{ref}} \leftarrow k_{\mathrm{ref}}\,(n - n_{\mathrm{ref}})$, with $\tau_{\mathrm{ref}} = 20\,\mathrm{s}$
      $\theta_{\mathrm{ref}} \leftarrow k_{\mathrm{ref}}\,(\theta - \theta_{\mathrm{ref}})$ ▷ Track slow changes of norm and dip
    else
      disturbed $\leftarrow$ true
      $T_{\mathrm{undist}} \leftarrow 0$
    end if
  end if
end procedure
procedure NewMagFieldAcceptance($n, \theta, \|\boldsymbol{\omega}\|$)
  if $|n - n_{\mathrm{cand}}| < 0.1 n_{\mathrm{cand}}$ and $|\theta - \theta_{\mathrm{cand}}| < 10°$ **then**
    if $\|\boldsymbol{\omega}\| \geq 20\,°/\mathrm{s}$ **then** ▷ Only count the time if there is movement
      $T_{\mathrm{cand}} \leftarrow T_{\mathrm{cand}} + T_{\mathrm{s}}$
    end if
    $n_{\mathrm{cand}} \leftarrow k_{\mathrm{ref}}\,(n - n_{\mathrm{cand}})$
    $\theta_{\mathrm{cand}} \leftarrow k_{\mathrm{ref}}\,(\theta - \theta_{\mathrm{cand}})$
    if disturbed and $T_{\mathrm{cand}} \geq 20\,\mathrm{s}$ **then** ▷ Accept candidate as new reference
      disturbed $\leftarrow$ false
      $n_{\mathrm{ref}} \leftarrow n_{\mathrm{cand}}$
      $\theta_{\mathrm{ref}} \leftarrow \theta_{\mathrm{cand}}$
    end if
  else ▷ Reset candidate to current value
    $T_{\mathrm{cand}} \leftarrow 0$
    $n_{\mathrm{cand}} \leftarrow n$
    $\theta_{\mathrm{cand}} \leftarrow \theta$
  end if
end procedure
procedure MagDistRejection
  if disturbed **then**
    if $T_{\mathrm{reject}} < 60\,\mathrm{s}$ **then**
      $T_{\mathrm{reject}} \leftarrow T_{\mathrm{reject}} + T_{\mathrm{s}}$
      do not perform heading correction
    else
      perform heading correction with $\frac{1}{2} k_{\mathrm{mag}}$
    end if
  else
    $T_{\mathrm{reject}} \leftarrow \max(T_{\mathrm{reject}} - 2T_{\mathrm{s}}, 0)$
    perform heading correction with k_{mag}
  end if
end procedure

undisturbed, the reference values are slowly updated to track slow changes in the norm and dip angle.

The magnetic disturbance *rejection* adjusts the speed of the first-order filter used for heading correction if magnetic disturbances are detected. For disturbances of up to 60 s, the magnetometer update is fully disabled. For longer periods that are considered to be disturbed, updates are performed, but at a lower speed.

Finally, the new magnetic field *acceptance* is used to deal with sudden changes in the environment, e.g., after changing the terrain from outdoor to indoor or moving to a different indoor room with a different local magnetic field. Whenever the magnetic field is considered to be disturbed but seems homogeneous (for a sufficiently long time during which the IMU was not stationary), the norm and dip angle of the current magnetic field is used as the new reference.

3.6.7 Offline Variant of the Orientation Estimation Algorithm

In application scenarios in which the complete time series of recorded data is available (offline data processing), we can employ acausal signal processing methods to further improve accuracy. As commonly done in signal processing for zero-phase filtering [90], we first run the filtering steps forward and then again backward in time. This allows us to leverage the existing real-time implementation to create the offline variant OfflineVQF detailed in Algorithm 4.

In short, the steps performed for offline orientation estimation are:

1. Run the proposed VQF algorithm twice, once forward and once backward in time.
2. Average both gyroscope bias estimates, using the inverse of the variance as weight.

Algorithm 4 Offline Orientation Estimation Algorithm

procedure OfflineVQF($\boldsymbol{\omega}[t_{1:N}], \mathbf{a}[t_{1:N}], \mathbf{m}[t_{1:N}]$)
  $\ldots, \mathrm{dist}_1, \hat{\mathbf{b}}_1, \mathbf{P}_1 \leftarrow \mathrm{VQF}(\boldsymbol{\omega}[t_{1:N}], \mathbf{a}[t_{1:N}], \mathbf{m}[t_{1:N}])$ ▷ Run real-time filter in forward direction
  $\ldots, \mathrm{dist}_2, \hat{\mathbf{b}}_2, \mathbf{P}_2 \leftarrow \mathrm{VQF}(-\boldsymbol{\omega}[t_{N:1}], \mathbf{a}[t_{N:1}], \mathbf{m}[t_{N:1}])$ ▷ Run real-time filter in backward direction
  $\mathrm{dist}[t_{1:N}] \leftarrow \mathrm{dist}_1[t_{1:N}] \land \mathrm{dist}_2[t_{1:N}]$ ▷ Regard magnetic field as disturbed if both runs detected disturbances
  $\hat{\mathbf{b}}[t_{1:N}] \leftarrow (\mathbf{P}_1[t_{1:N}]^{-1} + \mathbf{P}_2[t_{1:N}]^{-1})^{-1}(\mathbf{P}_1[t_{1:N}]^{-1}\hat{\mathbf{b}}_1[t_{1:N}] - \mathbf{P}_2[t_{1:N}]^{-1}\hat{\mathbf{b}}_2[t_{1:N}])$ ▷ Average bias estimates of both filter runs via covariance
  ${}^{\mathcal{S}_i}_{\mathcal{I}_i}\mathbf{q}[t_{1:N}] \leftarrow \mathrm{integrateGyr}(\boldsymbol{\omega}[t_{1:N}] - \hat{\mathbf{b}}[t_{1:N}])$ ▷ Perform gyroscope strapdown integration
  $[\mathbf{a}]_{\mathcal{I}_i}[t_{1:N}] \leftarrow {}^{\mathcal{S}_i}_{\mathcal{I}_i}\mathbf{q}[t_{1:N}] \otimes \mathbf{a}[t_{1:N}] \otimes {}^{\mathcal{S}_i}_{\mathcal{I}_i}\mathbf{q}[t_{1:N}]^{-1}$ ▷ Transform acceleration into $\mathcal{I}_i$ frame
  $[\mathbf{a}_{\mathrm{LP}}]_{\mathcal{I}_i}[t_{1:N}] \leftarrow \mathrm{filtfiltLPF}([\mathbf{a}]_{\mathcal{I}_i}[t_{1:N}], \tau = \tau_{\mathrm{acc}})$ ▷ Forward-backward low-pass filtering
  ${}^{\mathcal{I}_i}_{\mathcal{E}_i}\mathbf{q}[t_{1:N}] \leftarrow$ perform inclination correction based on $[\mathbf{a}_{\mathrm{LP}}]_{\mathcal{I}_i}[t_{1:N}]$
  $[\, m_x \;\; m_y \;\; m_z \,]^\intercal[t_{1:N}] \leftarrow \left({}^{\mathcal{I}_i}_{\mathcal{E}_i}\mathbf{q}[t_{1:N}] \otimes {}^{\mathcal{S}_i}_{\mathcal{I}_i}\mathbf{q}[t_{1:N}]\right) \otimes \mathbf{m}[t_{1:N}] \otimes \left({}^{\mathcal{I}_i}_{\mathcal{E}_i}\mathbf{q}[t_{1:N}] \otimes {}^{\mathcal{S}_i}_{\mathcal{I}_i}\mathbf{q}[t_{1:N}]\right)^{-1}$
  $\delta_{\mathrm{mag}}[t_{1:N}] \leftarrow \mathrm{atan2}(m_x[t_{1:N}], m_y[t_{1:N}])$
  $\delta_i[t_{1:N}] \leftarrow$ run heading correction filter with magnetic disturbance rejection on $\delta_{\mathrm{mag}}[t_{1:N}]$
  $\delta_i[t_{N:1}] \leftarrow$ run heading correction filter with magnetic disturbance rejection on $\delta_i[t_{N:1}]$
  return ${}^{\mathcal{I}_i}_{\mathcal{E}_i}\mathbf{q}[t_{1:N}] \otimes {}^{\mathcal{S}_i}_{\mathcal{I}_i}\mathbf{q}[t_{1:N}]$, ▷ 6D sensor orientation ${}^{\mathcal{S}_i}_{\mathcal{E}_i}\mathbf{q}$
    $[\cos\frac{\delta_i[t_{1:N}]}{2} \;\; 0 \;\; 0 \;\; \sin\frac{\delta_i[t_{1:N}]}{2}]^\intercal \otimes {}^{\mathcal{I}_i}_{\mathcal{E}_i}\mathbf{q}[t_{1:N}] \otimes {}^{\mathcal{S}_i}_{\mathcal{I}_i}\mathbf{q}[t_{1:N}]$ ▷ 9D sensor orientation ${}^{\mathcal{S}_i}_{\mathcal{E}}\mathbf{q}$
end procedure

VQF: real-time implementation, returns magnetic disturbance state, bias estimate, and bias estimation covariance
integrateGyr: gyroscope strapdown integration by (3.14)
filtfiltLPF: forward-backward filtering with second-order Butterworth low-pass filter

3. Transform the accelerometer measurements into the $\mathcal{I}_i$ frame and perform acausal forward-backward low-pass filtering, then use this filtered acceleration to perform the inclination correction.

4. Regard the magnetic field as disturbed if both the forward and backward estimates detected magnetic disturbances.

5. Run the first-order filter for the state δ_i twice, once forward and once backward in time, with magnetic disturbance rejection.

3.6.8 Open-Source Implementation

Implementations of the proposed orientation estimation algorithm are available at `https://github.com/dlaidig/vqf` under the MIT license. Native implementations are provided in C++, Python, and Matlab. Furthermore, the fast C++ implementation can easily be used from Python code. The Python package is available at `https://pypi.org/project/vqf/` and can be installed via pip. Documentation is available at `https://vqf.readthedocs.io/`.

3.7 Evaluation of the Proposed IOE Algorithm

In this section, we evaluate the performance of the proposed IOE algorithm on six publicly available datasets and compare the results obtained with the proposed method to results obtained with eight state-of-the-art IOE algorithms.

3.7.1 Datasets and Algorithms

To evaluate the accuracy of IOE, we consider publicly available datasets consisting of IMU measurements and a ground truth orientation obtained from marker-based optical motion capture (OMC). In the present evaluation, we use the BROAD dataset introduced in Section 3.4 and all datasets containing data that is suitable for IOE accuracy evaluation as reviewed in Section 3.3, i.e.,

- BROAD (Section 3.4): 39 trials (23 undisturbed trials with different motion types and speeds and 16 trials with various deliberate disturbances),
- Sassari [53]: 18 trials (3 speeds, 3 IMU models, and 2 IMUs of each model),
- RepoIMU [83]: 21 trials (*T-Stick* only; test 5, test 6 trial 1, and test 10 excluded due to artifacts, as explained in Section 3.3),
- OxIOD [85]: 71 trials (only *handbag*, *handheld*, *pocket*, *running*, *slow walking*, and *trolley* trials),
- TUM VI [87]: 6 trials (*room* only; no magnetometer data),
- EuRoC MAV [86]: 6 trials (*Vicon room* only; no magnetometer data).

Combined, the collection of evaluation data consists of 161 trials with a total duration of 12.9 h. The data includes motions of handheld IMUs (various combinations of fast and slow rotations and translations), walking and running, as well as flight data from a micro aerial vehicle. It contains data from eight different IMU models, recorded at sampling rates ranging from 100 Hz to 286 Hz. This large collection of experimental data allows us to evaluate the robustness of the proposed method for different motion characteristics, different sensor hardware, and different sampling rates.

For comparison with the proposed method, we use the eight state-of-the-art algorithms listed in Table 3.1 of Section 3.2.

3.7.2 Algorithm Parametrization

Before assessing the IOE accuracy, we need to determine suitable tuning parameters for each algorithm. Section 3.4.6 introduced a metric to assess the performance of an IOE algorithm, the TAGP. This metric is defined as the smallest possible RMSE, averaged over all 39 trials of the BROAD dataset, that can be obtained with a common algorithm parametrization for all trials. The associated parametrization can then be expected to provide good results for a wide variety of motions and disturbance scenarios.

However, one limitation of the BROAD dataset is that all trials are performed with the same IMU model. To find parameters that are not only robust against movement speed, type of motion, and various disturbances, but also work well for different sensor characteristics, we define an extended TAGP metric, the TAGP_x.

Similar to the TAGP, the TAGP_x is the smallest possible RMSE, averaged over the aforementioned trials for each of the six datasets. The errors are first averaged separately for each dataset. Then, the resulting errors are averaged, where the dedicated benchmark dataset BROAD is given a five times larger weight than all other datasets, which are weighted equally. For trials without magnetometer data (and for RIANN, which does not support magnetometers), the inclination error, as defined in Section 3.4.5, is used instead of the orientation error.

Figure 3.21 shows how the weighted error as defined above depends on the tuning parameters for the default and the basic variant of the proposed VQF algorithm. The TAGP_x is the

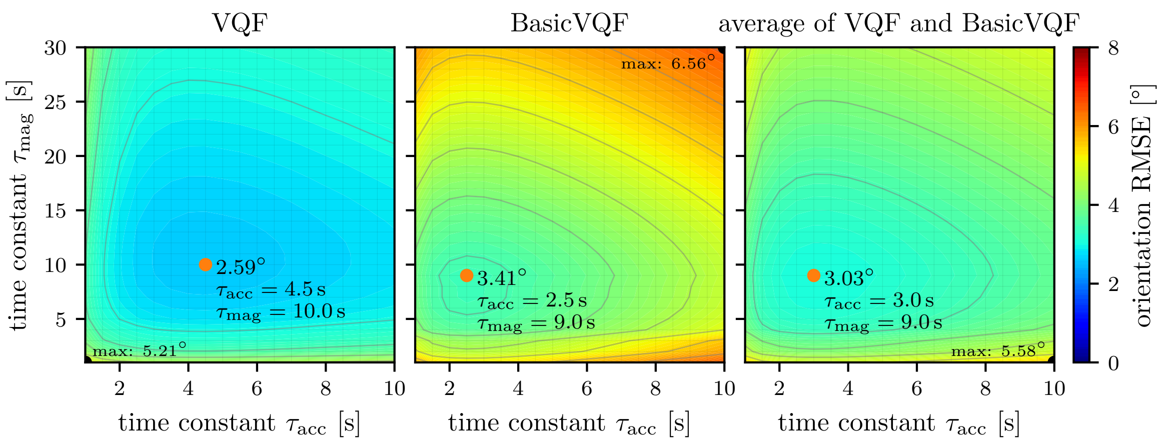

Figure 3.21: RMSE (weighted average over all datasets) achieved with the proposed VQF algorithm and with the reduced BasicVQF variant, for different values of the tuning parameters. The default algorithm parameters are chosen such that the mean of both errors is minimized, i.e., $\tau_\text{acc} = 3\,\text{s}$ and $\tau_\text{mag} = 9\,\text{s}$.

Table 3.4: Results of TAGP_x-based parameter tuning for all IOE algorithms used in the evaluation.

Algorithm	TAGP_x	Parameter	Value	Search grid (start : step : end)
VQF	2.64°	τ_acc	3	1 : 0.5 : 10
		τ_mag	9	1 : 1 : 30
MAH [73]	14.83°	K_P	1.44	0.02 : 0.02 : 4
		K_I	0.0027	0 : 0.0001 : 0.004
MAD [74]	12.01°	β	0.29	0.01 : 0.01 : 1
		ζ_bias	0	0 : 0.00001 : 0.001
VAC [75]	5.63°	α_acc	0.00085	0.0001 : 0.00005 : 0.001
		β_mag	0.0005	0.0001 : 0.00005 : 0.001
		α_bias	0.00055	0.0001 : 0.00005 : 0.001
		b_est	true	{false, true}
		α_adapt	false	{false, true}
FKF [71]	9.19°	σ^2_gyr	0.001	0.001 : 0.001 : 0.001
		σ^2_acc	0.002	0.001 : 0.0001 : 0.005
		σ^2_mag	0.0033	0.001 : 0.0001 : 0.005
SEL [76]	4.58°	τ_acc	3.2	1 : 0.2 : 5
		τ_mag	10	1 : 1 : 20
		ζ_bias	5	0 : 1 : 10
		r_acc	2	0 : 1 : 10
MKF	7.58°	σ^2_acc	0.00028171	MKF parameters were iteratively determined with line searches instead of a grid search.
		σ^2_mag	14.55188	
		σ^2_gyr	0.15625	
		σ^2_gyrdrift	3×10^{-21}	
		σ^2_linacc	0.49128	
		d_linacc	0.81297	
		σ^2_magdist	0.12329	
		d_magdist	0.51005	
KOK [81]	11.70°	σ_gyr	0.185	0.01 : 0.005 : 0.5
		ζ_bias	0	0 : 0.00001 : 0.001
		m_est	true	{false, true}
RIANN [57]	1.32°	no parameters		
	TAGP_x value not comparable to other algorithms because the inclination RMSE is used instead of the orientation RMSE.			

minimum value of this error, i.e., 2.59° for VQF and 3.41° for BasicVQF, which shows that gyroscope bias estimation and magnetic disturbance rejection lead to improved accuracy. The optimal values for the time constants τ_{acc} and τ_{mag} are similar for both variants, but not equal. To avoid having to specify different default parameters for VQF and BasicVQF, we simply use the average of the errors obtained with both variants to determine the default values $\tau_{\mathrm{acc}} = 3\,\mathrm{s}$ and $\tau_{\mathrm{acc}} = 9\,\mathrm{s}$.

To provide a fair comparison between the proposed and the state-of-the-art methods, we also optimize the parameters for all other algorithms according to the $\mathrm{TAGP_x}$, i.e., we find the parameters that allow each algorithm to provide the best possible performance across all datasets. To determine the parameters, a grid search was performed, i.e., the algorithm performance was evaluated on a grid defined by the Cartesian product of the linearly spaced parameter sets presented in Table 3.4. This search grid was iteratively adjusted to ensure that the distance between parameter values is sufficiently small and that the $\mathrm{TAGP_x}$ parameters do not lie at the border of the grid. The resulting averaged error, the associated parameters, and the parameter search range are presented in Table 3.4.

Due to the high dimensionality of the search space and the slow implementation, the parameters for MKF were only evaluated using a line search, i.e., only one parameter was changed while the other parameters are kept at the previously found minimum. The search range was also iteratively adjusted until it converged to a stable minimum.

In the following, we always use the optimal parameters given in Table 3.4 to evaluate and compare algorithm performance.

3.7.3 Orientation Estimation Accuracy

To assess the performance of all algorithms, we apply each to the data of all trials of all datasets. In the case of 6D (magnetometer-free) sensor fusion, we determine the inclination error (Section 3.4.5), and for 9D sensor fusion the orientation error, in each case between the IMU-based estimate and the OMC ground truth. We then calculate the RMSE while only considering the motion phases. Since the TUM VI and EuRoC MAV datasets do not include

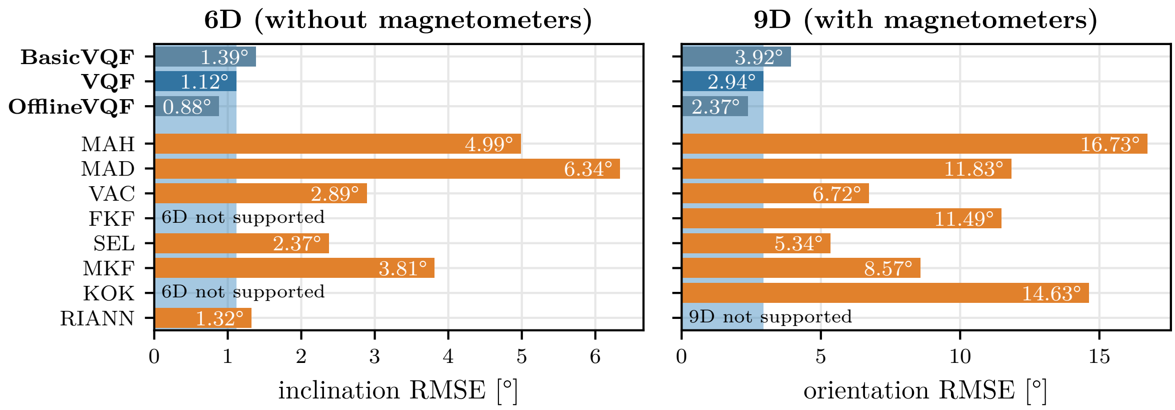

Figure 3.22: RMSE (weighted average over all datasets) for the proposed VQF algorithm and all state-of-the-art algorithms. VQF outperforms all eight literature methods, and only RIANN provides similar 6D performance. Even the errors obtained with the simple BasicVQF variant are clearly lower than for the other seven algorithms. When real-time capability is not required, using the offline variant is advisable to further increase the accuracy of the orientation estimates.

magnetometer data, they are only considered for the 6D results. We average the errors by dataset analogously to the definition of the $\mathrm{TAGP_x}$ in Section 3.7.2. The resulting values for all algorithms are presented in Figure 3.22.

One main observation from this figure is that the proposed method VQF consistently provides considerably lower errors than the existing orientation estimation algorithms. For 9D IOE, there is a 1.8-fold to 5-fold increase in accuracy. For 6D IOE, the increase is 17 % for RIANN and between 2.1-fold and 5-fold for the other methods. The only algorithm that achieves similar inclination errors is the neural network RIANN. It should be noted that this algorithm cannot perform 9D sensor fusion and was trained on some of the datasets that are used in the present evaluation (see [57] for details).

Figure 3.22 also allows us to compare the variants of the proposed method. Unsurprisingly, the errors obtained with the BasicVQF variant (no bias estimation and no magnetic disturbance rejection) are slightly larger. However, with the exception of RIANN, even the 6D and 9D errors of BasicVQF are still clearly lower than the corresponding errors obtained with any of the existing algorithms. Compared to the real-time-capable implementation, the offline variant OfflineVQF is able to further increase the estimation accuracy by 20 percent. Therefore, employing this variant is advisable when analyzing recorded data.

While Figure 3.22 shows a clear improvement in accuracy with respect to the state of the art when looking at errors averaged over a large number of trials, a comprehensive comparison should also include a closer look at individual trials. Figure 3.23 differentiates the errors by dataset and shows a marker for each single trial. Comparing medians, the interquartile ranges, the lengths of the whiskers, or the distributions of outliers yields the same conclusion: The proposed method not only performs better on average but consistently and robustly provides lower errors than the existing methods.

It is noticeable that unusually large errors of $\sim 23°$ are observed for some trials of the OxIOD dataset. As those large errors are observed across all methods, the most likely cause of those errors are irregularities in the measurement or ground truth data that have been discussed in Section 3.3.

To go beyond the level of comparing performance on different datasets, we now investigate algorithm performance for seven different motion characteristics and six different disturbance characteristics. This is facilitated by the different trial groups of the BROAD dataset. Figure 3.24 compares the average RMSE across those groups of trials. In each case, the proposed VQF method is compared with the best of the other 9D-capable algorithms, i.e., the algorithm that achieves the lowest errors for the respective group of trials. Except for the *tapping* and *vibration* groups, VQF always achieves lower errors than even the best of the other algorithms. For the *vibration* group, it is worth noticing that, while the orientation error is slightly larger than the error obtained with FKF, the inclination errors obtained with VQF are clearly lower.

In summary, compared with eight other IOE algorithms and using a collection of six publicly available datasets that cover a wide range of motions, speeds, disturbances, and different sensor hardware, the proposed method VQF consistently provides the best IOE accuracy, both for 6D and 9D orientation estimation.

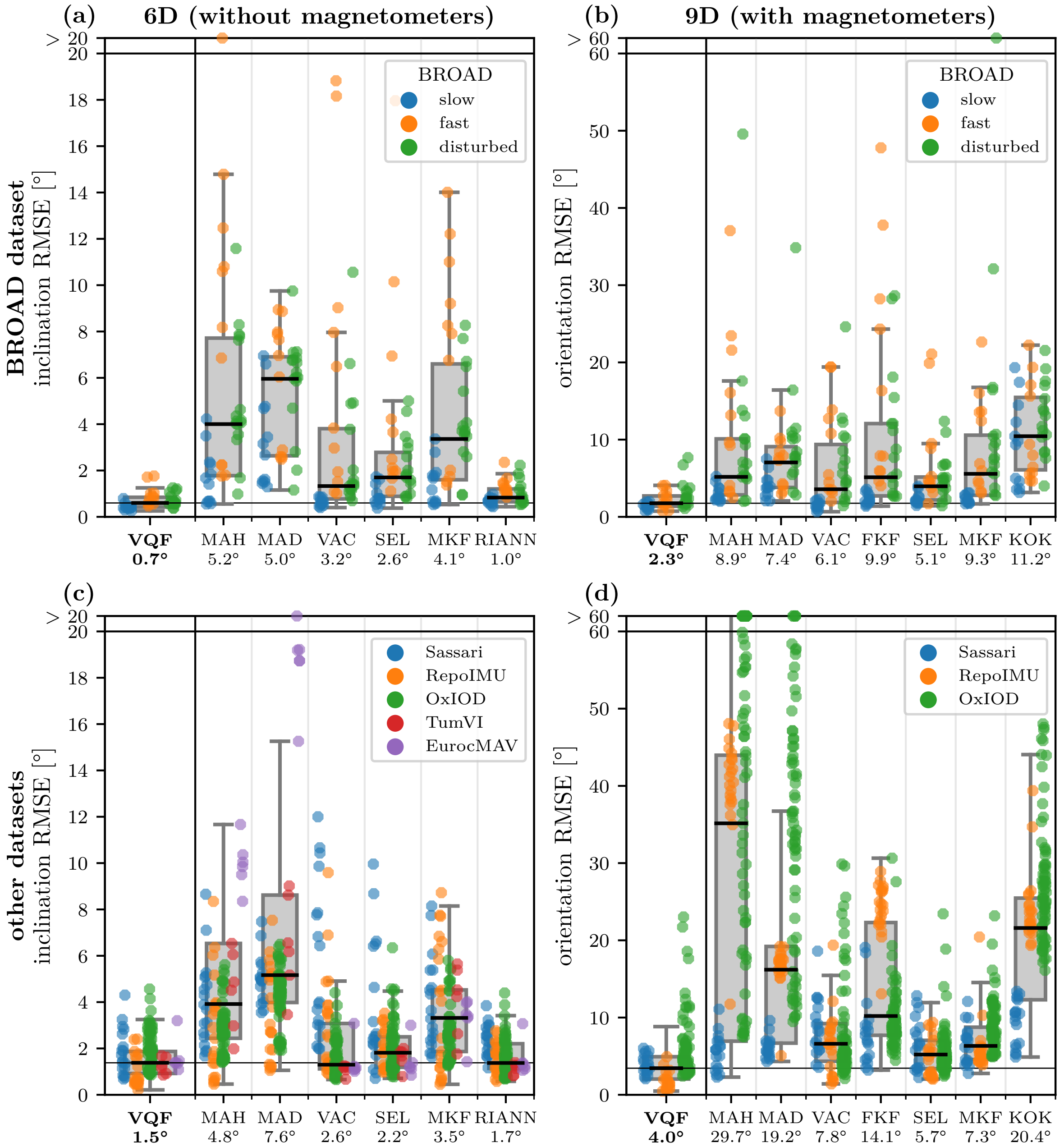

Figure 3.23: Orientation estimation errors for all evaluated algorithms and for all trials of the **(a, b)** BROAD dataset and **(c, d)** the five other datasets and for **(a, c)** 6D and **(b, d)** 9D sensor fusion. The numbers below the algorithm names indicate the RMSE averaged over all trials. For **(c, d)**, the boxplots and average values are weighted to give each dataset the same weight regardless of the number of trials. The proposed VQF algorithm consistently provides the best performance.

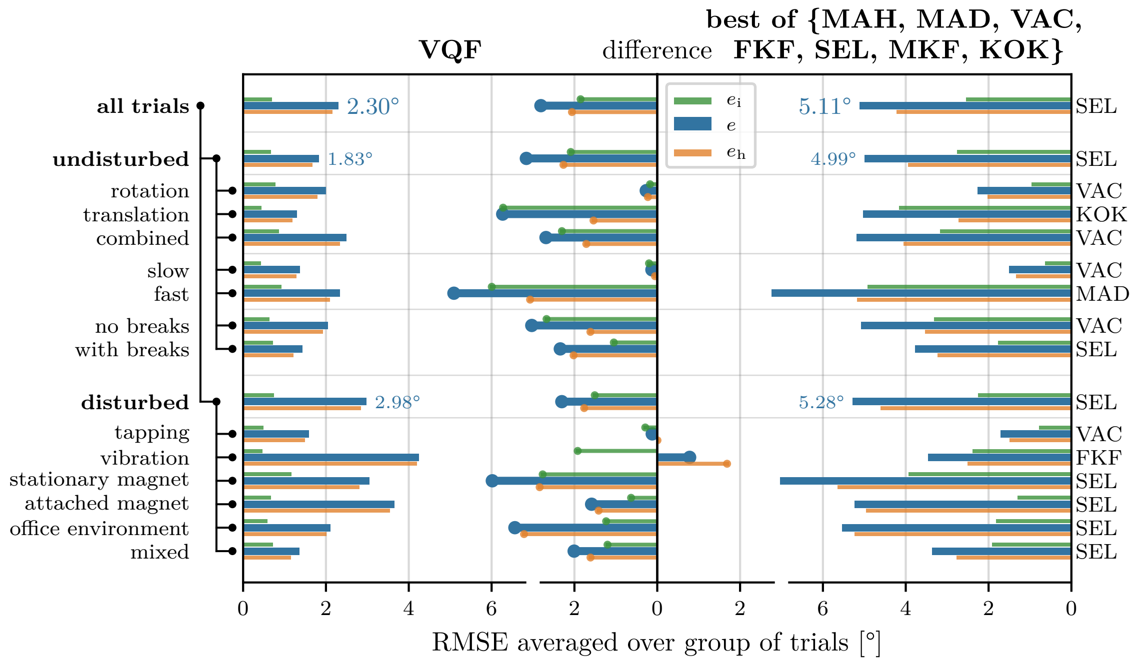

Figure 3.24: Averaged RMSE errors for various groups of trials of the BROAD dataset. The proposed algorithm VQF is compared with the best of the seven other evaluated 9D-capable algorithms, i.e., the algorithm that provides the lowest orientation error for the respective group of trials. The lines originating from the center highlight the difference between the errors. For all groups except for the *tapping* and *vibration* trials, the proposed algorithm outperforms even the best-performing literature method.

3.7.4 Algorithm Execution Time

In addition to accuracy, the execution time of an IOE algorithm is often relevant, especially in real-time applications or when the algorithm is running on low-powered microcontrollers directly on the IMU. To compare the execution times, we repeatedly process the entire BROAD dataset with all algorithms on an AMD Ryzen 5 3600 CPU while measuring the elapsed time. Figure 3.25 shows the average execution time for one update step in combination with the orientation estimation error for the respective algorithm. The results show that execution time mostly depends on the programming language used for the implementation and that the algorithms written in C++ are considerably faster than the algorithms written in Matlab or using the ONNX machine learning runtime. While the VQF algorithms achieve clearly higher accuracy, the execution times are in the same order of magnitude as for the existing state-of-the-art methods with a C++ implementation. VQF is fast enough for use on microcontrollers, which was verified by integrating it into an IMU firmware running on a Cortex M4 with a comparatively high IMU sampling rate of 1600 Hz.

3.7.5 Gyroscope Bias Estimation

We now investigate the performance of the gyroscope bias estimation method. Besides the proposed algorithm, we also evaluate the performance of the five other algorithms that are able to estimate gyroscope bias.

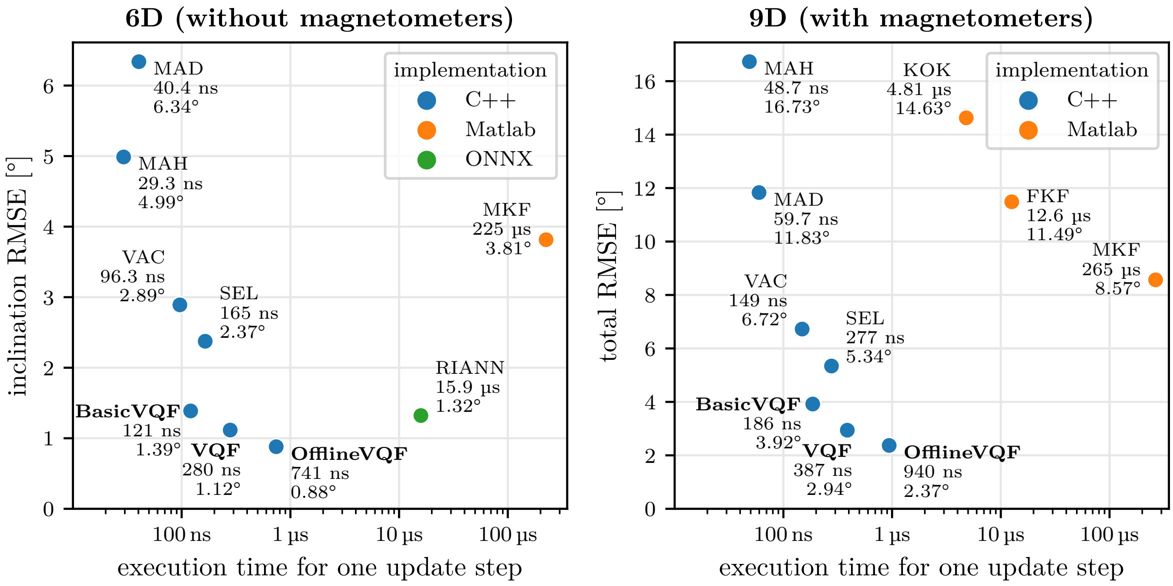

Figure 3.25: Execution time for one update step on an AMD Ryzen 5 3600 CPU vs. orientation estimation RMSE (weighted average over all datasets) for the proposed VQF and all state-of-the-art algorithms. Accuracies vary largely, and execution times mainly depend on the programming language used for implementing the algorithm. The execution time of VQF is in the same order of magnitude as for the other algorithms implemented in C++, while the errors are clearly smaller.

For the BROAD and Sassari datasets, we derive a ground truth for the gyroscope bias by averaging the gyroscope measurements during the rest phases at the beginning and at the end of each trial and linearly interpolating in between to account for slow changes in bias. For each IOE algorithm, we calculate the root-mean-square over time of the residual bias norm, i.e., of the norm of the difference between the estimated bias and the true bias. Figure 3.26 shows the achieved relative reduction of the gyroscope bias, the true bias norm, and the residual bias norm, averaged over all trials for each dataset. Since the proposed VQF and the literature method VAC use rest detection for bias estimation, while the other algorithms do not, we also test the performance of all algorithms on a cut version of the BROAD dataset, in which the initial and final rest phases were removed.

For the proposed algorithms VQF and OfflineVQF, we present the bias estimates obtained with the default parameters. For the existing methods, the parameters that yield the best orientation estimation results often do not yield the best bias estimates. We therefore optimize, separately for each dataset, all parameters of all literature methods (except MKF) across the search grid presented in Table 3.4, such that the bias estimation error is minimized. Despite this disparity, the proposed method clearly outperforms the bias estimation methods of all other IOE algorithms. Even though the results obtained with the cut BROAD dataset are worse than for the datasets with long rest phases, the proposed method is still able to reduce the bias by 39 %, while the best literature method only achieves a reduction of 18 %. As with orientation estimation, using the OfflineVQF variant further improves the accuracy in comparison to the real-time capable VQF algorithm. MKF only achieves a slight reduction of gyroscope bias for the Sassari dataset, while for BROAD the bias norm increases compared to the original bias found in the measurement data.

	BROAD (true bias: 0.332 °/s) bias reduction	BROAD residual bias	BROAD (cut) (true bias: 0.332 °/s) bias reduction	BROAD (cut) residual bias	Sassari (true bias: 0.855 °/s) bias reduction	Sassari residual bias	Parameters
VQF	90 %	0.033 °/s	39 %	0.204 °/s	89 %	0.092 °/s	default
OfflineVQF	97 %	0.008 °/s	58 %	0.138 °/s	96 %	0.037 °/s	default
MAH	7 %	0.309 °/s	1 %	0.329 °/s	30 %	0.601 °/s	optimized
MAD	17 %	0.276 °/s	3 %	0.321 °/s	33 %	0.572 °/s	optimized
VAC	79 %	0.069 °/s	18 %	0.274 °/s	39 %	0.522 °/s	optimized
SEL	51 %	0.162 °/s	6 %	0.312 °/s	67 %	0.280 °/s	optimized
MKF	0 %	1.021 °/s	0 %	1.094 °/s	10 %	0.773 °/s	$TAGP_x$
KOK	15 %	0.283 °/s	3 %	0.323 °/s	34 %	0.567 °/s	optimized

Figure 3.26: Bias estimation results for different IOE algorithms. Green bars and percentages indicate the reduction of the bias norm with respect to the true bias contained in the measurement data. For all datasets, VQF with default parameters surpasses the best possible performance of the existing algorithms. Using the OfflineVQF variant further improves accuracy.

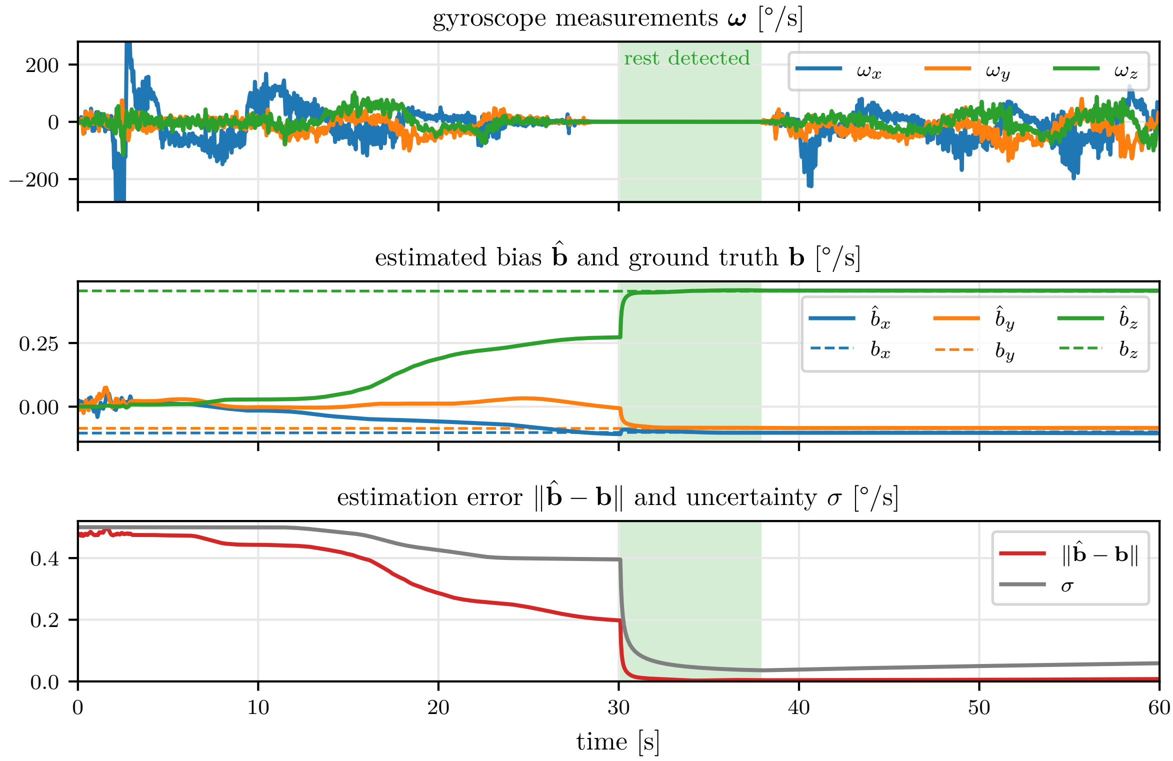

Figure 3.27: Behavior of the bias estimation method for the first 60 seconds of trial 4 of the BROAD dataset (undisturbed slow rotation with breaks, initial rest cut). During motion, the estimated bias slowly converges toward the true value. Once rest is automatically detected by Algorithm 2, the convergence speed increases, and the error and the estimation uncertainty suddenly drop.

To illustrate how the bias estimation method of VQF works, Figure 3.27 shows the estimated bias, the estimation error, and the estimation uncertainty for an exemplary trial of the BROAD dataset. It can be seen that the bias estimation method works as intended: During the initial motion phase, the estimated bias slowly converges to the true bias. Once rest is automatically detected, the alternative update is used, causing the estimate to rapidly converge.

In summary, both in a systematic comparison and in an exemplary case study, the proposed gyroscope bias estimation method was found to work reliably and to clearly outperform existing bias estimation approaches.

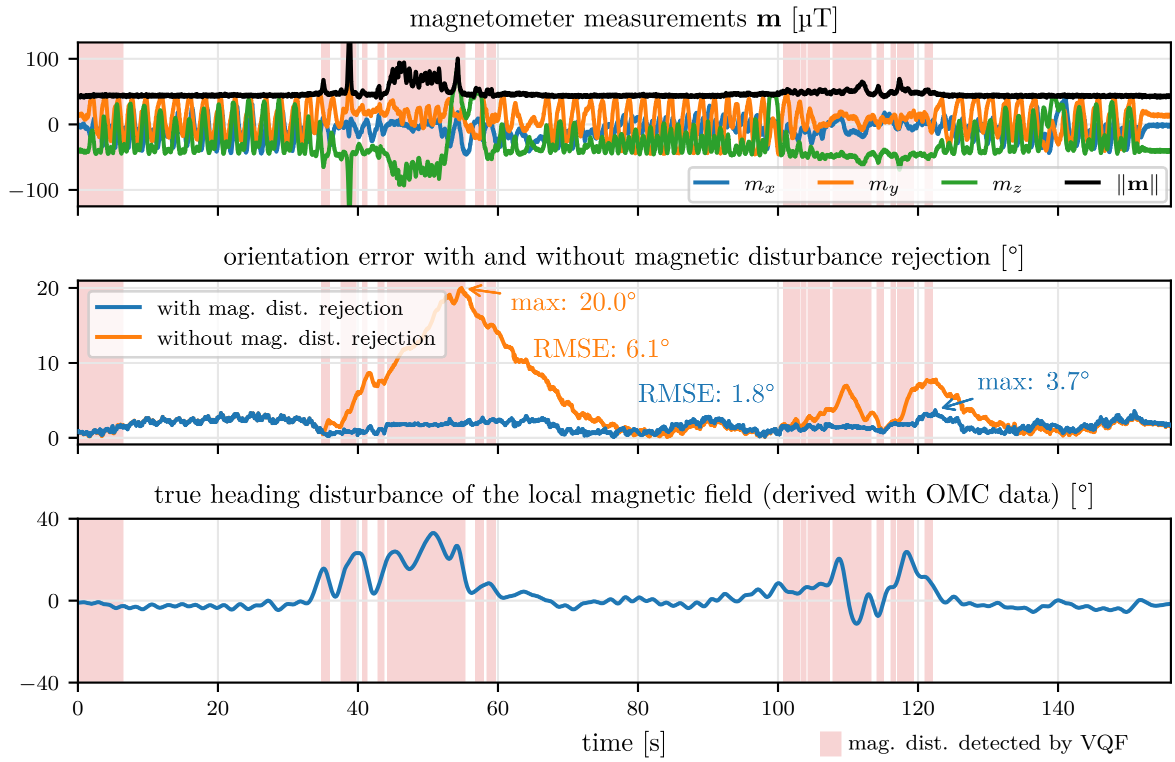

Figure 3.28: Performance of the magnetic disturbance rejection method for trial 37 of the BROAD dataset (disturbed office environment). Whenever magnetic disturbances are detected by Algorithm 3 (light red background), the magnetometer-based correction is automatically disabled. In comparison to the same algorithm with disabled magnetic disturbance rejection, the RMSE is considerably reduced, and the large error peak of 20° is avoided.

3.7.6 Magnetic Disturbance Rejection

To further illustrate the difference in performance between the proposed BasicVQF and VQF algorithms, we now take a brief look at the performance of the magnetic disturbance detection and rejection method. Figure 3.28 shows the behavior of this extension on an example of the BROAD dataset. For the sake of evaluation, OMC data was used to determine the true disturbance of the local magnetic field caused by ferromagnetic material and electric devices in the office environment. This ground truth information shows that the detection is triggered whenever disturbances are present. Without magnetic disturbance rejection, the orientation estimation error reaches a maximum of 20.0°, and the RMSE is 6.1°. In contrast, enabling magnetic disturbance rejection reduces the maximum error to just 3.7° and the RMSE to 1.8°, which translates to an at least three times better accuracy. This example demonstrates how the optional magnetic disturbance rejection can improve the reliability of 9D IOE in real-world scenarios inside buildings, near ferromagnetic material and electric devices.

3.7.7 Summary of the Results

The proposed VQF algorithm achieved an average RMSE of 2.9° for 9D IOE, while the average errors obtained with state-of-the-art methods range from 5.3° to 16.7°. For 6D IOE, VQF attained an average RMSE of 1.1°, compared to 2.4°–6.3° obtained with existing methods, and it achieved even 17 % lower errors than a neural network that was trained on large portions of the benchmark data. For the 13 characteristic trial groups of the BROAD dataset, the proposed method outperforms even the best-performing literature method for all seven motion characteristics and for four out of six disturbance characteristics. Furthermore, the gyroscope bias estimation of VQF clearly outperformed all existing state-of-the-art literature methods and compensated $\sim 90\,\%$ of the bias. Even for the challenging case without rest phases, the bias could still be reduced by $\sim$40–60 %, while the existing algorithms barely achieved any bias reduction. For an exemplary case in a simulated office environment, the magnetic disturbance rejection algorithm was shown to achieve a five-fold reduction of the maximum orientation error.

Even the variant BasicVQF, without bias estimation and magnetic disturbance rejection, was shown to provide clearly more accurate 9D orientation estimates than all state-of-the-art methods. For applications in which real-time capability is not required, the variant OfflineVQF can be used to further increase accuracy.

3.8 Conclusions

This chapter introduced a novel IOE algorithm that simultaneously performs 6D and 9D sensor fusion, estimates gyroscope bias, and performs magnetic disturbance detection and rejection. An open-source implementation is provided in C++, Python, and Matlab, making it easy to use the algorithm.

The validation of novel IOE algorithms is typically performed with not-openly-available application-specific datasets that only contain certain types of motions. This makes it difficult to compare performance across different algorithms, to gain insight into the robustness of different algorithms in a broad range of scenarios, and to investigate the influence of tuning parameters. There is a lack of publicly available datasets that are suitable for robust IOE accuracy evaluation.

The proposed BROAD benchmark contributes toward filling this gap, both for the evaluation of the proposed IOE algorithm VQF and for a range of other potential applications. In contrast to previously published datasets, it encompasses a wide range of undisturbed motions as well as motions in disturbed environments. As shown in the exemplary case study with two widely used orientation estimation algorithms, this benchmark dataset allows for

1. the determination of robust algorithm parameters for a given IOE algorithm that perform well for a broad range of motions and environmental conditions,
2. an in-depth analysis of strengths and weaknesses of a given IOE algorithm in different scenarios, while considering heading and inclination separately,
3. a detailed comparison of the performance of different algorithms with respect to a wide range of possible application and motion scenarios,
4. an objective comparison of different literature algorithms as well as targeted development of new algorithms with improved performance by using the well-defined benchmark metrics described in Section 3.4.6.

The BROAD benchmark is particularly useful for the objective assessment of IOE algorithms across different types of motions and environmental conditions. Therefore, together with five other publicly available datasets, it provided the main dataset used for the evaluation of the proposed IOE algorithm in comparison with eight other IOE algorithms. As summarized in Section 3.7.7, the proposed algorithm VQF consistently provided the best performance, both for 6D and 9D orientation estimation, as well as for gyroscope bias estimation, and it proved capable of magnetic disturbance rejection.

The proposed method provides a highly accurate out-of-the-box performance, which means that – unlike existing literature methods – VQF requires no parameter tuning for a vast range of motions and application scenarios. For rare edge cases, the proposed method facilitates easy and intuitive tuning via the time constants τ_{acc} and τ_{mag}.

The achieved improvements in ease of use and in orientation estimation accuracy are expected to advance the broad field of inertial motion tracking by enabling more accurate IMU-based position and velocity estimation, joint angle estimation, and 3D visualization. This, in turn, leads to improved performance in many existing application areas of miniature inertial sensor technology, and it likewise facilitates the applicability in novel application domains with increased accuracy demands.

To further broaden the development of robust and accurate IOE algorithms for human motion analysis, future research should aim at complementing the BROAD dataset by adding existing or newly recording data from human motion trials with a reliable, synchronized, and aligned optical ground truth as well as recordings obtained with different IMU hardware.

Besides employing the VQF algorithm in various applications (for example in Chapters 4, 5, and 6), future work on the IOE algorithm should focus on integrating continuous and automatic magnetometer calibration.

4

Automatic Anatomical Calibration via Kinematic Constraints

After estimating *sensor* orientations, e.g., with the algorithm introduced in the previous chapter, a common next step in inertial human motion tracking is the derivation of *segment* orientations based on a physiologically meaningful segment coordinate system. To avoid the need for laborious and error-prone precise calibration motions or manual precise sensor placement, this chapter introduces methods for automatic anatomical calibration (also known as sensor-to-segment calibration) by exploiting kinematic constraints of joints with two degrees of freedom (DoF).

Text, figures, and tables found in this chapter have been previously published, with slight modifications, in the following works:

[91] D. Laidig, P. Müller, and T. Seel. "Automatic Anatomical Calibration for IMU-based Elbow Angle Measurement in Disturbed Magnetic Fields". In: *Current Directions in Biomedical Engineering* 3.2 (2017), pp. 167–170. DOI: 10.1515/cdbme-2017-0035.

[92] D. Laidig, I. Weygers, and T. Seel. "Self-Calibrating Magnetometer-Free Inertial Motion Tracking of 2-DoF Joints". In: *Sensors* 22.24 (24 Dec. 2022), Article 9850. ISSN: 1424-8220. DOI: 10.3390/s22249850.

While the rotation-based constraint was first published in [91], most of the content of this chapter is based on the more extensive description found in [92].

4.1 Introduction

In order to derive anatomically meaningful kinematic quantities, e.g., joint angles, from IMU measurements, the orientation of each IMU with respect to its body segment must be known, as illustrated in Figure 4.1. Even small misalignments between the assumed and actual orientation of the IMUs on the body lead to errors in the obtained kinematic quantities. To ensure accurate motion tracking, it is therefore desirable to accurately determine this orientation.

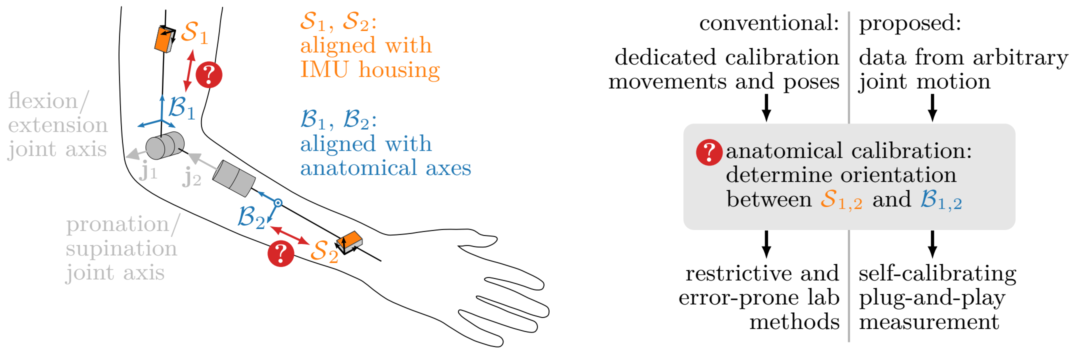

Figure 4.1: Anatomical calibration, also called sensor-to-segment calibration, is the task of determining how the IMUs are attached to the body segments. To be more specific, the rotations between the IMU coordinate systems $\mathcal{S}_{1,2}$, defined by the sensor housing, and the corresponding body segments $\mathcal{B}_{1,2}$, defined by anatomical axes such as the joint axes $\mathbf{j}_{1,2}$, have to be determined. Conventional methods rely on precisely defined calibration movements and poses, whereas the proposed methods use kinematic constraints to derive this information from arbitrary joint motion.

In practice, this is often achieved by manual placement of the IMUs on the respective body segments in a specified orientation [93], which is error-prone, especially when the attachment of sensors is to be performed by patients or by non-medical personnel.

An alternative is to employ a procedure that determines the orientation of each IMU with respect to its body segment based on data measured by the sensors. This procedure is called *anatomical calibration* or *sensor-to-segment calibration*, which is not to be confused with sensor calibration. Sensor calibration determines parameters such as scaling and bias in order to increase the accuracy of the sensor orientation estimates. Anatomical calibration determines how the sensors are attached to the body segments to ensure that the rotation axes used for calculating joint angles match the anatomical axes of joint rotation.

As detailed in Section 4.2, anatomical calibration traditionally relies on precisely defined calibration poses or motions. Less restrictive approaches aim for anatomical calibration based on arbitrary joint motion. Such approaches have been proposed for (approximate) hinge joints [94, 95]. In the following, we consider the more challenging case of 2-DoF joints, such as the elbow joint (capable of flexion/extension and pronation/supination), the metacarpophalangeal joints (MCP) of the finger (capable of flexion/extension and adduction/abduction), or the ankle joint (capable of plantar-/dorsiflexion and inversion/eversion). This chapter introduces methods for self-calibrating joint angle tracking that

- use two kinematic constraints for 2-DoF joints, one that must be fulfilled by the angular rates and a constraint that must be fulfilled by the relative segment orientations at any time and for any motion,
- do not make use of magnetometer measurements and are therefore insensitive to magnetic disturbances (otherwise, temporary magnetic disturbances could permanently deteriorate accuracy until calibration is repeated),
- instead simultaneously estimate the heading offset to facilitate magnetometer-free joint angle tracking.

The methods are evaluated based on two experiments. The first experiment, with a known sensor attachment as ground truth, compares a simple and a complex motion and is used to show that estimation over a short time window of just ten seconds of joint motion yields plausible and consistent joint axes. The second experiment, with OMC as ground truth, is used to validate that the proposed self-calibrating joint angle tracking provides the same accuracy as a conventional IMU-based approach while being less restrictive.

4.2 State of the Art in Anatomical Calibration

Anatomical calibration is the task of determining how the IMUs are attached to the body segments. In a broader sense, this also encompasses the pairing of IMUs to body segments [96, 97] and the estimation of joint center positions [98, 99, 100, 101]. The most relevant aspect, however, is to determine how the sensor coordinate system is rotated with respect to anatomical body segment axes (cf. Figure 4.1). In order to uniquely define this orientation, the coordinates of two anatomical axes need to be known in the sensor frame (or vice versa). Since errors in the sensor-to-segment orientations lead to kinematic cross-task and thus directly cause errors in the obtained joint angles [102, 103, 104], the reliability and accuracy of anatomical calibration methods are of fundamental interest in IMU-based motion analysis.

There are four main approaches for how to deal with the need for sensor-to-segment alignment in IMU-based human motion analysis [93]:

1. relying on a precisely defined sensor attachment (*assumed alignment*),
2. calibration via measurements from additional devices (*augmented data*),
3. calibration based on precisely defined poses or motions (*functional alignment*),
4. calibration from arbitrary motions (*model-based alignment*).

Using a precisely defined attachment of the sensors on the body is a common approach and, according to the survey by Vitali et al. [93], used by 42 % of recent publications. The advantage of this approach is that it is simple to implement and only requires minimum effort from the subject, i.e., no extra calibration movements are required. However, placing the sensors on the body so that predefined sensor axes correspond to functional joint axes is error-prone even for experienced medical personnel and even more so when patients themselves attach the sensors. In a study with three operators, Bouvier et al. [105] report reproducibility in the range of 4° to 12° and agreement with OMC in the range of 8° to 23°.

An example of an augmented data method for anatomical calibration is the use of an additional custom device equipped with an IMU that is used to determine the sensor orientation with respect to anatomical landmarks [106, 107].

The third approach is to ask the subject to assume precisely defined postures or perform a sequence of precisely defined motions. In the simplest form, this consists of a single pose calibration, often in the N-pose or T-pose [108, 109, 110, 111], and requires magnetometers in order to be able to define two axes from one pose. A magnetometer-free alternative is to use two poses, e.g., one standing up and one lying down [112], or to derive the anatomical axes from angular rate measurements of precisely defined motions, typically around the functional axes of the joint [113, 114, 115]. Often, both approaches are combined, and one axis is derived from a static pose and one from a functional motion. Those hybrid approaches have been demonstrated for the upper body [116, 117] and lower body [118, 119, 120]. For thorax and lumbar joint angles, however, a recent study by Cottam et al. [121] found that calibration via functional motions did not improve accuracy in comparison to relying on manual sensor placement. Bouvier et al. [105] observe similar accuracy for precise attachment and for various calibration approaches based on precise poses and motions and point out that accuracy depends more on the rigor of the experimental procedure and operator training than on the calibration method. Furthermore, performing those motions can be tedious for the subject, especially considering that a precise execution is required. For patients with motor disabilities, performing precise motions can be hard or impossible. Even after solving those obstacles, the main drawback of those methods is that the accuracy of the calibration depends on the accuracy of performing the motion. An elegant recent approach is to use the actual motions of interest for calibration, e.g., during cycling [122] or walking [123]. However, this is only feasible in a limited amount of applications and relies on strong assumptions on the analyzed motions.

In many cases, e.g., clinical applications, it would render the use of IMUs much more practical if both a precisely known attachment and precisely specified calibration poses and motions could be avoided by determining the sensor-to-segment orientations from arbitrary motions, usually by relying on kinematic constraints of biomechanical models. This was demonstrated for the knee joint by exploiting a kinematic constraint in the angular rates of (approximate) hinge joints [94, 99]. Furthermore, it was shown that extending this constraint for a combined optimization of a three-segment chain improves robustness [124] and that other methods, such as principal component analysis [125] and factor graph optimization [126, 127], can be used to exploit hinge joint constraints. In [95, 128], the gyroscope-based hinge joint constraint introduced in [99] and an accelerometer-based constraint are combined with an elaborate sample selection strategy, and in [129], both constraints are analyzed for observability of the joint axis. Taetz et al. [130] introduce an approach based on sliding-window weighted least-squares optimization that uses hinge-joint and range-of-motion constraints and a body-shape prior to simultaneously estimate the sensor-to-segment orientation along with the body motion. Zimmermann et al. [97] demonstrate that deep learning can be used for lower body anatomical calibration from just two seconds of walking data.

For anatomical calibration based on arbitrary motions of 2-DoF joints, the existing work is limited. Müller et al. [131] introduce a gyroscope-based kinematic constraint for 2-DoF joints such as the elbow. Norden et al. [132] demonstrate that the same constraint can be employed for real-time estimation of hip and knee joint axes. However, the constraint used in both [131] and [132] assumes knowledge of the relative sensor orientation and therefore requires magnetometers. This poses a severe limitation for the applicability of those methods in indoor environments [38] and implies that temporary magnetic disturbances during calibration can lead to wrong joint axis estimates and thus permanently deteriorate the accuracy of the obtained joint angles.

4.3 Kinematic Model of 2-DoF Joints

The methods proposed in this chapter perform automatic anatomical calibration for joints with two degrees of freedom (DoF). Those methods are suitable for any 2-DoF joint and can be applied to a range of biological or robotic 2-DoF joints. To improve comprehensibility, the following description of the kinematic model and the calibration method focuses on the human elbow joint as an exemplary joint, which is later also used in the experimental evaluation.

Furthermore, even though in the following we always only consider two body segments connected by a single joint, the proposed methods can be used to analyze longer kinematic chains consisting of multiple segments. In this case, the calibration methods can be applied to each pair of segments that are connected by a 2-DoF joint.

Figure 4.2 shows an anatomical model of the elbow joint as an exemplary biological 2-DoF joint. This joint can perform two functional motions. Flexion and extension (FE) are performed by the humeroulnar joint, while pronation and supination (PS) are the result of the radius pivoting around the ulna.

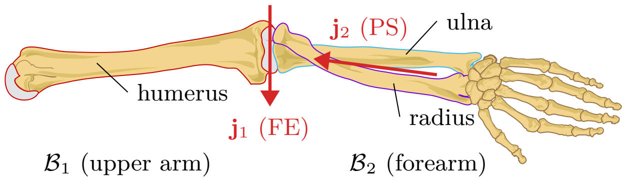

Figure 4.2: Anatomical model of the elbow joint. The humeroulnar joint is a hinge joint with the rotation axes $\mathbf{j}_1$, allowing for flexion and extension (FE). The radioulnar joint also has one degree of freedom ($\mathbf{j}_2$) and allows for pronation and supination (PS). In this chapter, we refer to the combined joint with two degrees of freedom as *elbow joint*.

As an approximation, we can model this joint – as well as any other 2-DoF joint – as a kinematic chain consisting of two hinge joints and one fixed rotation in between, as depicted in Figure 4.3. Including the fixed rotation, the sequence of rotations consists of flexion and extension (FE), a fixed carrying angle [47], and pronation and supination (PS).

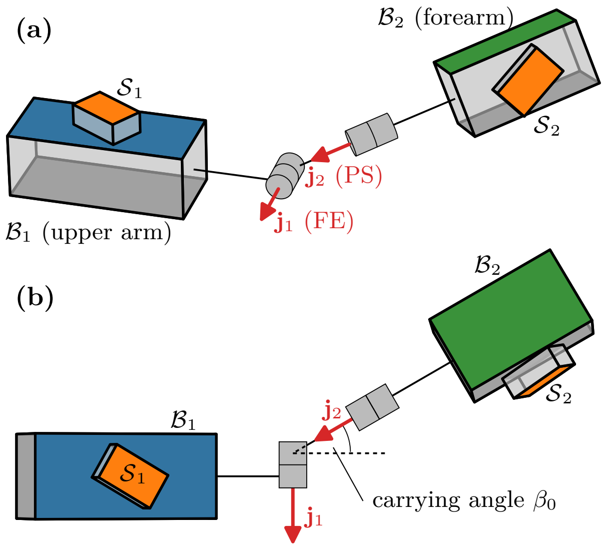

Figure 4.3: **(a)** Geometric kinematic model of the elbow joint. Inertial sensors $\mathcal{S}_1$ and $\mathcal{S}_2$ are placed in arbitrary orientation on the upper arm $\mathcal{B}_1$ and forearm $\mathcal{B}_2$. Upper arm and forearm are connected by two hinge joints that allow for FE ($\mathbf{j}_1$) and PS ($\mathbf{j}_2$). **(b)** View onto the $\mathbf{j}_1$-$\mathbf{j}_2$ plane. The fixed rotation between FE and PS is called *carrying angle*.

Mathematically, we can express the orientation of the forearm $\mathcal{B}_2$ relative to the upper arm $\mathcal{B}_1$ using the FE joint angle $\alpha(t)$, the carrying angle β_0, and the PS angle $\gamma(t)$ as

$$^{\mathcal{B}_2}_{\mathcal{B}_1}\mathbf{q} = (\alpha(t) \,@\, \mathbf{j}_1) \otimes (\beta_0 \,@\, \mathbf{j}_1 \times \mathbf{j}_2) \otimes (\gamma(t) \,@\, \mathbf{j}_2)\,. \tag{4.1}$$

The ISB [47] also recommends this joint model for the elbow and precisely defines coordinate systems $\mathcal{B}_1$ and $\mathcal{B}_2$ so that $[\mathbf{j}_1]_{\mathcal{B}_1} = [0\ \ 0\ \ 1]^\intercal$ and $[\mathbf{j}_2]_{\mathcal{B}_2} = [0\ \ 1\ \ 0]^\intercal$. When using this definition, the joint angles are intrinsic z-x'-y'' Euler angles of $^{\mathcal{B}_2}_{\mathcal{B}_1}\mathbf{q}$. Please note that this also means that the axis $\mathbf{j}_1$ (FE) is fixed in the coordinate system of a sensor attached to the upper arm, while the axis $\mathbf{j}_2$ (PS) is fixed in the coordinate system of a sensor attached to the forearm.

Instead of using regular Euler angles, we could consider modeling a 2-DoF joint with axes that are all potentially non-orthogonal (including the carrying angle axis). However, as Appendix B.1 shows, any generic model with non-orthogonal axes can also be expressed using standard z-x'-y'' Euler angles by redefining the segment coordinate systems accordingly. This means that the choice of z-x'-y'' Euler angles according to the ISB recommendations [47] does not restrict the generality of the proposed methods. Also, note that the orientation of the IMUs on the body segments is independent of this definition. The goal of anatomical calibration is to determine the fixed coordinates $\mathbf{j}_1$ and $\mathbf{j}_2$ of the functional joint axes in the local coordinate systems of the respective IMUs.

4.4 Proposed Methods for Anatomical Calibration

Two IMUs $\mathcal{S}_1$ and $\mathcal{S}_2$ are placed on the subject in unknown orientations, one on each body segment connected by the 2-DoF joint (i.e., in case of the elbow, one on the upper arm and one on the forearm). Assume that we can estimate the sensor orientation quaternions $^{\mathcal{S}_1}_{\mathcal{E}}\mathbf{q}(t_k)$, $^{\mathcal{S}_2}_{\mathcal{E}}\mathbf{q}(t_k)$ relative to a common inertial frame $\mathcal{E}$. We also measure the angular rates $\boldsymbol{\omega}_1(t_k) \in \mathbb{R}^3$, $\boldsymbol{\omega}_2(t_k) \in \mathbb{R}^3$ of the IMUs, in their respective local coordinate systems. All measurements are sampled at times $t_k = kT_\mathrm{s}, k \in \{1, 2, \ldots, N\}, T_\mathrm{s} \in \mathbb{R}_{>0}$. Note that the assumption of a common reference frame $\mathcal{E}$ is restrictive in practice as it assumes 9D sensor fusion in a perfectly homogeneous magnetic field and will later be dropped.

In the following, we derive two different kinematic constraints for 2-DoF joints, one based on the joint rotation and one based on the relative segment orientations. Both constraints are suitable for 6D sensor fusion with unknown heading offset. Given a short sequence of recorded IMU data, we use the Gauss-Newton algorithm to determine the joint axis coordinates in the sensor frame and the heading offset that best fit either the rotation-based or the orientation-based constraint in a least-squares sense. We use these joint axis coordinates to determine segment orientations from the sensor orientations and use the heading offset to align the reference frames of the 6D orientations. From this result, we calculate the relative segment orientation, which we then decompose via Euler angles to obtain magnetometer-free estimates of the joint angles.

4.4.1 Rotation-Based Kinematic Joint Constraint

As shown in Section 4.3, a 2-DoF joint cannot perform arbitrary joint rotation in all directions. Instead, rotation is only possible around the two joint axes. In the following, we will investigate how this translates to a kinematic constraint in the angular rates measured by the two IMUs. We will later exploit this constraint to estimate joint axes from arbitrary joint motion.

Using the addition theorem for angular velocities, we express the relationship between the gyroscope measurements $\boldsymbol{\omega}_1(t_k)$ and $\boldsymbol{\omega}_2(t_k)$ as

$$[\boldsymbol{\omega}_2]_{\mathcal{E}} = [\boldsymbol{\omega}_1]_{\mathcal{E}} + \omega_{j_1}\,[\mathbf{j}_1]_{\mathcal{E}} + \omega_{j_2}\,[\mathbf{j}_2]_{\mathcal{E}}\,. \tag{4.2}$$

The scalars ω_{j_1} and ω_{j_2} are the rotation rates of the joint around the respective joint axes. In case of joints with two degrees of freedom according to the model in Figure 4.3, this corresponds to the anatomical joint motions, i.e., in case of the elbow, ω_{j_1} is the FE angular rate and ω_{j_2} the PS angular rate. In other words, the angular rate $\boldsymbol{\omega}_2$ measured by the forearm IMU $\mathcal{S}_2$ is composed of three components:

1. the common rotation of the whole arm, also observed by IMU $\mathcal{S}_1$ as $\boldsymbol{\omega}_1$,
2. the FE rotation ω_{j_1} around $\mathbf{j}_1$,
3. the PS rotation ω_{j_2} around $\mathbf{j}_2$.

Note that the carrying angle does not appear since it is time-invariant. Also note that in (4.2), the angular rates and joint axes are transformed into a common coordinate system, here $\mathcal{E}$.

Let us first take a look at hinge joints, for which a similar constraint has already been proposed in [94]. For hinge joints, there is only one rotation axis, which has different coordinates in both sensors' local coordinate systems depending on how the sensors are placed on the body, i.e., $\mathbf{j}_1 \neq \mathbf{j}_2$. However, when transforming those axes into the global frame, the coordinates are the same, i.e., $[\mathbf{j}_1]_{\mathcal{E}} = [\mathbf{j}_2]_{\mathcal{E}} =: [\mathbf{j}]_{\mathcal{E}}$. Therefore, we can write

$$[\boldsymbol{\omega}_1]_{\mathcal{E}} + \omega_{j_1}\,[\mathbf{j}]_{\mathcal{E}} = [\boldsymbol{\omega}_2]_{\mathcal{E}} - \omega_{j_2}\,[\mathbf{j}]_{\mathcal{E}}\,. \tag{4.3}$$

Taking the cross product with $[\mathbf{j}]_{\mathcal{E}}$ on both sides yields

$$[\boldsymbol{\omega}_1]_{\mathcal{E}} \times [\mathbf{j}]_{\mathcal{E}} = [\boldsymbol{\omega}_2]_{\mathcal{E}} \times [\mathbf{j}]_{\mathcal{E}}\,, \tag{4.4}$$

and when only considering the Euclidean norm, we can calculate the cross product using local sensor coordinates and obtain the constraint as given in [94]:

$$\|\boldsymbol{\omega}_1 \times \mathbf{j}_1\| - \|\boldsymbol{\omega}_2 \times \mathbf{j}_2\| = 0. \tag{4.5}$$

Since this version of the constraint only uses quantities given in local sensor coordinates, it is independent of sensor orientations with respect to a fixed frame and thus not affected by magnetic disturbances.

For joints with two degrees of freedom, we need to know the relative sensor orientation or sensor orientations with respect to a common fixed frame. In order to derive a similar constraint from (4.2) for 2-DoF joints, we calculate the scalar product with the normalized[1] axis $[\mathbf{j}_1]_\mathcal{E} \times [\mathbf{j}_2]_\mathcal{E}$ on both sides, i.e.,

$$([\boldsymbol{\omega}_2]_\mathcal{E} - \omega_{j_2}\, [\mathbf{j}_2]_\mathcal{E}) \cdot \frac{[\mathbf{j}_1]_\mathcal{E} \times [\mathbf{j}_2]_\mathcal{E}}{\|[\mathbf{j}_1]_\mathcal{E} \times [\mathbf{j}_2]_\mathcal{E}\|} = ([\boldsymbol{\omega}_1]_\mathcal{E} + \omega_{j_1}\, [\mathbf{j}_1]_\mathcal{E}) \cdot \frac{[\mathbf{j}_1]_\mathcal{E} \times [\mathbf{j}_2]_\mathcal{E}}{\|[\mathbf{j}_1]_\mathcal{E} \times [\mathbf{j}_2]_\mathcal{E}\|} \tag{4.6}$$

and employ the fact that $\mathbf{a} \cdot (\mathbf{a} \times \mathbf{b}) = \mathbf{a} \cdot (\mathbf{b} \times \mathbf{a}) = 0$. This yields

$$([\boldsymbol{\omega}_1]_\mathcal{E} - [\boldsymbol{\omega}_2]_\mathcal{E}) \cdot \frac{[\mathbf{j}_1]_\mathcal{E} \times [\mathbf{j}_2]_\mathcal{E}}{\|[\mathbf{j}_1]_\mathcal{E} \times [\mathbf{j}_2]_\mathcal{E}\|} = 0. \tag{4.7}$$

For perfect 2-DoF joints and ideal IMU measurements, this constraint must be fulfilled for each sampling instant. For biological joints, and when taking soft tissue motion and measurement errors into account, the constraint is still valid in a least-squares sense when considering a short motion sequence consisting of multiple samples.

However, the constraint as formulated in (4.7) uses the reference frame $\mathcal{E}$ and is only suitable for use in combination with 9D IOE, i.e., with the use of magnetometers. Since magnetic fields are often severely disturbed [38], we want to avoid using magnetometer measurements and therefore only employ 6D sensor fusion to estimate the sensor orientations, e.g., using the VQF algorithm proposed in Chapter 3. This implies that the heading of the estimated orientations is not well-defined. Mathematically, this can be described by the estimated orientations ${}^{\mathcal{S}_1}_{\mathcal{E}_1}\mathbf{q}$ and ${}^{\mathcal{S}_2}_{\mathcal{E}_2}\mathbf{q}$ being given in different global reference frames $\mathcal{E}_1$ and $\mathcal{E}_2$, which are rotated around the vertical global z-axis, i.e.,

$${}^{\mathcal{E}_2}_{\mathcal{E}_1}\mathbf{q} = (\delta(t) \,@\, [\,0 \;\; 0 \;\; 1\,]^\intercal) = \begin{bmatrix}\cos\left(\frac{\delta(t)}{2}\right) & 0 & 0 & \sin\left(\frac{\delta(t)}{2}\right)\end{bmatrix}^\intercal. \tag{4.8}$$

The heading offset $\delta(t)$ has an unknown initial value and then slowly drifts due to gyroscope bias. Please note that both $\mathcal{E}_1$ and $\mathcal{E}_2$ have some unknown heading offset with respect to the fixed frame $\mathcal{E}$ used in 9D sensor fusion and defined by gravity and the Earth's magnetic field. However, knowing those individual offsets is not necessary for calculating relative orientations and joint angles.

We take the heading offset into account by evaluating the constraint (4.7) in one of the slowly-drifting global frames (here $\mathcal{E}_1$), i.e.,

$$\underbrace{\left([\boldsymbol{\omega}_1]_{\mathcal{E}_1} - [\boldsymbol{\omega}_2]_{\mathcal{E}_1}\right)}_{=:\,\boldsymbol{\omega}_\mathrm{rel}} \cdot \underbrace{\frac{[\mathbf{j}_1]_{\mathcal{E}_1} \times [\mathbf{j}_2]_{\mathcal{E}_1}}{\left\|[\mathbf{j}_1]_{\mathcal{E}_1} \times [\mathbf{j}_2]_{\mathcal{E}_1}\right\|}}_{=:\,\mathbf{j}_\mathrm{n}/\|\mathbf{j}_\mathrm{n}\|} = 0. \tag{4.9}$$

This version of the constraint implicitly depends on δ, as we need the quaternion ${}^{\mathcal{S}_2}_{\mathcal{E}_1}\mathbf{q} = {}^{\mathcal{E}_2}_{\mathcal{E}_1}\mathbf{q}(\delta) \otimes {}^{\mathcal{S}_2}_{\mathcal{E}_2}\mathbf{q}$ to transform $\boldsymbol{\omega}_2$ and $\mathbf{j}_2$ into $\mathcal{E}_1$ coordinates. This means that instead of (4.7) we can use (4.9) with magnetometer-free 6D orientations and that, in addition to the joint axes coordinates, we also identify the current heading offset $\delta(t)$ as an additional parameter.

[1] Normalizing the axis was found to improve robustness compared to the constraint presented in [91].

4.4.2 Orientation-Based Kinematic Joint Constraint

As an alternative, we derive a second kinematic joint constraint. In contrast to the constraint introduced in the previous section, this constraint is not based on the joint rotation but on the joint orientation, i.e., the relative orientation between the two body segments connected by the joint.

As in Section 4.4.1, assume that we have 6D sensor orientation estimates ${}^{\mathcal{S}_1}_{\mathcal{E}_1}\mathbf{q}(t_k)$, ${}^{\mathcal{S}_2}_{\mathcal{E}_2}\mathbf{q}(t_k)$, e.g., estimated with the VQF algorithm proposed in Chapter 3. As before, our aim is to identify $[\mathbf{j}_1]_{\mathcal{S}_1}$, $[\mathbf{j}_2]_{\mathcal{S}_2}$, and the heading offset $\delta(t)$. For any given estimate of those values, we are able to calculate joint angles. If the joint follows the 2-DoF joint model introduced in Section 4.3, the following statement holds true: With the correct sensor-to-segment orientation and the correct heading offset, the second joint angle (for the elbow joint: the carrying angle) is constant.

Mathematically, we can formulate this by calculating the joint orientation and then decomposing this orientation into Euler angles. First, we determine the shortest-possible rotations that align the estimated joint axes in sensor coordinates with the defined joint axes:

$$ {}^{\mathcal{B}_1}_{\mathcal{S}_1}\mathbf{q} = \left(\arccos\left([0\ \ 0\ \ 1]^\intercal \cdot [\mathbf{j}_1]_{\mathcal{S}_1}\right) @\, [0\ \ 0\ \ 1]^\intercal \times [\mathbf{j}_1]_{\mathcal{S}_1}\right), \tag{4.10} $$

$$ {}^{\mathcal{B}_2}_{\mathcal{S}_2}\mathbf{q} = \left(\arccos\left([0\ \ 1\ \ 0]^\intercal \cdot [\mathbf{j}_2]_{\mathcal{S}_2}\right) @\, [0\ \ 1\ \ 0]^\intercal \times [\mathbf{j}_2]_{\mathcal{S}_2}\right) \tag{4.11} $$

and calculate the rotation quaternion between the reference frames

$$ {}^{\mathcal{E}_2}_{\mathcal{E}_1}\mathbf{q} = (\delta \,@\, [0\ \ 0\ \ 1]^\intercal). \tag{4.12} $$

Using those quaternions, we calculate the joint orientation

$$ {}^{\mathcal{B}_2}_{\mathcal{B}_1}\mathbf{q} = {}^{\mathcal{S}_1}_{\mathcal{B}_1}\mathbf{q} \otimes \underbrace{{}^{\mathcal{E}_1}_{\mathcal{S}_1}\mathbf{q} \otimes {}^{\mathcal{E}_2}_{\mathcal{E}_1}\mathbf{q} \otimes {}^{\mathcal{S}_2}_{\mathcal{E}_2}\mathbf{q}}_{={}^{\mathcal{S}_2}_{\mathcal{S}_1}\mathbf{q}} \otimes {}^{\mathcal{B}_2}_{\mathcal{S}_2}\mathbf{q}, \tag{4.13} $$

which depends on the sensor orientations, the estimated joint axes $\mathbf{j}_1$ and $\mathbf{j}_2$, and the heading offset δ.

Therefore, ${}^{\mathcal{B}_2}_{\mathcal{B}_1}\mathbf{q} =: [\,q_w\ \ q_x\ \ q_y\ \ q_z\,]^\intercal$ can be calculated from the measured data and the estimated parameters. The second intrinsic z-x'-y'' Euler angle of this quaternion, i.e., the estimated carrying angle, is

$$ \hat{\beta}_0 = \arcsin\left(2q_wq_x + 2q_yq_z\right). \tag{4.14} $$

Due to the joint constraint, this angle has to be constant over the whole measurement window, i.e., with the fixed constant carrying angle β_0,

$$ \arcsin\left(2q_wq_x + 2q_yq_z\right) = \beta_0. \tag{4.15} $$

Similar to (4.9), the constraint (4.15) can be used to identify the joint axes coordinates and the heading offset δ. Additionally, unless the actual value of the carrying angle β_0 is known, β_0 has to be identified as an additional parameter.

4.4.3 Parametrization of Joint Axes

The aim of the anatomical calibration is to identify the joint axes $\mathbf{j}_1 \in \mathbb{R}^3$ and $\mathbf{j}_2 \in \mathbb{R}^3$ with $\|\mathbf{j}_\mathrm{i}\| = 1$, $i = 1, 2$. Parametrizing the axes as Cartesian vectors in an optimization problem is inconvenient as we would need an additional constraint to ensure unit length. Therefore, we employ spherical coordinates and represent each axis by two parameters φ_i and θ_i, e.g.,

$$\mathbf{j}_\mathrm{i} = [\sin\theta_i \cos\varphi_i \quad \sin\theta_i \sin\varphi_i \quad \cos\theta_i]^\intercal, \quad i = 1, 2. \tag{4.16}$$

With the parametrization given in (4.16), $\frac{\partial \mathbf{j}_\mathrm{i}}{\partial \varphi_i} = 0$ if $\sin\theta_i = 0$. To avoid this singularity, we introduce an alternative spherical representation of the same joint axis vector, as shown in Figure 4.4. During optimization, we always use a parametrization with $|\sin\theta_i| \gg 0$ by converting the axis to Cartesian coordinates and then to the other representation whenever the current representation comes close ($< 30°$) to that singularity.

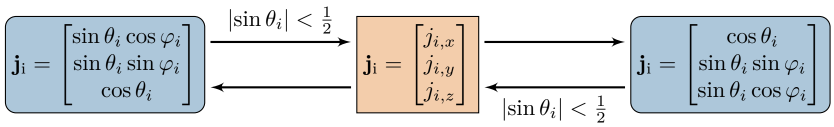

Figure 4.4: Two spherical parametrizations are used to represent the joint axes $\mathbf{j}_\mathrm{i}$, $i = 1, 2$, with two parameters each, θ_i and φ_i. To avoid the derivative becoming close to zero, we convert the respective axis to Cartesian coordinates and then to the other representation whenever $|\sin\theta_i| < 0.5$.

Note that both spherical parametrizations represent exactly the same 3D vector. Therefore, changing the parametrization in between optimization iterations does not influence the joint axis vectors or the value of the cost function but ensures that the derivatives with respect to the joint axis parameters are always sufficiently sensitive.

4.4.4 Cost Function and Optimization

Sample selection is performed to fill a sample buffer of M data sets

$$\left\{ {}^{\mathcal{S}_1}_{\mathcal{E}_1}\mathbf{q}(t_k), {}^{\mathcal{S}_2}_{\mathcal{E}_2}\mathbf{q}(t_k), [\boldsymbol{\omega}_1]_{\mathcal{E}_1}(t_k), [\boldsymbol{\omega}_2]_{\mathcal{E}_2}(t_k) \right\} \tag{4.17}$$

for the rotation-based constraint and

$$\left\{ {}^{\mathcal{S}_1}_{\mathcal{E}_1}\mathbf{q}(t_k), {}^{\mathcal{S}_2}_{\mathcal{E}_2}\mathbf{q}(t_k) \right\} \tag{4.18}$$

for the orientation-based constraint from the 6D orientation quaternions and angular rates measured at a (potentially very high) sampling frequency of f_s. The proposed method employs a regular (equidistant) sample selection strategy that stores one sample every 0.05 s. Note that this method can easily be extended by more sophisticated sample selection strategies since the optimization procedure does not require equidistant sampling.

In order to determine the joint axes and heading offset that best satisfy the rotation-based constraint (4.9) in a least-squares sense, we define the error for each sampling instant t_k as

$$e(\boldsymbol{\Phi}, t_k) := \boldsymbol{\omega}_\mathrm{rel}(\delta, t_k) \cdot \frac{\mathbf{j}_\mathrm{n}(\boldsymbol{\Phi}, t_k)}{\|\mathbf{j}_\mathrm{n}(\boldsymbol{\Phi}, t_k)\|}, \tag{4.19}$$

with the parameter vector $\mathbf{\Phi} := [\,\theta_1 \;\; \varphi_1 \;\; \theta_2 \;\; \varphi_2 \;\; \delta\,]^\intercal$. Note that we assume the heading offset $\delta(t)$ to be constant for all samples in the current buffer, which is valid for short window lengths.

Similarly, for the orientation-based constraint (4.15), we define the error as

$$e(\mathbf{\Phi}, t_k) := \arcsin\left(2q_w q_x + 2q_y q_z\right) - \beta_0, \tag{4.20}$$

with a parameter vector $\mathbf{\Phi} := [\,\theta_1 \;\; \varphi_1 \;\; \theta_2 \;\; \varphi_2 \;\; \delta \;\; \beta_0\,]^\intercal$ that additionally includes the carrying angle.

To estimate the joint axes $\mathbf{j}_1$ and $\mathbf{j}_2$ and the heading offset δ given a set of M samples, we find the parameter vector $\hat{\mathbf{\Phi}}$ that minimizes the sum of squares of either the error defined in (4.19) (for the rotation-based constraint) or (4.20) (for the orientation-based constraint), i.e.,

$$\hat{\mathbf{\Phi}} = \arg\min_{\mathbf{\Phi}} \sum_{t_k \in B} e(\mathbf{\Phi}, t_k)^2 = \arg\min_{\mathbf{\Phi}} \mathbf{e}(\mathbf{\Phi})^\intercal \mathbf{e}(\mathbf{\Phi}), \tag{4.21}$$

with $\mathbf{e} \in \mathbb{R}^{M\times 1}$ being the error vector and B denoting the set of M sampling times t_k in the buffer.

For any given parameter vector, we can evaluate the Jacobian $\mathbf{J}$ with

$$[\mathbf{J}]_{ij} = \frac{\partial e_i}{\partial \Phi_j}. \tag{4.22}$$

Analytical expressions for all elements of $\mathbf{J}$ that only depend on the parameters $\mathbf{\Phi}$ and on the measurements are given in Appendix B.2 for the rotation-based constraint and in Appendix B.3 for the orientation-based constraint.

The Gauss-Newton algorithm [133] is used to minimize the error. Starting with an initial parameter vector $\mathbf{\Phi}_0$, we iteratively obtain the estimate by

$$\mathbf{\Phi}_{l+1} = \mathbf{\Phi}_l + \alpha \mathbf{p}_l \text{ with } \mathbf{J}^\intercal \mathbf{J} \mathbf{p}_l = \mathbf{J}^\intercal \mathbf{e} \tag{4.23}$$

until convergence is achieved, with the iteration index $l \in \mathbb{N}$, the step direction $\mathbf{p}_l$, and the step length $\alpha = 1$. In between iterations, we switch from one joint axis representation to the other via Cartesian coordinates if $|\sin\theta_i| < \frac{1}{2}$, $i = 1, 2$ (cf. Section 4.4.3).

Note that the proposed optimization method can not only be applied to recorded datasets but is also suitable for real-time application. In the simplest case, samples are saved while the subject performs a motion, and afterward, the optimization is performed on the stored samples, and the resulting calibration parameters are applied to all subsequent samples. For an improved online implementation that continuously updates the axes estimates (if desired) and that starts to provide estimates as early as possible, the method can be extended to the following moving window approach:

1. New samples are continuously selected every 0.05 s and stored in a ring buffer containing $M = 200$ data sets, i.e., old data sets are automatically discarded.

2. As soon as the buffer is half full, optimization starts.

3. One Gauss-Newton step is performed every time a sample is added to the buffer (to continuously update the solution while spreading the computational load over time).

Note that it is also possible to keep the parameters for the joint axes θ_1, φ_1, θ_2, and φ_2 fixed after the initial estimate and only track the heading offset δ – a concept that is investigated in depth in Chapter 5.

Further note that, for the orientation-based constraint, the value of the carrying angle β_0 is only included in the parameter vector to provide the necessary degree of freedom in joints with an unknown carrying angle. The value obtained via the optimization is not used further for joint angle calculation. If the true carrying angle is known or expected to be zero, it is equally possible to remove this degree of freedom in the optimization and instead insert a fixed value or zero into the cost function.

As a result of the optimization step, we obtain the joint axes $\mathbf{j}_1$ and $\mathbf{j}_2$ in the coordinate systems of sensors $\mathcal{S}_1$ and $\mathcal{S}_2$, respectively, and the heading offset δ between the reference frames $\mathcal{E}_1$ and $\mathcal{E}_2$.

4.4.5 Joint Angle Calculation

Using the optimization results, we calculate FE and PS joint angles based on the ISB recommendations [47]. Those joint angles are defined as intrinsic z-x'-y'' Euler angles of the forearm $\mathcal{B}_2$ relative to the upper arm $\mathcal{B}_1$, i.e., ${}^{\mathcal{B}_2}_{\mathcal{B}_1}\mathbf{q}$, with $\mathcal{B}_1$ and $\mathcal{B}_2$ being the segment coordinate systems as defined in [47].

From 6D IOE, we get the sensor orientation quaternions ${}^{\mathcal{S}_1}_{\mathcal{E}_1}\mathbf{q}$ and ${}^{\mathcal{S}_2}_{\mathcal{E}_2}\mathbf{q}$. After performing the optimization, we know the coordinates of both joint axes $\mathbf{j}_1$ and $\mathbf{j}_2$ in local sensor coordinates and the heading offset δ. Note that additional knowledge is needed to determine the absolute value of the joint angles without any offset – for example, for the elbow joint, which joint orientation corresponds to zero flexion and zero pronation is only a matter of convention and not an inherent property of the 2-DoF joint. To obtain offset-free angles, we employ reference values of the FE and PS joint angles at one arbitrary time instant t_{ref}, e.g., obtained from a known pose or by exploiting the maximum range of motion of the joint. With those values, the joint angles can be calculated by the algorithm described below:

First, we calculate ${}^{\mathcal{E}_2}_{\mathcal{E}_1}\mathbf{q}$ via (4.8) and use this to obtain ${}^{\mathcal{S}_2}_{\mathcal{E}_1}\mathbf{q} = {}^{\mathcal{E}_2}_{\mathcal{E}_1}\mathbf{q} \otimes {}^{\mathcal{S}_2}_{\mathcal{E}_2}\mathbf{q}$. Then we determine rotations that ensure that the identified joint axes match the joint axes defined in [47]:

$$ {}^{\mathcal{B}'_1}_{\mathcal{S}_1}\mathbf{q} = (\arccos([0\ 0\ 1]^\intercal \cdot \mathbf{j}_1) \,@\, [0\ 0\ 1]^\intercal \times \mathbf{j}_1)\,, \tag{4.24} $$

$$ {}^{\mathcal{B}'_2}_{\mathcal{S}_2}\mathbf{q} = (\arccos([0\ 1\ 0]^\intercal \cdot \mathbf{j}_2) \,@\, [0\ 1\ 0]^\intercal \times \mathbf{j}_2)\,. \tag{4.25} $$

Using those rotations, we calculate the relative segment orientation

$$ {}^{\mathcal{B}'_2}_{\mathcal{B}'_1}\mathbf{q} = \left({}^{\mathcal{S}_1}_{\mathcal{E}_1}\mathbf{q} \otimes {}^{\mathcal{B}'_1}_{\mathcal{S}_1}\mathbf{q}\right)^{-1} \otimes {}^{\mathcal{S}_2}_{\mathcal{E}_1}\mathbf{q} \otimes {}^{\mathcal{B}'_2}_{\mathcal{S}_2}\mathbf{q}. \tag{4.26} $$

For any quaternion $\mathbf{q} =: [\,q_w \;\; q_x \;\; q_y \;\; q_z\,]^\intercal$, the z-x'-y'' Euler angles (α, β, γ) can be calculated as

$$ \alpha = \operatorname{atan2}(2q_wq_z - 2q_xq_y, q_w^2 - q_x^2 + q_y^2 - q_z^2), \tag{4.27} $$

$$ \beta = \arcsin(2q_wq_x + 2q_yq_z), \tag{4.28} $$

$$ \gamma = \operatorname{atan2}(2q_wq_y - 2q_xq_z, q_w^2 - q_x^2 - q_y^2 + q_z^2). \tag{4.29} $$

By calculating z-x'-y'' Euler angles $(\alpha', \beta', \gamma')$ of ${}^{\mathcal{B}_2'}_{\mathcal{B}_1'}\mathbf{q}$, we obtain the FE angle α' and the PS angle γ' that only differ from the well-defined joint angles according to [47] by a constant offset that depends on the actual placement of the IMUs.

We can eliminate this offset by exploiting knowledge of the actual joint angles α_{ref} and γ_{ref} at the time instant $t = t_{\text{ref}}$. The segment-to-sensor orientations

$$ {}^{\mathcal{B}_1}_{\mathcal{S}_1}\mathbf{q} = {}^{\mathcal{B}_1'}_{\mathcal{S}_1}\mathbf{q} \otimes \left(\alpha'(t_{\text{ref}}) - \alpha_{\text{ref}} \,@\, [0\ 0\ 1]^\intercal\right), \tag{4.30} $$

$$ {}^{\mathcal{B}_2}_{\mathcal{S}_2}\mathbf{q} = {}^{\mathcal{B}_2'}_{\mathcal{S}_2}\mathbf{q} \otimes \left(\gamma_{\text{ref}} - \gamma'(t_{\text{ref}}) \,@\, [0\ 1\ 0]^\intercal\right) \tag{4.31} $$

allow us to calculate ${}^{\mathcal{B}_2}_{\mathcal{B}_1}\mathbf{q} = ({}^{\mathcal{S}_1}_{\mathcal{E}_1}\mathbf{q} \otimes {}^{\mathcal{B}_1}_{\mathcal{S}_1}\mathbf{q})^{-1} \otimes {}^{\mathcal{S}_2}_{\mathcal{E}_1}\mathbf{q} \otimes {}^{\mathcal{B}_2}_{\mathcal{S}_2}\mathbf{q}$. The Euler angles $(\alpha, \beta_0, \gamma)$ of ${}^{\mathcal{B}_2}_{\mathcal{B}_1}\mathbf{q}$ are the offset-free FE and PS joint angles α and γ, respectively, and the carrying angle β_0 (cf. Figure 4.3), which is almost constant and rarely reported [47].

4.4.6 On-Chip Sensor Fusion, Soft Tissue Motions, and Axis Ambiguity

In the following, we introduce an optional extension that allows for the rotation-based constraint to be used when only orientation data is available (e.g., if on-chip sensor fusion is used), add a low-pass filter to reduce the influence of soft tissue motion artifacts, and discuss options for how to resolve the ambiguity in the signs of the joint axes.

4.4.6.1 Extension to On-Chip 6D Sensor Fusion

Especially in wireless inertial sensor networks, it is desirable to perform on-chip sensor fusion, potentially with a high sampling rate of the gyroscopes, and then to only transmit the orientation quaternions at a regular (and typically much lower) sampling rate to the processing unit. However, the constraint (4.9) is based on angular rates, i.e., on the gyroscope measurements.

Instead of transmitting the gyroscope measurements as well, which requires extra bandwidth, increases power consumption, and might not be possible without changing hardware or communication protocols, the angular rates can easily be approximated from the change of orientation

$$ \left[{}^{\mathcal{S}_i(t_k)}_{\mathcal{S}_i(t_{k-1})}\mathbf{q}\right]_{\mathcal{E}_i} = {}^{\mathcal{S}_i(t_k)}_{\mathcal{E}_i}\mathbf{q} \otimes {}^{\mathcal{S}_i(t_{k-1})}_{\mathcal{E}_i}\mathbf{q}^{-1} =: [\, q_w \ \ q_x \ \ q_y \ \ q_z \,]^\intercal, \quad i = 1, 2, \tag{4.32} $$

by

$$ [\boldsymbol{\omega}(t_k)]_{\mathcal{E}_i} = \frac{2}{T_\text{s}} \arccos(q_w) \frac{[\, q_x \ \ q_y \ \ q_z \,]^\intercal}{\|[\, q_x \ \ q_y \ \ q_z \,]^\intercal\|}. \tag{4.33} $$

Note that due to the order of quaternion multiplication, we already obtain the angular rate in each sensor's global frame $\mathcal{E}_i$, thus avoiding another transformation step.

Of course, when the gyroscope and accelerometer readings are available, it is equally possible to perform 6D sensor fusion in the processing unit, e.g., using the VQF algorithm proposed in Chapter 3, and directly employ the angular rates measured by the gyroscopes for evaluation of the kinematic constraint. Therefore, this proposed extension is not restrictive but instead broadens the scope of applicability of the method.

Note that the orientation-based constraint is already quaternion-based and does not require any other measurement data. Therefore, employing the proposed extension is not necessary when using this constraint.

4.4.6.2 Measurement and Soft Tissue Motion Artifact Reduction

Measurement anomalies, such as the sensor accidentally touching objects, or soft tissue motion can cause artifacts in the measured angular rates $\boldsymbol{\omega}_1$ and $\boldsymbol{\omega}_2$. This leads to high-frequency disturbances (compared to the frequency of the functional joint motions) that violate the rotation-based constraint (4.9) and therefore deteriorate the estimation accuracy. Low-pass filtering of the angular rates used for evaluating the rotation-based constraint with a cutoff frequency of $f_\mathrm{c} = 5\,\mathrm{Hz}$ improves the accuracy and robustness of the anatomical calibration.

4.4.6.3 Ambiguity in the Signs of the Joint Axes

The joint constraints cannot be used to determine the signs of the joint rotation axes, as for any pair of axes, the value of the cost function for $(\mathbf{j}_1, \mathbf{j}_2)$, $(-\mathbf{j}_1, -\mathbf{j}_2)$ and also $(\mathbf{j}_1, -\mathbf{j}_2)$ is exactly the same. Correspondingly, whether, for example, supination is defined as a positive or negative rotation around an axis pointing proximally along the right forearm is only a matter of convention and not an inherent property of the 2-DoF joint.

In practical applications, it is essential to ensure that a specific definition is always followed, e.g., the ISB recommendations [47]. In order to determine the sign, two approaches are practical: The first is to ensure a sensor placement that is roughly known, i.e., the half-space in which each joint axis points is predetermined. The second is to exploit the joint's range of motion in combination with the offset-removal method described in Section 4.4.5. For example, by defining that an extended and supinated elbow corresponds to $\alpha = 0, \gamma = 0$ and choosing the signs of the joint axes so that the mean joint angles during calibration are positive, we ensure that we follow the definitions given in [47].

4.5 Experimental Evaluation

We evaluate the proposed magnetometer-free anatomical calibration and joint angle calculation methods based on two experiments.

The first experiment is designed to evaluate if the obtained joint axis estimates are plausible and consistent. To this end, IMU data from two different motions is recorded from five subjects and a mechanical joint, while carefully attaching the sensors in a known orientation. Each trial is split into overlapping time windows to which the anatomical calibration methods are applied. The obtained joint axis estimates are compared to the axes obtained by the more restrictive method of careful manual sensor placement. Furthermore, this experiment is used to evaluate the sensitivity of the method with respect to the choice of cutoff frequency, sample selection frequency, and window duration.

The second experiment is designed for the evaluation of the accuracy of the joint angles obtained with the proposed self-calibrating magnetometer-free joint angle calculation method. This experiment consists of recordings of natural everyday life motions of two subjects. It uses marker-based OMC as a reference, which allows for the comparison of the obtained joint angles to joint angles obtained from optical markers and from a conventional 9D IMU-based approach. As a further validation step, we consider the variability of the expected-to-be-constant carrying angle as a metric for how well the estimated joint axes describe the functional joint motion.

Note that in all experiments, the sensors are carefully attached in a known orientation to facilitate a plausibility check of the obtained results. To still verify that the proposed methods do not make assumptions regarding the sensor orientation, we simulate a random sensor attachment by multiplying all gyroscope and accelerometer measurements with a random rotation matrix that is different for each analyzed time window.

The extension for on-chip sensor fusion introduced in Section 4.4.6.1 is always used, i.e., the angular rates used for evaluating the rotation-based kinematic constraint are derived from the orientation estimates. Since the impact on the results is negligible, the results obtained using the actual gyroscope measurements are not shown separately.

4.5.1 Robustness of Joint Axis Estimation

The first experiment is performed to answer the following two research questions:

1. Are the estimated joint axes plausible, i.e., do they agree with the values expected based on careful manual placement?
2. Are the estimated joint axes consistent, i.e., do we always obtain the same result when using different parts of the trial?

Data from five healthy subjects is recorded. The subjects are adult volunteers with no history of upper-limb injury that might affect upper-limb movement. Inertial sensors (Xsens MTw, Xsens Technologies B.V., Netherlands) are placed on the upper arm close to the elbow and on the forearm close to the wrist. The sensors are placed in a defined orientation on the skin so that one local sensor axis coincides roughly with the functional joint axis.

We define two different motions:

1. The *simple motion* consists of FE of the elbow and PS of the forearm, performed alternatingly while keeping the longitudinal axes of upper arm and forearm parallel to the sagittal plane.
2. For the *complex motion*, we ask the subject to perform random combinations of FE and PS, allowing for 3D rotation of the shoulder including humeral rotation.

Each subject performs both motions for approximately one minute.

In addition to the five human subjects, an additional dataset is recorded using a mechanical joint. This joint has dimensions similar to the human arm and consists of two hinge joints as shown in Figure 4.3. During the recordings, the joint was held in hand and moved in a way that mimics the motions performed by the five subjects.

For each recording, the proposed methods are applied to 21 partially overlapping moving windows w, $w = 1, 2, \dots, 21$, of length $10\,\mathrm{s}$ with data sets taken every $0.05\,\mathrm{s}$. Note that we will later investigate the effect of window length and sampling time and show that this window length is usually sufficient to identify the joint axes and that collecting data sets more frequently does not considerably improve the robustness.

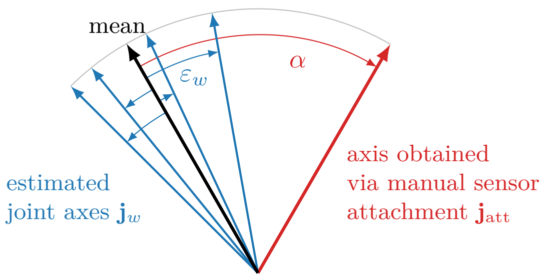

Figure 4.5: Variability angle ε_w and misalignment angle α used to evaluate the axis estimation results. The variability angle ε_w is the angle between the estimated axis for a single window and the mean estimate. The misalignment angle α is the angle between the mean estimate and the axis obtained by careful manual sensor attachment. For a good anatomical calibration method, ε_w should be small, showing that the estimates are consistent, and α should be within 30°, showing that the estimates are plausible.

Since the only available ground truth are approximate axis coordinates that we know due to the orientation in which the sensor was attached, we define suitable evaluation metrics that allow us to quantify the consistency and plausibility of the estimates. See Figure 4.5 for an illustration of the definitions. First, denote the estimated joint axes $\mathbf{j}_w$, with w being the index for the estimation window.[2] To assess if the estimates are consistent, we define the *variability angle*

$$\varepsilon_w = \sphericalangle(\mathbf{j}_w, \mathbf{j}_{\mathrm{mean}}), \tag{4.34}$$

where $\sphericalangle$ denotes the positive angle between two 3D vectors and

$$\mathbf{j}_{\mathrm{mean}} = \frac{1}{21} \sum_{w=1}^{21} \mathbf{j}_w \tag{4.35}$$

is the mean of all estimates. In other words, ε_w is the angular deviation between the estimate for window w and the mean of all estimates. If this angle is always small, the estimation results agree well for all time windows.

To also check if this result is plausible, we introduce the *misalignment angle*

$$\alpha = \sphericalangle(\mathbf{j}_{\mathrm{mean}}, \mathbf{j}_{\mathrm{att}}), \tag{4.36}$$

with $\mathbf{j}_{\mathrm{att}}$ being the joint axis obtained via careful manual sensor attachment. Therefore, α is the angle between the mean estimation result and the axis obtained via manual sensor attachment. While precise manual sensor attachment is hard and error-prone, we can at least expect both axes to coincide roughly and therefore consider the result plausible if $\alpha \leq 30°$.

Figure 4.6 shows the results obtained in the first experiment with the rotation-based and orientation-based constraints. In general, we see that the proposed methods for anatomical calibration produce good results: with both constraints, the methods are able to determine plausible FE and PS joint axes from 10-second recordings, and in all cases except for Subject 2 with the orientation-based constraint and the complex motion, the median of the variability angle ε_w is below 10°. In other words, almost all time windows lead to axis estimates within the

[2]For a compact notation, we now omit the segment index $i = 1, 2$, denoting whether the axis is a FE axis or a PS axis.

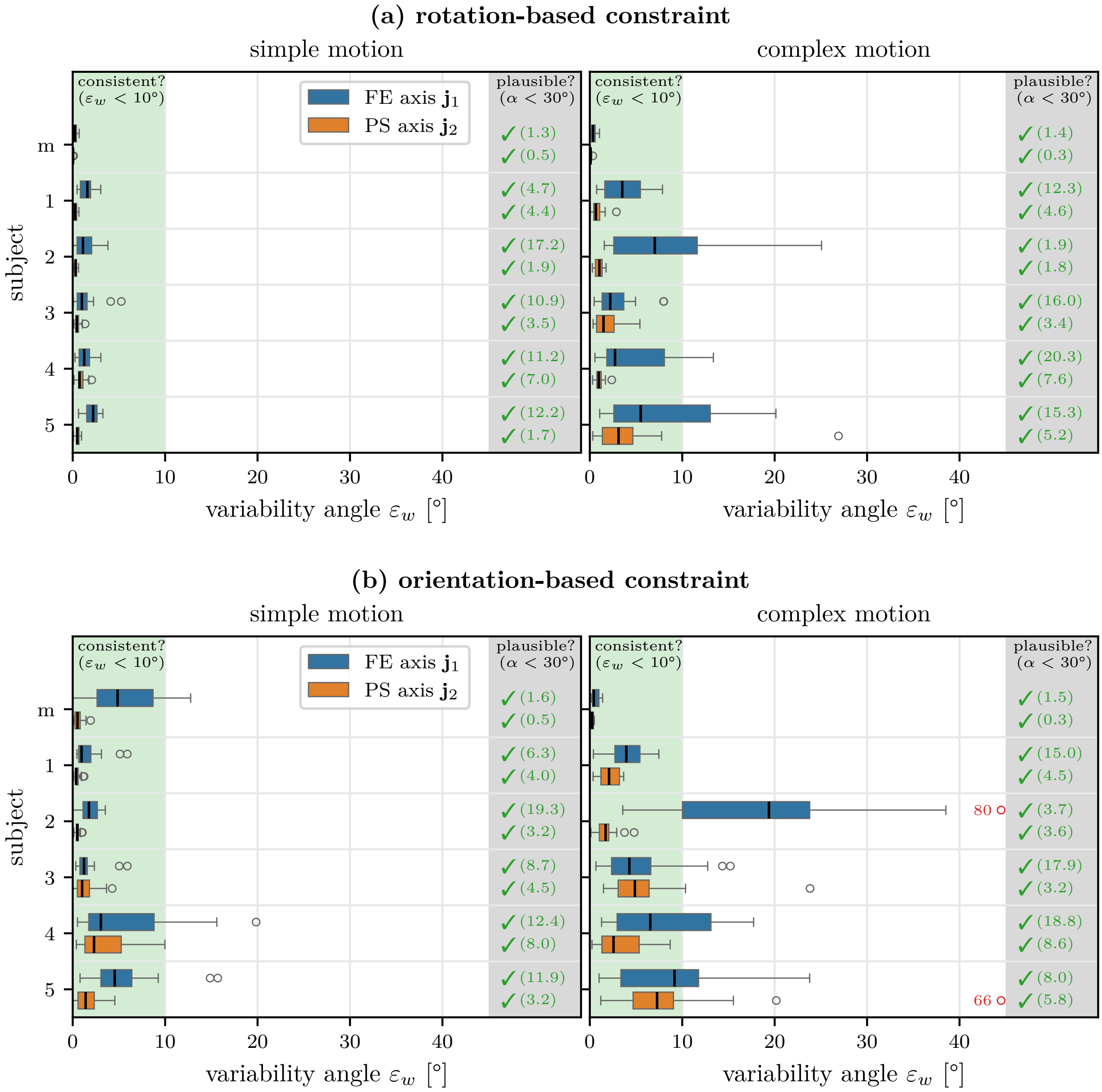

Figure 4.6: Consistency and plausibility results for the first experiment with the **(a)** rotation-based constraint and the **(b)** orientation-based constraint, for two motion types and for five human subjects and a mechanical joint (m). The proposed methods estimate plausible axes for all subjects and all motions. The rotation-based constraint yields more consistent estimates than the orientation-based constraint, and the simple motion leads to better results than the complex motion.

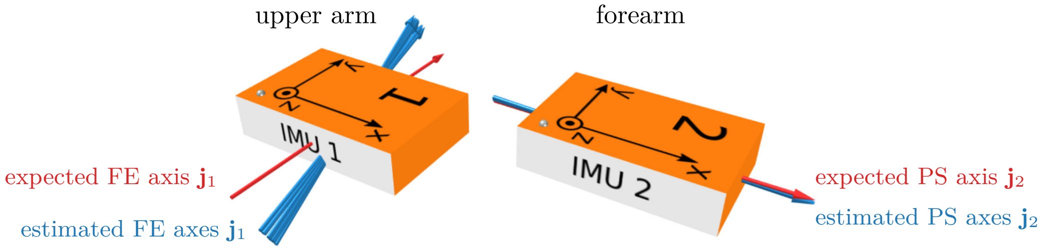

Figure 4.7: 3D visualization of the estimation results for an exemplary trial (Subject 2, simple motion, rotation-based constraint). The joint axis estimates from all windows agree well (blue arrows). The PS axis agrees very well with the expected value (red arrow), while for the FE axis there is a misalignment of 17°, most likely due to imprecise manual sensor attachment.

expected range. As a main result, it is noticeable that the rotation-based constraint performs better than the orientation-based constraint and that a slight increase in the variability angles ε_w can be observed in the complex motion. This is likely due to soft tissue motion caused by humeral rotation. Furthermore, the randomness of the complex motion can lead to longer periods of motion that do not excite both degrees of freedom of the joint.

The results obtained with the mechanical joint agree very well with the expected axes ($\alpha \leq 2°$), and the joint axis estimates are more consistent than for the biological elbow joints. This is to be expected since precisely attaching the sensors is easier with the mechanical joints, there are no soft tissue motion artifacts, and the mechanical joint constructed with two hinge joints follows the kinematic model (Figure 4.3) more precisely than the human elbow.

To facilitate an intuitive understanding of the results, Figure 4.7 shows the estimated and expected joint axes in a 3D visualization of the respective IMU coordinate systems. We can see that, for both FE and PS, the joint axis estimates of all time windows agree well. While the PS axis agrees very well with the axis expected due to sensor alignment, a systematic disagreement of $\sim 17°$ between the estimated and expected FE axes is noticeable. Since all estimates are very consistent, this is most likely due to an imprecise manual attachment of the sensor, causing the y-axis of the IMU to disagree with the functional FE axis of the joint. In general, we see in Figure 4.6 that the misalignment angle α is larger for the FE axis $\mathbf{j}_1$ than for the PS axis $\mathbf{j}_2$. This is plausible, given the fact that the longitudinal x-axis of the IMU is easier to precisely align with the longitudinal axis of the forearm, whereas aligning the y-axis of the upper arm IMU, corresponding to a shorter dimension of the sensor case, with the functional FE axis was found to be much harder while conducting the experiments.

However, it is noticeable that also for the variability angle ε_w, the values are typically larger for the FE axis than for the PS axis, indicating that it is not only harder to perform a precise manual alignment of this axis but it is also harder for the proposed methods to accurately and consistently estimate this axis. This effect is especially pronounced for the complex motion.

To investigate one potential effect, we take a closer look at Subject 2 and the rotation-based constraint. In the complex motion trials, Subject 2 stands out as the range of motion of the upper arm IMU is considerably lower than for the other subjects (to be more specific, the mean pairwise orientation difference within a window is 16° for Subject 2 and between 46° and 56° for the other four subjects) while the FE axis deviations are larger than for all other subjects. In Figure 4.8a, we visualize the estimated FE joint axes and notice that all estimates lie approximately within the y-z-plane of the sensor. During the trial, the x-axis of the upper arm IMU was approximately vertical, i.e., the y-z-plane was approximately horizontal. When calculating the angle of the joint axis in this y-z-plane and plotting this angle together with the estimated heading offset δ in Figure 4.8b, we notice that there is an obvious correlation.

This correlation can be explained when considering the kinematic constraint in (4.9) for the special case in which the upper arm does not move, i.e., the orientation ${}^{\mathcal{B}_1}_{\mathcal{E}_1}\mathbf{q}$ is constant, $\boldsymbol{\omega}_1 = 0$, and the coordinates of $[\mathbf{j}_1]_{\mathcal{E}_1}$ are constant. In this case, there is no difference between a change in δ, i.e., the heading offset between $\mathcal{E}_1$ and $\mathcal{E}_2$, and a rotation of the joint axis estimate $\mathbf{j}_1$ around the vertical axis. The observation in Figure 4.8 is likely caused by the real

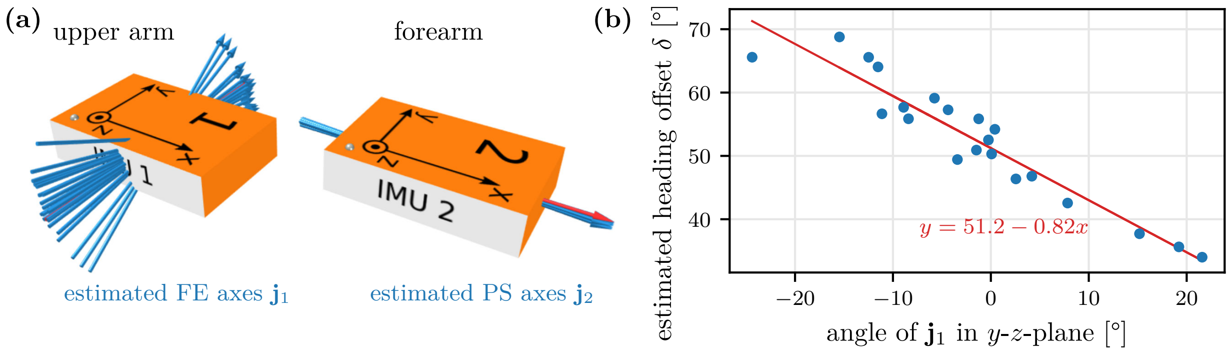

Figure 4.8: Investigation into the variability of the FE axis estimates (Subject 2, complex motion, rotation-based constraint). **(a)** 3D visualization of the axis estimates for all windows. **(b)** Plot of the estimated heading offset δ and the angle of the FE axis in the (approximately horizontal) y-z-plane of the upper arm IMU coordinate system. There is an obvious correlation, indicating that without sufficient upper arm movement, the kinematic constraint does not allow for distinguishing between a heading rotation of the joint axis and a heading offset between the sensor orientations.

situation being too close to this singular case. To mitigate this, care should be taken to avoid calibration motions during which one of the body segments is always stationary.

In summary, the evaluation of the first experiment has shown that the proposed methods yield consistent and plausible joint axis estimates. The rotation-based constraint performs better than the orientation-based constraint. To ensure that the axes converge, the subject's motion should include sufficient motion from both the upper arm and the forearm.

4.5.2 Sensitivity to Cutoff Frequency, Sample Selection Frequency, and Window Duration

As a further part of the evaluation, we use the data from the first experiment to investigate the influence of the following parameters:

- the cutoff frequency f_c for measurement and soft tissue motion artifact reduction (employed value: 5 Hz, cf. Section 4.4.6.2, rotation-based constraint only),
- the sample selection frequency (employed value: 20 Hz, $T_s = 0.05$ s),
- the duration of the measurement window (employed value: 10 s).

We apply the proposed methods to all trials of the five subjects of the first experiment for different values of the respective parameter while keeping the other two parameters at the previously employed default value. In order to condense the obtained information (cf. Figure 4.6), we calculate the mean and the 99th percentile of the variability angles ε_w of all windows of all trials.

For the angular rate cutoff frequency f_c for measurement and soft tissue motion artifact reduction, the obtained results are shown in Figure 4.9. If the cutoff frequency is chosen too low ($f_c = 2$ Hz), the mean and 99th percentile of ε_w increase compared to the smallest possible value. At those frequencies, valuable information about the movement gets lost, leading to more inconsistent estimation results. However, when choosing $3\,\text{Hz} \leq f_c \leq 7\,\text{Hz}$, the results are more consistent than without any low-pass filter. Therefore, we can conclude that low-pass

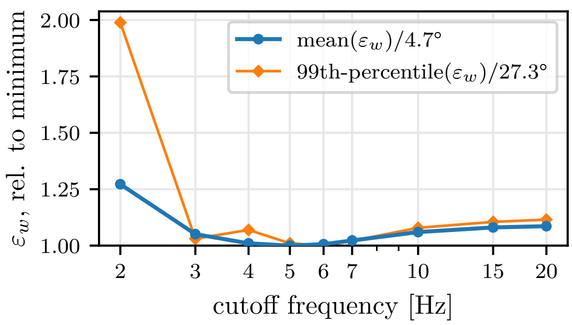

Figure 4.9: Variability of the obtained axis estimates (mean and 99th percentile of ε_w, relative to minimum value) for different values of the cutoff frequency of the soft tissue motion artifact reduction low-pass filter. Low-pass filtering of the angular rates increases the consistency of the axis estimates, but for too low cutoff frequencies, important information gets lost, and the deviations increase. Choosing a cutoff frequency of 5 Hz gives robust estimates.

filtering of the angular rates helps to increase robustness and that $f_c = 5\,\text{Hz}$ is a reasonable choice for the cutoff frequency.

To determine how much data is needed to get consistent estimates, we repeat the same evaluation for the other two parameters, i.e., window duration and sample selection frequency, which is shown for both constraints in Figure 4.10. As expected, using more data in the optimization, i.e., increasing the window duration or increasing the sample selection frequency, leads to more consistent estimates. However, this comes at a cost. Longer window durations cause inconvenience for the subject that has to perform the movements and limit the applicability of the method. Therefore, the duration of 10 s was chosen as a compromise between ease of use and accuracy, and to demonstrate that such short durations lead to good results. If the data is available, employing longer motion sequences should be considered (up to a point where the assumption of δ being constant is not valid anymore due to integration drift). The sampling selection frequency is less critical as it only affects the computational time. However, the results show that increasing the frequency past 10 Hz does not substantially affect the results. The chosen frequency of 20 Hz is more than sufficient while still considerably reducing the number of samples compared to typical IMU raw data sampling rates of 50–500 Hz.

4.5.3 Accuracy of Magnetometer-Free Joint Angle Tracking

The second experiment is performed to validate that the proposed methods can be used to obtain accurate elbow joint angles for functional motions without relying on a precisely known sensor attachment and without relying on the magnetic field. An optical motion capture system (Vicon Motion Systems Ltd. UK) is used as reference. In addition to the two inertial sensors positioned as in the previous experiment, optical markers are placed on bony landmarks in a way that facilitates joint angle measurement as recommended by the ISB [47]. Note that by placing reflective markers on anatomical landmarks and not, like many previous works, on the IMUs, we ensure that we compare against the gold standard for measuring joint angles, taking soft tissue motion into account.

Two healthy adult volunteers, with no history of upper-limb injury that might affect upper-limb movement, performed two motions:

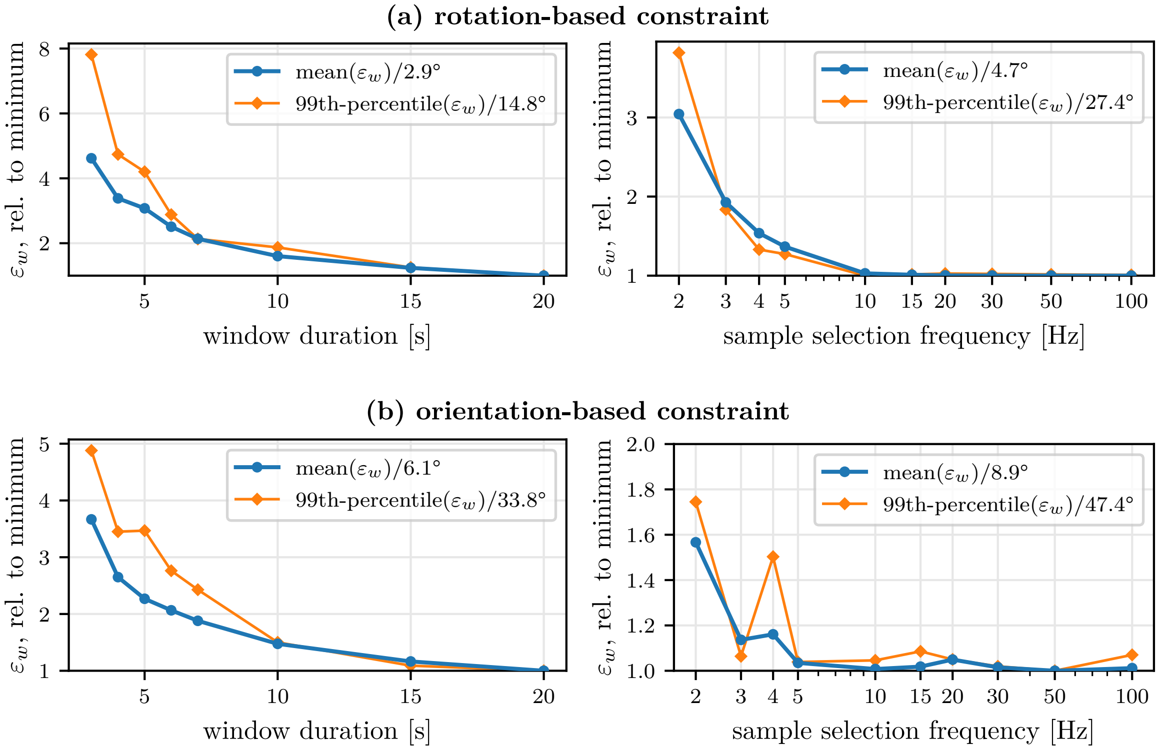

Figure 4.10: Variability of the obtained axis estimates (mean and 99th percentile of ε_w, relative to minimum value) for different values of the window duration and the sample selection frequency for **(a)** the rotation-based constraint and **(b)** the orientation-based constraint. In general, using more data (long windows at high sampling rates) leads to more consistent estimates but increases inconvenience for the subject and processing time.

1. During the *pick-and-place* motion, the subject placed a small box in a sequence of predefined orientations and locations on a table.

2. The *drinking* motion consists of the subject repeatedly placing the hand on a table, grabbing a cup, simulating a drinking motion, and then placing the cup back on the table.

Each of the two subjects repeats the two motions four times (twice slow and twice fast), resulting in a total of 16 trials, with durations between 14 and 44 s.

For each trial, calculate four different types of joint angles.

1. The OMC-based *ground truth* angles are derived from the optical markers placed on anatomical landmarks and calculated as described in [47].

2. *Conventional* IMU-based joint angles are calculated using 9D sensor fusion (with the VQF algorithm proposed in Chapter 3), i.e., using the magnetic field to determine the heading and relying on the careful placement of the sensors on the body.

3. In contrast, the *proposed* IMU-based joint angles use 6D sensor fusion (with the VQF algorithm proposed in Chapter 3), and the joint axes and heading offset are identified from the trial motion using the

   - *rotation-based* joint constraint and the
   - *orientation-based* joint constraint.

Note that the application of the proposed methods tests the most challenging case, i.e., we use a standard everyday motion to identify the joint axes and the heading offset without requiring a separate calibration phase.

To determine the sign and the required offset for the joint angles, we use the OMC-based angles. The IMU-based joint angles obtained by the different methods are compared to the OMC-based ground truth, and the RMSE is calculated. Results from all trials are shown in Figure 4.11.

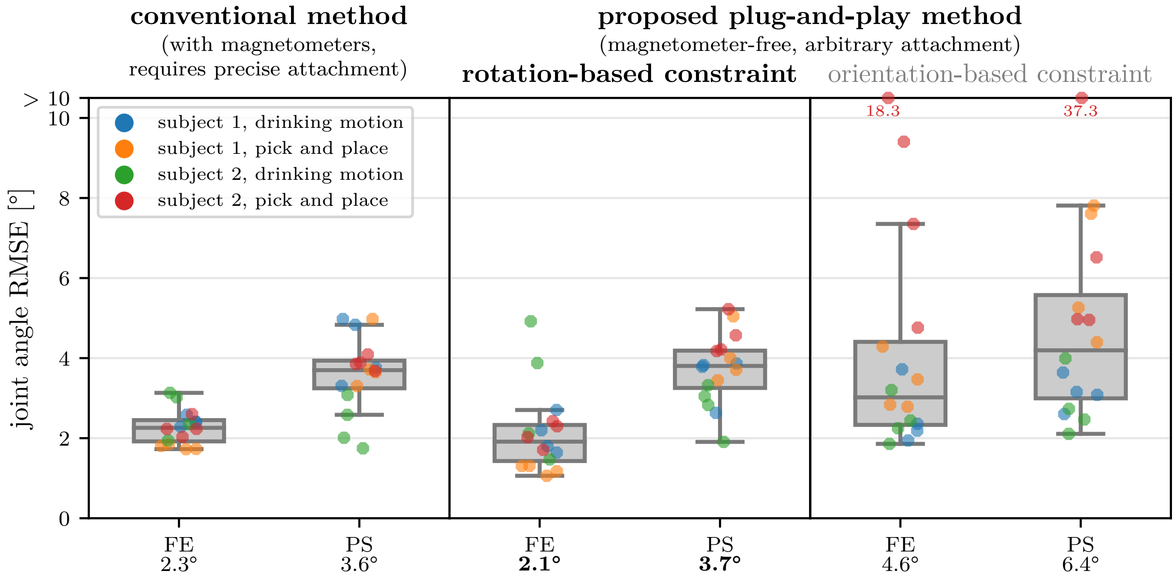

Figure 4.11: Joint angle estimation errors for all trials with a conventional 9D approach and with the proposed plug-and-play magnetometer-free methods, using OMC-based angles as ground truth. The numbers below the axis labels indicate the mean RMSE of all 16 trials. The proposed method with the rotation-based constraint yields the same accuracy as the more restrictive conventional 9D method.

When comparing the two variants of the proposed method, we see that the rotation-based constraint outperforms the orientation-based constraint. This coincides with the results of the first experiment presented in Section 4.5.3. It is noteworthy that for many trials, the accuracy achieved with both constraints is comparable, and the difference in the mean accuracy is caused by several outliers obtained with the orientation-based constraint, which is consistent with the lower robustness observed for this constraint in Figure 4.6.

However, when considering the results obtained with the proposed method and the rotation-based constraint, the accuracy is similar to the conventional 9D IMU-based method. For the FE angles, the mean RMSE of 2.1° is 0.2° lower than for the conventional method, while for the PS angles, the mean RMSE of 3.7° is 0.1° larger. In contrast to the results with the orientation-based constraint, there are no outliers, and the maximum RMSE of the proposed method and the conventional method is comparable. Note that the conventional method relies on properly calibrated magnetometer measurements, a controlled environment without ferromagnetic material or electric devices, and a precise and known sensor attachment and is therefore more restrictive than the proposed magnetometer-free plug-and-play method.

To illustrate the performed motions and the obtained results, Figure 4.12 shows the OMC ground truth joint angles, the conventional IMU-based joint angles, and the proposed joint

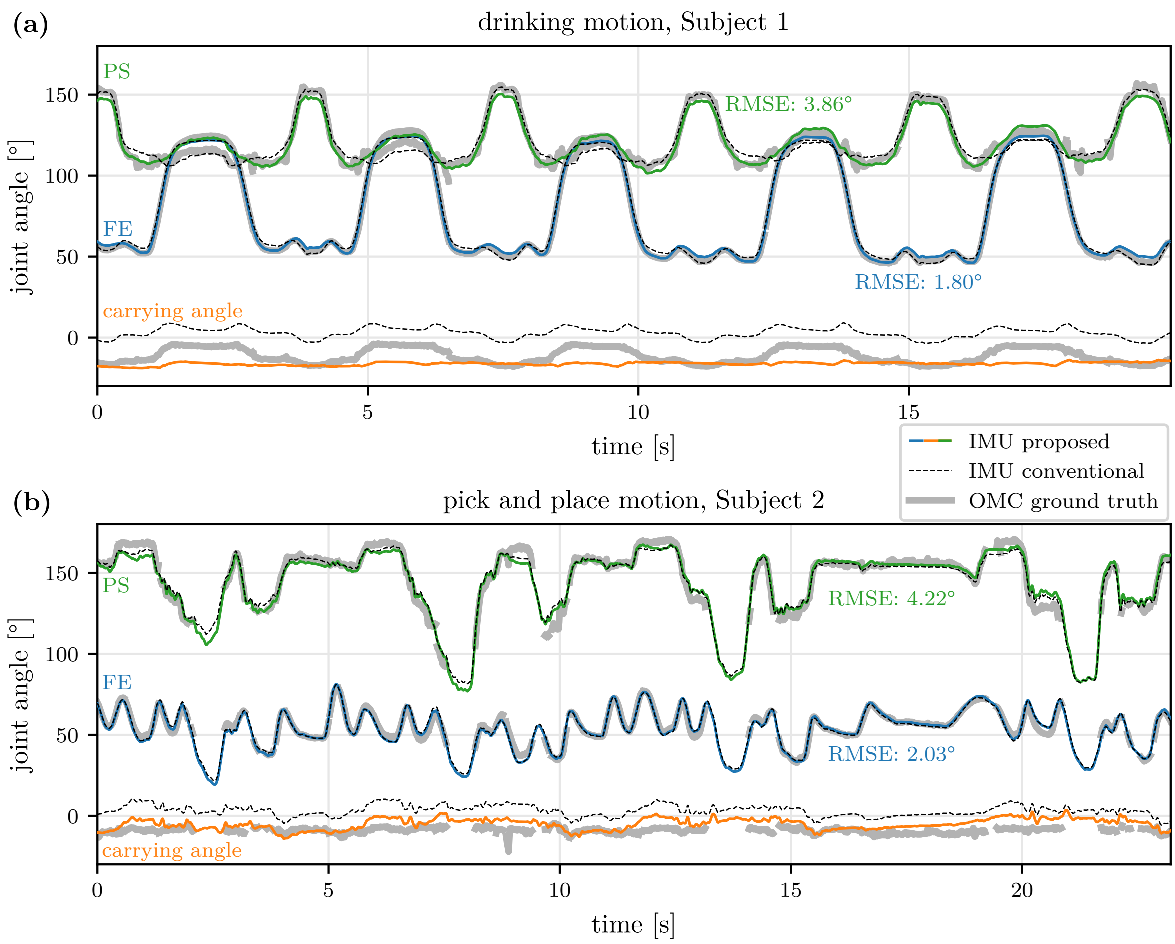

Figure 4.12: Joint angle trajectories for an exemplary **(a)** drinking and **(b)** pick-and-place trial obtained with the proposed IMU-based method (and the rotation-based constraint), the conventional 9D IMU-based approach, and the OMC ground truth. While being less restrictive, the proposed method is able to obtain FE and PS joint angles that agree well with the angles obtained with the other two methods.

angles with the rotation-based constraint for two exemplary trials. In several short time periods, ground truth data is not available due to occlusion, i.e., at least one of the required markers could not be tracked by the OMC system. Those phases were excluded from the RMSE calculation. As can be seen, the joint angles obtained with the proposed plug-and-play method agree well with both the conventional IMU-based joint angles and the OMC-based ground truth angles.

Note that the joint constraint is only used for identifying the joint axes and that the joint angle calculation uses standard Euler angles and is therefore not directly restricted by this constraint. As a result, the obtained carrying angles, which are also shown in Figure 4.12 but rarely reported in practice, are not perfectly constant.

We can use the carrying angle as an indicator of how well the measured joint motion adheres to the 2-DoF joint model (Figure 4.3). For a perfect 2-DoF joint, we would expect a perfectly constant carrying angle, while a 3-DoF joint will show considerable movement in all three joint angles. Also, if the joint is in fact a 2-DoF joint but the joint axis estimates are wrong, the Euler decomposition will show variability in all three joint angles.

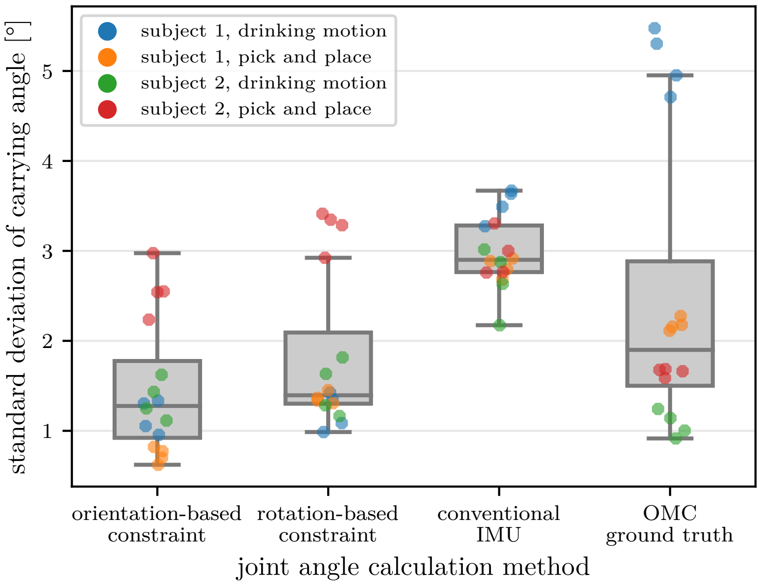

Figure 4.13: Standard deviation of the carrying angle for all trials with the different angle calculation methods. The proposed method induces the smallest variation in the assumed-to-be-constant carrying angle. This indicates that the estimated joint axes describe the functional motion axes better than the axes obtained via careful manual IMU placement (conventional IMU) and via placing markers on anatomical landmarks (OMC ground truth).

Therefore, we calculate the standard deviation of the carrying angle as a measure of variability, which is shown in Figure 4.13 for all 16 trials and all four angle calculation methods. With both constraints, the median of the standard deviations is slightly lower than for the conventional IMU-based joint angles and the OMC-based ground truth. This indicates that the joint axis estimates obtained with the proposed method are better suited to describe the functional motion of the joint than the axes obtained via careful IMU placement and the axes obtained via the placement of optical markers on anatomical landmarks. This agrees with previous research showing that anatomical joint axes defined based on anatomical landmarks do not coincide with the rotation axes of functional joint motion [134]. For joint angle calculation, the use of functional rotation axes seems preferable in order to minimize kinematic cross-talk.

In summary, the evaluation of the second experiment has shown that for the challenging case of using recordings of everyday motions for calibration, the proposed methods are able to obtain joint angles with the same accuracy as a conventional IMU-based approach while not relying on precise sensor placement or magnetometer measurements. As also shown via the first experiment, the rotation-based constraint performs better than the orientation-based constraint and should therefore be used for anatomical calibration.

4.6 Conclusions

This chapter introduced methods for automatic anatomical calibration for 2-DoF joints, such as the elbow, that do not require the subject to perform precise calibration movements but instead work on arbitrary motions by exploiting one of two kinematic constraints: a rotation-based constraint for the angular rates and an orientation-based constraint. The methods do not make use of magnetometer measurements. Instead, the heading offset is simultaneously estimated via the kinematic constraint, which facilitates plug-and-play magnetometer-free joint angle estimation.

The proposed methods were evaluated using two experiments. The first experiment, without OMC ground truth, showed that the proposed methods yield consistent and plausible joint axis estimates from only ten seconds of motion data. The second experiment, performed with OMC as ground truth, showed that the proposed plug-and-play method can estimate accurate joint angles while being less restrictive than a conventional IMU-based approach. In both experiments, the rotation-based joint constraint performed better than the orientation-based joint constraint.

The proposed methods overcome mounting and calibration restrictions and facilitate magnetometer-free motion tracking. Therefore, they are highly suitable for indoor environments and improve the practical usability of IMU-based motion tracking in many clinical and biomedical applications.

In the subsequent chapter, we will consider the case in which the joint axes are already known, either via the proposed calibration method or by other means, and the kinematic constraints are only used to determine the relative heading information to facilitate long-term stable magnetometer-free motion tracking.

To further advance the proposed methods, it should be evaluated if combining the rotation-based and the orientation-based constraint can increase the robustness and consistency of the joint axes estimates. Furthermore, introducing and evaluating metrics to quantify the estimation uncertainty and methods for automatic (re-)triggering of the calibration when suitable motions are detected are important next steps to increase the usability of the method.

5

Magnetometer-Free Motion Tracking of Kinematic Chains

When magnetometer measurements are not used, the heading of each sensor's orientation estimate has a different arbitrary heading offset. This circumstance impedes many possible applications that require knowledge of at least the relative heading between body segments, such as joint angle calculation and 3D visualization. This chapter introduces methods to obtain this relative heading information from kinematic constraints.

Text, figures, and tables found in this chapter have been previously published in the following works:

[135] D. Laidig, T. Schauer, and T. Seel. "Exploiting Kinematic Constraints to Compensate Magnetic Disturbances When Calculating Joint Angles of Approximate Hinge Joints from Orientation Estimates of Inertial Sensors". In: *2017 International Conference on Rehabilitation Robotics (ICORR)*. London, UK, July 17–20, 2017, pp. 971–976. DOI: 10.1109/ICORR.2017.8009375.

[136] D. Lehmann, D. Laidig, and T. Seel. "Magnetometer-Free Motion Tracking of One-Dimensional Joints by Exploiting Kinematic Constraints". In: *Proceedings on Automation in Medical Engineering* 1.1 (Feb. 16, 2020), Article 027. URL: https://www.journals.infinite-science.de/index.php/automed/article/view/335.

[137] D. Laidig, D. Lehmann, M.-A. Bégin, and T. Seel. "Magnetometer-Free Realtime Inertial Motion Tracking by Exploitation of Kinematic Constraints in 2-DoF Joints". In: *2019 41st Annual International Conference of the IEEE Engineering in Medicine and Biology Society (EMBC)*. Berlin, Germany, July 23–27, 2019, pp. 1233–1238. DOI: 10.1109/EMBC.2019.8857535.

Sections 5.3 and 5.4 have been previously published in [135]. The extended version found in this chapter includes an additional magnetometer-free variant of the proposed method. Sections 5.5 and 5.6 have been previously published in [136] and [137]. In this chapter, the experimental evaluations performed in [136] and [137] are combined in order to provide a consistent analysis of 1-DoF and 2-DoF joints. Sections 5.1 and 5.7 include content from both [135] and [137]. Section 5.2 was added in this thesis and extends the information found in [135, 136, 137].

5.1 Introduction

In order to measure joint angles with IMUs, an IMU is attached to each of the two body segments connected by the joint, as illustrated in Figure 5.1. The raw measurements are fused in order to estimate the sensor orientations (cf. Chapter 3). Then, anatomical calibration (sensor-to-segment calibration) is performed in order to determine the relation between sensor axes and segment or joint axes (cf. Chapter 4). With this information, segment orientations and then joint angles can be calculated.

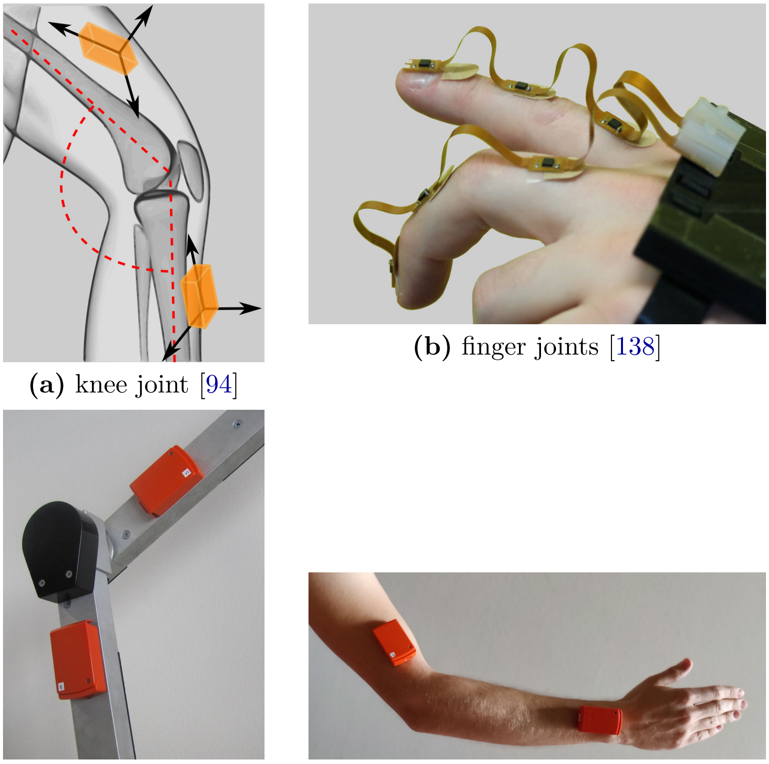

(a) knee joint [94]

(b) finger joints [138]

(c) mechanical joints

(d) elbow joint

Figure 5.1: Examples of IMU motion analysis for mechanical and biological joints. In many cases, the joints under consideration have only one or two degrees of freedom (DoF).

9D sensor fusion, i.e., the fusion of gyroscope, accelerometer, and magnetometer measurements, yields the orientation of the sensors with respect to a common inertial frame, which is crucial for determining the joint angles between neighboring segments in robotic or biomechanical limbs. However, 9D sensor fusion only yields accurate orientation estimates if the magnetic field is homogeneous. Magnetometer readings are known to be highly unreliable in indoor environments and near ferromagnetic material and electronic devices. Abundant research shows that inside buildings, the local magnetic field vector may easily vary by more than a factor of two in less than 20 centimeters [37, 38, 39, 40], cf. Section 2.3. Therefore, 9D sensor fusion fails in numerous environments that are relevant for most robotic and biomechanical applications [138].

In 6D inertial sensor fusion, the magnetometer readings are omitted, and the orientations of the sensors are determined only from the measured accelerations and angular rates. The heading of such an orientation exhibits an unknown and arbitrary offset, i.e., there is no absolute heading information (cf. Section 3.6).

This offset is often recovered via a calibration pose that ensures precise initial alignment of the sensors at the beginning of a measurement. As shown in [138], this approach improves results compared to conventional 9D sensor fusion, especially in realistic indoor environments. However, the heading still drifts slowly due to the integration of gyroscope bias around the vertical axis. Even with very precise bias calibration, this drift can easily reach 90° and more within a few minutes. This renders it impossible to determine long-time stable joint angles from 6D sensor orientations.

One way to suppress the influence of magnetic disturbances in 9D sensor fusion or to obtain the missing relative heading information in 6D sensor fusion is to exploit the kinematic models and constraints of different joint types. An overview of existing approaches is given in Section 5.2. In this chapter, we make use of the fact that biological and mechanical joints are often approximate hinge joints with a single degree of freedom or approximate 2-DoF joints.

Experimental validation in previous studies has almost exclusively been carried out under idealistic assumptions of either

1. rigid mechanical setups with perfect joint kinematics,
2. short time durations without sufficient focus on long-time stability, or
3. motions that avoid poses near singularities of the kinematic constraints and thus yield sufficient relative-heading information at all times.

Motions during which the joint segments remain close to singularities of the constraints (i.e., poses with unobservable relative heading) for more than a few seconds have barely been considered or discussed in previous studies.

This chapter presents two methods for relative heading tracking via kinematic constraints. First, we consider the task of IMU-based joint angle measurements for approximate hinge joints moving in inhomogeneous magnetic fields and introduce a quaternion-based method that uses the hinge joint constraint to determine and correct the error in heading, caused either by magnetic disturbances or by missing magnetometer measurements. Unlike previous methods, we employ a filter for singularity treatment. Using simulations, we test the performance of this method in homogeneous and in heavily disturbed magnetic fields and investigate the sensitivity to the joint not being a perfect hinge joint and to errors in the sensor-to-segment calibration.

Building on this method, we introduce a window-based magnetometer-free method for real-time motion tracking in 1-DoF and 2-DoF joints. This method exploits two different orientation-based constraints to determine the relative heading by window-based online optimization. In contrast to previous approaches, the proposed method requires neither an initial-pose calibration nor sensor-to-joint position parameters, its long-time stability is validated experimentally in human finger joints and mechanical joints, and its advantage over a conventional magnetometer-free method is demonstrated.

5.2 State of the Art in Magnetometer-Free Motion Tracking

While some motion parameters can be derived without heading information and thus without magnetometers [139], many applications require knowledge of the relative orientation between body segments. When magnetometers are not available or deliberately not used due to disturbances, the missing heading information has to be directly or indirectly estimated by other means. In practice, this is often achieved by asking the subject to initially or periodically assume a known pose [117, 138]. To facilitate non-restrictive long-term stable measurement, various approaches can be used to automatically estimate the missing heading information from joint constraints.

Ample research exists on exploiting the fact that two adjacent segments of a kinematic chain are connected at the joint center of rotation. This connection constraint can be formulated based on the joint center's position, velocity, or acceleration. The three formulations are mathematically equivalent with regard to observability [140].

Kok et al. [141] use the position-based connection constraint in an optimization-based smoothing approach that also allows for additional hinge joint constraints. This method requires prior knowledge about segment lengths and the positions of the IMUs with respect to the joint center. Taetz et al. [130] extend this method by a real-time capable sliding-window approach and simultaneously estimate joint center positions. For an EKF-based approach using the position-based connection constraint, Teufl et al. [142] evaluate lower extremity motion tracking during walking and report joint angle errors of 2.4° with respect to optical markers attached to the IMUs. The position-based formulation of the connection constraint was recently exploited via factor graph optimization [126, 127], and it was demonstrated that EKF-based tracking of a kinematic chain with the connection constraint can be combined with magnetometer measurements from a single IMU to achieve 9D motion tracking of the whole kinematic chain [143].

Wenk et al. [144] employ a velocity-based formulation of the connection constraint as part of the measurement model of an EKF.

Fasel et al. [145] propose a method that expresses the joint center acceleration in the reference frames of both segments and derives a correction quaternion to align those reference frames. Similarly, the approaches based on two cascaded Kalman filters proposed in [146, 147, 148] first estimate the 6D orientation and then exploit the acceleration-based connection constraint to correct the estimates. In contrast, the optimization-based smoothing approach and the EKF-based filtering approach proposed by Weygers et al. [149] tightly couple IOE and the connection constraint to estimate relative orientations, without assuming that the accelerometer measurements are dominated by gravity. For a robotic joint and with the smoothing method, an RMSE of 0.9° is achieved. For the knee joint and with respect to optical markers attached to the IMUs, the reported errors are 1.9° to 3.7° for the smoothing method and 2.4° to 4.5° for the filtering method. Remmerswaal et al. [150] propose a computationally efficient method to exploit the acceleration-based connection constraint with a complementary filter.

While the connection constraint has the advantage that it can potentially be applied to any joint type, knowledge of the joint center positions is required, either as prior knowledge or by estimation methods such as [99]. The observability analysis by Kok et al. [140] shows that, with perfect measurements, the relative heading is almost always observable via the connection constraint. In practice, soft tissue motion and measurement errors play a large role, and information about the heading offset is contained in the horizontal components of the joint center acceleration, which is often small compared to gravity. Thus, it is not surprising that validation of existing work is commonly performed either with mechanical or robotic joints [144, 146, 147, 148] or on walking [141, 142, 149] or other high-excitation motions [130, 145, 150] of the lower body. To the best of the author's knowledge, there are no validation results of the connection constraint for upper body or finger motions.

A promising alternative is to exploit kinematic constraints resulting from the limited degrees of freedom or range of motion of many joints (cf. Chapter 4). For the knee joint as an approximate hinge joint, it was shown that the flexion angle can be calculated from orientations with uncertain heading [151] or directly from accelerometer and gyroscope measurements via a complementary filter, skipping the estimation of orientations [94]. Vitali et al. [152] propose a method for knee angle estimation that transforms the hinge joint axis into global coordinates and then calculates a correction quaternion. In contrast to the methods introduced in this chapter, the correction is not restricted to a rotation around the vertical axis, and violations of the joint constraint can therefore affect the inclination as well as the heading. Kortier et al. [153] propose a method to estimate hand kinematics that integrates 1-DoF and 2-DoF joint constraints in the measurement model of an EKF. Luinge et al. [115] propose a least-squares filter for 2-DoF elbow angle measurement that constrains the carrying angle to zero. Caruso et al. [154] introduce an optimization-based approach to determine orientations that agree with a kinematic model of the upper limb while matching the IOE orientations as closely as possible. For 3-DoF joints, the fact that most joints have a limited range of motion can be exploited to recover heading information [155, 156]. In [157], it has been shown that the methods presented in this chapter can be generalized for arbitrary joints with range-of-motion constraints. Finally, Butt et al. [110] demonstrated that full body tracking with a sparse 6-IMU setup can be achieved via deep learning and using the pitch and roll angles of the IMU orientations as input.

The existing approaches for magnetometer-free motion tracking often tightly couple IOE and heading tracking. As a result, errors in the joint model can potentially influence the inclination estimates, and errors from 6D IOE and from heading tracking are hard to separate. The present chapter presents a modular approach that builds upon the 6D IOE method introduced in Chapter 3 and limits the estimation to the heading offset angle.

5.3 Method for Heading Tracking of Hinge Joints

Consider a hinge joint with one IMU on each segment, as illustrated in Figure 5.2. The joint moves freely in three-dimensional space. Each IMU performs 9D sensor fusion to determine its orientation with respect to a fixed inertial frame. Furthermore, assume that the sensor-to-segment orientations have been identified, e.g., from arbitrary joint motions using the methods in [99]. Thus, we are given two quaternions ${}^{\mathcal{B}_1}_{\mathcal{E}}\mathbf{q}(t)$ and ${}^{\mathcal{B}_2}_{\mathcal{E}}\mathbf{q}(t)$ that describe the orientations of the two body segments $\mathcal{B}_1$ and $\mathcal{B}_2$ relative to a common fixed inertial frame $\mathcal{E}$.

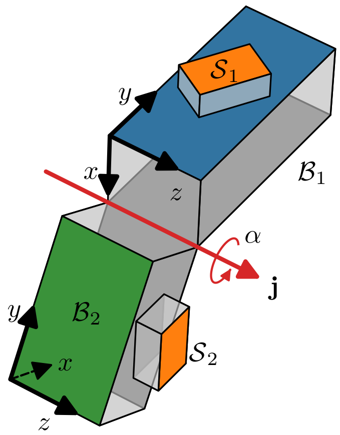

Figure 5.2: Kinematic model of a hinge joint with the joint axis $\mathbf{j}$ (red) and coordinate systems of segments $\mathcal{B}_1$ and $\mathcal{B}_2$ (black axes). The coordinate systems of IMUs $\mathcal{S}_1$ and $\mathcal{S}_2$ do not have to be aligned with the segment coordinate systems. The relative orientation between $\mathcal{B}_1$ and $\mathcal{B}_2$ is a rotation of the joint angle α around the joint axis $\mathbf{j}$.

Denote the coordinates of the hinge joint axis in the coordinate system of $\mathcal{B}_1$ by $\mathbf{j}_1$ and the coordinates of the hinge joint axis in the coordinate system of $\mathcal{B}_2$ by $\mathbf{j}_2$. Note that $\mathbf{j}_1$ and $\mathbf{j}_2$ do not change when the joint moves. Furthermore, transformed into the fixed inertial frame $\mathcal{E}$, $\mathbf{j}_1$ and $\mathbf{j}_2$ have the same coordinates, i.e.,

$$^{\mathcal{B}_1}_{\mathcal{E}}\mathbf{q}(t) \otimes \mathbf{j}_1 \otimes {}^{\mathcal{B}_1}_{\mathcal{E}}\mathbf{q}(t)^{-1} = {}^{\mathcal{B}_2}_{\mathcal{E}}\mathbf{q}(t) \otimes \mathbf{j}_2 \otimes {}^{\mathcal{B}_2}_{\mathcal{E}}\mathbf{q}(t)^{-1} \tag{5.1}$$

holds for all times t.

However, the estimates of the sensor orientations ${}^{\mathcal{B}_1}_{\mathcal{E}}\mathbf{q}$ and ${}^{\mathcal{B}_2}_{\mathcal{E}}\mathbf{q}$ are only accurate if the magnetic field is homogeneous. When magnetic disturbances occur, the IMU can no longer determine its true orientation since accelerometer and magnetometer readings are required to compensate integration drift effects that are due to gyroscope bias. When the sensor fusion algorithm of an IMU uses disturbed magnetometer data, then the inclination and the heading portion of the orientation are typically affected. However, it was demonstrated recently that sensor fusion can be carried out in a way that assures accurate inclination even in severely disturbed magnetic fields, e.g., in [76], which is also the case for the VQF algorithm introduced in Chapter 3.

We assume that such an algorithm is employed, and therefore only the heading portions of the estimated segment orientations become inaccurate. Due to these heading errors, the measured segment orientations ${}^{\mathcal{B}_1}_{\mathcal{E}_1}\mathbf{q}$ and ${}^{\mathcal{B}_2}_{\mathcal{E}_2}\mathbf{q}$ no longer describe the orientation of the segments with respect to a common fixed frame but with respect to two reference frames $\mathcal{E}_1$ and $\mathcal{E}_2$. With respect to the common ENU reference frame $\mathcal{E}$, those reference frames are shifted by a rotation around the vertical z-axis (by the angles δ_1 and δ_2, respectively):

$$^{\mathcal{B}_1}_{\mathcal{E}}\mathbf{q} = {}^{\mathcal{E}_1}_{\mathcal{E}}\mathbf{q} \otimes {}^{\mathcal{B}_1}_{\mathcal{E}_1}\mathbf{q} = (\delta_1 \,@\, [\,0 \;\; 0 \;\; 1\,]^\intercal) \otimes {}^{\mathcal{B}_1}_{\mathcal{E}_1}\mathbf{q}, \tag{5.2}$$

$$^{\mathcal{B}_2}_{\mathcal{E}}\mathbf{q} = {}^{\mathcal{E}_2}_{\mathcal{E}}\mathbf{q} \otimes {}^{\mathcal{B}_2}_{\mathcal{E}_2}\mathbf{q} = (\delta_2 \,@\, [\,0 \;\; 0 \;\; 1\,]^\intercal) \otimes {}^{\mathcal{B}_2}_{\mathcal{E}_2}\mathbf{q}. \tag{5.3}$$

In the unrealistic case that both orientation estimates are affected in exactly the same way, $\mathcal{E}_1$ and $\mathcal{E}_2$ coincide. In general, however, the relative orientation ${}^{\mathcal{B}_2}_{\mathcal{B}_1}\mathbf{q} = {}^{\mathcal{B}_1}_{\mathcal{E}}\mathbf{q}^{-1} \otimes {}^{\mathcal{B}_2}_{\mathcal{E}}\mathbf{q}$ between the first and second segment can only be calculated if the rotation between $\mathcal{E}_1$ and $\mathcal{E}_2$ is known:

$$\begin{aligned} {}^{\mathcal{B}_2}_{\mathcal{B}_1}\mathbf{q} &= ({}^{\mathcal{E}_1}_{\mathcal{E}}\mathbf{q} \otimes {}^{\mathcal{B}_1}_{\mathcal{E}_1}\mathbf{q})^{-1} \otimes {}^{\mathcal{E}_2}_{\mathcal{E}}\mathbf{q} \otimes {}^{\mathcal{B}_2}_{\mathcal{E}_2}\mathbf{q} \\ &= {}^{\mathcal{B}_1}_{\mathcal{E}_1}\mathbf{q}^{-1} \otimes \underbrace{{}^{\mathcal{E}_1}_{\mathcal{E}}\mathbf{q}^{-1} \otimes {}^{\mathcal{E}_2}_{\mathcal{E}}\mathbf{q}}_{=:\ {}^{\mathcal{E}_2}_{\mathcal{E}_1}\mathbf{q}} \otimes {}^{\mathcal{B}_2}_{\mathcal{E}_2}\mathbf{q}, \end{aligned} \tag{5.4}$$

where ${}^{\mathcal{E}_2}_{\mathcal{E}_1}\mathbf{q}$ represents the combined effect of both disturbances and corresponds to a rotation around the global z-axis:

$${}^{\mathcal{E}_2}_{\mathcal{E}_1}\mathbf{q} = (\delta \,@\, [0\ \ 0\ \ 1]^\intercal) = \left[\cos\left(\tfrac{\delta}{2}\right) \quad 0 \quad 0 \quad \sin\left(\tfrac{\delta}{2}\right)\right]^\intercal, \tag{5.5}$$

with $\delta(t) = \delta_2(t) - \delta_1(t)$ being the heading offset of ${}^{\mathcal{B}_2}_{\mathcal{B}_1}\mathbf{q}$ that is caused by the magnetic disturbance. In order to determine the correct relative orientation ${}^{\mathcal{B}_2}_{\mathcal{B}_1}\mathbf{q}$ and then calculate accurate joint angles, the heading offset $\delta(t)$ must be determined.

In addition to 9D IOE, the introduced method can also be used in combination with 6D IOE. In 6D IOE, i.e., when magnetometer readings are not used, we observe a similar situation: As detailed in Section 3.6, the magnetometer-free orientation estimates are provided in sensor-specific almost-inertial reference frames that differ from the common ENU reference frame $\mathcal{E}$ by a slowly drifting heading offset. Mathematically, we can describe this in the same way with orientation estimates ${}^{\mathcal{B}_1}_{\mathcal{E}_1}\mathbf{q}$ and ${}^{\mathcal{B}_2}_{\mathcal{E}_2}\mathbf{q}$, the heading offsets $\delta_1(t)$ and $\delta_2(t)$ with respect to the ENU frame, and the relative heading offset $\delta(t)$. Compared to the heading offset due to magnetic disturbances, the heading offset found in 6D sensor fusion differs in two ways:

1. In 9D sensor fusion, the heading offset is small if the magnetic field is homogeneous and the maximum value is limited by the severity of the magnetic disturbances. In 6D sensor fusion, the heading offset has an arbitrary value that depends on the initial conditions of the orientation estimation algorithm.

2. In 9D sensor fusion, the heading offset may change rapidly when magnetic disturbances occur. In 6D sensor fusion, the heading offset drifts slowly, and the rate of change is limited by the typical values of gyroscope bias (i.e., $\leq 1\,°/\mathrm{s}$).

5.3.1 Determining the Heading Offset

We determine the heading offset $\delta(t)$ as follows. First, we transform the coordinates of the local joint axis vectors of both segments into their respective reference frames:

$$[\mathbf{j}_1]_{\mathcal{E}_1} = {}^{\mathcal{B}_1}_{\mathcal{E}_1}\mathbf{q} \otimes \mathbf{j}_1 \otimes {}^{\mathcal{B}_1}_{\mathcal{E}_1}\mathbf{q}^{-1} =: [\, j_{1x}\ \ j_{1y}\ \ j_{1z}\,]^\intercal, \tag{5.6}$$

$$[\mathbf{j}_2]_{\mathcal{E}_2} = {}^{\mathcal{B}_2}_{\mathcal{E}_2}\mathbf{q} \otimes \mathbf{j}_2 \otimes {}^{\mathcal{B}_2}_{\mathcal{E}_2}\mathbf{q}^{-1} =: [\, j_{2x}\ \ j_{2y}\ \ j_{2z}\,]^\intercal. \tag{5.7}$$

According to the joint constraint (5.1), $[\mathbf{j}_1]_{\mathcal{E}_1}$ and $[\mathbf{j}_2]_{\mathcal{E}_2}$ should have the same coordinates. Due to magnetic disturbances and other errors, the measured values will deviate in practice. Since we know that ${}^{\mathcal{E}_2}_{\mathcal{E}_1}\mathbf{q}$ is a rotation around the z-axis, we project those vectors in the x-y-plane, i.e., we set j_{1z} and j_{2z} to zero. Then, the heading offset δ is given by the difference of the

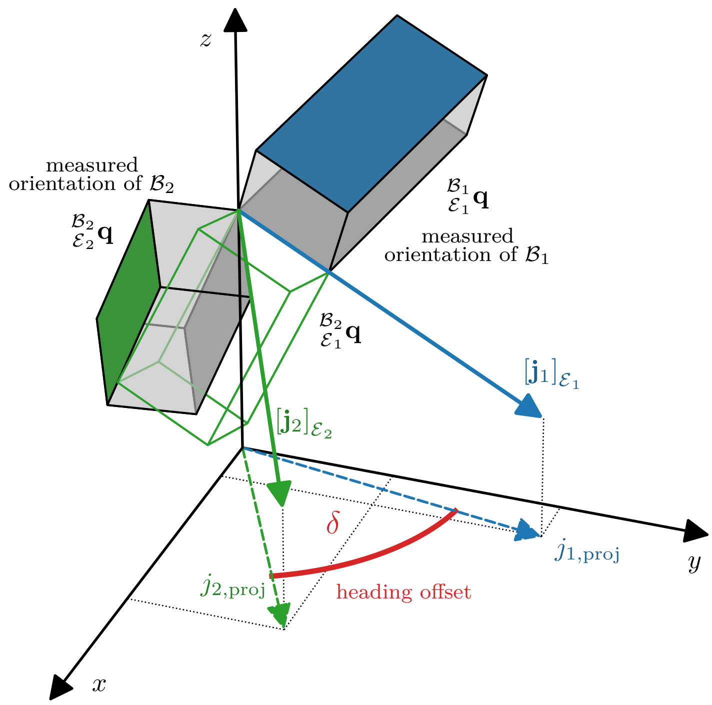

Figure 5.3: Two segments $\mathcal{B}_1$ and $\mathcal{B}_2$ are connected by a hinge joint. Due to magnetic disturbances, the measured orientations are subject to the heading offset δ. This heading offset can be obtained from the projections of the joint axes into the global x-y-plane.

angles of the projected vectors in the x-y-plane, i.e.,

$$\delta = \operatorname{atan2}(j_{2y},\, j_{2x}) - \operatorname{atan2}(j_{1y},\, j_{1x})\,. \tag{5.8}$$

See Figure 5.3 for a graphical illustration of this approach.

5.3.2 Heading Correction and Joint Angle Calculation

From $\delta(t)$, we calculate ${}^{\mathcal{E}_2}_{\mathcal{E}_1}\mathbf{q}(t)$ and obtain segment orientations in a common reference frame[1], e.g., by

$${}^{\mathcal{B}_2}_{\mathcal{E}_1}\mathbf{q} = {}^{\mathcal{E}_2}_{\mathcal{E}_1}\mathbf{q} \otimes {}^{\mathcal{B}_2}_{\mathcal{E}_2}\mathbf{q}. \tag{5.9}$$

This allows us to obtain the relative orientation of one segment with respect to the other, i.e., the joint orientation

$${}^{\mathcal{B}_2}_{\mathcal{B}_1}\mathbf{q} = {}^{\mathcal{B}_1}_{\mathcal{E}_1}\mathbf{q}^{-1} \otimes {}^{\mathcal{B}_2}_{\mathcal{E}_1}\mathbf{q} =: [\, q_w \;\; q_x \;\; q_y \;\; q_z \,]^\intercal. \tag{5.10}$$

We then calculate the joint angle from the joint orientation quaternion. Without loss of generality, we define the segment coordinate systems so that the joint axis is the local z-axis, i.e., $\mathbf{j}_1 = \mathbf{j}_2 = [\,0 \;\; 0 \;\; 1\,]^\intercal$.

The most commonly used approach is to calculate Euler angles and discard the two angles that are assumed to be zero. Using z-x'-y'' Euler angles, as recommended by the ISB for the interphalangeal finger joints [47], the angle around the z-axis can be obtained from ${}^{\mathcal{B}_2}_{\mathcal{B}_1}\mathbf{q}$ as

$$\alpha = \operatorname{atan2}(2q_zq_w - 2q_yq_x,\; q_w^2 + q_y^2 - q_x^2 - q_z^2). \tag{5.11}$$

[1]Note that any common reference frame will work, i.e., instead of adjusting the orientation of $\mathcal{B}_2$, we can also bring the orientation of $\mathcal{B}_1$ to $\mathcal{E}_2$.

The drawback of this approach is that the arbitrary choice of a rotation axis sequence will have an influence on the joint angle. In practice, when there is almost no rotation around the x and y-axes, the effect will be small, but using z-y'-x'' Euler angles and discarding the last two angles will yield a slightly different joint angle than using z-x'-y'' Euler angles.

To avoid this effect, we use an alternative joint angle calculation method. Using the quaternion projection method introduced in Section 2.4, we split the joint orientation into a rotation around the z-axis and a residual quaternion, i.e.,

$$^{\mathcal{B}_2}_{\mathcal{B}_1}\mathbf{q} = \begin{bmatrix}\cos\left(\frac{\alpha}{2}\right) & 0 & 0 & \sin\left(\frac{\alpha}{2}\right)\end{bmatrix}^\intercal \otimes \mathbf{q}_{\text{res}}. \tag{5.12}$$

Then, the joint angle α that minimizes the rotation angle of the residual quaternion $\mathbf{q}_{\text{res}}$ is given by

$$\alpha = 2\,\mathrm{atan2}(q_z,\, q_w). \tag{5.13}$$

5.3.3 Singularity Treatment

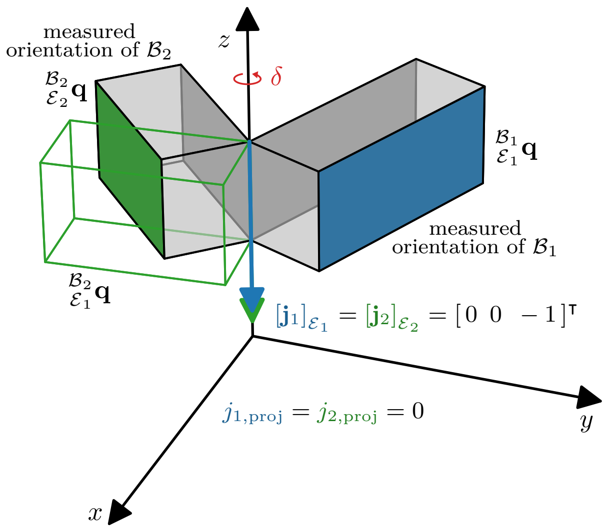

Figure 5.4: When the two segments $\mathcal{B}_1$ and $\mathcal{B}_2$ are oriented so that the joint axis is vertical, it is impossible to differentiate between joint rotation and changes in the heading offset δ. When this happens, the horizontal projections of the joint axes are zero.

When the segments are oriented so that the joint axis is vertical, it is impossible to differentiate between joint rotation and heading offsets induced by magnetic disturbances or integration drift, as illustrated in Figure 5.4. In this case, the kinematic constraint becomes useless, and δ cannot be calculated since the horizontal projections of the joint axes become zero.

To suppress the correction during time periods with vertical joint axis, we design a filter that gives small trust to new values of the heading offset $\delta(t)$ when the joint axis is almost vertical and large trust when being far from this singularity.

Assume that $\delta(t_k)$ is calculated according to (5.8) at a fixed sampling rate $f_\text{s} = T_\text{s}^{-1}$, sampled at times $t_k = kT_\text{s}, k \in \{1, 2, \ldots, N\}, T_\text{s} \in \mathbb{R}_{>0}$.

At each sampling instant, we determine the Euclidean norms of the horizontal projections of the joint axes (dashed arrows in Figure 5.3) and use their product as the trust rating[2]

$$r(t_k) := j_{1,\mathrm{proj}} j_{2,\mathrm{proj}}, \tag{5.14}$$

with $j_{1,\mathrm{proj}} := \|[\, j_{1x}(t_k) \;\; j_{1y}(t_k)\,]^\intercal\|$ and $j_{2,\mathrm{proj}} := \|[\, j_{2x}(t_k) \;\; j_{2y}(t_k)\,]^\intercal\|$.

The filtered heading offset $\delta_\mathrm{f}(t_k)$ is obtained with an extended version of an exponential weighted moving average, starting with $\delta_\mathrm{f}(t_0) = \delta_0$:

$$\delta_\mathrm{f}(t_k) = \delta_\mathrm{f}(t_{k-1}) + r(t_k) \left(1 - \exp\left(-\frac{T_\mathrm{s}}{\tau_\delta}\right)\right) \mathrm{clip}(\delta(t_k) - \delta_\mathrm{f}(t_{k-1})), \tag{5.15}$$

with the time constant $\tau_\delta = 0.05\,\mathrm{s}$. The clip function

$$\mathrm{clip}(\delta) := \begin{cases} -0.2 & \delta \leq -0.2, \\ 0.2 & \delta \geq 0.2, \\ \delta & \text{else} \end{cases} \tag{5.16}$$

limits the angle difference to $\pm 0.2\,\mathrm{rad}$ and therefore restrains the filter from following quick changes, which may occur close to the singularity.

5.3.4 Optimality of the Constraint

The geometric approach of extracting the heading offset $\delta(t)$ from the horizontal joint axis projections, as described in Section 5.3.1, is intuitive and easy to implement. When considering an ideal hinge joint with perfect inclination estimates, it is easy to see that this method provides the correct result, as illustrated in Figure 5.3. However, it is not immediately clear in which sense the solution is ideal in case of additional errors, e.g., if the joint is not a perfect hinge joint or if the inclination of the orientation estimates is wrong.

Therefore, we now consider an alternative approach based on the quaternion projection method introduced in Section 2.4. We decompose the joint orientation into a rotation around the joint axis $\mathbf{q_j} = (\alpha \,@\, \mathbf{j})$ and residual quaternion $\mathbf{q}_\mathrm{res}$:

$$^{\mathcal{B}_2}_{\mathcal{B}_1}\mathbf{q} = {^{\mathcal{B}_1}_{\mathcal{E}_1}\mathbf{q}}^{-1} \otimes {^{\mathcal{E}_2}_{\mathcal{E}_1}\mathbf{q}} \otimes {^{\mathcal{B}_2}_{\mathcal{E}_2}\mathbf{q}} = \mathbf{q_j} \otimes \mathbf{q}_\mathrm{res}. \tag{5.17}$$

Minimizing the absolute rotation angle of the residual quaternion

$$\mathbf{q}_\mathrm{res}(\alpha, \delta) = (\alpha \,@\, \mathbf{j})^{-1} \otimes {^{\mathcal{B}_1}_{\mathcal{E}_1}\mathbf{q}}^{-1} \otimes {^{\mathcal{E}_2}_{\mathcal{E}_1}\mathbf{q}}(\delta) \otimes {^{\mathcal{B}_2}_{\mathcal{E}_2}\mathbf{q}} \tag{5.18}$$

leads to a unique combination of joint angle α and heading offset δ (except at singularities). Numerical simulations show that the obtained heading offsets are exactly the same as for the geometric approach. Therefore, this approach does not provide a new method but demonstrates in which sense the solution provided by the geometric approach is ideal.

[2] In contrast to [135], we now use the product of the two axis norms instead of the minimum. This change does not affect the conclusions drawn from the evaluation but improves consistency with the methods introduced later in this chapter.

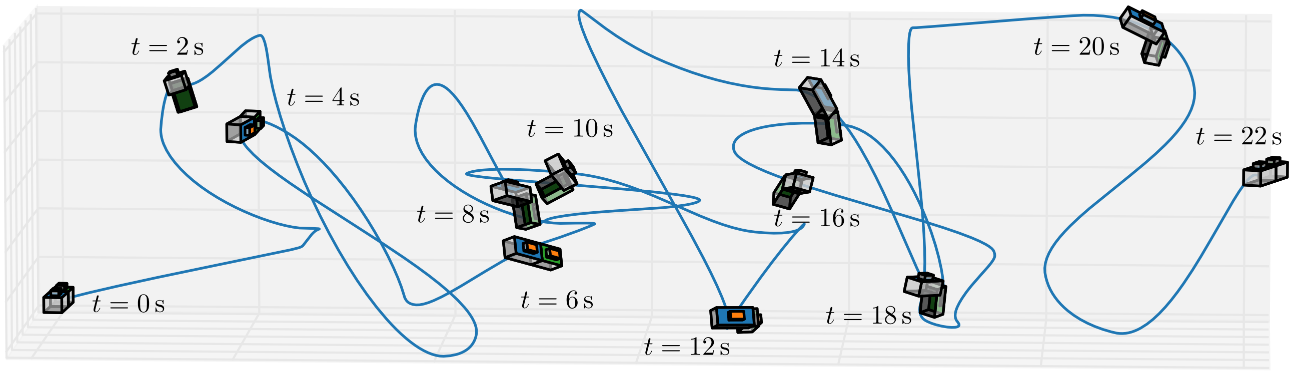

Figure 5.5: 3D visualization of the reference movement. The motion is designed to mimic a fast three-dimensional finger motion, with repeated phases in which the joint axis is almost vertical.

5.4 Validation by Simulation Study

To evaluate the proposed method, we perform a validation study in which we simulate an approximate hinge joint that moves through an experimentally determined inhomogeneous magnetic field. Unlike an experimental evaluation with optical motion capture as reference, this approach has the advantage of perfect repeatability and perfectly known reference values (i.e., without measurement errors of a reference system). Furthermore, it allows us to investigate the effect of an imprecise sensor-to-segment calibration and of the joint not being a perfect hinge joint.

5.4.1 Simulation

We simulate the motion of two segments, each with an IMU attached centrally and both connected by an approximate hinge joint. The motion and segment sizes are chosen to mimic a fast three-dimensional motion of an interphalangeal finger joint with a duration of 22 s. To obtain a challenging example, the movement is chosen to excite all translatory and rotational degrees of freedom and to avoid any periods of translational or rotational rest.

In light of the discussion of the singularity of the joint constraint in Section 5.3.3, we choose the motion such that the inclination of the joint axis is close to 90°, i.e., vertical, for several time periods throughout the course of the motion. See Figure 5.5 for an illustration of the movement.

The simulation consists of the following steps (cf. Figure 5.6):

1. We generate IMU raw measurement data (angular rate, acceleration, and magnetic field) at $f_\mathrm{s} = 100\,\mathrm{Hz}$ using a realistic measurement model that includes noise on all measurements and a randomized time-variant bias for the gyroscope.

2. We estimate the segment orientation using the BasicVQF algorithm described in Chapter 3.

3. We calculate joint angles, once without and once with the proposed heading correction.

Three scenarios are considered. The undisturbed scenario is based on a perfectly homogeneous magnetic field. In addition to this unrealistic case, we consider a magnetic

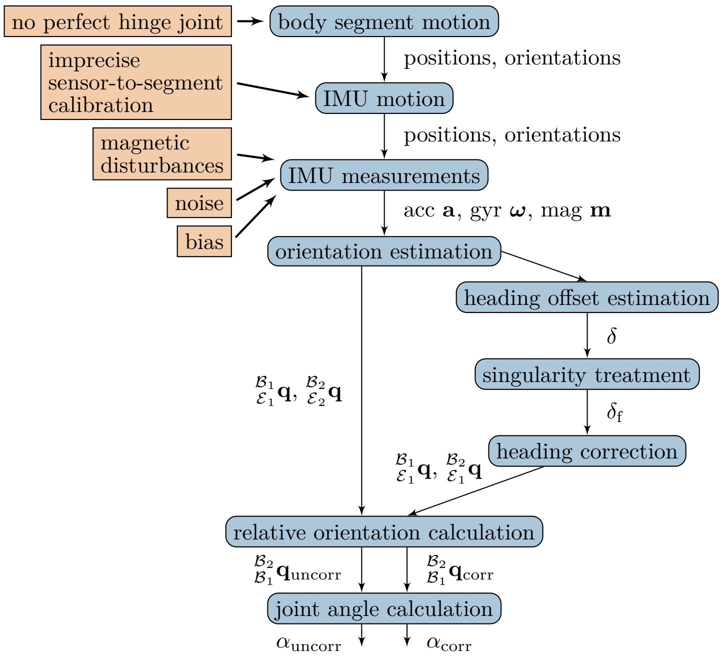

Figure 5.6: Overview of the data processing steps and the error sources considered in the simulation study. Simulated IMU measurements with various errors and disturbances are generated, and joint angles are calculated with and without the proposed heading correction method.

disturbance that was determined experimentally by moving an IMU in the proximity of ferromagnetic metal plates. A marker-based optical motion capture system was used as a reference to allow extraction of the disturbance from the magnetometer readings. Under the influence of the disturbance, both the dip angle and the heading of the magnetic field vector varied by about 100°. As a third scenario, we do not make use of the magnetometer measurements at all and use the 6D orientation estimates provided by BasicVQF. Note that in this scenario, estimating the heading offset is necessary for the calculation of the joint orientation, and we therefore cannot calculate joint angles without heading correction.

5.4.2 Segment and Motion Dimensions

To ensure that the results are not limited to the case of small body segments, we repeat all simulations for segment dimensions and movement space dimensions that are ten times larger than the initially used finger segment dimensions. The segment lengths are increased from about 4 cm to about 40 cm, and the horizontal distance traveled is increased from about 1 m to about 10 m, which leads to much larger accelerations. Thereby, the simulated motion is changed to resemble a quick acrobatic motion of a human knee.

5.4.3 Results

We perform the described simulation with and without the magnetic disturbance and calculate joint angles with and without the proposed correction. To account for noise, we perform 100 simulation runs for each case. First, consider a perfect sensor-to-segment calibration and a perfect hinge joint. For this case, the obtained RMSE values are given in Table 5.1.

When the magnetic field disturbance is not applied to the simulated magnetometer measurements, the obtained joint angle estimates are found to have an RMSE of about

Table 5.1: RMSE (mean and standard deviation) for different parameter combinations

	9D, homogeneous	9D, disturbed	6D, magnetometer-free
Correction off	0.57° ± 0.18°	21.60° ± 0.22°	
Correction on	0.55° ± 0.21°	1.59° ± 0.15°	0.56° ± 0.22°

0.6°. This result is in the same range as accuracies reported for similar experimental studies [94] and thus verifies that the IMU measurement model is sufficiently realistic.

Comparing "Correction on/off" without the simulated disturbance shows that the heading correction does not increase the error. However, enabling the simulated magnetic disturbance leads to large errors in the uncorrected joint angles. With the proposed heading correction method, the errors slightly increase compared to the undisturbed scenario but are clearly lower than without correction.

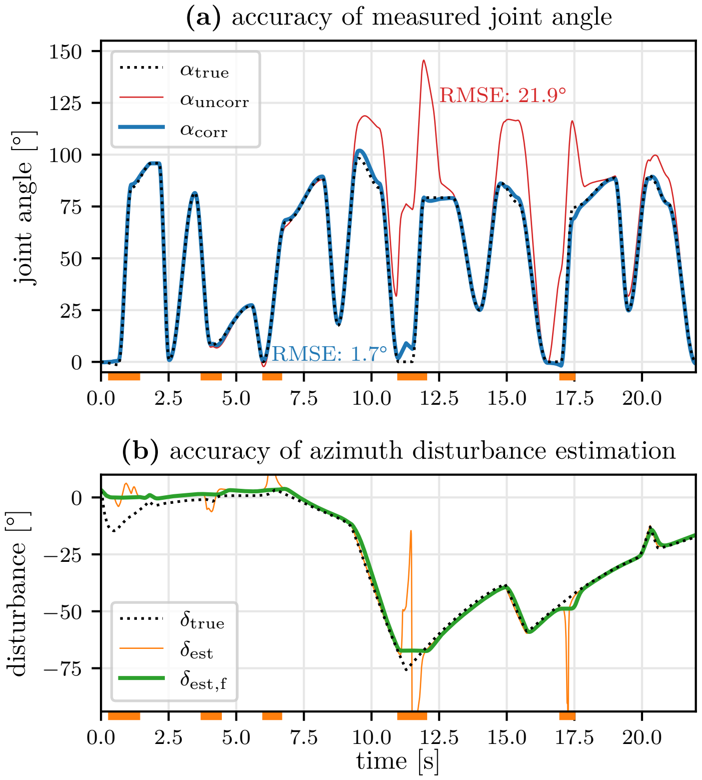

Figure 5.7: Joint angles and heading offsets for a simulation with a strong magnetic disturbance. **(a)** True (α_{true}), uncorrected (α_{uncorr}), and corrected (α_{corr}) joint angle. **(b)** True (δ_{true}), unfiltered (δ_{est}), and filtered ($\delta_{\mathrm{est,f}}$) estimated heading offset. Orange bars mark time periods in which the joint axis is near vertical ($< 10°$). The heading filter increases accuracy, especially when the joint axis is near vertical, and the corrected joint angles exhibit much smaller errors than the uncorrected joint angles.

For the numbers highlighted in Table 5.1, which indicate the errors with enabled magnetic disturbance, one typical corresponding angle-over-time plot is given in Figure 5.7. This figure also shows the estimated heading offset before (δ_{est}) and after ($\delta_{\mathrm{est,f}}$) filtering, as well as the true value δ_{true}.

The magnetic disturbance causes a heading offset of up to 90° in the estimated orientations, which leads to very large errors in the uncorrected joint angles (21.9° RMSE). The joint axis is almost vertical during five time periods (marked by orange bars), including sampling instants in which it is perfectly vertical. During those periods, the estimated heading offset δ_{est} fluctuates notably. The filter limits the deviation due to the singularity while tracking the calculated heading offset closely at other times. With the filtered heading offset, we obtain joint angles with a considerably lower error (1.7° RMSE) compared to the uncorrected angles (21.9° RMSE).

The magnetometer-free method is able to provide joint angles with the same accuracy as the 9D methods but, as magnetometer measurements are not used, is not affected by magnetic disturbances at all. Since the proposed method does not make assumptions that the heading offset $\delta(t)$ is typically small (when the magnetic field is homogeneous), employing magnetometer measurements does not provide any benefits. In contrast, the fast-changing offset due to the strong magnetic disturbance is detrimental to the performance of the heading filter (5.15). With 6D orientation estimates, the cutoff frequencies of this filter could be lowered to exploit the fact that the rate of change of the heading offset $\delta(t)$ is limited, making the estimation even more robust. When possible, the magnetometer-free approach should therefore be preferred.

5.4.4 Sensitivity to Joint and Attachment Errors

We now investigate how sensitive the heading-corrected angles are when we simulate an error in the IMU attachment and allow for small joint rotations around other axes.

Sensor-to-segment error In practice, the accuracy of the sensor-to-segment calibration may vary depending on the employed calibration method. With the parameter E_{S}, we model the fact that the sensor-to-segment orientations are not precisely known, for example, due to inaccurate anatomical calibration or because the sensors slipped after the calibration. We consider a large number of different combinations of possible sensor-to-segment errors, for each of which both sensor orientations are rotated by random angles around random axes. To quantify the overall magnitude of the modeled error, denote the absolute sum of the two rotation angles by E_{S}.

Joint constraint violation Biological joints, such as the knee joint or the interphalangeal joints, are only approximate hinge joints and allow for small rotations around other axes. Therefore, we introduce additional rotations around the second and third axis[3] of the joint. Both angles are modeled as sinusoids with random amplitude and phase. To quantify the overall magnitude of the modeled error, denote the absolute sum of both amplitudes by E_{J}.

Again, for each parameter value, 100 simulation runs with the simulated magnetic disturbance are evaluated. The results are shown in Figure 5.8. On average, an additional error of $E_{\text{S}} = 5.0°$ in the sensor-to-segment orientation raises the RMSE from 1.6° to 3.4°. Likewise, the RMSE increases from 1.6° to 2.4° when we relax the hinge joint assumption and allow for rotations around the second and third joint axis with an amplitude sum of $E_{\text{J}} = 5.0°$.

[3]Without loss of generality, we model the joint orientation using z-x'-y'' Euler angles as recommended for finger joints by the ISB [47].

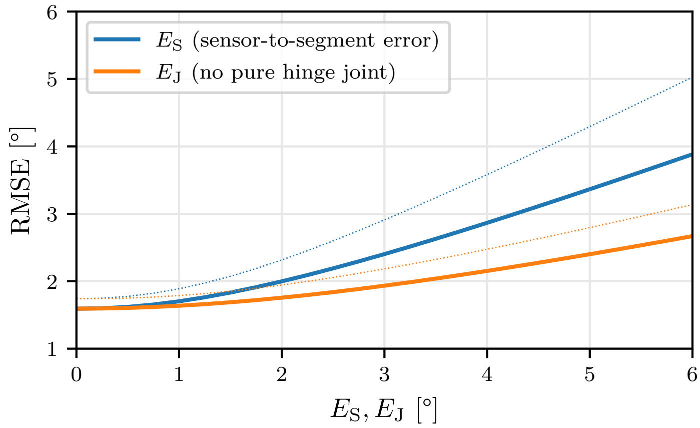

Figure 5.8: Sensitivity of the RMSE of the heading-corrected joint angles to errors in the IMU attachment E_S and joint rotations around other axes E_J. The dashed lines indicate mean + standard deviation. An IMU attachment error of 5.0° increases the joint angle error from 1.6° to 3.4°, and a hinge joint violation of 5.0° increases the joint angle error from 1.6° to 2.4°.

Note that the effect of the error depends on the axis, which is chosen randomly for both simulated errors. This explains that the standard deviation of the RMSE considerably increases when simulating joint rotation and sensor attachment errors.

Finally, comparing the simulation results for small (finger) and large (leg) motions did not yield any notable differences. The error with magnetic disturbance and heading correction slightly increased from 1.6° to 1.8°, but overall, the presented results are equally valid for both cases.

5.5 Window-Based Heading Tracking Method

In the following, we extend the method introduced in Section 5.3 to be suitable for 2-DoF joints in addition to hinge joints and to be more robust, especially for biological joints. This robustness is achieved by employing an approach based on moving windows and by improved handling of phases near singularities and phases without motion. Based on the findings of Section 5.4, we directly design the method to not make use of magnetometer measurements.

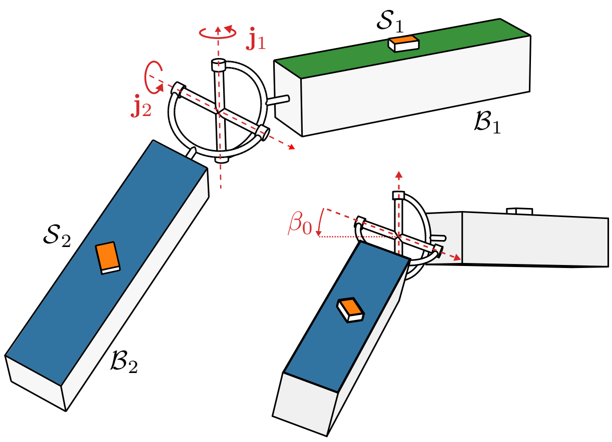

Figure 5.9: Kinematic model of a 2-DoF joint with segments $\mathcal{B}_1$, $\mathcal{B}_2$, joint axes $\mathbf{j}_1$, $\mathbf{j}_2$, and IMUs $\mathcal{S}_1$, $\mathcal{S}_2$. *Right:* View in the $\mathbf{j}_1$-$\mathbf{j}_2$-plane. The 2-DoF joint can be modeled as a kinematic chain of two hinge joints. The angle β_0 describes the deviation of the angle between $\mathbf{j}_1$ and $\mathbf{j}_2$ from 90°.

Two segments, $\mathcal{B}_1$ and $\mathcal{B}_2$, are connected by a hinge joint (Figure 5.2) or a joint with two degrees of freedom, which can be modeled as a kinematic chain of two hinge joints, as shown in Figure 5.9. Denote the joint axes as $\mathbf{j}_1, \mathbf{j}_2 \in \mathbb{R}^3$, with $\|\mathbf{j}_1\| = \|\mathbf{j}_2\| = 1$. The coordinates of $\mathbf{j}_1$ are fixed in frame $\mathcal{B}_1$, and the coordinates of $\mathbf{j}_2$ are fixed in frame $\mathcal{B}_2$. For hinge joints, we define the coordinate systems $\mathcal{B}_1$ and $\mathcal{B}_2$ so that $\mathbf{j}_1 = \mathbf{j}_2 = [0\ \ 0\ \ 1]^\intercal$ (cf. Section 5.3). Without loss of generality, for 2-DoF joints, we define the coordinate systems $\mathcal{B}_1$ and $\mathcal{B}_2$ such that $\mathbf{j}_1 = [0\ \ 0\ \ 1]^\intercal$ and $\mathbf{j}_2 = [0\ \ 1\ \ 0]^\intercal$.

For 2-DoF joints, the angle between $\mathbf{j}_1$ and $\mathbf{j}_2$ is fixed but not necessarily 90°. As shown in Figure 5.9, we use β_0 to denote the deviation of this angle from 90°.[4] This kinematic model is general enough to describe many different joints, such as saddle joints, Cardan joints, and the human wrist, elbow, or ankle joints (cf. Section 4.3).

Two IMUs, $\mathcal{S}_1$ and $\mathcal{S}_2$, are placed on the segments in known orientation, i.e., the orientations of the sensors w.r.t. the segments ${}^{\mathcal{S}_1}_{\mathcal{B}_1}\mathbf{q}$ and ${}^{\mathcal{S}_2}_{\mathcal{B}_2}\mathbf{q}$ are known. This can be achieved by precise attachment or by using the automatic sensor-to-segment calibration methods introduced in [95] or in Chapter 4. The sensors measure the angular rates $\boldsymbol{\omega}_1(t)$ and $\boldsymbol{\omega}_2(t)$ as well as the accelerations $\mathbf{a}_1(t)$ and $\mathbf{a}_2(t)$ in local coordinates, perform 6D sensor fusion, potentially on-chip and with the algorithm described in Chapter 3, and report their orientations, described by the quaternions ${}^{\mathcal{S}_1}_{\mathcal{E}_1}\mathbf{q}(t)$ and ${}^{\mathcal{S}_2}_{\mathcal{E}_2}\mathbf{q}(t)$. We can easily calculate the body segment orientations ${}^{\mathcal{B}_i}_{\mathcal{E}_i}\mathbf{q}(t) = {}^{\mathcal{S}_i}_{\mathcal{E}_i}\mathbf{q}(t) \otimes {}^{\mathcal{B}_i}_{\mathcal{S}_i}\mathbf{q}$, $i = 1, 2$.

Without the use of magnetometers, the absolute heading of each sensor is unknown, which can be described by the orientations being estimated in two different reference frames, $\mathcal{E}_1$ and $\mathcal{E}_2$. At each moment in time, the difference between the reference frames $\mathcal{E}_1$ and $\mathcal{E}_2$ is only a rotation around the vertical axis, which has the coordinates $[0\ \ 0\ \ 1]^\intercal$ in both $\mathcal{E}_1$ and $\mathcal{E}_2$. Let $\delta(t)$ be the angle of this rotation. Then the corresponding quaternion is

$$
{}^{\mathcal{E}_2}_{\mathcal{E}_1}\mathbf{q}(\delta) = (\delta\,@\,[0\ \ 0\ \ 1]^\intercal) = \left[\cos\left(\tfrac{\delta}{2}\right) \quad 0 \quad 0 \quad \sin\left(\tfrac{\delta}{2}\right)\right]^\intercal. \tag{5.19}
$$

In 6D sensor fusion, without a common reference for the heading, $\delta(t=0)$ is unknown. Even if $\delta(t=0)$ would be known, for example from a known initial calibration pose, this knowledge soon loses its value because $\delta(t)$ drifts slowly due to non-zero gyroscope bias in both IMUs.

5.5.1 Orientation-Based Kinematic Constraint for Hinge Joints

As detailed in Section 5.3, the joint axis of hinge joints must have the same coordinates when transformed into a common coordinate system, i.e.,

$$
\underbrace{{}^{\mathcal{B}_1}_{\mathcal{E}_1}\mathbf{q}(t) \otimes \mathbf{j}_1 \otimes {}^{\mathcal{B}_1}_{\mathcal{E}_1}\mathbf{q}(t)^{-1}}_{[\mathbf{j}_1]_{\mathcal{E}_1}} = \underbrace{{}^{\mathcal{B}_2}_{\mathcal{E}_1}\mathbf{q}(t) \otimes \mathbf{j}_2 \otimes {}^{\mathcal{B}_2}_{\mathcal{E}_1}\mathbf{q}(t)^{-1}}_{[\mathbf{j}_2]_{\mathcal{E}_1}}, \tag{5.20}
$$

and for each sampling instant, the heading offset can be calculated from the horizontal projection of the joint axes as

$$
\delta = \operatorname{atan2}(j_{2y}, j_{2x}) - \operatorname{atan2}(j_{1y}, j_{1x}), \tag{5.21}
$$

[4] For the elbow joint, this angle β_0 is commonly called *carrying angle* and is approximately 5–15°, see for example [47].

with $[\mathbf{j}_1]_{\mathcal{E}_1} =: [\, j_{1x} \;\; j_{1y} \;\; j_{1z} \,]^\intercal$ and $[\mathbf{j}_2]_{\mathcal{E}_2} =: [\, j_{2x} \;\; j_{2y} \;\; j_{2z} \,]^\intercal$.

This allows us to express (5.20) as a constraint that can be evaluated using the orientations ${}^{\mathcal{B}_1}_{\mathcal{E}_1}\mathbf{q}$ and ${}^{\mathcal{B}_2}_{\mathcal{E}_2}\mathbf{q}$ and an estimate of the heading offset $\hat{\delta}(t)$ as

$$\operatorname{atan2}(j_{2y}, j_{2x}) - \operatorname{atan2}(j_{1y}, j_{1x}) - \hat{\delta}(t) = 0. \tag{5.22}$$

5.5.2 Orientation-Based Kinematic Constraint for 2-DoF Joints

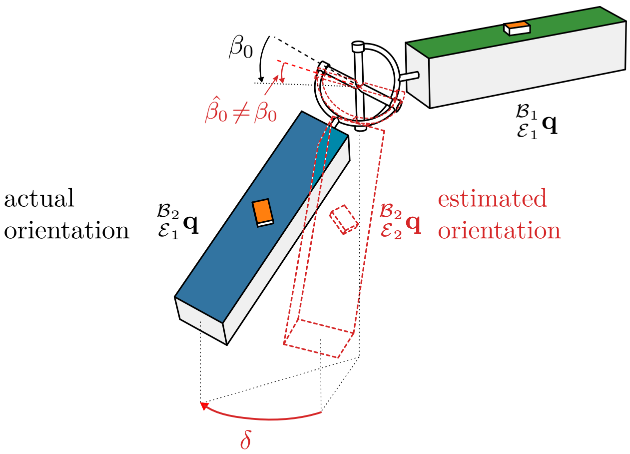

Figure 5.10: Orientations of segments $\mathcal{B}_1$ and $\mathcal{B}_2$. Calculating the relative orientation between ${}^{\mathcal{B}_1}_{\mathcal{E}_1}\mathbf{q}$ and ${}^{\mathcal{B}_2}_{\mathcal{E}_2}\mathbf{q}$ without accounting for the heading offset δ leads to a wrong joint orientation and wrong joint angles.

Calculating relative segment orientations and joint angles directly from ${}^{\mathcal{B}_1}_{\mathcal{E}_1}\mathbf{q}$ and ${}^{\mathcal{B}_2}_{\mathcal{E}_2}\mathbf{q}$ while ignoring the difference between $\mathcal{E}_1$ and $\mathcal{E}_2$ leads to false results, as illustrated in Figure 5.10. Instead, we must first determine an estimate $\hat{\delta}(t)$ of the heading offset $\delta(t)$ and use it to bring both body segment orientations into a common reference frame, i.e.,

$${}^{\mathcal{B}_2}_{\mathcal{B}_1}\mathbf{q} = {}^{\mathcal{B}_1}_{\mathcal{E}_1}\mathbf{q}^{-1} \otimes {}^{\mathcal{B}_2}_{\mathcal{E}_1}\mathbf{q} = {}^{\mathcal{B}_1}_{\mathcal{E}_1}\mathbf{q}^{-1} \otimes {}^{\mathcal{E}_2}_{\mathcal{E}_1}\mathbf{q}(\hat{\delta}(t)) \otimes {}^{\mathcal{B}_2}_{\mathcal{E}_2}\mathbf{q}. \tag{5.23}$$

Note that any estimate $\hat{\delta}(t)$ yields a relative orientation ${}^{\mathcal{B}_2}_{\mathcal{B}_1}\mathbf{q} =: [\, q_w \;\; q_x \;\; q_y \;\; q_z \,]^\intercal$. The intrinsic z-x'-y'' Euler angle decomposition of this relative orientation is

$$\hat{\alpha} = \operatorname{atan2}(2q_wq_z - 2q_xq_y,\, q_w^2 - q_x^2 + q_y^2 - q_z^2), \tag{5.24}$$

$$\hat{\beta}_0 = \arcsin(2q_wq_x + 2q_yq_z), \tag{5.25}$$

$$\hat{\gamma} = \operatorname{atan2}(2q_wq_y - 2q_xq_z,\, q_w^2 - q_x^2 - q_y^2 + q_z^2). \tag{5.26}$$

According to the definitions of $\mathcal{B}_1$ and $\mathcal{B}_2$ above, $\hat{\alpha}$ and $\hat{\gamma}$ are estimates of the joint angles, corresponding to rotations around $\mathbf{j}_1$ and $\mathbf{j}_2$, respectively, and the angle $\hat{\beta}_0$ corresponds to the fixed angle between $\mathbf{j}_1$ and $\mathbf{j}_2$. In general, a false $\hat{\delta}(t) \neq \delta(t)$ leads to a false $\hat{\beta}_0 \neq \beta_0$, cf. Figure 5.10. This deliberation leads to the orientation-based constraint

$$\arcsin(2q_wq_x + 2q_yq_z) - \beta_0 = 0, \tag{5.27}$$

which can be exploited to find the true heading offset $\delta(t)$ without using any magnetometer readings.

5.5.3 Singularity Detection

The kinematic constraints (5.22) and (5.27) become singular, i.e., yield no relative-heading information if the segment orientations are such that one of the joint axes is perfectly vertical. In such a case, a change of relative heading and a rotation around the vertical joint axis cannot be distinguished, and the constraint is perfectly fulfilled for arbitrary values of $\hat{\delta}$.

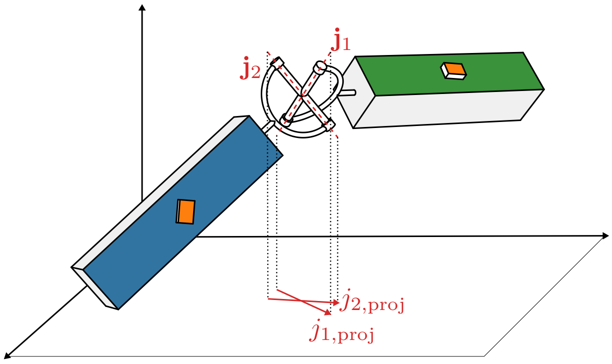

Figure 5.11: Projections of the joint axes $\mathbf{j}_1$ and $\mathbf{j}_2$ in the horizontal plane. When a joint axis becomes close to vertical, corresponding to the singularity of the kinematic constraint, the length of the horizontal projection becomes close to zero.

Due to inaccuracies in the estimated segment orientations, this singularity will already deteriorate the results if any of the joint axes are close to vertical. In order to obtain a measure of how close the axes are to vertical, we transform the joint axis vectors into their respective 6D reference frame

$$[\mathbf{j}_1]_{\mathcal{E}_1}(t) = {}^{\mathcal{B}_1}_{\mathcal{E}_1}\mathbf{q}(t) \otimes [\mathbf{j}_1]_{\mathcal{B}_1} \otimes {}^{\mathcal{B}_1}_{\mathcal{E}_1}\mathbf{q}(t)^{-1} =: [\, j_{1x} \;\; j_{1y} \;\; j_{1z} \,]^\intercal, \tag{5.28}$$

$$[\mathbf{j}_2]_{\mathcal{E}_2}(t) = {}^{\mathcal{B}_2}_{\mathcal{E}_2}\mathbf{q}(t) \otimes [\mathbf{j}_2]_{\mathcal{B}_2} \otimes {}^{\mathcal{B}_2}_{\mathcal{E}_2}\mathbf{q}(t)^{-1} =: [\, j_{2x} \;\; j_{2y} \;\; j_{2z} \,]^\intercal \tag{5.29}$$

and define the *sample rating* $r(t)$ as the product of the lengths of their horizontal projections (cf. Figure 5.11):

$$r(t) := j_{1,\mathrm{proj}} j_{2,\mathrm{proj}}, \tag{5.30}$$

$$j_{1,\mathrm{proj}} := \|[\, j_{1x} \;\; j_{1y} \,]^\intercal\|, \tag{5.31}$$

$$j_{2,\mathrm{proj}} := \|[\, j_{2x} \;\; j_{2y} \,]^\intercal\|, \tag{5.32}$$

which approaches zero if any of the axes get close to vertical.

Note that for hinge joints, both $\mathbf{j}_1$ and $\mathbf{j}_2$ will get close to vertical at the same time. It is still useful to consider both vectors to account for measurement inaccuracies.

5.5.4 Optimization-Based Estimation of the Heading Offset

Instead of using the constraint sample-by-sample to estimate $\delta(t)$ like in Section 5.3, we employ a window-based estimation method. This is done to account for measurement inaccuracies and for the fact that biological joints only approximately fulfill the joint constraint.

At regular time intervals T_{est}, we perform an estimation of $\delta(t)$ based on data in a time window immediately preceding the estimation time. We denote the corresponding quantities with an index $w \in \mathbb{N}^{+}$, i.e., the estimation time instants are

$$t_w := wT_{\text{est}}. \tag{5.33}$$

Each window consists of N samples with a sample index $k = 1, \ldots, N$, taken with a regular sampling interval T_{s} (which might be larger than the sampling interval of the sensor at which orientation estimation is performed) at the sampling instants

$$t_{w,k} := wT_{\text{est}} + (k - N)T_{\text{s}}, \tag{5.34}$$

leading to a window duration of $T_{\text{win}} := T_{\text{s}}\,N$.

This implies that only previous data is used to estimate $\delta(t)$, making this approach suitable for real-time applications. See Figure 5.12 for a visual representation of the estimation time windows. Note that for applications in which real-time capability is not needed, the approach can easily be modified to use windows centered around the estimation time instants t_w in order to improve accuracy.

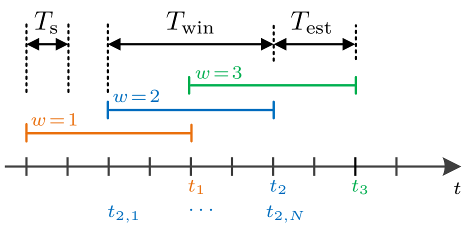

Figure 5.12: Graphical representation of the estimation windows, the estimation time instants t_w, the sample time instants $t_{w,k}$, and the durations T_{s}, T_{est}, T_{win}. Estimation is performed on overlapping moving windows. Each window consists of N samples and has a duration of T_{win}. After each estimation, the window is shifted by T_{est}.

Let $[\mathbf{j}_1]_{\mathcal{E}_1} =: [\, j_{1x} \;\; j_{1y} \;\; j_{1z} \,]^\intercal$ and $[\mathbf{j}_2]_{\mathcal{E}_2} =: [\, j_{2x} \;\; j_{2y} \;\; j_{2z} \,]^\intercal$ be the joint axis vectors in the respective 6D reference frames and ${}^{\mathcal{B}_2}_{\mathcal{B}_1}\mathbf{q}(t_{w,k}) =: [\, q_w \;\; q_x \;\; q_y \;\; q_z \,]^\intercal$ be the relative orientation that (5.23) yields for a given $\hat{\delta}$. For each sample of the window, we define the weighted constraint error

$$e_{w,k}(\hat{\delta}) = \text{wrapToPi}(\text{atan2}\,(j_{2y},\, j_{2x}) - \text{atan2}\,(j_{1y},\, j_{1x}) - \hat{\delta})\, r_{w,k} \tag{5.35}$$

in case the joint is a hinge joint and

$$e_{w,k}(\hat{\delta}) = (\arcsin(2q_wq_x + 2q_yq_z) - \beta_0)\, r_{w,k} \tag{5.36}$$

in case the joint is a 2-DoF joint, with $r_{w,k} := r(t_{w,k})$ and wrapToPi being a function that brings angles into the interval $[-\pi, \pi]$ by adding integer multiples of 2π.

Since the heading offset $\delta(t)$ only changes slowly over time, we assume that it is constant during each window and find the angle δ_w that minimizes the sum of squares of the errors given in (5.35) or (5.36) over the window w:

$$\delta_w = \arg\min_{\hat{\delta}} \sum_{k=1}^{N} e_{w,k}(\hat{\delta})^2. \tag{5.37}$$

We use analytical expressions for the Jacobian $\mathbf{J}_w \in \mathbb{R}^{N\times 1}$ (see Appendix B.3) with

$$[\mathbf{J}_w]_k = \frac{\partial e_{w,k}}{\partial \hat{\delta}} \tag{5.38}$$

and employ the Gauss-Newton algorithm to minimize the error for each window w, while using the estimate of the previous window as the initial value for each new window.

5.5.5 Singularity Treatment and Heading Filter

The sample rating $r_{w,k}$ allows the method to focus on the parts of a window that contain most relative-heading information. However, if the segments stay close to the singularity for durations that exceed the window duration T_{win}, the estimate of the corresponding windows might be wrong. To mitigate this, we first introduce the *window rating*

$$r_w := \sqrt{\frac{1}{N}\sum_{k=1}^{N} r_{w,k}^2}. \tag{5.39}$$

Then we design a filter that

- smoothes the δ_w trajectory, taking the rating into account,
- extrapolates linearly if the rating is below a certain threshold,
- does not introduce a delay if δ_w changes linearly.

To achieve this, we determine a filtered estimate $\delta_{\text{f},w}$ by applying the following nested adaptive filter that estimates the heading bias b_w and uses it to extrapolate the heading offset whenever the rating is below a certain threshold:

$$b_w = b_{w-1} + s_w k_{b,w} \operatorname{wrapToPi}(\delta_w - \delta_{w-1} - b_{w-1}), \tag{5.40}$$

$$\delta_{\text{f},w} = \delta_{\text{f},w-1} + b_w + s_w k_{\delta,w} \operatorname{wrapToPi}(\delta_w - \delta_{\text{f},w-1} - b_w), \tag{5.41}$$

$$s_w = \begin{cases} r_w & r_w \geq r_{\min} \\ 0 & \text{else,} \end{cases} \tag{5.42}$$

with a rating threshold $r_{\min} \in [0, 1]$ and filter gains

$$k_{b,w} := \max\left(1 - \exp\left(-\ln 2 \frac{T_{\text{s}}}{\tau_b}\right), \frac{1}{w}\right), \tag{5.43}$$

$$k_{\delta,w} := \max\left(1 - \exp\left(-\ln 2 \frac{T_{\text{s}}}{\tau_\delta}\right), \frac{1}{w}\right). \tag{5.44}$$

The parameters τ_b and τ_δ are tunable half-error time constants for the bias and heading filter, respectively. The filter gains are increased for small w to ensure fast initial convergence.

5.5.6 Rest Detection

To further improve the heading tracking robustness during phases in which the segments do not move, we extend the heading filter by a rest detection algorithm. Rest is detected when, for both segments, the mean of the angular velocity norm is below ω_{rest} for a duration of at least T_{rest}.

If both segments are at rest, the joint orientation, i.e., the relative orientation of both segments, does not change. We can exploit this fact to accurately track the drift in the heading offset $\delta(t)$ as long as rest is detected.

As soon as rest is detected, we store a reference ${}^{\mathcal{B}_2}_{\mathcal{B}_1}\mathbf{q}_{\text{ref}}$ for the joint orientation based on the orientation estimates and the estimate of the heading at the current time t_{rest}:

$$ {}^{\mathcal{B}_2}_{\mathcal{B}_1}\mathbf{q}_{\text{ref}} = {}^{\mathcal{B}_1}_{\mathcal{E}_1}\mathbf{q}(t_{\text{rest}})^{-1} \otimes \left(\hat{\delta}(t_{\text{rest}}) \,@\, [\,0\ \ 0\ \ 1\,]^\intercal\right) \otimes {}^{\mathcal{B}_2}_{\mathcal{E}_2}\mathbf{q}(t_{\text{rest}}). \tag{5.45} $$

At any later time instant t during the current rest phase, we can use this reference orientation to estimate the current heading offset $\delta(t)$. The quaternion representing the heading offset ${}^{\mathcal{E}_2}_{\mathcal{E}_1}\mathbf{q} = (\delta \,@\, [\,0\ \ 0\ \ 1\,]^\intercal)$ can be calculated from the current orientation estimates and the reference joint orientation by rearranging (5.45):

$$ {}^{\mathcal{E}_2}_{\mathcal{E}_1}\mathbf{q}(t) = {}^{\mathcal{B}_1}_{\mathcal{E}_1}\mathbf{q}(t) \otimes {}^{\mathcal{B}_2}_{\mathcal{B}_1}\mathbf{q}_{\text{ref}} \otimes {}^{\mathcal{B}_2}_{\mathcal{E}_2}\mathbf{q}(t)^{-1}. \tag{5.46} $$

${}^{\mathcal{E}_2}_{\mathcal{E}_1}\mathbf{q}(t)$ will typically be mostly a rotation around the vertical z-axis, corresponding to the current heading offset, and small rotations in other directions due to measurement errors and minimal joint movement. To recover the heading angle, we employ the quaternion projection method introduced in Section 2.4.5, i.e.,

$$ \hat{\delta}(t) = 2\,\text{atan2}(q_z, q_w), \text{ with } {}^{\mathcal{E}_2}_{\mathcal{E}_1}\mathbf{q}(t) =: [\,q_w\ \ q_x\ \ q_y\ \ q_z\,]^\intercal. \tag{5.47} $$

As long as rest is detected, we set the filter output $\delta_{\text{f},w}$ to this heading offset.

5.5.7 Heading Correction

We finally use (5.19), (5.23) and the filtered estimate $\delta_{\text{f}}(t)$ to determine the correction quaternion

$$ {}^{\mathcal{E}_2}_{\mathcal{E}_1}\mathbf{q}(t) = (\delta_{\text{f}}(t) \,@\, [\,0\ \ 0\ \ 1\,]^\intercal) = \left[\cos\left(\tfrac{\delta_{\text{f}}(t)}{2}\right) \quad 0 \quad 0 \quad \sin\left(\tfrac{\delta_{\text{f}}(t)}{2}\right)\right]^\intercal, \tag{5.48} $$

the orientation of the second segment $\mathcal{B}_2$ in the reference frame of the first segment $\mathcal{E}_1$

$$ {}^{\mathcal{B}_2}_{\mathcal{E}_1}\mathbf{q}(t) = {}^{\mathcal{E}_2}_{\mathcal{E}_1}\mathbf{q}(t) \otimes {}^{\mathcal{B}_2}_{\mathcal{E}_2}\mathbf{q}(t), \tag{5.49} $$

and the relative orientation between both segments, i.e., the joint orientation

$$ {}^{\mathcal{B}_2}_{\mathcal{B}_1}\mathbf{q}(t) = {}^{\mathcal{B}_1}_{\mathcal{E}_1}\mathbf{q}^{-1} \otimes {}^{\mathcal{E}_2}_{\mathcal{E}_1}\mathbf{q}(t) \otimes {}^{\mathcal{B}_2}_{\mathcal{E}_2}\mathbf{q}(t). \tag{5.50} $$

The resulting quaternions can be used for joint angle calculation and for 3D visualization.

5.6 Experimental Validation

The proposed method is validated experimentally with a mechanical 3D-printed hinge joint and human finger joints. For the mechanical joint, marker-based OMC is used as ground truth. For the finger joints, we design an experiment that allows us to obtain an approximate ground truth for the heading offset $\delta(t)$. The motions are chosen to facilitate investigation of the long-time stability of the obtained estimates during phases with and without sufficient excitation, i.e., during motions that yield sufficient relative-heading information and during motions for which the segments remain close to the singularity.

5.6.1 Setup

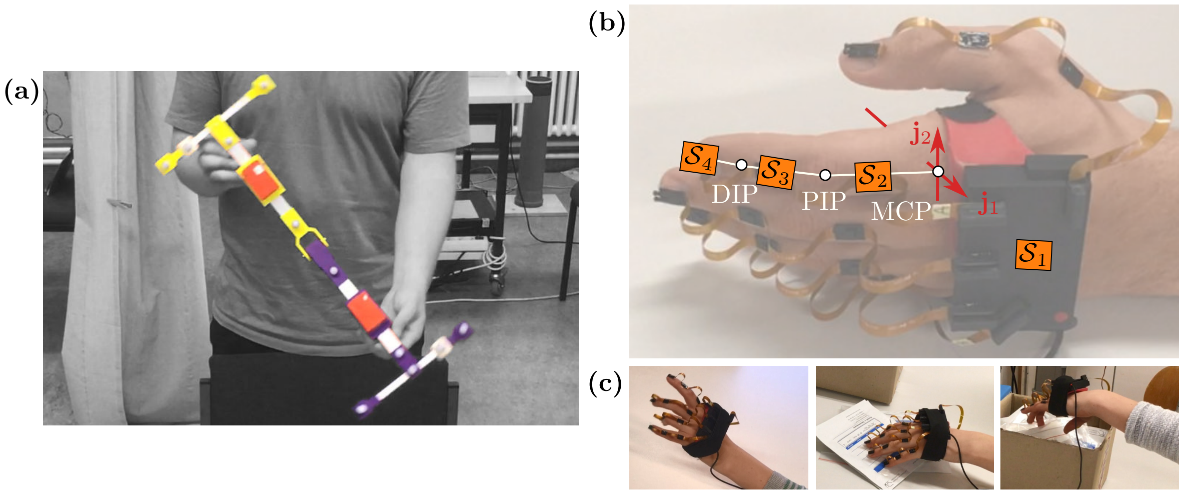

Figure 5.13: Experimental setup and example scenes from the conducted experiments. **(a)** The mechanical joint data was recorded with a 3D-printed hinge joint, XSens MTw IMUs, and marker-based OMC as reference. **(b)** For the hand data, a recently developed modular system [138, 158] was used. **(c)** The hand experiments consist of functional motions and of rest phases near the singularities of the kinematic constraints.

The 3D-printed mechanical hinge joint is shown in Figure 5.13a. Each segment is equipped with one IMU (Xsens MTw, Xsens Technologies B.V., Netherlands) and five optical markers, which are tracked by Flex13 cameras of an Optitrack OMC system (NaturalPoint, Inc., USA). Due to the custom mount for IMUs and optical markers, the segment coordinate systems are precisely known. The IMUs measure the angular velocity and the acceleration at a rate of 50 Hz, and 6D sensor fusion is performed using the BasicVQF algorithm presented in Chapter 3.

To measure the 6D orientation of the finger segments, a recently developed modular finger and hand motion capturing system [138, 158] is used, as shown in Figure 5.13b. One inertial sensor is attached to the back of the hand and tracks the movements of the metacarpal bones of the fingers. Six additional sensors are attached to the phalanges of the index and middle finger. The sensor-to-segment attachment is known due to a precise and careful attachment of the IMUs to the finger segments. The IMUs measure the angular velocity and the acceleration at a rate of 100 Hz, and 6D sensor fusion is performed using the BasicVQF algorithm presented in Chapter 3.

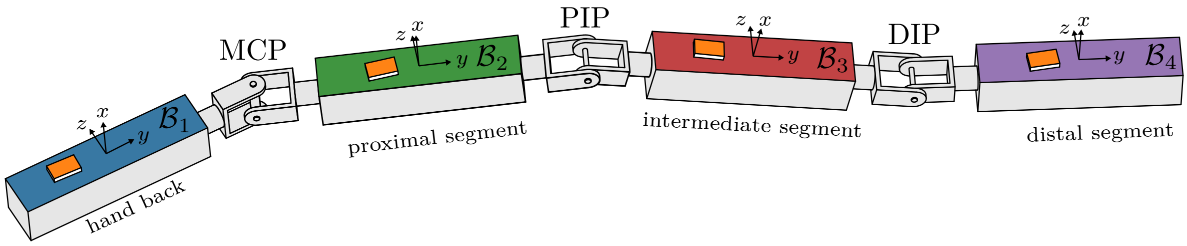

Figure 5.14: Kinematic model of a finger (excluding the thumb). The metacarpophalangeal joint (MCP) connects the metacarpal bone and the proximal phalanx and can be modeled as a 2-DoF joint. The proximal interphalangeal joint (PIP) and the distal interphalangeal joint (DIP) connect the proximal, intermediate, and distal phalanges and can be modeled as hinge joints.

We consider the metacarpophalangeal joint (MCP), the proximal interphalangeal joint (PIP), and the distal interphalangeal joint (DIP) of the index and middle finger. As illustrated in Figure 5.14, the finger can be modeled as a kinematic chain consisting of four segments. The MCP, which connects the proximal finger segments to the metacarpals, is an approximate 2-DoF joint. The *abduction axis* $\mathbf{j}_1$ of the MCP is fixed in the coordinate system of the back of the hand. The *flexion axis* $\mathbf{j}_2$ is fixed in the coordinate system of the proximal phalange. Since the axes are approximately perpendicular, we assume that $\beta_0 = 0$. The PIP and DIP, which connect the phalanges, are only capable of flexion and therefore approximate hinge joints.

5.6.2 Conducted Experiments

To evaluate the mechanical hinge joint, seven experiments were conducted in which the joint was held and excited by both hands (cf. Figure 5.13a). The individual trials have a duration ranging from 60 s to 6 min 56 s. Several of the trials include phases in which the joint axis is near vertical and phases in which the joint is stationary.

To evaluate the PIP and DIP joints of the finger, three long-time experiments were conducted, with durations of 10 min 54 s, 12 min 7 s, and 7 min 25 s. In the first experiment, vertical joint axes were avoided, while the second experiment consists of distinct phases with various speeds and rest phases with horizontal and vertical joint axis, as detailed in Table 5.2. The third experiment consists of natural functional hand motions (Figure 5.13c).

To evaluate the MCP joints of the finger, two long-time experiments were conducted. The first experiment, with a total duration of 8 min 41 s, was designed with distinct movement phases that include phases with natural movement and longer phases with rest near the singularities. See Table 5.3 for an overview of the different movement phases and their duration. The motion phases were chosen to include phases with and without excitation.

Table 5.2: Movement phases of the second experiment for the PIP/DIP joints

Phase	Description	Start	End	Duration
M1	normal movement	0 s	121 s	121 s
M2	slow movement	121 s	264 s	143 s
M3	no movement, $\mathbf{j}$ horizontal	264 s	363 s	99 s
M4	normal movement	363 s	497 s	134 s
M5	no movement, $\mathbf{j}$ vertical	497 s	602 s	105 s
M6	normal movement	602 s	727 s	125 s

Table 5.3: Movement phases of the first experiment for the MCP joint

Phase	Description	Start	End	Duration
M1	normal movement	0 s	90 s	90 s
M2	slow movement	90 s	153 s	63 s
M3	normal movement	153 s	247 s	94 s
M4	no movement, $\mathbf{j}_2$ vertical	247 s	290 s	43 s
M5	normal movement	290 s	382 s	92 s
M6	no movement, $\mathbf{j}_1$ vertical	382 s	424 s	42 s
M7	normal movement	424 s	521 s	97 s

Phases with movement are expected to yield good estimation results (M1, M3, M5, M7). During phases with approximately vertical axes (M4, M6), the data contains almost no heading information, but the singularity treatment and rest detection, as described in Sections 5.5.5 and 5.5.6, should mitigate this. The second experiment consists of functional movements like counting, typing, and moving objects in and out of a box to test the method in real-world scenarios (Figure 5.13c). The second experiment has a total duration of 3 min 26 s.

5.6.3 Real-Time Heading Tracking

To evaluate the performance of real-time estimation of $\delta(t)$, the proposed algorithm is applied to the recorded data. For the estimation at a given time instant t_w, only data from the past is used. The parameters are chosen as follows: Every $T_{\text{est}} = 1\,\text{s}$, we analyze a window with a duration of $T_{\text{win}} = 5\,\text{s}$ for the mechanical joint and $T_{\text{win}} = 25\,\text{s}$ for the finger joints, consisting of $N = 25$ or $N = 125$ samples taken every $T_{\text{s}} = 0.2\,\text{s}$. We choose the filter time constants as $\tau_b = 8\,\text{s}$ and $\tau_\delta = 8\,\text{s}$, with a rating threshold of $r_{\min} = 0.4$. For the rest detection algorithm, we choose a duration of $T_{\text{rest}} = 3\,\text{s}$ and a threshold of $\omega_{\text{rest}} = 5\,°/\text{s}$.

5.6.4 Comparison with Conventional 6D and 9D Sensor Fusion

For comparison, we additionally evaluate a conventional 6D and a conventional 9D method.

For the conventional 6D comparison, we employ the method proposed in [138]. During a phase without movement at the start of the measurement, the gyroscope readings are averaged to obtain an estimate of the gyroscope bias. After removing this bias, 6D sensor fusion is performed. At the beginning of the measurement, an initial-pose reset is performed, which makes use of the known initial pose to determine and correct the heading offset. However, it is an inevitable fact that the resulting orientations are only valid for a limited time until they are deteriorated by integration drift resulting from residual and from time-varying gyroscope bias.

For the conventional 9D method, we directly use the 9D orientation estimates provided by the BasicVQF method introduced in Chapter 3.

5.6.5 Obtaining an Approximate Ground Truth

For validation of the experiments with the mechanical hinge joints, we compare the 6D IMU orientations of each segment to the OMC-based orientations and use the heading/inclination decomposition introduced in Section 2.5 to split the relative orientation into a heading offset and a residual rotation angle. The difference of the heading offsets for both segments, denoted

δ_{ref}, serves as ground truth for the heading offset $\delta_{\mathrm{f}}(t)$ that we estimate with the proposed method. To account for noise in the OMC marker positions, we apply a low-pass filter to this slowly changing ground truth trajectory.

For validation of the finger experiments, for which an OMC ground truth is not available, we define a reference pose that is taken several times during the experiment: The hand is lying flat on a horizontal surface with all fingers straight. For that pose, the coordinate systems of all sensors are approximately aligned. Therefore, whenever that pose is taken, the ground truth δ_{ref} is determined as the heading offset that minimizes the rotation angle of the relative quaternion ${}^{\mathcal{B}_2}_{\mathcal{B}_1}\mathbf{q}$ in (5.23). Assuming that the heading drift is slow and approximately linear, we linearly interpolate δ_{ref} between the reference time instants. Since this method relies on the precise attachment of the sensors as well as the exact positioning of the hand during the resting phases, it yields only an approximate ground truth. Still, this ground truth is suitable for determining whether the relative heading estimates $\delta_{\mathrm{f}}(t)$ of the proposed method are long-time stable.

To mitigate some of the inaccuracy of the heading ground truth due to relying on a precise sensor attachment, we apply a small constant offset for each trial based on the mean difference between the estimated heading offset and the ground truth. The average absolute value of the applied offset is 1.6°, with a maximum of 4.8°.

5.6.6 Error of the Relative Orientation

As explained above, accurate relative heading estimation is crucial for obtaining accurate relative segment orientations, which are required to determine joint angles and forward kinematics. We use $\delta_{\mathrm{ref}}(t)$ to determine the approximate true relative orientation for each joint and calculate the absolute rotation angle between this orientation and the relative segment orientation that is estimated by the proposed method. Denote this error by $e_{\mathrm{relori}}(t)$. For each trial, we further condense this error to a single value by calculating the RMSE.

The results for all trials of all three joint types are presented in Figure 5.15 and summarized in Table 5.4.

Table 5.4: Average relative orientation RMSE for the different joints with the proposed heading tracking method (HT) and a conventional 6D and 9D method

Joint	DoF	Trials	HT	9D	6D
Mechanical hinge joint	1	7	**0.3°**	3.1°	3.3°
Biological (finger, PIP+DIP)	1	12	**1.7°**	5.9°	55.7°
Biological (finger, MCP)	2	4	**3.9°**	12.5°	19.3°

For the mechanical joint, the proposed method yields very good results with an average error of 0.3°. Also, for the biological finger joints, the average errors of 1.7° and 3.9° are very low and within the accuracy of the approximate ground truth. The slightly larger error for the biological 2-DoF joint compared to the hinge joints fits the expectation that the additional degree of freedom in the joint movement impedes accurate estimation of the heading offset. However, as the errors are still within the accuracy of the approximate ground truth, the observed difference in the error might be coincidental or caused by other differences in the performed experiments.

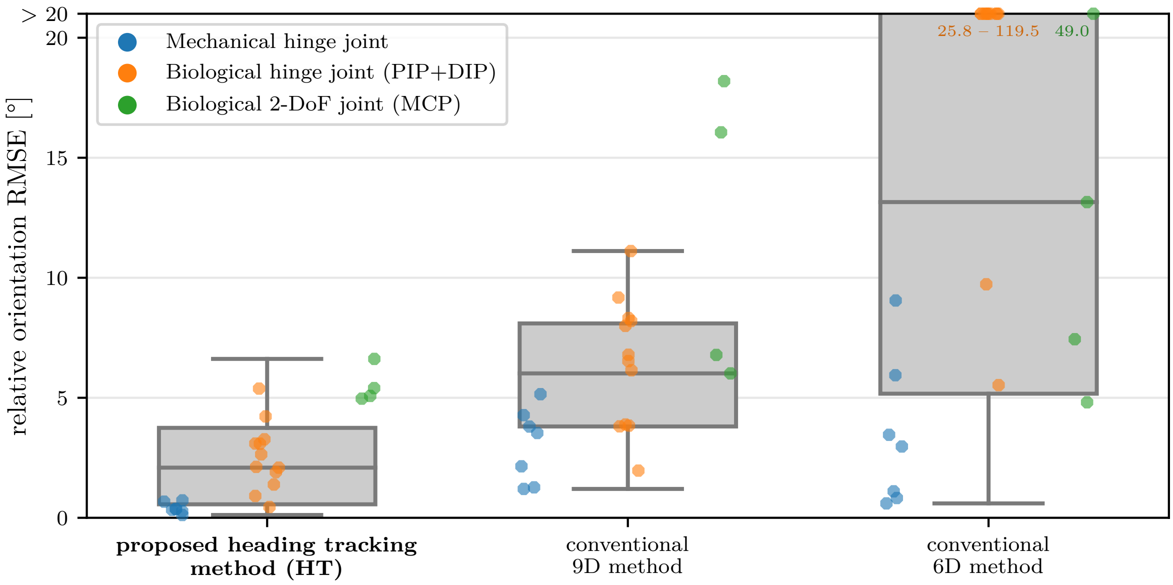

Figure 5.15: Relative orientation RMSE for the three different joint types with the proposed heading tracking method and conventional 6D and 9D methods for comparison. The proposed heading tracking method consistently provides the smallest relative orientation errors.

Considering the long duration of the performed experiments, we can conclude that the proposed method achieved stable tracking of the heading offset for all trials. This cannot be said for the conventional methods. Due to the long trial durations, the accumulated gyroscope drift is substantial, leading to large errors when using the conventional 6D method with initial reset. The magnitude of this error depends on the duration of the trial, the quality of the IMUs, as well as the accuracy of the gyroscope bias estimate.

With the conventional 9D method, the error depends mostly on the homogeneity of the magnetic field and the quality of the magnetometer calibration. Even for the mechanical joint, where the RMSE of 3.1° does not suggest substantial issues with the magnetometer measurements, the errors obtained with the proposed method are considerably smaller than the errors obtained with the 9D method.

5.6.7 Cost Function Analysis and Evaluation of Singularity Treatment

For a detailed analysis of the behavior of the proposed method, we take a detailed look at one exemplary trial for each joint type: Figure 5.16 shows results for the mechanical joint, Figure 5.17 for a DIP joint, and Figure 5.18 for an MCP joint.

To analyze the properties of the optimization problem for the different motion phases, we evaluate the cost function in (5.37) for each time instant t_w and for many evenly spaced angles $\delta \in [0°, 360°]$. The result is shown in Figures 5.16a, 5.17a, and 5.18a, with a red dot indicating the location of the minimum for the respective time instant. In general, for hinge joints, there is one distinct minimum for each time instant, while the 2-DoF constraint exhibits a second local minimum. Still, it can be seen that a distinct global minimum exists for phases with movement. In contrast, the cost function becomes flat and exhibits a distinct second local minimum for phases without movement and a vertical joint axis (M4 and M6). During those phases, no relative-heading information is available, and the minima do not reflect the true value of δ.

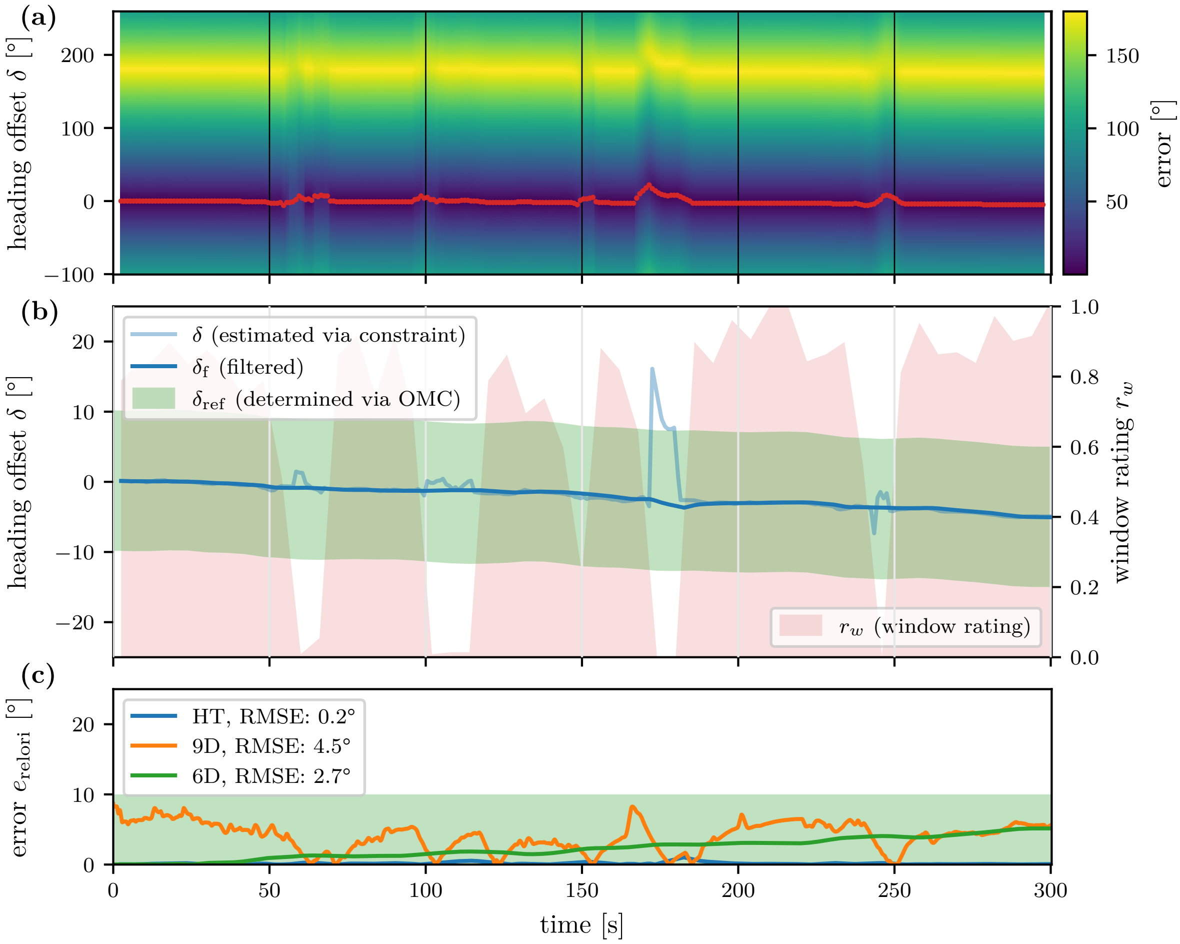

Figure 5.16: Results for an exemplary trial with the mechanical hinge joint, showing **(a)** the value of the cost function and the minimum for each time instant (red), **(b)** the unfiltered and filtered heading offset as well as the window rating, and **(c)** the orientation errors for the proposed heading tracking method (HT) and the conventional 6D and 9D approaches. The mechanical hinge joint allows for very accurate heading tracking (RMSE: 0.2°), even in phases when the joint axis is near vertical and the window rating r_w is small.

From the overall trend, it can be seen that the minimum remains almost constant in 5.16a, indicating good sensor calibration and small gyroscope bias, and drifts slowly with an approximately constant slope of 0.6 °/s in 5.18a. In 5.17a, it is noticeable that the drift of the heading offset is quite slow, except during phase M5, in which the joint axis is vertical. This is likely due to gyroscope bias being larger in the sensor axis corresponding to the joint axis. Since extrapolation of the previous heading drift will not lead to a good estimate, this presents a challenging case for the heading filter.

Figures 5.16b, 5.17b, and 5.18b show the time series of the estimated heading offsets $\delta(t)$ and $\delta_\mathrm{f}(t)$ as well as the approximate ground truth $\delta_\mathrm{ref}(t)$ and the window rating r_w. The ground truth is depicted with a band of ±10° to indicate the low accuracy. It can be seen that during the phases with a small window rating r_w, the unfiltered estimate $\delta(t)$ diverges from the ground truth. However, the filtered estimate $\delta_\mathrm{f}(t)$ remains close to the true value, even for long time periods near the singularities, especially in motion phase M5 in Figure 5.17 and motion phases M4 and M6 in Figure 5.18 with deliberate rest with a vertical joint axis. This is especially noteworthy for the challenging case mentioned above, i.e., M5 in Figure 5.17, and

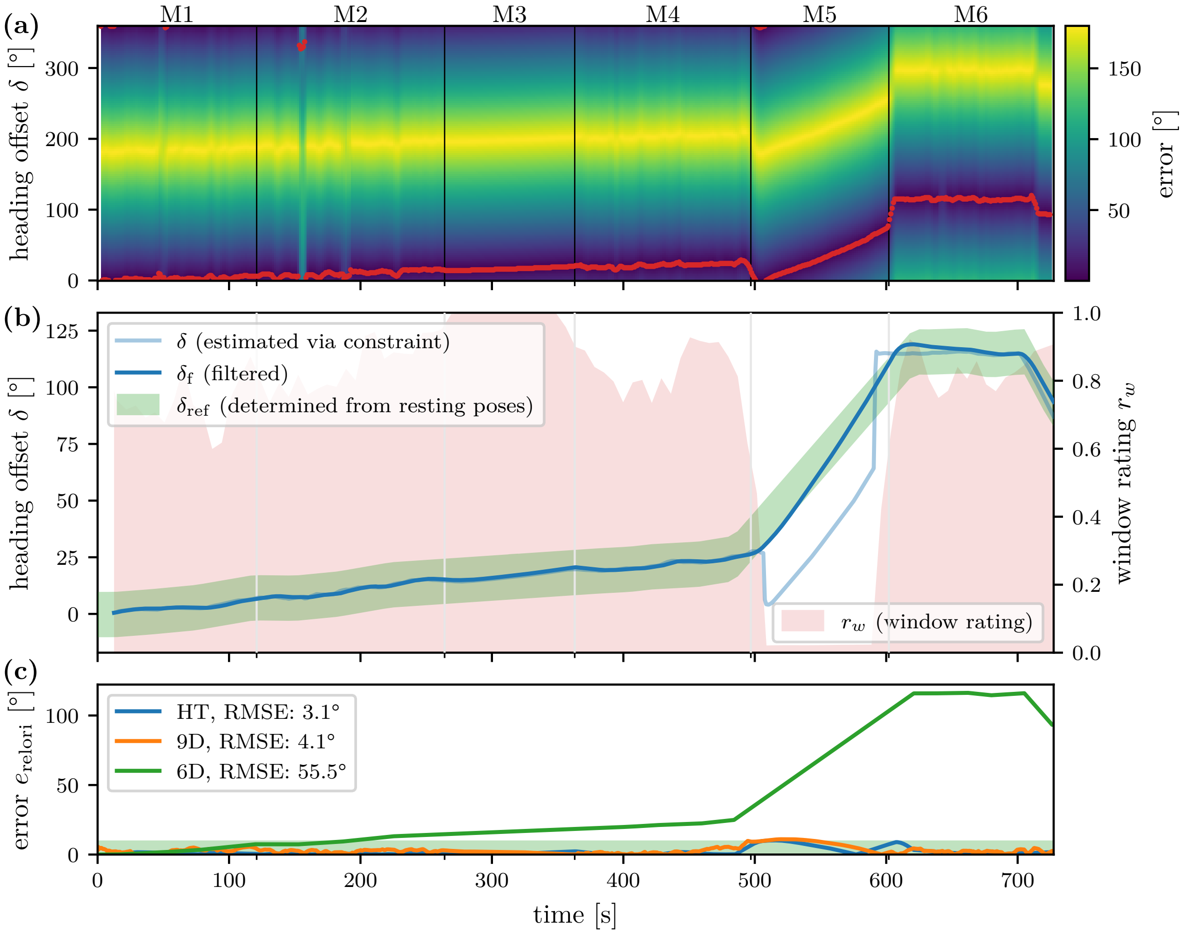

Figure 5.17: Results for the 1-DoF DIP joint of the index finger and the second experiment, showing **(a)** the value of the cost function and the minimum for each time instant (red), **(b)** the unfiltered and filtered heading offset as well as the window rating, and **(c)** the orientation errors for the proposed heading tracking method (HT) and the conventional 6D and 9D approaches. For a short duration during M2 (slow movement) and, as expected, during M5 with a near-vertical joint axis, the kinematic constraint does not yield the correct heading offset δ, which is mitigated by the singularity treatment.

shows that the rest detection algorithm works as intended and is able to accurately track the previously unknown heading drift.

Finally, the relative orientation errors $e_{\text{relori}}(t)$ for the proposed and the conventional methods are shown in Figures 5.16c, 5.17c, and 5.18c. For the conventional 6D method presented in [138], the error e_{relori} is zero at the start of the measurement and then slowly increases to values $> 100°$ after several minutes. To obtain long-time stable motion tracking, the subject would have to repeat the initial reset procedure at least once per minute. The conventional 9D method does not exhibit drift but yields large errors. Accurate motion tracking with 9D sensor fusion requires accurately calibrated magnetometers and a laboratory environment that is kept free of any potential magnetic disturbances. In contrast, the proposed constraint-based heading tracking method yields accurate results throughout the entire measurement, and for all three examined trials, the relative orientation error $e_{\text{relori}}(t)$ always stays within the accuracy band of the approximate ground truth.

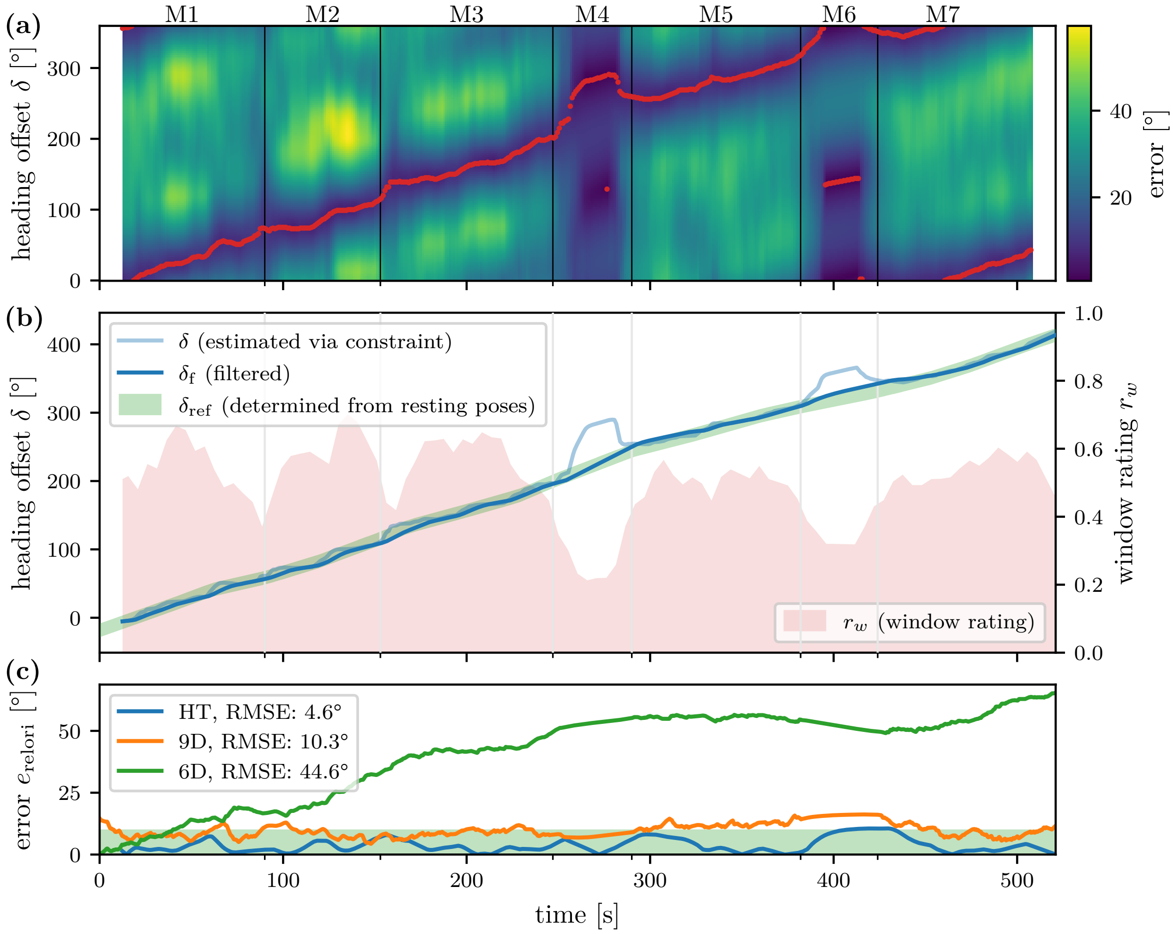

Figure 5.18: Results for the 2-DoF MCP joint of the index finger and the first experiment, showing **(a)** the value of the cost function and the minimum for each time instant (red), **(b)** the unfiltered and filtered heading offset as well as the window rating, and **(c)** the orientation errors for the proposed heading tracking method (HT) and the conventional 6D and 9D approaches. In contrast to the hinge joint constraint, the 2-DoF constraint often exhibits a second local minimum. During phases M4 and M6, one joint axis is near vertical, and the constraint does not yield the correct heading offset δ, which is mitigated by the singularity treatment.

5.7 Conclusions

This chapter introduced two methods for magnetometer-free motion tracking of kinematic chains based on exploiting kinematic constraints of the joints.

The first sample-based method is designed for approximate hinge joints and works on 9D orientation estimates obtained in inhomogeneous magnetic fields as well as on magnetometer-free 6D orientation estimates. The method uses an orientation-based constraint to determine the relative heading between the sensor orientations. Since the constraint becomes singular when the joint axis becomes vertical, a filter was designed that allows for accurate tracking with a temporarily vertical joint axis. The results of the performed simulation study indicate that the method is highly useful in the presence of ferromagnetic material or other magnetic disturbances. Furthermore, the results show that the method still gives good results when the ideal conditions of a perfect hinge joint and a perfect sensor-to-segment calibration are not met and that the dimensions of the segments and the motion volume hardly influence the accuracy of the method.

Based on the first method, an extended method for magnetometer-free inertial motion tracking was introduced. This method is suitable for hinge joints and joints with two degrees of freedom. A real-time-capable window-based optimization scheme was introduced to increase robustness. Furthermore, a method for rating the reliability of the optimization result was proposed, and an adaptive filter was introduced that takes this rating into account and extrapolates the estimate when no relative-heading information is available. The experimental validation based on a mechanical hinge joint and the MCP, PIP, and DIP joints of the fingers shows that the method facilitates accurate and long-term stable motion tracking, in contrast to conventional 6D and 9D methods.

With the proposed method, it is possible to track the relative orientations and joint angles of joints with one or two degrees of freedom in real-world applications with realistic magnetic environments. The method is real-time capable in the sense that only current and previous information is used. It is therefore highly suitable for rehabilitation applications, including real-time visualization of motions and feedback control of rehabilitation robotics or functional electrical stimulation systems. While previous research is often limited to short-time analysis of rich motions, the proposed method yields long-time stable results and is capable of handling phases in which no movement is performed or in which the movement does not contain heading information. Furthermore, in contrast to previously proposed methods, the current method works on arbitrary motions without the need to perform an initial reset with a predefined pose and without the need to determine sensor-to-joint position parameters.

In future work, the proposed heading tracking method should be combined with the automatic anatomical calibration methods introduced in Chapter 4 to enable plug-and-play magnetometer-free motion tracking.

6

Non-restrictive Gait Assessment by Foot-Worn IMUs

Gait assessment is an essential tool in various medical and therapeutic fields and is typically performed by trained medical experts and with expensive and restrictive stationary motion capture systems. As an emerging alternative, IMUs can be employed to provide objective, low-cost gait assessment that is non-restrictive and can be used outside of laboratory environments. To facilitate this development, this chapter introduces a modular set of methods to detect gait events and derive various spatiotemporal gait parameters and 3D foot position and angle trajectories.

Text, figures, and tables found in this chapter have been previously published or submitted for publication, with slight modifications, in the following works:

- [159] D. Laidig, A. J. Jocham, B. Guggenberger, K. Adamer, M. Fischer, and T. Seel. "Calibration-Free Gait Assessment by Foot-Worn Inertial Sensors". In: *Frontiers in Digital Health* 3 (2021), Article 147. ISSN: 2673-253X. DOI: `10.3389/fdgth.2021.736418`.
- [160] A. J. Jocham, D. Laidig, B. Guggenberger, and T. Seel. "Measuring Highly Accurate Foot Position and Angle Trajectories with Foot-Mounted IMUs in Clinical Practice". [Manuscript submitted for publication]. 2023.

Most of the content of this chapter has been published in [159]. While most of Section 6.2 has been published in [159], the version found in this chapter was extended to cover 3D position and angle trajectory tracking in addition to the derivation of spatiotemporal gait parameters. Sections 6.3.11 to 6.3.13 and Section 6.5 have been submitted for publication in [160]. Sections 6.6 and 6.7 have been slightly extended from the version published in [159] to cover the results of Section 6.5.

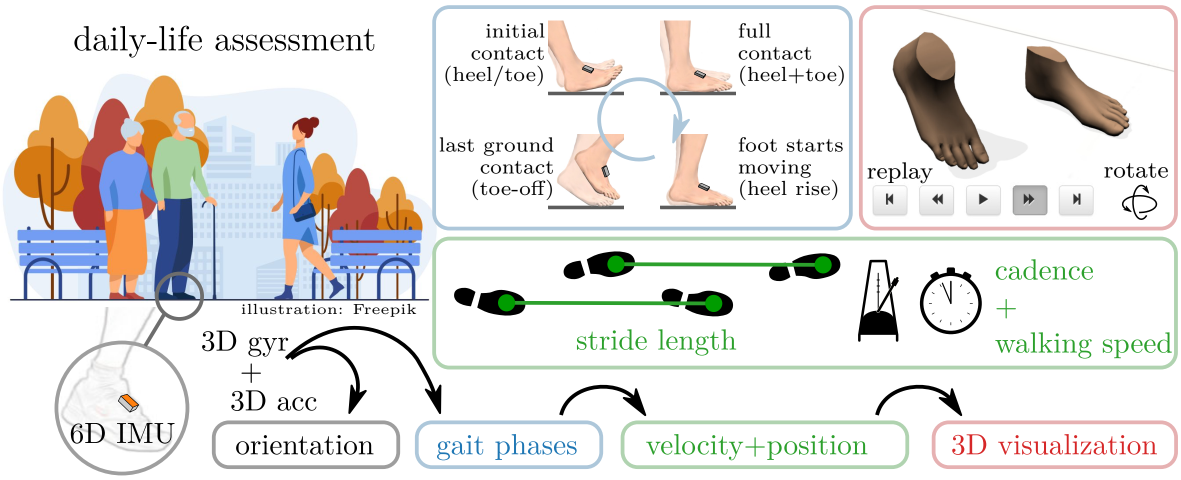

Figure 6.1: Inertial gait analysis can be realized with two miniaturized IMUs on the shoes, enabling daily-life assessment outside of laboratory environments. From the raw sensor data, the foot orientation, gait phases, and velocity and position trajectories can be estimated. Parameters commonly used in gait analysis, such as stride length, cadence, and walking speed, can easily be derived from this.

6.1 Introduction

Walking is a central activity of daily life, and restrictions of this ability lead to a reduction in the quality of life [161, 162]. Therefore, gait analysis is an important tool in different medical and therapeutic fields [163, 164]. The measurement of various gait characteristics can either facilitate diagnosis or be used to track the progress of rehabilitation. Gait can be measured by spatial (e.g., step or stride length) and temporal (e.g., stride time, cadence) parameters, relative durations of gait phases, and kinematic and kinetic gait variables [165]. These parameters are used to quantify gait deviation in both clinical practice and research, and their use varies with the medical field, the research question, and the analysis options. While gait assessment in clinical practice is mostly based on visual observation by medical experts [166], it is desirable to support expert knowledge and time by objective measurements. This is also important because relevant gait changes are often too subtle to be detected by the naked eye [167].

Traditionally, sensor-based gait assessment is performed with stationary systems like marker-based optical motion tracking, instrumented treadmills, or pressure-sensitive walkways [166, 168]. Besides being expensive, one major drawback of those systems is that they are limited to a small capture space or require the subject to walk on a treadmill [164, 169, 170, 171, 172]. Furthermore, the use of walking aids is often not possible or restricted in combination with such systems.

A promising, more ambulatory, and less restrictive alternative is inertial gait analysis, i.e., gait analysis with inertial sensor technology. Lightweight and battery-powered IMUs are used, which transmit the data wirelessly.

The transition from expensive stationary systems to small wearable sensors opens up possibilities that go beyond replacing the measurement technology used for gait assessment in clinical settings. Integrating objective long-term gait monitoring into day-to-day life – as illustrated in Figure 6.1 – could provide more powerful tools for clinicians to help patients in rehabilitation and to gain further insight into disease progression. Furthermore, non-obtrusive wearable plug-and-play systems facilitate applications in neuroprosthetics [173] or exoskeletons and can be used to provide biofeedback [174]. In the last years, wireless battery-powered IMUs have become smaller, lighter, more accurate, and, at the same time, cheaper and more energy-efficient. It is to be expected that this development will continue. For those new trends, it is important to develop methods that can provide a wide variety of gait parameters that are useful to medical experts. At the same time, the methods need to be robust so that the system can be used by patients in unsupervised settings, outdoors as well as indoors.

It has been shown by previous contributions [16, 175, 176] that major gait parameters can be determined with two IMUs that are placed on the feet or the shoes, as illustrated in Figure 6.1. This includes stride length, gait phase durations (e.g., stance and swing percentage), and also cadence and walking speed.

This chapter aims to propose methods for gait assessment that meet the requirements for daily life monitoring in unsupervised settings and that are validated on a broad group of subjects, including patients with various gait pathologies. The proposed methods do not assume a precisely fixed orientation of the sensor on the foot and do not require the subject to perform dedicated calibration movements. Furthermore, magnetometers are not used since the magnetic field is known to be severely disturbed in indoor environments [38]. This makes the use of inertial gait analysis easy and practical in clinical settings and facilitates future applications of ubiquitous gait analysis in home environments.

6.2 State of the Art in IMU-Based Gait Assessment

Several methods have been proposed that employ IMUs to obtain gait parameters. In the following, we first consider methods that estimate spatiotemporal parameters. At the end of the section, we take a brief look at the estimation of position and angle trajectories.

For spatiotemporal parameter estimation, we take a brief overview of the current state of the art and summarize the different hardware setups that are used, which parameters are calculated, and how the methods were validated. Table 6.1 categorizes 23 publications that provide a range of examples for the variety of existing approaches in the estimation of spatiotemporal gait parameters with IMUs.

There are different hardware setups based on the number of IMUs and their placement. The chosen setup impacts which and how many parameters can be derived from the measured data. The most commonly used setup consists of two IMUs. As shown in Table 6.1, sensors are typically placed on the feet or shoes and sometimes on the shank. This setup is occasionally extended by adding a third sensor on the pelvis or lumbar spine [177, 178]. Note that it has even been shown that temporal gait events can be obtained from a single IMU at the pelvis [179], but the potential for extracting further spatial parameters is limited. Full (lower) body motion tracking opens up additional possibilities, as demonstrated with 7 IMUs on the lower body and pelvis in [180] and with 8 to 15 IMUs in [181]. Another, less common, option consists of combining IMUs with further measurement devices, e.g., a camera on one foot and LEDs on the other foot to facilitate the direct measurement of relative positions [182].

Table 6.1: Overview of IMU-based spatiotemporal gait parameter estimation literature

Employed sensor setup	
2 IMUs on feet/shoes	[16, 176, 183, 184, 185, 186, 187, 188, 191, 192, 193, 194, 195, 196, 197]
2 IMUs on shank	[173, 175, 187, 189, 190, 195]
3 or more IMUs	[177, 178, 180, 181]
Detected gait phases	
stance/swing	[173, 175, 176, 178, 180, 183, 184, 187, 189, 190, 195]
4 unilateral events	[16, 185, 186, 191, 192, 193]
single/double support	[181, 197]
Ground truth used for evaluation	
optical motion capture (OMC)	[177, 180, 185, 186, 188, 192, 196, 197]
pressure-sensitive walkways	[175, 176, 178, 184, 189, 190]
instrumented treadmills	[194, 195]
pressure insoles	[16, 187]
others/none	[181, 183, 191, 193]
Non-healthy subjects included in evaluation	
none (healthy only)	[177, 180, 181, 183, 185, 186, 193, 194, 195, 196]
≤ 20	[178, 187, 188, 190, 192]
> 20	[16, 175, 176, 184, 189, 197]

A total of 23 publications that describe the estimation of spatiotemporal gait parameters with IMUs are categorized based on sensor setup, detected gait phases, and the ground truth and number of non-healthy subjects for evaluation.

Some methods require that a known orientation of the sensor axes with respect to the anatomical foot axes has to be ensured by precise placement. Many literature methods are based on such assumptions, including [16, 173, 175, 176, 183, 184, 185, 186, 187, 188, 189, 190]. In practice, however, ensuring a precise placement is a challenge, especially in non-supervised application scenarios and during activities of daily life. Alternatives are to develop methods that are agnostic to the sensor-to-segment orientation – e.g., by relying only on signal norms – or to determine this orientation in a process commonly called anatomical calibration (cf. Chapter 4).

The calculation of spatiotemporal gait parameters is usually implemented in a two-stage approach. In the first step, gait events and corresponding gait phases are detected. In the second step, spatial parameters are calculated.

Existing methods vary in the set of detected gait phases or events. In many cases, the focus is only on the separation between stance and swing (cf. Table 6.1), although sometimes additional events, such as mid-swing [190], are also detected. It is also common to detect four events that occur during the gait cycle and are only defined by the ipsilateral (same) foot. Those events are initial contact, full contact, heel rise, and toe-off, although the terminology varies. Despite being common practice in gait analysis [165, 198], employing bilateral information, i.e., combining information from both feet to define the gait phase, is far less common in IMU-based methods. One example is [181], in which single and double limb support durations are calculated.

There are various approaches for the detection of gait phases or events using IMUs. It has been shown that exploiting features of the angular rate signal in the sagittal plane is sufficient to achieve reliable gait event detection [175, 183, 185, 187, 189]. Many other methods use both accelerometers and gyroscopes and detect characteristic signal features in the IMU data, including [16, 173, 176, 184, 188, 190, 191, 192, 193]. Sometimes automatic adaptation mechanisms are used to adjust thresholds based on the subject's walking style [190, 191, 192, 193]. An alternative to the signal-based methods is to rely on a kinematic model to detect gait events [180, 181]. Machine learning methods, often based on hidden Markov models [178, 186], are also used for event detection, cf. [199].

In addition to the detection of gait events, spatial parameters, such as stride length and walking speed, are often calculated. Those parameters are obtained by either signal integration, human gait models, or by machine learning methods [200]. By far the most common approach is numerical strapdown integration of the accelerations [175, 176, 180, 183, 188, 189, 195, 196]. The cyclic nature of gait and the fact that there is frequent ground contact are exploited to correct for drift resulting from double integration. It has been shown that Fourier-based integration is an alternative to numerical integration [177], that spatial parameters can be obtained from kinematic models [181, 195], and that convolutional neural networks can also be used to estimate spatial parameters [184].

Most publications focus on common spatiotemporal parameters such as stride length, walking speed, and cadence. Other than those spatiotemporal parameters, there is a multitude of spatiotemporal gait parameters that are relevant in a clinical context for various pathologies [166]. Examples that can be estimated using IMUs include step width [180] and swing width [180, 188].

Some publications [173, 185, 190, 191, 192, 193] focus on real-time detection of events, e.g., to trigger FES in a drop foot stimulator [20, 201]. While the approaches used are usually similar to the ones used in offline gait analysis, this typically implies a focus on minimizing the detection delay rather than the accuracy of the reported values.

As shown in Table 6.1, evaluation is often performed with marker-based optical motion capture as ground truth. Systems based on the detection of pressure, such as pressure-sensitive walkways, instrumented treadmills, and pressure insoles, are a common alternative. In some cases, no validation with respect to a gold standard is performed. Instead, the settings of a (calibrated) treadmill are used as the ground truth for walking speed and incline [183], a manually counted number of steps is combined with the detection of irregularities [193], validation is performed by visual inspection of the results [191], or the focus is only on test-retest reliability [181].

Even though it has been shown that the accuracy of gait analysis methods decreases when applied to non-healthy subjects [199], the evaluation of inertial gait analysis methods is often only based on healthy subjects. When data obtained from non-healthy subjects is part of the evaluation, the number of subjects is often small, for example, five transfemoral amputees [192], ten stroke patients [190], ten hemiparetic patients and ten Huntington's disease patients [178], or ten patients with Parkinson's disease [188].

To the best of the author's knowledge, few publications [16, 175, 176, 184, 189, 197] exist that propose methods for IMU-based spatiotemporal gait parameter estimation *and* validate the methods on a larger set of subjects with gait pathologies. In the following, we briefly summarize those publications.

In [16], sensors are placed on the forefoot in a known orientation, and four different unilateral gait events are detected based on features of the angular velocity in the sagittal plane, the norm of the accelerometer signal, and the derivative of the angular velocity norm. Using pressure insoles as reference, the method is validated on ten healthy and 32 orthopaedic subjects.

The commercial Gait Up system is evaluated in [197] with 25 subacute stroke patients as subjects and marker-based optical motion capture as reference.

Gait events and stride length are calculated in [175] based on shank-mounted IMUs. Events are detected based on the angular rate in the sagittal plane, and stride length is obtained via double integration of the accelerations. The latter relies on the proprietary orientation estimation algorithm provided by the sensor manufacturer. Experimental evaluation is performed using the GAITRite pressure-sensitive walkway as reference on ten healthy elderly and 30 non-healthy subjects.

In [189], the same method is validated on a much larger group of subjects, consisting of 236 community-living older adults, including 31 mild cognitive impaired subjects and 125 Parkinson's disease patients.

In [176], IMUs are placed laterally on the shoe in a fixed orientation, stance and swing durations are calculated based on characteristic signal features, and the stride length is obtained via double integration. The method is evaluated using a large dataset of 101 geriatric inpatients, with reference data obtained from a GAITRite pressure-sensitive walkway.

Using the same gait event detection method and the same dataset for evaluation as [176], [184] estimates stride length, stride width, mediolateral change in foot angle, heel contact times, and toe contact times using deep convolutional neural networks.

In comparison to IMU-based gait analysis via spatiotemporal parameters, the amount of publications that investigate the calculation of position and angle trajectories is more limited. Many studies focus on the estimation of a single metric, such as foot clearance [196, 202, 203, 204] or the foot progression angle [205, 206]. Other publications only evaluate the foot pitch angle [207, 208, 209, 210], often not over time but only at certain gait events [207, 209]. There is a lack of studies such as [211] that evaluate the full 3D position and angle trajectories over time. The mentioned publications all employ marker-based OMC for validation, and the number of subjects ranges from four to 20.

In summary, the main shortcoming of existing approaches for the vision of plug-and-play ambulatory gait analysis is that most methods – especially those with broad validation – require a precise attachment of the sensor to the subject's foot. Some methods only focus on gait events and do not provide spatial parameters, and some methods rely on proprietary algorithms of the sensor manufacturers. Work on leveraging the full 3D position and angle trajectories that can be obtained by IMUs is limited. Furthermore, very few of the proposed methods are validated on a large group of subjects with diverse gait pathologies.

In the following section, a set of methods is introduced that combines the valuable achievements of existing methods with additional features that overcome the remaining limitations.

6.3 Methods

In the following, a set of methods to determine gait parameters from two foot-worn IMUs is introduced. The proposed methods are based on the following assumptions and requirements: An IMU is attached to each foot or shoe in an arbitrary orientation. This implies that the proposed method does not make any assumption about the orientation of the sensor coordinate system, which means it does not require any specific sensor axis to be aligned with an anatomical or functional axis of the foot. In order to avoid artifacts caused by toe or ankle motions and also to not limit the subject's freedom of movement, we propose to attach the IMU on the instep, i.e., the dorsal side of the midfoot. If functional foot motion angles (yaw, pitch, and roll) are to be determined, we have to impose one slight restriction to the mounting of the sensor: In this case, one known sensor axis has to lie in the sagittal plane, pointing roughly forward (which is usually easy to achieve when mounting the IMU on the instep). The calculation of all other gait parameters does not make use of this assumption.

We obtain the gyroscope and accelerometer readings of both IMUs at a fixed sampling rate (typically in the range 50–1000 Hz). We assume that data for several steps is processed at

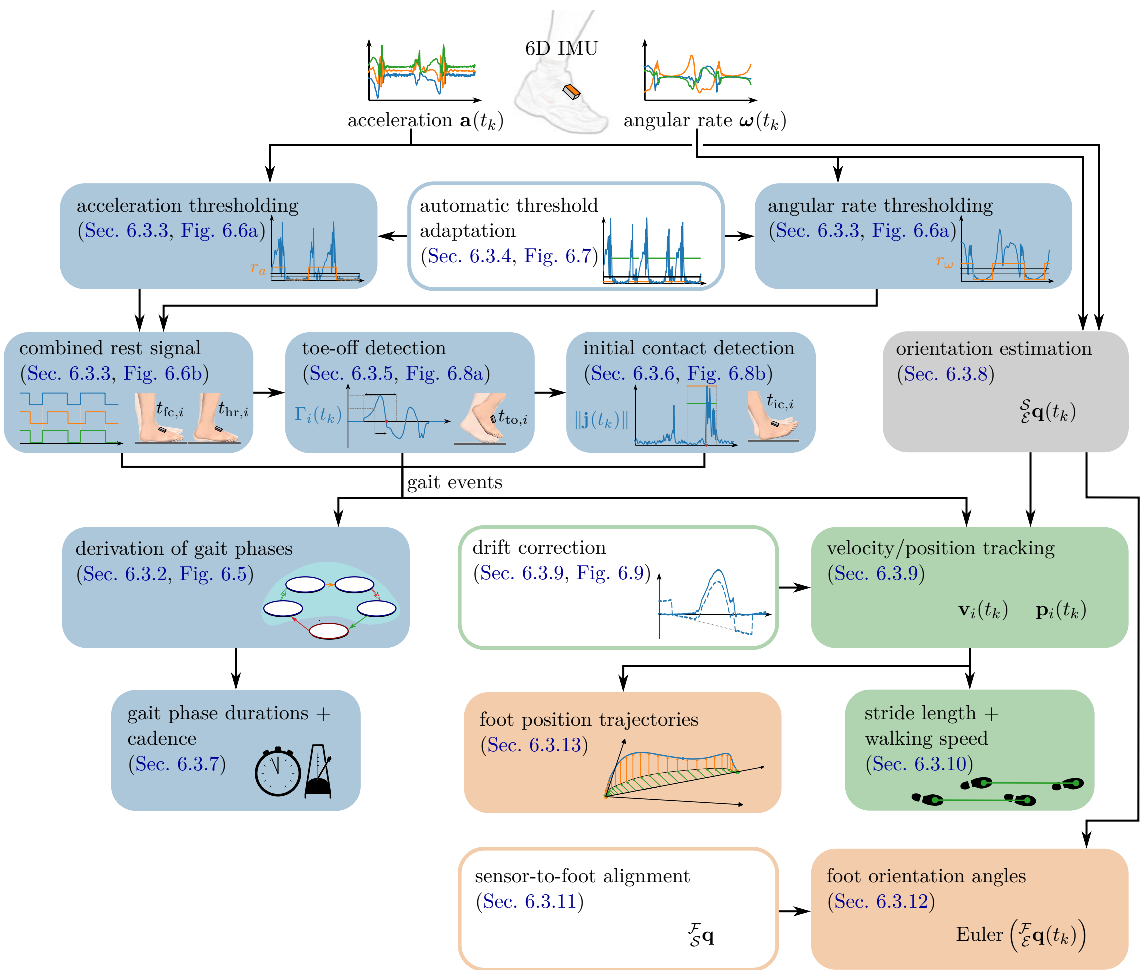

Figure 6.2: Overview of the proposed modular set of methods to determine spatiotemporal gait parameters and position/angle trajectories from foot-worn IMUs. While gait phase durations and cadence are determined from gait events, stride length and walking speed are derived from a position trajectory obtained via piecewise strapdown integration of the acceleration.

once, which allows us to employ acausal signal processing to increase the accuracy compared to sample-by-sample real-time capable methods. This processing can either be performed in batches while the subject is walking, e.g., for use in biofeedback applications, or after the recording is completed. During the recording, the subject walks either on a treadmill or on indoor or outdoor ground.

The set of proposed methods is explained in the following subsections, and the presentation is structured as follows. Separately for each foot, we use the recorded sensor data to separate phases in which the foot is in full contact with the ground from phases in which the foot moves, i.e., we detect when strides take place (Section 6.3.3). For each detected stride, we then detect toe-off (Section 6.3.5) and initial contact (Section 6.3.6). The gait events from the ipsilateral and contralateral foot are combined to define gait phases. We calculate the relative duration of each gait phase and the cadence (Section 6.3.7). We then estimate the sensor orientation by sensor fusion of the gyroscope and accelerometer readings (Section 6.3.8) and double-integrate the acceleration to obtain the position (Section 6.3.9). From this position, we obtain the stride length and the walking speed (Section 6.3.10) as well as the vertical lift and lateral shift position trajectories (Section 6.3.13). Based on a sensor-to-foot alignment (Section 6.3.11), we derive physiologically meaningful yaw, pitch, and roll angles from the sensor orientation (Section 6.3.12). Figure 6.2 provides an overview of the proposed set of methods.

In the remainder of this section, we define several parameters that are used by the method. For an overview of those parameters and proposed values, please refer to Table 6.2 in Section 6.4. Note that we define the parameters in a way so that they are not sensitive to different gait styles or velocities. Section 6.4 demonstrates that this approach works by only employing one common set of parameters for validation on a very broad dataset with healthy and non-healthy subjects walking at different speeds.

6.3.1 Notation

Denote the gyroscope readings $\boldsymbol{\omega}(t_k) \in \mathbb{R}^3$ and the accelerometer readings $\mathbf{a}(t_k) \in \mathbb{R}^3$, sampled at times $t_k = kT_\mathrm{s}$, $k \in \{1, 2, \dots, N\}$, $T_\mathrm{s} \in \mathbb{R}_{>0}$.

In the following, all times t with any index are multiples of T_s. If any calculation yields a time that is not a multiple of T_s, we assume that this value is rounded to the nearest multiple of T_s and do not explicitly write this for the sake of a compact notation. Furthermore, any summation over τ should be interpreted as a summation with a non-integer step size of T_s, i.e., we write $\sum_{\tau=t_1}^{t_2} x(\tau)$ instead of the longer but mathematically precise notation $\sum_{k=k_1}^{k_2} x(t_k), k_1 = \frac{t_1}{T_\mathrm{s}}, k_2 = \frac{t_2}{T_\mathrm{s}}$.

6.3.2 Gait Events and Gait Phases

According to standard literature [198] and as illustrated in Figure 6.3, the gait cycle starts at initial contact. Each stride can be separated into *stance* and *swing*. Stance consists of the gait phases *loading response*, *mid-stance*, *terminal stance*, and *pre-swing*. Swing can be separated into *initial swing*, *mid-swing*, and *terminal swing*. The combination of mid-stance and terminal stance is called *single limb support* and corresponds to the swing phase of the contralateral foot. In standard literature [198], the initial contact is commonly considered to be a very short gait phase with a duration of 2 %. As it is common practice in IMU-based gait

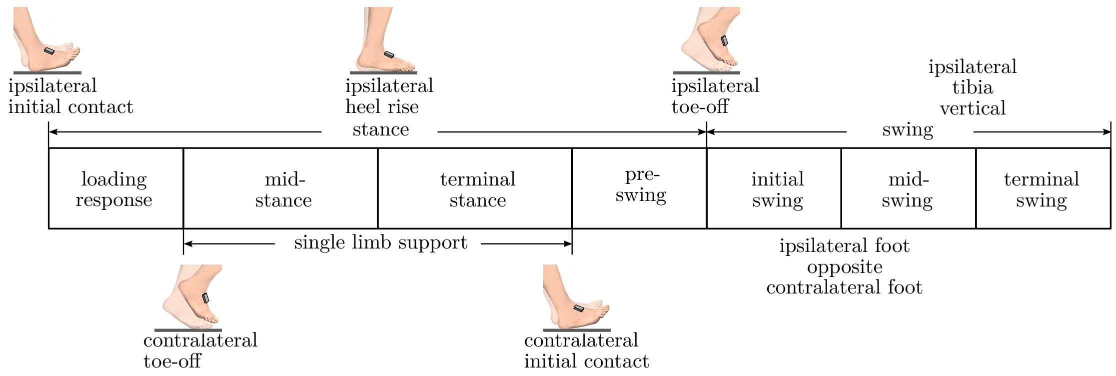

Figure 6.3: Definition of gait phases as used in standard literature, cf. [198], and transitions based on gait events of the ipsilateral and contralateral foot. While the distinction between stance and swing is only based on the movement of the respective foot, determining the full set of gait phases requires information from both feet.

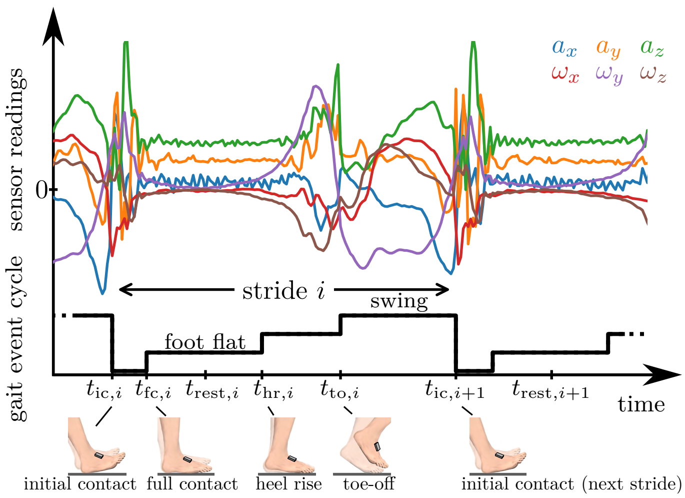

Figure 6.4: Raw accelerometer and gyroscope sensor readings and representation of the gait event cycle with a staircase-shaped signal. We define time instants $t_{\mathrm{ic},i}$, $t_{\mathrm{fc},i}$, $t_{\mathrm{hr},i}$, $t_{\mathrm{to},i}$ that mark characteristic events and a rest instant $t_{\mathrm{rest},i}$ in the middle of the phase in which the foot is fully on the ground (foot flat).

analysis [16, 186, 191, 193], we define the initial contact as an event without duration. Note that sometimes the initial contact is also called foot strike [186] or heel strike [16].

The separation between stance and swing and the separation of stance into loading response, mid-stance, terminal stance, and pre-swing is defined based on three events that describe a change of ground contact of the feet: *initial contact*, *heel rise*, and *toe-off*. In contrast, the separation of swing into initial swing, mid-swing, and terminal swing is based on positional information of the feet and on the tibia orientation. The gait phases are defined based on bilateral events, i.e., the gait phase of the ipsilateral foot is not only described based on the events of the same (ipsilateral) foot but also based on toe-off and initial contact of the other (contralateral) foot.

We will now discuss how to use IMUs to determine five of those gait phases (swing and the four sub-phases of stance) in a two-step approach. First, we detect four gait events independently for each foot. We then use this gait event cycle of both feet to derive gait phases for each foot.

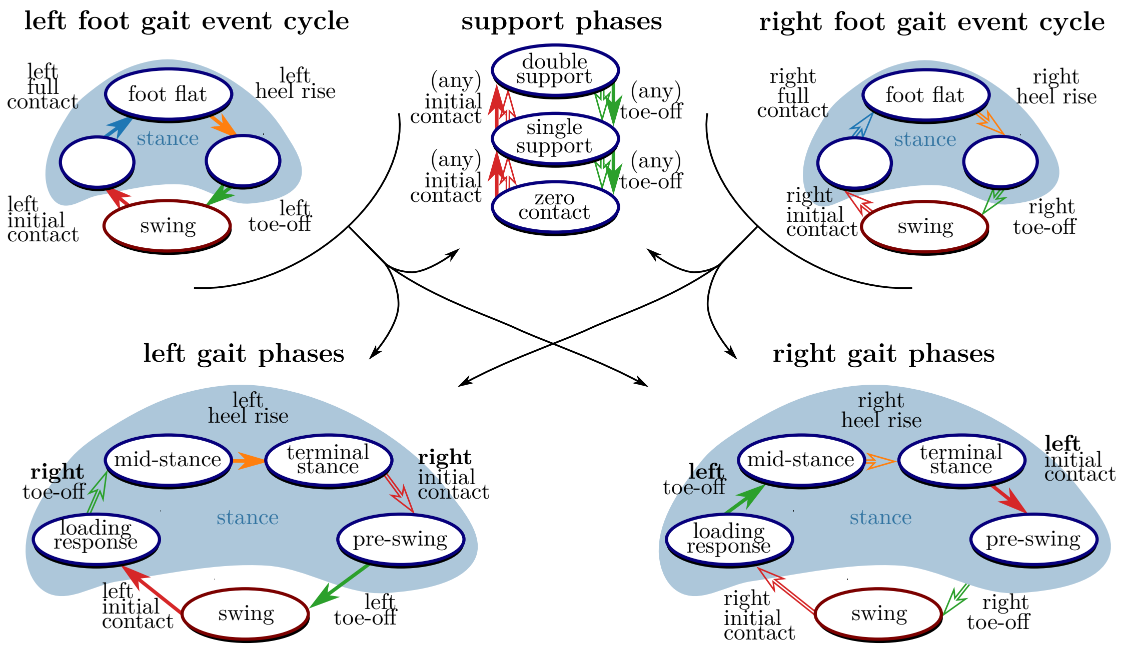

Figure 6.5: Derivation of clinically relevant gait phases from the gait event cycles. Following standard literature [198], events from both the left foot (filled arrows) and the right root (outlined arrows) are necessary to define the gait phase of each foot. Furthermore, support phases based on the number of feet that are in contact with the ground can be defined based on the gait events.

To this end, for each stride $i \in \{1, 2, \ldots, M\}$, we define the following events that we aim to detect independently for the right and left foot from the raw measurement data of the corresponding IMU:

- initial contact – $t_{\mathrm{ic},i}$,
- full contact – $t_{\mathrm{fc},i}$,
- heel rise – $t_{\mathrm{hr},i}$,
- toe-off – $t_{\mathrm{to},i}$.

Note that in addition to the three events used to define gait phase transitions in Figure 6.3, we introduce an event called *full contact*, which indicates that the foot is in full contact with the ground. For various processing steps, such as zero-velocity updates and position integration, we further define a rest instant $t_{\mathrm{rest},i}$ in the middle of the foot flat phase, i.e.,

$$t_{\mathrm{rest},i} := \frac{1}{2}\left(t_{\mathrm{fc},i} + t_{\mathrm{hr},i}\right). \tag{6.1}$$

See Figure 6.4 for a plot of the raw accelerometer and gyroscope data measured during one stride, along with a graphical representation of the gait event cycle defined by the introduced events. In the following subsections, we will discuss in detail how we determine those time instants from the raw sensor data.

After having determined the gait events for both feet, we use the gait event cycles from both feet to determine the gait phase according to the commonly used definitions by [198]. As shown in Figure 6.5, finite automata for the gait phases of the left and right foot are each driven by the gait event cycles of both feet.

Since time instants from both sensors are used for the definition of the gait phase transitions, both feet must be equipped with sensors, and precise time synchronization is required. However, note that the separation into stance and swing directly follows from the gait event cycle (as shown in Figure 6.5) and is independent of the contralateral foot. Therefore, we can determine stance and swing regardless of the synchronization between the sensors. This is also useful if only one foot is equipped with a sensor and facilitates on-chip data processing.

Note that the three sub-phases of stance in the gait event cycle hold further information that is not directly captured by the standard gait phase definitions as given in Figure 6.3. We denote the phase from $t_{\mathrm{fc},i}$ to $t_{\mathrm{hr},i}$, in which the foot is fully on the ground, as *foot flat*. Note that the other two sub-phases of the stance phase, $t_{\mathrm{ic},i}$ to $t_{\mathrm{fc},i}$ and $t_{\mathrm{hr},i}$ to $t_{\mathrm{to},i}$, are sometimes called loading response and pre-swing [191, 193] but do not correspond to the phases with the same name as defined in standard literature [198].

Furthermore, as also shown in Figure 6.5, time-synchronized events from both feet also allow for the distinction of *double support*, *single support*, and (during running [198]) *zero-contact* phases.

6.3.3 Foot Flat Detection

As the first step of gait phase detection, the phases in which the foot is fully on the ground (foot flat) are detected. When the foot is fully on the ground, the Euclidean norm of the accelerometer readings will be close to $9.81\,\mathrm{m/s^2}$, and the norm of the gyroscope readings will be close to zero. During a stride, we will typically see an increase in the signal norms. However, it is possible that during the motion phase, there are long periods with only small changes in velocity or small rotations. To obtain a robust stride detection, we therefore first find activity using either the accelerometer or the gyroscope readings and then combine this information.

For an acceleration-based rest signal $r_a(t_k)$, in which zero denotes rest and one denotes motion, we consider the absolute difference of the accelerometer norm from $9.81\,\mathrm{m/s^2}$,

$$a(t_k) := \left|\|\mathbf{a}(t_k)\| - 9.81\right|. \tag{6.2}$$

We then perform acausal thresholding using a threshold a_{th} and a hysteresis factor h_a by applying hysteresis in forward and backward direction, i.e.,

$$r_a^*(t_k) := \begin{cases} 1 & a(t_k) > (1+h_a)a_{\mathrm{th}} \\ 0 & a(t_k) < (1-h_a)a_{\mathrm{th}} \\ r_a(t_{k-1}) & \text{otherwise,} \end{cases} \tag{6.3}$$

$$r_a(t_k) := \begin{cases} 1 & r_a^*(t_k) = 1 \\ 0 & a(t_k) < (1-h_a)a_{\mathrm{th}} \\ r_a(t_{k+1}) & \text{otherwise,} \end{cases} \tag{6.4}$$

with $r_a^*(0) = 0$ and $r_a(t_N) = r_a^*(t_N)$. In the resulting signal, zero-phases shorter than $T_{0,\min}$ are set to one, and afterward, one-phases shorter than $T_{1,\min}$ are set to zero.

The same acausal thresholding with the removal of short phases is applied to the gyroscope norm signal $\omega(t_k) := \|\boldsymbol{\omega}(t_k)\|$ using a threshold ω_{th} and hysteresis factor h_ω, which yields

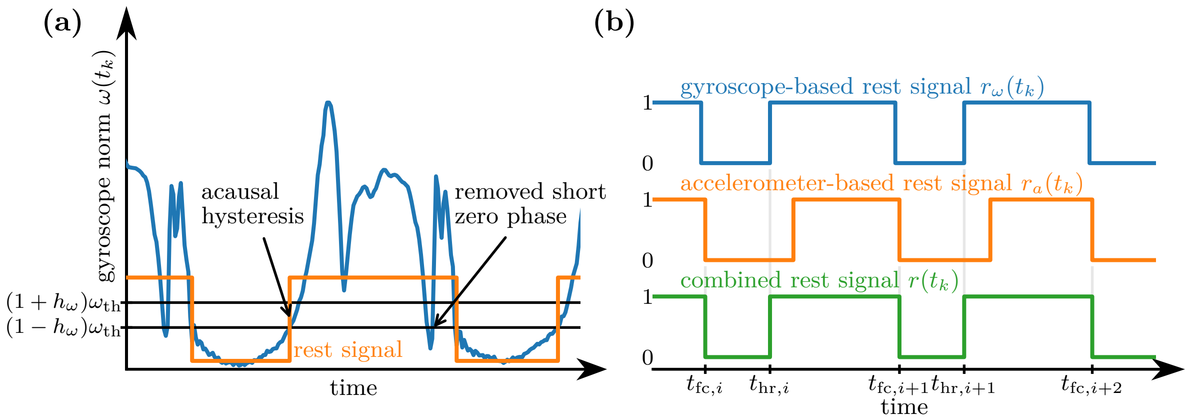

Figure 6.6: Foot flat detection. **(a)** Illustration of the thresholding algorithm. Acausal hysteresis and the removal of short phases ensure the robust detection of the desired rest phase. **(b)** Illustration of the combination of $r_\omega(t_k)$ and $r_a(t_k)$ into $r(t_k)$. By using the Boolean *OR* combination of the accelerometer- and gyroscope-based signals, we are able to robustly detect when the foot is not fully on the ground.

a gyroscope-based rest signal $r_\omega(t_k)$. See Figure 6.6a for an illustration of the thresholding method.

Both rest signals, $r_a(t_k)$ and $r_\omega(t_k)$, are combined into $r(t_k)$, which is set to one if at least one of the two signals is one. Afterward, zero-phases shorter than $T_{0,\mathrm{min}}$ are set to one, and then one-phases shorter than $2T_{1,\mathrm{min}}$ are set to zero. This process is illustrated in Figure 6.6b. Each zero-to-one transition of the resulting signal marks a heel rise $t_{\mathrm{hr},i}$, and each one-to-zero transition marks a full contact $t_{\mathrm{fc},i+1}$.

6.3.4 Automatic Threshold Adaptation

A common issue with thresholding approaches is that the thresholds have to be adapted based on gait velocity and also other gait and sensor characteristics [191, 192]. Therefore, instead of performing the thresholding of the accelerometer and gyroscope norm using manually tuned thresholds a_{th} and ω_{th}, we employ an algorithm that automatically determines these thresholds for each trial based on the measured data.

The threshold a_{th} is determined using an iterative algorithm similar to [212], with $l \in \mathbb{N}$ being the iteration index and $w_a \in [0, 1]$ being a weighting parameter:

$$a_{\mathrm{th},0} = \frac{1}{2}\left(\max_{t_k\in[t_1,t_N]} a(t_k) + \min_{t_k\in[t_1,t_N]} a(t_k)\right), \tag{6.5}$$

$$T^+ = \{t_k \in [t_1, t_N] | a(t_k) > a_{\mathrm{th},l}\}, \tag{6.6}$$

$$T^- = \{t_k \in [t_1, t_N] | a(t_k) \leq a_{\mathrm{th},l}\}, \tag{6.7}$$

$$a_{\mathrm{th},l+1} = \frac{w_a}{|T^-|}\sum_{t_k\in T^-} a(t_k) + \frac{1-w_a}{|T^+|}\sum_{t_k\in T^+} a(t_k). \tag{6.8}$$

We perform 200 iterations to ensure convergence, i.e., $a_{\mathrm{th}} := a_{\mathrm{th},200}$. Figure 6.7 illustrates the result of this process. Further, we define a lower bound $a_{\mathrm{th,min}}$ for this threshold.

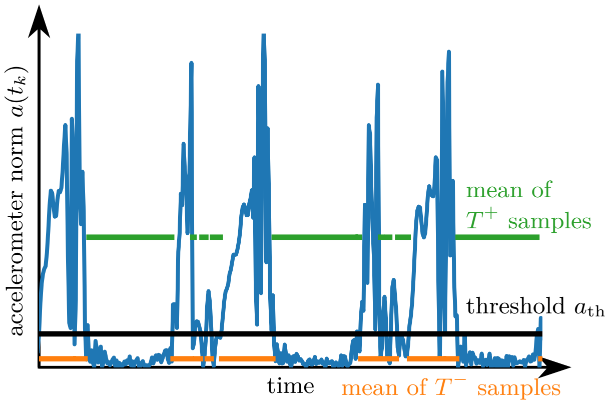

Figure 6.7: Illustration of the result of the automatic thresholding algorithm for a short segment of accelerometer data. The threshold a_{th} is chosen such that the mean of the values above and the mean of the values below are in a certain proportion.

Similarly, we determine the threshold ω_{th} based on the gyroscope norm $\omega(t_k)$ and a weighting factor w_ω.

6.3.5 Toe-off Detection

After determining heel rise and full contact, we detect the beginning of the swing phase, i.e., the toe-off. During toe-off, the foot first rotates approximately along the mediolateral axis as the heel rises, then loses contact with the ground and rotates in the opposite direction. An IMU attached to the foot cannot directly measure when the foot fully loses contact with the ground, in contrast to, e.g., pressure-sensitive walkways. Note that the accuracy of toe-off detection using pressure sensors also depends on calibration and the chosen thresholds [172].

As rotation can be measured precisely with IMUs, we exploit the fact that the direction of the foot rotation changes when transitioning from the phase in which the heel rises while the toe stays on the ground to the phase in which the toe leaves the ground. This approach is commonly used in existing literature, as detailed in Section 6.2. However, most methods directly rely on the angular rate measured in the sagittal plane and thereby require at least one sensor axis to be well-aligned with a functional axis of the foot.

To be independent of the sensor orientation and also to obtain a reliable detection if the subject exhibits strong inversion or eversion during toe-off, we define a signal called tilt-rate $\Gamma_i(t_k)$ [191], from each heel rise $t_{\text{hr},i}$ to the subsequent full contact $t_{\text{fc},i+1}$, as

$$\Gamma_i(t_k) := \boldsymbol{\omega}(t_k)^\intercal \frac{\sum_{\tau=t_{\text{hr},i}}^{t_k} \boldsymbol{\omega}(\tau)}{\left\| \sum_{\tau=t_{\text{hr},i}}^{t_k} \boldsymbol{\omega}(\tau) \right\|}, t_k \in [t_{\text{hr},i}, t_{\text{fc},i+1}]. \tag{6.9}$$

The rationale behind the definition of the tilt-rate $\Gamma_i(t_k)$ is to identify the main axis of rotation since the last heel rise and compute the current rate of rotation around this main axis. This enables us to detect a zero-crossing of the main rotation without making any assumptions about the orientation of the sensor with respect to the foot.

In general, the tilt-rate $\Gamma_i(t_k)$ will exhibit a change of sign after a distinct peak, as illustrated in Figure 6.8a. Since there might be noise, leading to frequent sign changes right after $t_{\text{hr},i}$,

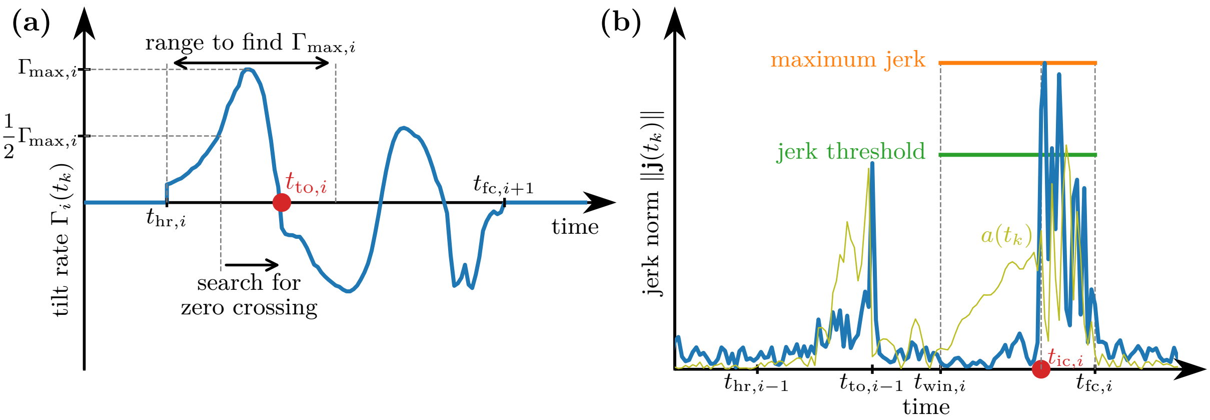

Figure 6.8: Detection of toe-off and initial contact events that define the swing phase. **(a)** Illustration of the toe-off detection. Between heel rise and full contact, the tilt rate might exhibit multiple local maxima and zero-crossings. For a robust detection of the correct zero-crossing, we first find the maximum value during the first half of the phase from $t_{\mathrm{hr},i}$ to $t_{\mathrm{fc},i+1}$ and search for the first zero-crossing after the tilt rate has reached half of this maximum. **(b)** Illustration of the initial contact detection based on the jerk norm. Note how the jerk norm reflects the sudden change when the foot touches the ground much better than the accelerometer norm signal $a(t_k)$.

as well as large peaks later during the stride, we employ the following strategy to robustly determine the sign change of interest:

Let $\Gamma_{\max,i}$ denote the maximum value of $\Gamma_i(t_k)$ during the first half of the movement phase:

$$\Gamma_{\max,i} := \max_{t_k \in [t_{\mathrm{hr},i}, \frac{1}{2}(t_{\mathrm{hr},i} + t_{\mathrm{fc},i+1})]} \Gamma_i(t_k). \tag{6.10}$$

We then find the first time instant for which $\Gamma_i(t_k) \geq \frac{1}{2}\Gamma_{\max,i}$. Starting from this time instant, we find the first time instant at which $\Gamma_i(t_k) \leq 0$. We assume this time instant to be the toe-off $t_{\mathrm{to},i}$, i.e., the start of the swing phase. Figure 6.8a illustrates this process.

Note that $t_{\mathrm{to},i}$ is defined based on a feature of the rotation of the foot and not directly as the lift-off of the toes. Using the maximum of the tilt rate or any weighted average of the maximum and zero-crossing time instant are also plausible approaches.

6.3.6 Initial Contact Detection

The initial contact marks the beginning of the loading response and can be detected by the jerk, i.e., the change of acceleration, caused by the foot touching the ground. We calculate the jerk using the first-order backward difference approximation, i.e.,

$$\mathbf{j}(t_k) := \frac{1}{T_\mathrm{s}} \left(\mathbf{a}(t_k) - \mathbf{a}(t_{k-1}) \right). \tag{6.11}$$

For every stride, we only consider a sub-window of the phase between toe-off and the beginning of the subsequent foot-flat phase and denote the start time of this window as $t_{\mathrm{win},i} := j_{\mathrm{win}} t_{\mathrm{to},i-1} + (1 - j_{\mathrm{win}}) t_{\mathrm{fc},i}$, $j_{\mathrm{win}} \in [0, 1]$. In this time window, we determine the maximum value of the jerk norm, i.e.,

$$j_{\max,i} := \max_{t_k \in [t_{\mathrm{win},i}, t_{\mathrm{fc},i}]} \|\mathbf{j}(t_k)\|. \tag{6.12}$$

We then mark the first time instant in this window with $\|\mathbf{j}(t_k)\| \geq j_{\text{th}} j_{\text{max},i}$ as the start of the loading response $t_{\text{ic},i}$. See Figure 6.8b for an illustration of the initial contact detection.

6.3.7 Stride and Gait Phase Durations and Cadence

For each detected stride, we calculate the stride duration as the duration from one initial contact to the subsequent initial contact of the same foot, i.e.,

$$T_{\text{stride},i} := t_{\text{ic},i+1} - t_{\text{ic},i}. \tag{6.13}$$

For each detected stride, the duration of the swing phase is the time between toe-off and initial contact of the subsequent stride, i.e.,

$$T_{\text{swing},i} := t_{\text{ic},i+1} - t_{\text{to},i}. \tag{6.14}$$

The stance duration is the remaining duration of the stride:

$$T_{\text{stance},i} := T_{\text{stride},i} - T_{\text{swing},i}. \tag{6.15}$$

Since relative gait phase durations are easier to interpret, we calculate

$$T_{\text{swing,rel},i} := \frac{T_{\text{swing},i}}{T_{\text{stride},i}}, \tag{6.16}$$

$$T_{\text{stance,rel},i} := \frac{T_{\text{stance},i}}{T_{\text{stride},i}}. \tag{6.17}$$

Similarly, for every stride, we calculate relative gait phase durations for loading response $T_{\text{lr,rel},i}$, single limb support $T_{\text{sl,rel},i}$, terminal stance $T_{\text{ts,rel},i}$, and pre-swing $T_{\text{ps,rel},i}$, based on the bilateral gait phases as defined in Figure 6.3. Note that analogously, we can also calculate absolute and relative durations for all other gait phases defined in Figure 6.3.

To calculate the cadence, we multiply the inverse of the stride duration by two in order to express the cadence as the number of steps per minute instead of strides per minute, i.e.,

$$c_i := \frac{2}{T_{\text{stride},i}}. \tag{6.18}$$

6.3.8 Orientation Estimation

By fusing the gyroscope and accelerometer measurements, we obtain an estimate of the sensor orientation ${}^{\mathcal{S}}_{\mathcal{E}}\mathbf{q}(t_k)$ with respect to a global frame that has a vertical z-axis and an arbitrary heading.[1] Since data is processed in batches, we employ the OfflineVQF method introduced in Chapter 3.

Note that in the version of this method published in [159], a predecessor of the OfflineVQF method was introduced. This predecessor used a moving average low-pass filter instead of a Butterworth low-pass filter for inclination correction and did not support gyroscope bias

[1] To avoid confusion with the stride index i, we omit the sensor index and use $\mathcal{E}$ instead of $\mathcal{E}_i$ to denote the slowly-drifting 6D reference frame.

estimation. In this thesis, the IOE algorithm is only changed for sake of consistency, and the impact on the obtained results is marginal.

6.3.9 Foot Velocity and Position Tracking

Using the estimated orientation, we perform double integration of the measured accelerations to estimate the length of each stride, i.e., the horizontal displacement between two adjacent foot-flat phases.

To integrate the accelerations, they are first transformed into the reference frame

$$[\mathbf{a}]_{\mathcal{E}}(t_k) := {}^{\mathcal{S}}_{\mathcal{E}}\mathbf{q}(t_k) \otimes \mathbf{a}(t_k) \otimes {}^{\mathcal{S}}_{\mathcal{E}}\mathbf{q}(t_k)^{-1}. \tag{6.19}$$

Assuming that the velocity is zero in the middle of the foot-flat phase, i.e., at $t_{\mathrm{rest},i}$, we integrate those accelerations for each stride which yields the velocity

$$\mathbf{v}_i(t_k) := T_{\mathrm{s}} \sum_{\tau=t_{\mathrm{rest},i}}^{t_k} \left([\mathbf{a}]_{\mathcal{E}}(\tau) - [\,0\ \ 0\ \ 9.81\,]^\intercal\right), \quad t_k \in [t_{\mathrm{rest},i}, t_{\mathrm{rest},i+1}]. \tag{6.20}$$

Due to measurement errors, mainly accelerometer bias and orientation estimation errors, this velocity is usually not zero at $t_{\mathrm{rest},i+1}$, even if the foot is perfectly at rest. We correct this drift linearly over the duration of the stride:

$$\mathbf{v}_{\mathrm{df},i}(t_k) := \mathbf{v}_i(t_k) - \frac{t_k - t_{\mathrm{rest},i}}{t_{\mathrm{rest},i+1} - t_{\mathrm{rest},i}} \mathbf{v}_i(t_{\mathrm{rest},i+1}), \quad t_k \in [t_{\mathrm{rest},i}, t_{\mathrm{rest},i+1}]. \tag{6.21}$$

See Figure 6.9 for an example velocity trajectory with and without drift correction.

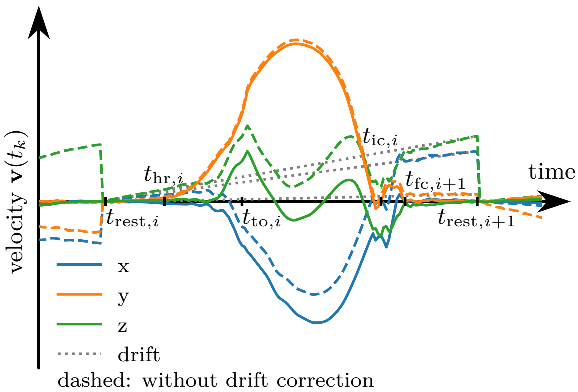

Figure 6.9: Velocity trajectories with (solid) and without (dashed) linear drift correction. The dotted lines represent the subtracted linear drift approximation. For demonstration purposes, the drift has been artificially increased by a factor of 10.

By integrating this drift-free velocity over the stride duration, we obtain a position trajectory

$$\mathbf{p}_i(t_k) := T_{\mathrm{s}} \sum_{\tau=t_{\mathrm{rest},i}}^{t_k} \mathbf{v}_{\mathrm{df},i}(\tau) =: [\,p_{i,x}(t_k)\ \ p_{i,y}(t_k)\ \ p_{i,z}(t_k)\,]^\intercal, \quad t_k \in [t_{\mathrm{rest},i}, t_{\mathrm{rest},i+1}]. \tag{6.22}$$

6.3.10 Stride Length and Walking Speed

We calculate the stride length L_i as the horizontal displacement during stride i. Since $\mathbf{p}_i(t_{\mathrm{rest},i}) = 0$,

$$L_i := \sqrt{p_{i,x}(t_{\mathrm{rest},i+1})^2 + p_{i,y}(t_{\mathrm{rest},i+1})^2}. \tag{6.23}$$

Note that this method does not make any assumption about the orientation in which the sensor is attached to the foot. Also, note that we integrate from $t_{\mathrm{rest},i}$ to $t_{\mathrm{rest},i+1}$ and not from $t_{\mathrm{ic},i}$ to $t_{\mathrm{ic},i+1}$ since this makes the zero-velocity assumption more robust.

By dividing the stride length by the stride duration, we obtain the walking speed

$$v_i := \frac{L_i}{T_{\mathrm{stride},i}}. \tag{6.24}$$

6.3.11 Sensor-to-Foot Alignment

To facilitate the derivation of physiological foot angles, sensor-to-foot alignment is performed, i.e., the relative orientation between the sensor coordinate system $\mathcal{S}$ and the foot coordinate system $\mathcal{F}$, as illustrated in Figure 6.10, is determined. To define this relative orientation, two axes of $\mathcal{F}$ need to be known in $\mathcal{S}$ coordinates.

An estimate for the z-axis $[\mathbf{z}_\mathcal{F}]_\mathcal{S}$ of the foot, expressed in sensor coordinates, is obtained by averaging the accelerometer measurements during all foot-flat phases and normalizing the resulting vector:

$$[\mathbf{z}_\mathcal{F}]_\mathcal{S} = \frac{\sum_{i=1}^{M} \sum_{\tau=t_{\mathrm{fc},i}}^{t_{\mathrm{hr},i}} \mathbf{a}(\tau)}{\left\| \sum_{i=1}^{M} \sum_{\tau=t_{\mathrm{fc},i}}^{t_{\mathrm{hr},i}} \mathbf{a}(\tau) \right\|}. \tag{6.25}$$

Making use of the fact that the negative y-axis of the IMU points forward and down (due to the sensor attachment on the instep), the y-axis of the foot in sensor coordinates is given by

$$[\mathbf{y}_\mathcal{F}]_\mathcal{S} = [\mathbf{z}_\mathcal{F}]_\mathcal{S} \times \begin{bmatrix} 0 & -1 & 0 \end{bmatrix}^\intercal. \tag{6.26}$$

Those two axes define the foot-to-sensor quaternion ${}^\mathcal{F}_\mathcal{S}\mathbf{q}$, which we obtain by converting the corresponding rotation matrix

$${}^\mathcal{F}_\mathcal{S}\mathbf{R} = \begin{bmatrix} \frac{[\mathbf{y}_\mathcal{F}]_\mathcal{S} \times [\mathbf{z}_\mathcal{F}]_\mathcal{S}}{\left\|[\mathbf{y}_\mathcal{F}]_\mathcal{S} \times [\mathbf{z}_\mathcal{F}]_\mathcal{S}\right\|} & \frac{[\mathbf{y}_\mathcal{F}]_\mathcal{S}}{\left\|[\mathbf{y}_\mathcal{F}]_\mathcal{S}\right\|} & \frac{[\mathbf{z}_\mathcal{F}]_\mathcal{S}}{\left\|[\mathbf{z}_\mathcal{F}]_\mathcal{S}\right\|} \end{bmatrix} \tag{6.27}$$

to a quaternion.

Finally, this foot-to-sensor quaternion ${}^\mathcal{F}_\mathcal{S}\mathbf{q}$ is used to determine the orientation of the foot $\mathcal{F}$ relative to the reference frame $\mathcal{E}$:

$${}^\mathcal{F}_\mathcal{E}\mathbf{q}(t_k) = {}^\mathcal{S}_\mathcal{E}\mathbf{q}(t_k) \otimes {}^\mathcal{F}_\mathcal{S}\mathbf{q}. \tag{6.28}$$

6.3.12 Foot Orientation Angles

Foot orientation angles are obtained by calculating intrinsic z-x'-y'' Euler angles of the foot orientation ${}^\mathcal{F}_\mathcal{E}\mathbf{q}(t_k)$.

The third Euler angle, corresponding to the y''-axis, is called pitch, and the sign is inverted so that dorsal flexion corresponds to a positive angle.

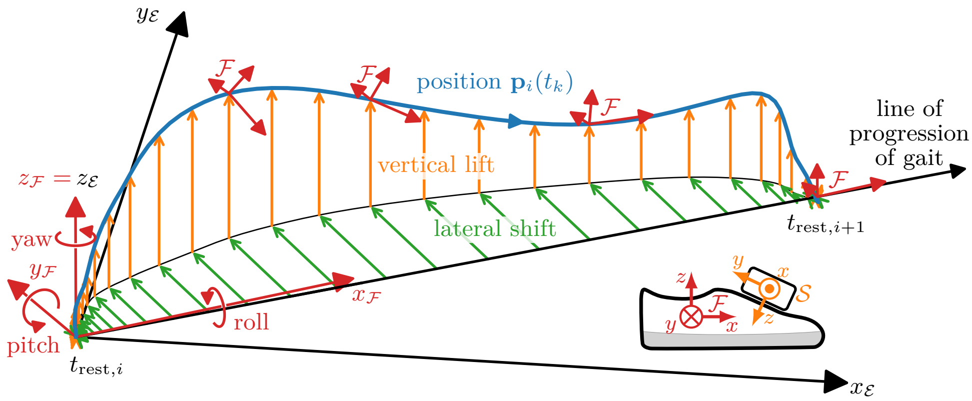

Figure 6.10: Illustration of the foot coordinate system and position trajectories for an exemplary gait cycle of a left foot. The foot coordinate system $\mathcal{F}$ is defined with the x-axis pointing forward, the y-axis pointing to the right, and the z-axis pointing up and, in general, different from the IMU coordinate system $\mathcal{S}$. The angles pitch, roll, and yaw are defined so that dorsal flexion, inversion, and out-toeing, respectively, are positive. (Notice the small amount of out-toeing at $t_{\text{rest},i}$). The position trajectories lateral shift and vertical lift are defined based on the line of progression of gait. For illustration purposes, the displayed lateral shift and vertical lift are increased by a factor of 3.

The second Euler angle (x') is roll. The sign is inverted for the left foot so that inversion corresponds to positive angles.

The first Euler angle (z) is yaw. Since magnetometers are not used, the original yaw angle has an arbitrary offset. To obtain the foot progression angle (i.e., an angle that is zero when the x-axis of the foot points along the line of progression of gait), the heading of the line of progression of gait is estimated from the position trajectory as

$$\delta_{\text{progression},i} = \operatorname{atan2}(p_{i,y}(t_{\text{rest},i+1}) - p_{i,y}(t_{\text{rest},i}), p_{i,x}(t_{\text{rest},i+1}) - p_{i,x}(t_{\text{rest},i})). \tag{6.29}$$

This offset $\delta_{\text{progression},i}$ is removed from the original yaw angle. To ensure that out-toeing corresponds to positive angles, the sign of the angle is inverted for the right foot.

6.3.13 Foot Position Trajectories

From the full 3D position $\mathbf{p}_i(t_k)$, two scalar position trajectories are derived: vertical lift and lateral shift. Vertical lift is defined as the vertical position of the IMU relative to the position during stance. Assuming level ground, a linear drift is subtracted for each stride, i.e., the vertical lift is calculated as

$$p_{\text{lift},i}(t_k) = p_{i,z}(t_k) - p_{i,z}(t_{\text{rest},i}) - \frac{t_k - t_{\text{rest},i}}{t_{\text{rest},i+1} - t_{\text{rest},i}} \left(p_{i,z}(t_{\text{rest},i+1}) - p_{i,z}(t_{\text{rest},i})\right). \tag{6.30}$$

The lateral shift $p_{\text{shift},i}(t_k)$ is defined as the deviation of the position in the horizontal plane from the straight line of progression of gait, i.e., the distance of the point $(p_{i,x}(t_k), p_{i,y}(t_k))$ from the line defined by the two points $(p_{i,x}(t_{\text{rest},i}), p_{i,y}(t_{\text{rest},i}))$ and $(p_{i,x}(t_{\text{rest},i+1}), p_{i,y}(t_{\text{rest},i+1}))$. Figure 6.10 illustrates the definitions of the foot coordinate systems, the angles, and the position trajectories.

6.3.14 Summary of the Estimated Parameters

After performing the steps presented above, the set of proposed methods provides the time instants of the defined gait events, the sensor orientation quaternion for each time instant, and velocity and position trajectories. From those time-based signals, the following scalar gait parameters are extracted for each stride i:

- swing duration $T_{\text{swing,rel},i}$ [%],
- stance duration $T_{\text{stance,rel},i}$ [%],
- analogously, relative durations for the other gait phases as defined in Figure 6.5,
- stride length L_i [cm],
- walking speed v_i [km/h],
- cadence c_i [steps/min].

The accuracy of those gait parameters is validated in Section 6.4.

Furthermore, the following position and angle trajectories are calculated for each stride i:

- pitch angle (positive angle: dorsal flexion) [°],
- roll angle (positive angle: inversion) [°],
- yaw angle (positive angle: out-toeing) [°],
- vertical lift position $p_{\text{lift},i}$ [cm],
- lateral shift position $p_{\text{shift},i}$ [cm].

The accuracy of those gait parameters is validated in Section 6.5.

Note that all quantities are calculated separately for each stride of each foot. In many cases, only the mean of those values over multiple steps will be of interest. However, this stepwise calculation also allows for the analysis of the variability and the detection of trends.

6.4 Experimental Validation of Spatiotemporal Parameters

This section validates that the less restrictive IMU-based setup combined with the methods proposed in Section 6.3 is able to determine the same parameters as stationary systems that are used in clinical practice while providing similar accuracy. To this end, with a large dataset consisting of three different subject groups, we compare the parameters calculated by the proposed methods with values reported by instrumented treadmills.

6.4.1 Setup

One IMU (PABLO Motion Sensor, Tyromotion GmbH, Graz, Austria) was attached to each shoe, as shown in Figure 6.11a. The sensors measure angular rate and acceleration at a sampling frequency of 110 Hz. Each sensor has a size of 56 mm × 34 mm × 21 mm and transmits the

(b)

(a)

Figure 6.11: Experimental setup. **(a)** Patient with inertial sensors attached to the shoe. **(b)** Instrumented treadmill at NTK Kapfenberg. Gait parameters are derived from the measurement data of the inertial sensors with the proposed methods and validated against parameters obtained from the instrumented treadmill serving as ground truth.

data wirelessly using Bluetooth. The sensors were attached to the subjects' shoes with special Velcro straps.

Zebris Rehawalk instrumented treadmills (Zebris Medical, Isny, Germany) were used as reference systems. Since the data collection took place in various institutions (FH Joanneum Graz, NTK Kapfenberg, Rehabilitation Center Kitzbühel), different systems with identical function were used. See Figure 6.11b for a picture of the setup at NTK Kapfenberg.

- FH Joanneum (Graz, Austria)
  - Treadmill: h-p-c Mercury Med Treadmill (HP Cosmos, Nussdorf, Germany), walking speed: 0–22 km/h in 0.1 km/h steps, walking surface: 150 cm × 50 cm.
  - Pressure measuring platform: FDM-THM-M-3i (Zebris Medical, Isny, Germany), 120 Hz, sensor area: 108.4 cm × 47.4 cm, 7168 sensors.
- NTK (Kapfenberg, Austria)
  - Treadmill: h-p-c Locomotion Med Treadmill (HP Cosmos, Nussdorf, Germany), walking speed: 0–10 km/h in 0.1 km/h steps, walking surface: 150 cm × 50 cm.
  - Pressure measuring platform: FDM-THM-M-2i (Zebris Medical, Isny, Germany), 120 Hz, sensor area: 111.8 cm × 49.5 cm, 3432 sensors.

- Rehabilitation Center Kitzbühel (Kitzbühel, Austria)
  - Treadmill: h-p-c Mercury Med Treadmill (HP Cosmos, Nussdorf, Germany), walking speed: 0–22 km/h in 0.1 km/h steps, walking surface: 150 cm × 50 cm.
  - Pressure measuring platform: FDM-THM-M-2i (Zebris Medical, Isny, Germany), 120 Hz, sensor area: 111.8 cm × 49.5 cm, 3432 sensors.

6.4.2 Subjects and Experimental Procedure

The data collection was carried out in three different institutions with different groups of subjects. Approval from the ethics committee of the University of Graz was obtained (GZ. 39/55/63 ex 2017/18, 28 May 2018), and an informed consent form was signed by all participants.

Healthy participants were recorded at three different walking speeds, each for two minutes: 1.5 km/h, 3 km/h, and 5 km/h. A prerequisite for participation was the ability to walk on a treadmill at different speeds. The healthy participants ($n = 39$) were recruited from the students at the Physiotherapy Institute of FH Joanneum Graz.

Non-healthy participants with affected ability to walk were asked to walk on a treadmill at a self-selected comfortable walking speed. Patients who were unable to walk on a treadmill were excluded during participant selection. The following groups of participants were recruited:

- Participants with different neurological diseases ($n = 36$) were recruited from patients who were in neurological inpatient rehabilitation at NTK Kapfenberg at the time of data collection. This comprises 20 post-stroke patients, six patients with Parkinson's disease, two with multiple sclerosis, two with meningioma, two after polytrauma, and one patient each with epilepsy, spinocerebellar ataxia, low back pain, and polyneuropathy.

- Participants with various orthopaedic diseases ($n = 62$) were recruited from the patients who were in orthopaedic inpatient rehabilitation at Rehabilitation Center Kitzbühel at the time of data collection. Of these, four patients had pathologies in the area of the ankle or lower leg (e.g., ankle joint fractures, tibia fractures), 21 patients at the knee (e.g., osteoarthritis, total knee arthroplasty), 18 patients in the area of the thigh and hip (e.g., osteoarthritis, total hip arthroplasty, femur fractures), 16 patients in the area of the lumbar spine (low back pain, lumbar vertebrae fractures) as well as three patients in whom different body areas were affected (polytrauma, polymyositis).

All participants had time to get used to walking on the treadmill prior to the data collection. All participants were free to use the treadmill support (handrail, fall protection system). For the data collection, two minutes of walking was recorded simultaneously by both systems. IMU data was recorded with a tool of the TyroS software (Tyromotion, Graz, Austria) that allows the export of raw gyroscope and accelerometer data. Zebris data was recorded, analyzed, and exported with the software FDM v1.18.38 (Zebris Medical, Isny, Germany).

6.4.3 Data Processing

For each trial, we obtain the following gait parameters from the Zebris Rehawalk instrumented treadmill:

- loading response duration,
- single limb support duration,
- pre-swing duration,
- swing duration,
- stride length,
- walking speed,
- cadence.

These parameters are reported as averages over the whole trial. The gait phase durations are given relative to the stride duration and reported separately for the left and right foot. We add the loading response, single limb support, and pre-swing durations to obtain the stance duration (cf. Figure 6.3).

From phases in which the treadmill is not moving and the foot is resting on the ground for approximately 5 s at the beginning and end of each trial, gyroscope turn-on bias is automatically estimated and removed. Using the methods described in Section 6.3, each recorded trial is processed with the parameter values given in Table 6.2. Note that we use the same set of parameters for all different subject groups and walking speeds in order to demonstrate that the method works well without adjusting the parameters for the specific gait velocity and style.

The sensor attachment used for recording the trials, as shown in Figure 6.11a, ensures that one sensor axis is always roughly aligned with the mediolateral axis of the foot. To show that the proposed methods do not make assumptions regarding the sensor orientation, we simulate a random sensor attachment by multiplying all gyroscope and accelerometer measurements with a random rotation matrix that is different for each trial.

Table 6.2: Parameter values used for the proposed IMU-based methods

Symbol	Description	Value
h_a	hysteresis factor for acceleration	0.23
h_ω	hysteresis factor for angular rate	0.23
w_a	factor for a_{th} auto-tuning	0.85
$a_{\text{th,min}}$	lower bound for a_{th}	$1.8\,\text{m/s}^2$
w_ω	factor for ω_{th} auto-tuning	0.8
$\omega_{\text{th,min}}$	lower bound for ω_{th}	$0\,\text{rad/s}$
$T_{0,\text{min}}$	minimum duration of zero-phase	120 ms
$T_{1,\text{min}}$	minimum duration of one-phase	180 ms
j_{win}	ratio of the window to look for initial contact	0.7
j_{th}	threshold for jerk norm (relative to maximum)	0.95

This parametrization is used for the processing of all trials, regardless of gait pathology, walking speed, or style, in order to show that the method works well without tuning the parameters for specific gait characteristics.

Finally, we calculate the same gait parameters as reported by the reference system by averaging the respective parameters, excluding the first and last three strides of each foot, and compare the resulting values to the values reported by the Zebris system. The results are found in the following section.

6.4.4 Results

For each trial, we first consider the five main parameters stance duration, swing duration, stride length, walking speed, and cadence, and evaluate the difference between the proposed methods (IMU) and the Zebris Rehawalk reference system (REF). The results are presented separately for each of the three subject groups in scatter plots and Bland-Altman plots [213] and can be found in Figure 6.12 for the healthy participants walking at three different speeds, in Figure 6.13 for the participants with orthopaedic diseases, and in Figure 6.14 for the participants with neurological diseases.

The error (mean ± standard deviation) for the relative stance duration is $1.05 \pm 1.34\,\%$ for healthy subjects, $-0.31 \pm 1.48\,\%$ for orthopaedic patients, and $2.07 \pm 1.63\,\%$ for neurological patients. For relative swing duration, the errors are $-1.02 \pm 1.35\,\%$ for healthy subjects, $0.34 \pm 1.50\,\%$ for orthopaedic patients, and $-2.02 \pm 1.64\,\%$ for neurological patients. This means that the average swing/stance duration error is in the range of 1–2 % for all subject groups.

For the stride length, the errors are $-1.47 \pm 1.60\,\mathrm{cm}$, $-1.62 \pm 1.66\,\mathrm{cm}$, and $0.69 \pm 1.32\,\mathrm{cm}$ for healthy subjects, orthopaedic patients, and neurological patients, respectively. This means that the average stride length error is below 2 cm for all subject groups.

The mean errors and standard deviations for the walking speed are $-0.02 \pm 0.06\,\mathrm{km/h}$ for healthy subjects, $-0.03 \pm 0.05\,\mathrm{km/h}$ for orthopaedic patients, and $0.03 \pm 0.03\,\mathrm{km/h}$ for neurological patients. This means that the average walking speed error is below 0.05 km/h for all subject groups.

The cadence estimates show deviations of 0.71 ± 0.52 steps/min for healthy subjects, 0.58 ± 0.31 steps/min for orthopaedic patients, and 0.57 ± 0.51 steps/min for neurological patients. This means that the average cadence error is below 1 step/min for all subject groups.

As an additional evaluation metric, we calculate the mean of the absolute difference (MAD) between the values reported by Zebris and the IMU-based analysis over all trials. Table 6.3 summarizes the results for the three subject groups and all 215 evaluated trials.

The MAD of the stance and swing durations is approximately 1.3 % for healthy subjects and orthopaedic patients and 2.2 % for neurological patients. Note that Table 6.3 also contains the deviations for the three sub-phases of stance that the Zebris Rehawalk reference system reports, i.e., loading response, single limb support, and pre-swing. The results show that the proposed methods can estimate the duration of those phases with the same accuracy as stance and swing.

To summarize, for all subject groups, the MAD is in the range of 1–2 % for the gait phase durations, below 2 cm for the stride length, below 0.05 km/h for the walking speed, and below 1 step/min for the cadence.

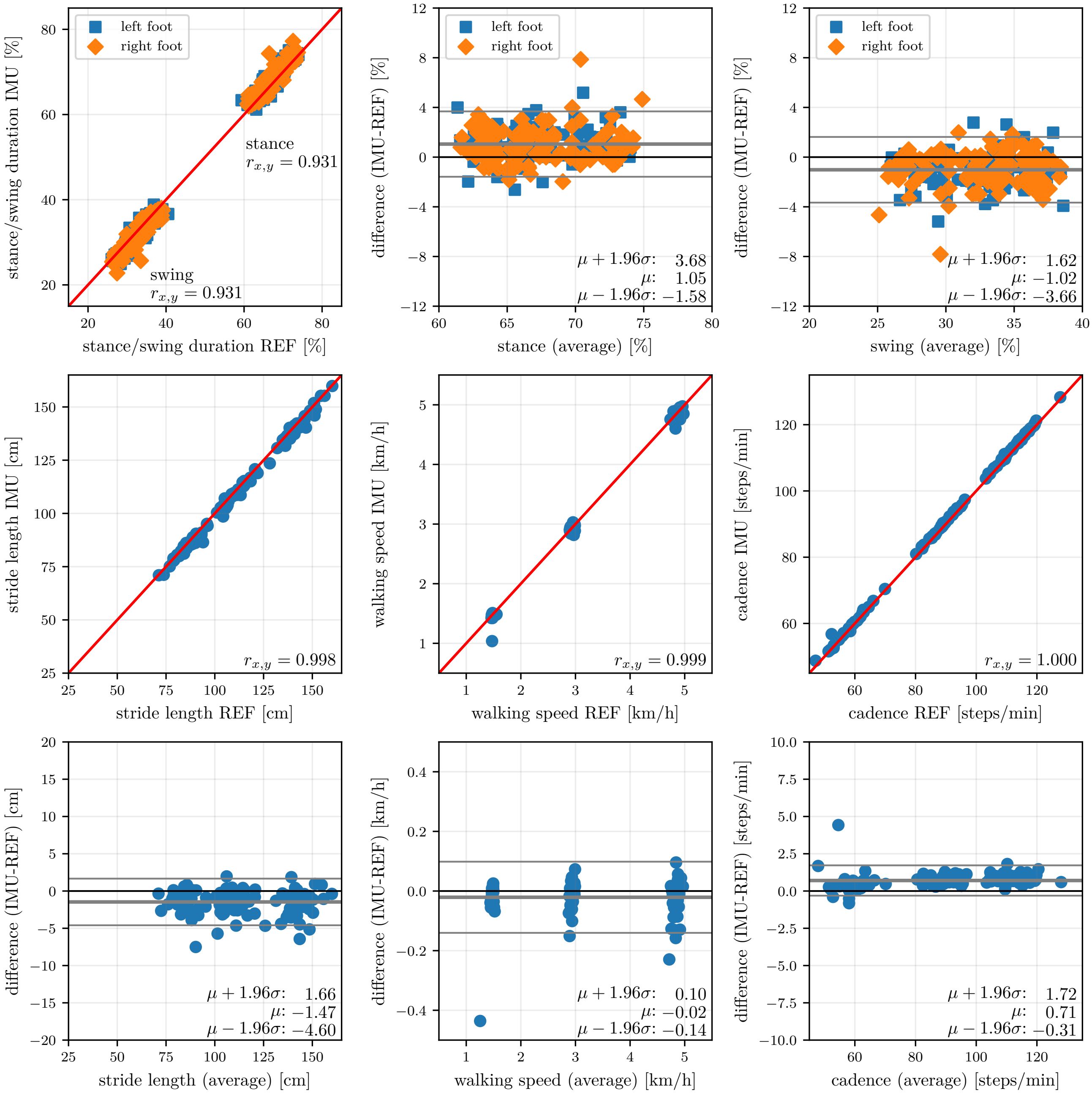

Figure 6.12: Scatter plots and Bland-Altman plots for stance and swing duration, stride length, walking speed, and cadence of 39 healthy subjects walking at 1.5, 3, and 5 km/h. Red: 45-degree lines ($y = x$). Values obtained with the proposed IMU-based methods (IMU) are compared to the ground truth from the Zebris reference system (REF). The average deviation is approximately 1 % for gait phase durations, below 2 cm for the stride length, below 0.05 km/h for the walking speed, and below 1 step/min for the cadence.

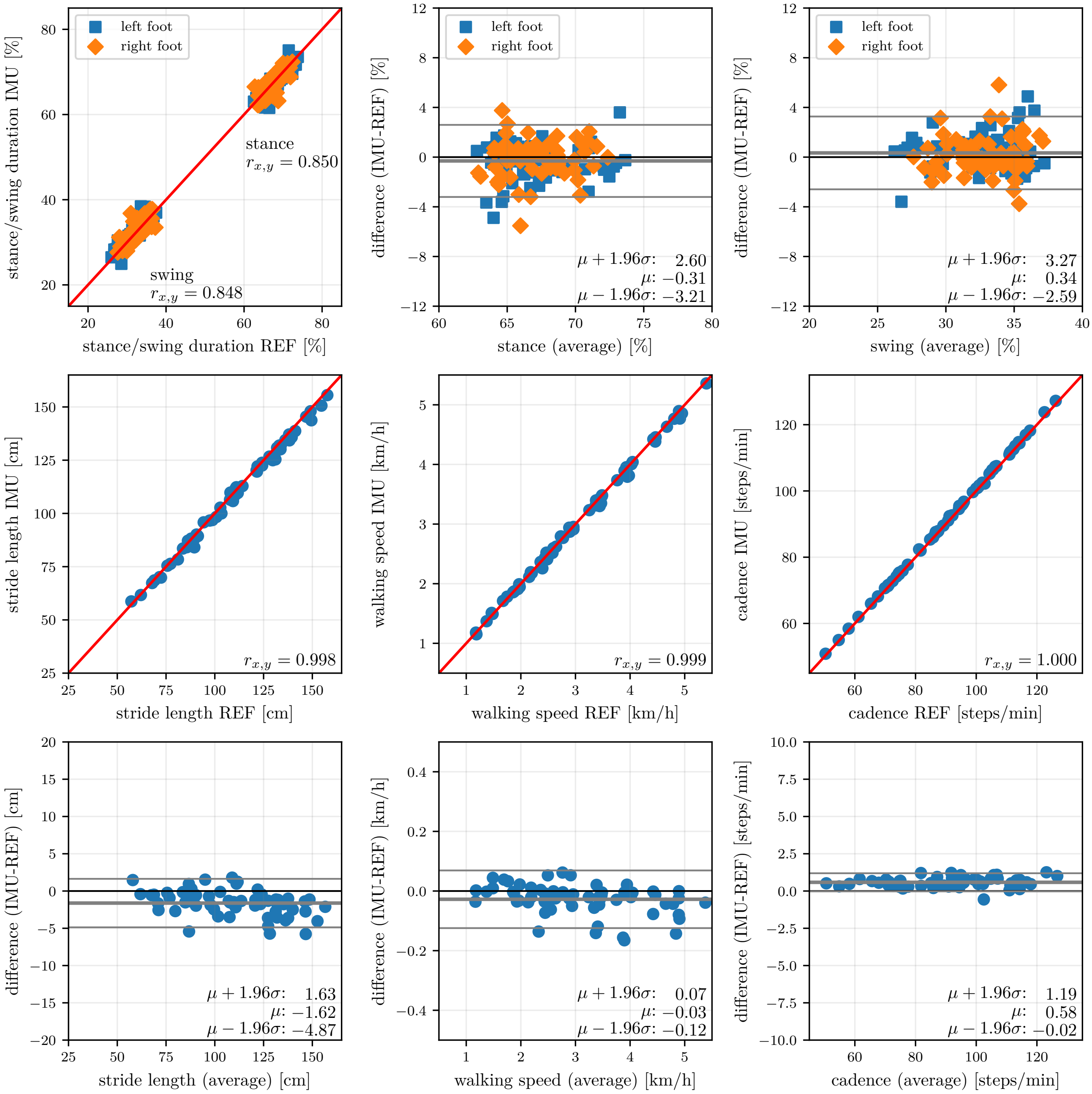

Figure 6.13: Scatter plots and Bland-Altman plots for stance and swing duration, stride length, walking speed, and cadence of 62 orthopaedic patients. Red: 45-degree lines ($y = x$). Values obtained with the proposed IMU-based methods (IMU) are compared to the ground truth from the Zebris reference system (REF). The average deviation is below 1 % for gait phase durations, below 2 cm for the stride length, below 0.05 km/h for the walking speed, and below 1 step/min for the cadence.

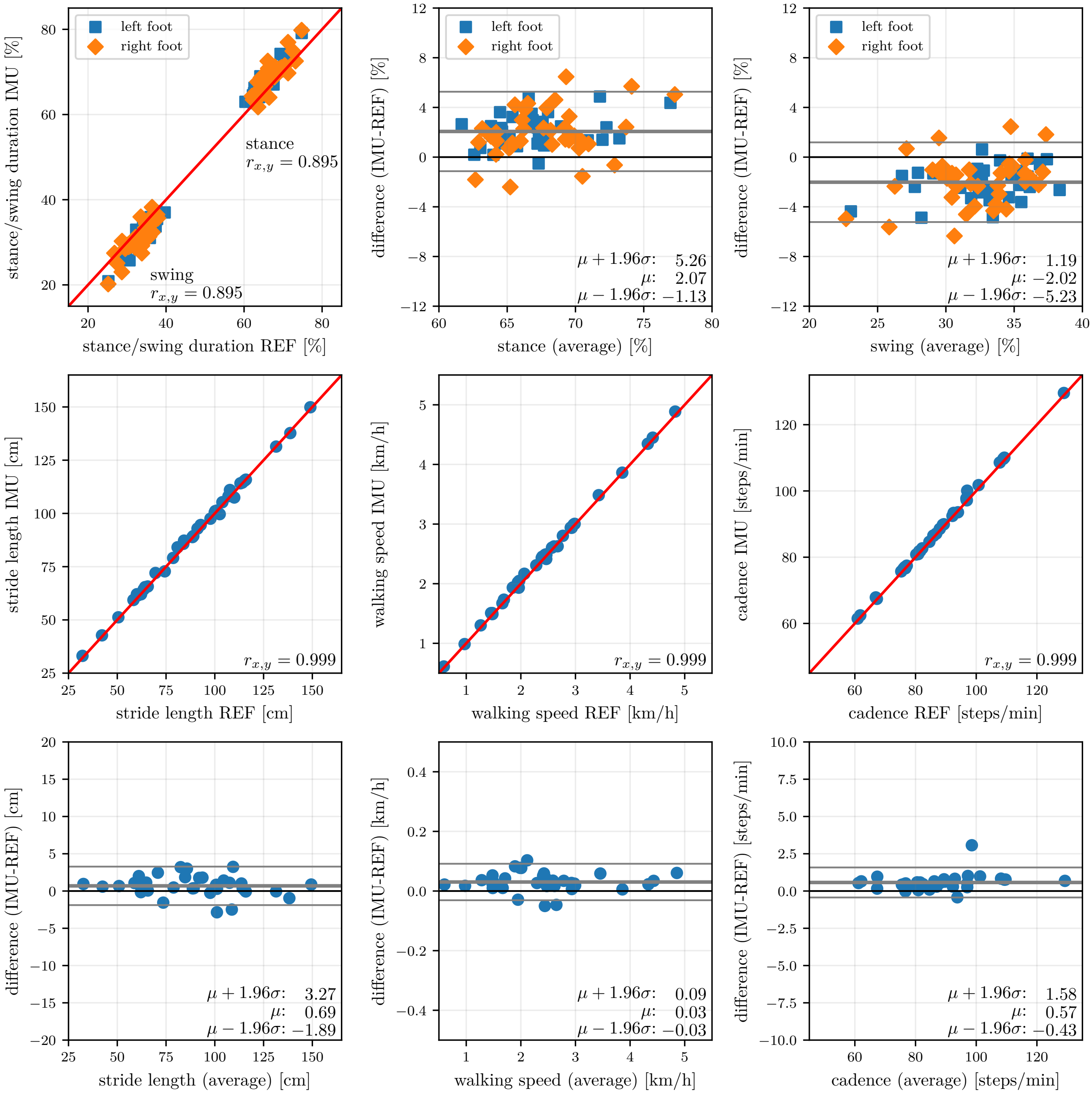

Figure 6.14: Scatter plots and Bland-Altman plots for stance and swing duration, stride length, walking speed, and cadence of 36 neurological patients. Red: 45-degree lines ($y = x$). Values obtained with the proposed IMU-based methods (IMU) are compared to the ground truth from the Zebris reference system (REF). The average deviation is approximately 2 % for gait phase durations, below 1 cm for the stride length, below 0.05 km/h for the walking speed, and below 1 step/min for the cadence.

Table 6.3: Deviation between IMU-based and Zebris gait parameters

	Stance [%]	**LR** [%]	**SLS** [%]	**PS** [%]	**Swing** [%]	**Stride length** [cm]	**Walking speed** [km/h]	**Cadence** [steps/min]
Healthy subjects ($n = 39$)								
MAD	**1.32**	**1.29**	**1.27**	**1.33**	**1.31**	**1.63**	**0.04**	**0.73**
$\mu \pm \sigma$	1.05±1.34	0.98±1.33	-0.98±1.30	1.05±1.35	-1.02±1.35	-1.47±1.60	-0.02±0.06	0.71±0.52
$r_{x,y}$	0.93	0.93	0.93	0.93	0.93	> 0.99	> 0.99	> 0.99
LoA	−1.58..3.68	−1.64..3.60	−3.54..1.57	−1.59..3.69	−3.66..1.62	−4.60..1.66	−0.14..0.10	−0.31..1.72
SDC	5.26	5.23	5.11	5.28	5.29	6.26	0.24	2.03
Orthopaedic patients ($n = 62$)								
MAD	**1.12**	**1.10**	**1.13**	**1.08**	**1.14**	**1.89**	**0.04**	**0.60**
$\mu \pm \sigma$	-0.31±1.48	-0.34±1.47	0.33±1.49	-0.30±1.45	0.34±1.50	-1.62±1.66	-0.03±0.05	0.58±0.31
$r_{x,y}$	0.85	0.85	0.85	0.85	0.84	> 0.99	> 0.99	> 0.99
LoA	−3.21..2.60	−3.22..2.54	−2.58..3.24	−3.14..2.54	−2.59..3.27	−4.87..1.63	−0.12..0.07	−0.02..1.19
SDC	5.80	5.76	5.82	5.68	5.86	6.50	0.19	1.22
Neurological patients ($n = 36$)								
MAD	**2.26**	**2.21**	**2.23**	**2.22**	**2.22**	**1.16**	**0.04**	**0.60**
$\mu \pm \sigma$	2.07±1.63	2.04±1.65	-2.04±1.64	2.07±1.65	-2.02±1.64	0.69±1.32	0.03±0.03	0.57±0.51
$r_{x,y}$	0.89	0.89	0.89	0.89	0.89	> 0.99	> 0.99	> 0.99
LoA	−1.13..5.26	−1.19..5.28	−5.26..1.18	−1.16..5.30	−5.23..1.19	−1.89..3.27	−0.03..0.09	−0.43..1.58
SDC	6.40	6.47	6.44	6.46	6.42	5.16	0.12	2.01
All trials (215 trials)								
MAD	**1.42**	**1.39**	**1.39**	**1.40**	**1.41**	**1.62**	**0.04**	**0.67**
$\mu \pm \sigma$	0.83±1.65	0.78±1.64	-0.78±1.63	0.83±1.64	-0.79±1.65	-1.15±1.78	-0.01±0.06	0.65±0.47
$r_{x,y}$	0.88	0.88	0.88	0.88	0.88	> 0.99	> 0.99	> 0.99
LoA	−2.40..4.06	−2.44..4.00	−3.98..2.41	−2.39..4.05	−4.03..2.44	−4.63..2.34	−0.13..0.10	−0.28..1.57
SDC	6.46	6.44	6.39	6.44	6.48	6.97	0.22	1.85

LR, SLS, PS: loading response, single limb support, pre-swing
MAD: mean absolute difference between IMU-based and Zebris values
$\mu \pm \sigma$: mean and standard deviation of difference between IMU-based and Zebris values
$r_{x,y}$: Pearson correlation coefficient ($p < 0.01$ for all values)
LoA: limits of agreement, $\mu - 1.96\sigma$ to $\mu + 1.96\sigma$
SDC: smallest detectable change, range between both LoA

6.5 Experimental Validation of Position and Angle Trajectories

In addition to the validation of the obtained spatiotemporal parameters in the previous section, we now validate the obtained position and angle trajectories. Since the pressure-based instrumented treadmill used in the previous section is not able to provide a ground truth for those gait parameters, we now employ marker-based OMC as the reference system.

6.5.1 Setup

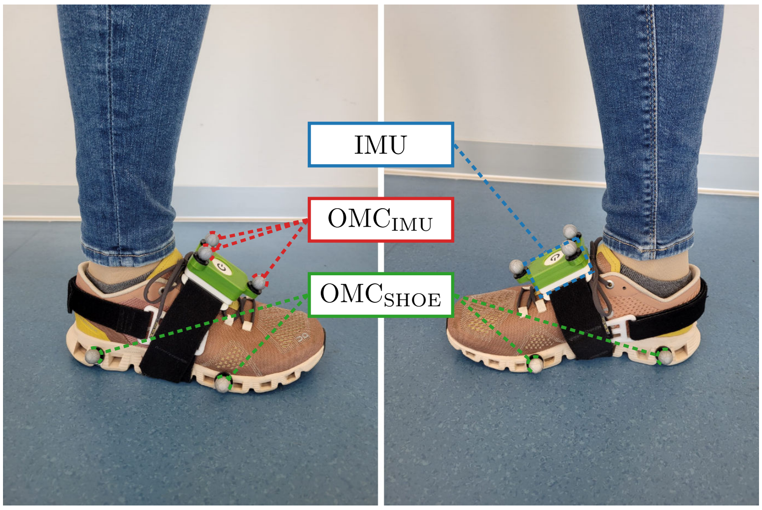

Figure 6.15: Experimental setup. An IMU is attached to the subject's shoe using Velcro straps, and reflective markers for OMC are attached to the sole of the shoe (OMC$_{SHOE}$) and to the IMU (OMC$_{IMU}$). The position and angle trajectories obtained from the IMU-based methods are compared to the ground truth obtained from the optical marker positions.

One IMU (PABLO Motion Sensor, Tyromotion GmbH, Graz, Austria) was attached on the instep of each shoe with three-point Velcro straps, as shown in Figure 6.15. Each sensor has a size of 56 mm × 34 mm × 21 mm, a weight of 40 g, and measures angular rate and acceleration at a rate of 110 Hz. For all measurements, the same set of IMUs and the same pairing of the IMUs to the left and right foot were used. An OMC system with 16 cameras (MX3, Vicon Inc., Oxford, UK) and an operating framerate of 120 Hz was used as the reference system. Three reflective markers were attached to a 3D printed console that was plugged onto the IMUs (OMC$_{IMU}$) and four on the edge of the sole of the subject's shoes (OMC$_{SHOE}$).

6.5.2 Subjects and Experimental Procedure

Twenty-three healthy volunteers (17 females, 6 males) with an average age of 24.8 ± 5.2 years, a height of 173.4 ± 8.9 cm, and a body weight of 67.2 ± 12.1 kg participated in this study. Since comparable studies analyzed data from 4 to 20 participants [196, 202, 203, 204, 205, 206, 207, 208, 209, 210, 211], a sample size of at least 20 participants was aimed for. To be included, participants had to be capable of walking on a treadmill at different speeds and with a simulated gait pathology. Exclusion criteria were current pain while walking or the presence of any disease that influences the gait pattern (e.g., due to orthopaedic or neurological conditions). All participants gave written informed consent prior to participation. The present study was approved by the Ethics Committee of the University of Graz (GZ. 39/55/63 ex 2017/18, 28 May 2018).

Gait data was recorded simultaneously with IMUs and OMC while walking on a motorized treadmill (mercury med, h/p/cosmos, Traunstein, Germany) without incline. Subjects were instructed to stand still with both feet side by side immediately before acceleration and after deceleration of the treadmill. The measurements were taken under four different conditions: very slow (1.5 km/h), slow (3 km/h), and normal walking speed (5 km/h), as well as with a simulated gait pathology at slow walking speed (3 km/h), for 90 seconds each. To simulate pathological gait, the range of motion of the subject's left knee joint was restricted with a brace fixed in neutral position. Prior to each trial, the subjects had time to get familiar with the respective condition. The participants were allowed to use the handrail of the treadmill, which none of them took advantage of.

6.5.3 Data Processing and Analysis

The IMU data is processed with the algorithms described in Section 6.3. As ground truth for comparison, analogous quantities are derived from the OMC marker positions. First, the IMU and OMC data is synchronized using the procedure described in Section 3.4.3. Then, a sensor orientation quaternion is derived from the three markers attached to the IMU (OMC_{IMU}, cf. Figure 6.15), and a sensor position trajectory is obtained by averaging the three marker positions. Further data processing is then carried out analogously to the IMU data processing. Additionally, the same processing steps are applied to the foot orientation obtained from the four markers attached to the shoe (OMC_{IMU}, cf. Figure 6.15).

The angles (pitch, roll, and yaw) and positions (vertical lift and lateral shift) are then time-normalized based on the gait cycle. Figure 6.16 shows an example over time for one subject. The gait cycle starts and ends at the initial contact, i.e., stride i occurs from $t_{\text{ic},i}$ (0 %)

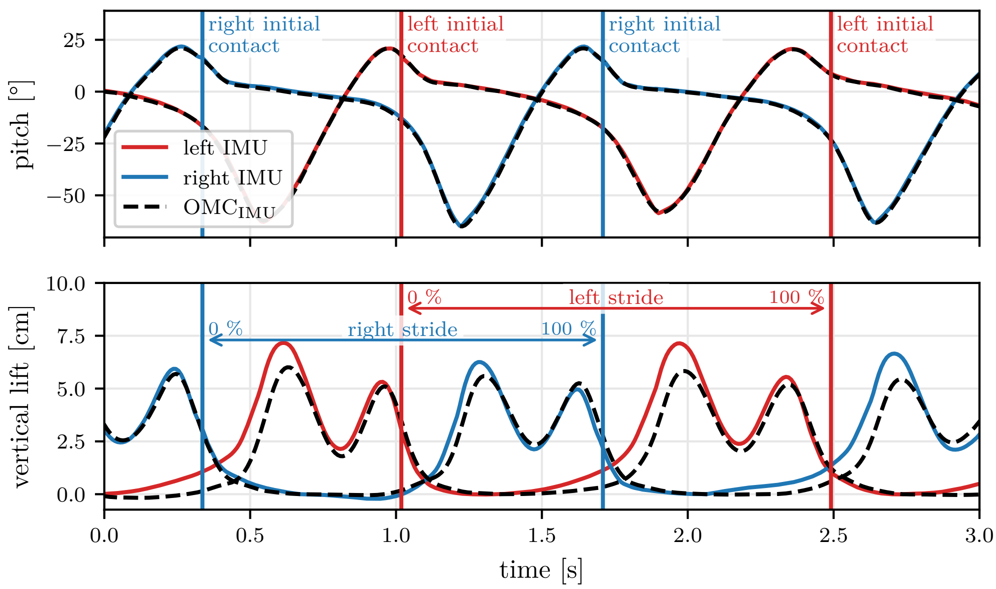

Figure 6.16: Example for the pitch angle and vertical lift trajectories over two gait cycles of one subject. The vertical lines represent the initial contacts of the corresponding foot, which mark the beginning and end of each gait cycle. The trajectories are time-normalized based on this gait cycle.

to $t_{\mathrm{ic},i+1}$ (100 %). For each stride, the values are resampled to a fixed length of 100 samples. The analyzed trajectories and their standard deviations are obtained by calculating the mean and standard deviation of the gait-cycle-normalized quantities for each trial while excluding the first and last five strides.

6.5.4 Results

All recorded trials of all subjects were analyzed, resulting in a total number of 9747 gait cycles (106 ± 30 gait cycles per trial).

The angle and position trajectories for IMU and $\mathrm{OMC_{IMU}}$ and the standard deviation for different walking conditions of one subject are presented in Figure 6.17a and Figure 6.18a. To compare the metrics for all subjects, the MAD is calculated. The results are shown in Figures 6.17b and 6.18b. The maximum MAD occurs at a walking speed of 5 km/h and is

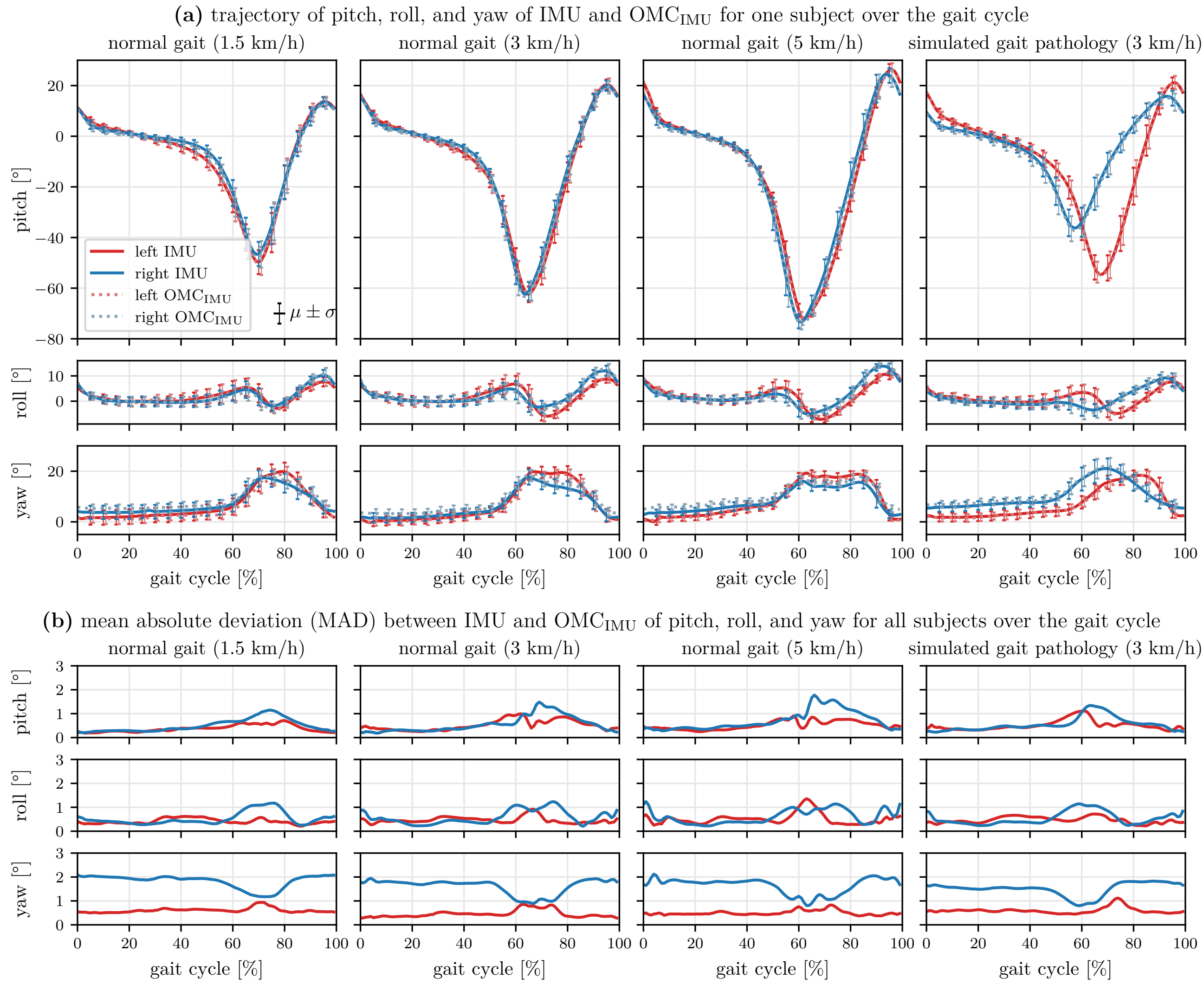

Figure 6.17: Results for the angle trajectories. **(a)** Time-normalized angle trajectories of one subject at different gait conditions. **(b)** MAD between IMU and $\mathrm{OMC_{IMU}}$ for the angle trajectories of all subjects ($n = 23$). The IMU and $\mathrm{OMC_{IMU}}$ trajectories agree well, and the MAD always stays below 2.2° during the whole gait cycle.

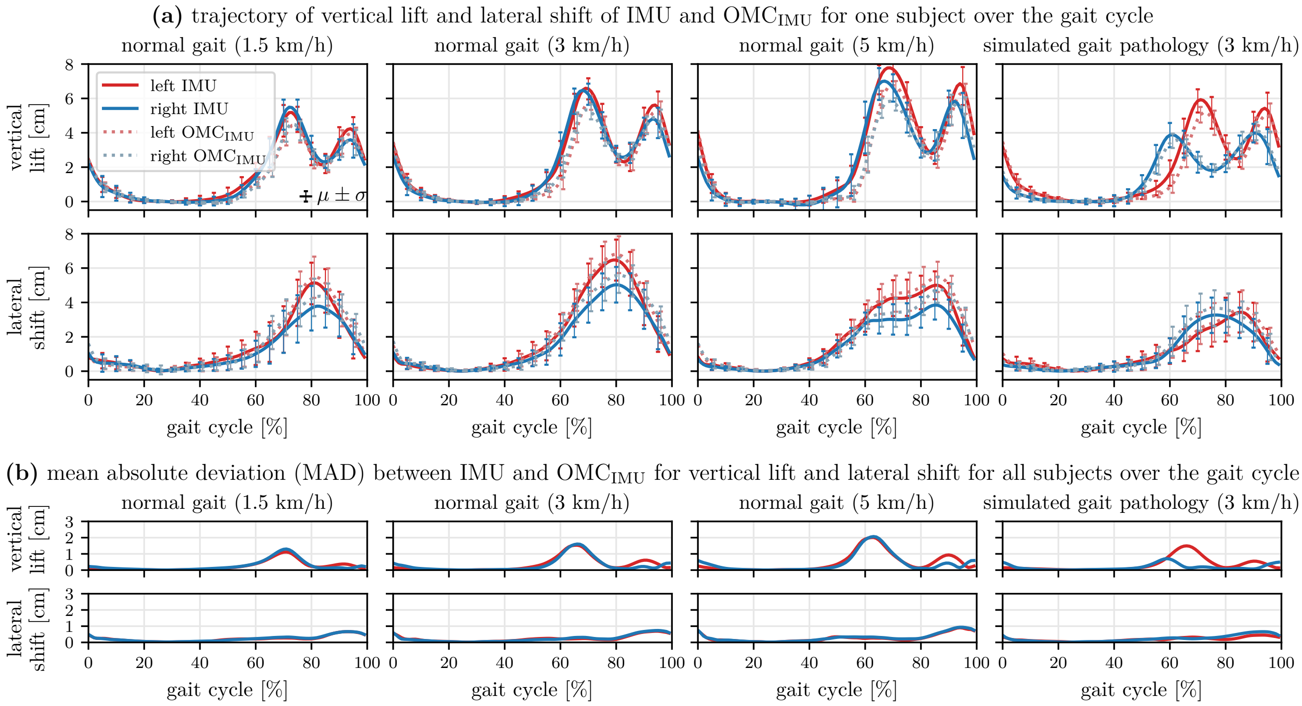

Figure 6.18: Results for the position trajectories. **(a)** Time-normalized position trajectories of one subject at different gait conditions. **(b)** MAD between IMU and OMC$_{\mathrm{IMU}}$ for the position trajectories of all subjects ($n = 23$). The IMU and OMC$_{\mathrm{IMU}}$ trajectories agree well, and the MAD always stays below 2.1 cm for vertical lift and 1 cm for lateral shift during the whole gait cycle.

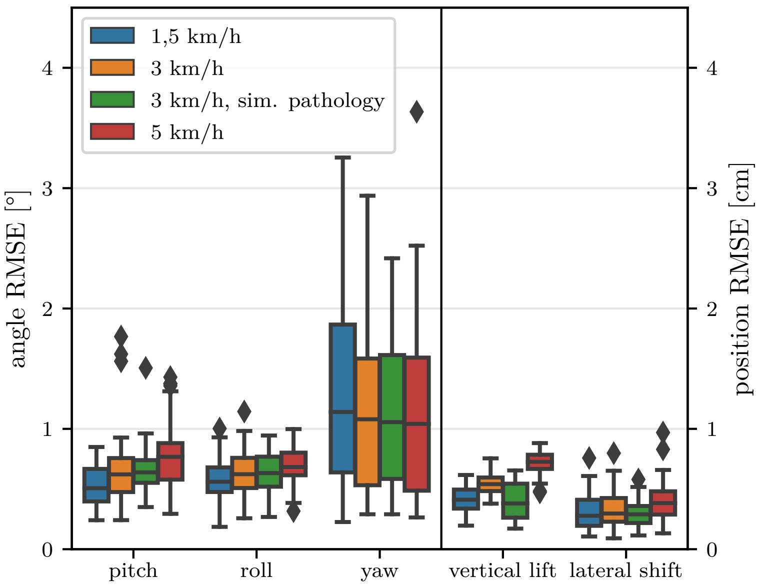

Figure 6.19: RMSE between IMU and OMC$_{\mathrm{IMU}}$ for angle and position trajectories of all subjects ($n = 23$) at different gait conditions. For pitch, roll, vertical lift, and lateral shift, the mean and median RMSE is well below 1° and 1 cm, respectively, while the errors for the yaw angle trajectory are slightly larger.

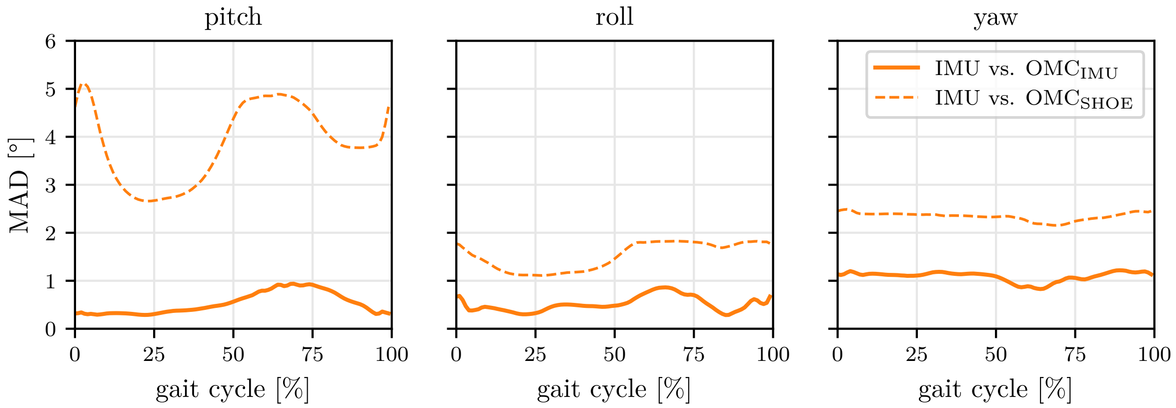

Figure 6.20: Time-normalized trajectories of the MAD between IMU and OMC$_{IMU}$ as well as IMU and OMC$_{SHOE}$ of all subjects ($n = 23$) and all 62 trials. When using the optical markers attached to the shoe instead of the markers attached to the IMU, the disagreement increases by approximately 4° for pitch and by approximately 1° for roll and yaw.

1.78° for pitch, 1.36° for roll, and 2.12° for yaw, as well as 2.07 cm for vertical lift and 0.93 cm for lateral shift.

Furthermore, for each trial, the RMSE between the IMU and OMC$_{IMU}$ trajectories is calculated and represented as a boxplot in Figure 6.19. The average RMSE of all trials 0.66 ± 0.26° for pitch, 0.63 ± 0.19° for roll, 1.17 ± 0.69° for yaw, 0.72 ± 0.10 cm for vertical lift, and 0.40 ± 0.17 cm for lateral shift.

Finally, to evaluate the influence of the motion of the IMU relative to the shoe, the MAD of the angle trajectories between the IMU-based values and OMC$_{IMU}$ and between IMU and OMC$_{SHOE}$ is calculated. The result is shown in Figure 6.20. It shows a maximum MAD between IMU and OMC$_{SHOE}$ of 5.11° for pitch, 1.83° for roll, and 2.49° for yaw. In contrast, the maximum MAD between IMU and OMC$_{IMU}$ is 0.94° for pitch, 0.86° for roll, and 1.22° for yaw.

6.6 Discussion

The present chapter introduced a set of methods for gait analysis based on two IMUs attached to the feet.

The methods allow for the calculation of the main spatiotemporal gait parameters that are also reported by stationary laboratory systems: gait phase durations, stride length, walking speed, and cadence. Using a large dataset consisting of healthy subjects walking at three different speeds, subjects with orthopaedic diseases, and subjects with neurological diseases, the calculation of those parameters was validated, using a Zebris Rehawalk instrumented treadmill as reference. All parameters show a very strong correlation (Pearson's r between 0.83 and 0.99, $p < 0.01$) [214]. Figures 6.12 to 6.14 display consistent results over this large and diverse group of subjects. Averaged over all trials, the MAD with respect to the reference system is 1.4 % for the gait phase durations, 1.6 cm for the stride length, 0.04 km/h for the walking speed, and 0.7 steps/min for the cadence.

Furthermore, the methods allow for the calculation of position and angle trajectories, which were evaluated using OMC as reference. The results in Figures 6.17 and 6.18 show a good agreement between the IMU and OMC trajectories. The maximum MAD between IMU and OMC_{IMU} over the gait cycle is below 2° for pitch and roll. The maximum occurs in the areas of the largest amplitudes in the respective angles during the swing phase, with a MAD generally below 1° for the remaining gait cycle. Comparable results can be seen for the trajectories of vertical lift as well as the lateral shift of the foot, with a maximum MAD of about 2 cm for vertical lift and 1 cm for lateral shift. For yaw, the MAD is larger due to an offset in the right yaw angle that is likely caused by inaccurate factory calibration of the right IMU. The average RMSE for all parameters and all conditions is clearly below 1.5° and 1 cm, respectively, as shown in Figure 6.19. A comparison of the results with those of other studies that investigate the measurement accuracy of foot-mounted IMUs for positions and angles is only possible to a limited extent, since samples, measurement protocols, and evaluated parameters differ considerably between studies. However, it can be stated that the measurement error of the presented method for angle trajectories is comparable to other publications [196, 203, 205, 206, 211] or even lower [207, 208, 209, 210]. The measurement error for position trajectories is comparable [196, 204] or lower [202, 203, 211].

In clinical practice and research, the obtained gait parameters are used to quantify gait abnormalities and to document changes in the walking behavior of patients. Associations between gait parameters and functional capacity, or increased mortality, have been demonstrated [215, 216, 217]. A positive correlation with cardiovascular-related mortality was found for cadence [218]. A reduction in walking speed has been shown to correlate with fall risk, frequency of hospitalization, and mortality [219, 220, 221]. Stride length describes a strong correlation with walking speed, according to the research of [222]. Slower walking speed, altered gait phase duration, and increased variability of walking increase the risk of falls [223]. Furthermore, it was found that psychological modalities, such as fear of falling, can also influence stride length and gait phase durations [224]. The minimal clinically important difference (MCID) can be used to determine how precisely these changes must be detected in order to make a statement about their relevance. Despite thorough research, specific values for the MCID could only be found for the walking speed, ranging from 0.36 to 0.72 km/h [225, 226, 227]. For IMU-based measurement with the proposed methods, the smallest detectable change (SDC) for walking speed is 0.21 km/h and clearly within the MCID for all examined groups. For the other parameters, no reported MCID values could be found, which is consistent with the statement of [197].

The SDC for the cadence is 2.01 steps/min across all studied groups of subjects. This allows for much smaller changes to be detected than those described as relevant in the literature (e.g., a reduction in cadence of 10 steps per minute increases mortality by 4 % [228]). The achieved SDC for the stride length of 5.3 cm in the patients with neurological diseases seems to be sufficiently accurate to capture the differences occurring, for example, in Parkinson's disease [229]. The stance and swing phase durations show an SDC of 6.5 % across all trials.

Unlike many existing contributions, the evaluation showed that the proposed methods reliably work on patients in addition to healthy subjects and still produce accurate results. This is noteworthy since it has been shown that pathological walking deteriorates the accuracy of many gait analysis methods [199] and specifically that neurologically induced gait abnormalities are challenging for IMU-based gait analysis [197].

A fundamental challenge of IMU-based gait event detection is that IMUs do not directly measure the gait parameters of interest. For toe-off detection, the time instant of load relief cannot directly be measured, and instead, the inversion of the direction of rotation is used. Similarly, initial contact is not detected based on the onset of load but based on the change of acceleration. It is therefore important to properly validate the IMU-based methods by comparing the estimated gait parameters to a reliable ground truth.

As reference system, treadmills instrumented with Zebris pressure measurement platforms were used, which are frequently employed for gait analysis in clinical practice as well as scientific data collection [172]. This system shows good reliability [230], but no studies could be found in which the validity of the gait parameters was investigated. It should be noted that due to the length of the pressure sensors (FDM-THM-M-3i: 0.85 cm; FDM-THM-M-2i: 1.27 cm), there may be inaccuracies in the recording of spatial parameters, which may have an effect on the results of the comparative measurements. Moreover, calibration and proper thresholding pose challenges in gait event detection based on pressure measurement [172].

For the neurological patients, the reported duration of stance is, on average, 2 % longer than the reference duration. While this is still a small deviation, it is worth noting because this bias suggests a pattern that is common to this subject group. One likely explanation is that toe-off is being detected later than with the Zebris system. This might be due to a comparatively long phase of load relief that causes the pressure to fall below the threshold too early. Furthermore, the reversal of the rotation direction might happen later than for healthy subjects or orthopaedic patients. Still, even though both systems measure inherently different phenomena, the observation deviation is only 2 %.

As a replacement for traditional stationary gait analysis systems, which are commonly used in clinical practice, IMU-based gait analysis offers several advantages. Measurement is possible both on treadmills and overground and not restricted to a dedicated laboratory. The small and lightweight IMUs do not restrict the movement of the subject and can be used in conjunction with walking aids such as wheeled walkers. Furthermore, only a very short setup time is required before starting the actual measurement.

Unlike most existing methods (cf. Section 6.2), the proposed method makes gait analysis easier and faster by not requiring any specific sensor attachment for the derivation of most gait parameters, which was demonstrated by simulating a different random sensor-to-foot orientation in each trial. It does not make use of magnetometers and can therefore be used in both indoor and outdoor environments.

While evaluation was limited to the gait phases reported by the reference system, the proposed set of methods further allows for the calculation of many gait phases (Figure 6.5), i.e., swing and stance for each foot, four unilateral gait phases for each foot, five bilateral gait phases following standard literature [198] for each foot, and finally the distinction between double and single support. To the best of the author's knowledge, no existing work on IMU-based gait analysis describes the calculation of this set of gait phases.

Besides the more fine-grained gait phases, there are many more parameters that can be extracted, e.g., from the velocity and position trajectories, such as the maximum velocity during swing, foot clearance, and symmetry parameters. While it is not surprising that the prevalence of pressure-based systems has led researchers to focus on features based on ground contact, it is to be expected that the focus of clinical gait analysis will be directed toward other parameters as IMU-based systems become more popular.

Furthermore, miniaturized lightweight sensors with a long battery life open up possibilities for objective gait analysis outside of clinical laboratories. Daily-life gait assessment over the course of multiple days can bring insight that is not possible with short sessions in a laboratory. If patients place the sensors on or in the shoes themselves in an unsupervised telemedicine setting, not requiring the sensor to be oriented in a special way becomes even more important.

Technological advancement also facilitates real-time biofeedback applications. While there are methods for real-time applications that require event detection during a step [94], e.g., to trigger FES, the proposed set of methods is real-time capable in the sense that during walking, sections of data containing a small number of strides can be processed and used to provide feedback to the subject.

In most applications, the IMUs are attached to or integrated into the shoe. This is especially relevant for applications in daily life, but also the case in almost all identified studies [196, 202, 203, 204, 205, 206, 207, 208, 209, 211] in which positions and angles were investigated with foot-mounted IMUs (except for [210], which includes additional barefoot measurements). However, none of the publications investigated the influence of the shoe on the results. In this context, the present setup with both $\mathrm{OMC}_{\mathrm{IMU}}$ and $\mathrm{OMC}_{\mathrm{SHOE}}$ yields new findings. As shown in Figure 6.20, the MAD between IMU and $\mathrm{OMC}_{\mathrm{IMU}}$ is considerably smaller than between IMU and $\mathrm{OMC}_{\mathrm{SHOE}}$ for all angle trajectories. This shows that the impact of OMC marker placement on the obtained measurement is as large or even larger than the disagreements between OMC and IMU-based measurements. For IMU-based gait analysis, attaching the IMUs on the shoe vs. the foot, the location of the IMUs on the shoe or foot, and the method of attachment are likely to affect the obtained results in a similar way. Future studies should clarify which sensor position and attachment on the shoe results in the least measurement error.

The presented work exhibits a few remaining limitations. In the statistical analysis, the gait parameters were averaged over the duration of the trial before comparison with the reference. While it allows for single-stride errors to cancel out, this methodology corresponds well with the use case of clinical gait analysis, in which a subject is asked to walk for several steps, and averaged parameters are then used to assess the gait. An additional stride-by-stride comparison was not performed because the employed Zebris reference system can only export averaged gait parameters. In addition, it should be noted that all recordings were made on treadmills and not while walking overground, which has an influence on the movement pattern of gait [231, 232]. Despite the known differences between treadmill walking and overground walking, treadmill gait analysis is considered a standard method in clinical practice [233, 234], especially when weight support and handrails are required for safety reasons. Furthermore, in contrast to the extensive validation of the spatiotemporal parameters with patient data, the experiments with OMC as reference were only performed with healthy subjects and with a simulated gait pathology.

6.7 Conclusions

The present chapter proposed a set of methods for IMU-based gait analysis. Based on gyroscope and accelerometer measurements from two IMUs on the feet, durations of five gait phases, stride length, walking speed, cadence, as well as position and angle trajectories are estimated. Using a Zebris Rehawalk instrumented treadmill as reference, the spatiotemporal parameters obtained with the proposed methods were validated based on a large dataset consisting of healthy subjects ($n = 39$) walking at three different speeds, subjects with orthopaedic diseases ($n = 62$), and subjects with neurological diseases ($n = 36$). Averaged over all trials, the MAD with respect to the reference system is 1.4 % for the gait phase durations, 1.6 cm for the stride length, 0.04 km/h for the walking speed, and 0.7 steps/min for the cadence. Position and angle trajectories obtained with the proposed method were validated using data from 23 healthy subjects and marker-based OMC as reference. The results showed that the obtained trajectories agree well and that, for all walking conditions, the average RMSE is below 1.5° for the angle trajectories and below 1 cm for the position trajectories. It was also demonstrated that the proposed methods work reliably not only in healthy subjects but also in patients and still provide accurate results under different pathological gait patterns.

This shows that the proposed setup, in combination with the proposed methods, can accurately calculate relevant gait parameters from the inertial sensor data and thus has the potential to replace traditional stationary gait analysis systems.

Furthermore, the validation showed that the proposed methods work well regardless of the orientation in which the sensor is attached to the foot, and dedicated calibration movements and magnetometer measurements are completely avoided. The combination of these advantages facilitates long-term ambulatory gait analysis in day-to-day situations without the need for supervision by health professionals.

Future research should focus on the estimation of additional gait parameters, on the validation on stairs and slopes, and on a detailed investigation of the motion artifacts introduced by attaching IMUs and optical markers on the shoe instead of directly placing them on the skin.

7

General Conclusions and Outlook

This thesis introduces a modular set of methods facilitating non-restrictive magnetometer-free inertial motion tracking in kinematic chains. This set of methods consists of four major parts: (1) a versatile orientation estimation algorithm, (2) methods for automatic anatomical calibration via kinematic constraints, (3) methods for heading tracking in kinematic chains with 1-DoF and 2-DoF joints, and (4) methods for non-restrictive inertial gait analysis.

7.1 General Summary

In Chapter 3, a versatile IOE algorithm is developed. This algorithm employs a novel approach of filtering the accelerometer measurements in an almost-inertial frame, simultaneously estimates the 6D and 9D orientation, and includes extensions for online gyroscope bias estimation and magnetic disturbance rejection. A comprehensive evaluation of the proposed algorithm shows that it provides highly accurate orientation estimates, with 1.8 to 5 times smaller errors than literature methods. For this evaluation, an extensive benchmark dataset, encompassing a wide range of undisturbed motions and motions in disturbed environments, is introduced, and the method is compared to eight state-of-the-art methods. Unlike most existing algorithms, the proposed algorithm works out of the box without requiring application-specific parameter tuning. IOE is the fundamental building block for almost all inertial motion-tracking applications and for the methods developed in Chapters 4 to 6. Therefore, the accuracy gain achieved by the proposed IOE algorithm is expected to benefit all those applications.

Chapter 4 presents methods for automatic anatomical calibration that are based on kinematic constraints of 2-DoF joints and do not use magnetometer measurements. They work with arbitrary motions, in contrast to most existing methods that require the subject to perform precisely defined motions or to assume precisely defined poses. The methods are evaluated using two experiments. The first experiment validates the consistency and plausibility of joint axes that are estimated from just ten seconds of motion. In the second experiment, the analyzed natural everyday life motions are directly used for anatomical calibration instead of recording a separate calibration motion, and accurate joint angles are obtained. The developed methods overcome mounting and calibration restrictions and facilitate plug-and-play motion tracking.

In Chapter 5, methods are developed that facilitate long-term stable magnetometer-free motion tracking in kinematic chains by exploiting kinematic constraints. In contrast to most existing approaches, the heading offset is represented via a scalar state, and information from the kinematic constraint is only used for heading correction, without affecting the inclination estimates. Robust estimation of the heading offset is achieved with the introduction of a real-time-capable window-based approach. It handles phases in which the kinematic constraint becomes singular and in which no movement is performed. The developed methods are validated with mechanical joints and with the MCP, PIP, and DIP joints of the fingers. The methods facilitate accurate long-term motion tracking, without magnetometers and without the need to repeatedly assume a known rest pose.

Chapter 6 considers gait analysis as an important application area of IMU-based motion analysis. A comprehensive set of non-restrictive methods for gait assessment via foot-worn IMUs is introduced. The methods support calculating various spatiotemporal parameters (such as gait phase durations, stride length, and cadence), as well as 3D foot position and angle trajectories. The accuracy of the obtained parameters is evaluated on a large dataset. It consists of walking data from healthy subjects and subjects with various diverse gait pathologies. The methods reliably work on patients in addition to healthy subjects and still produce accurate results, unlike many literature methods. In comparison to the stationary pressure-based systems that are the state of the art in gait analysis, the developed methods support the calculation of a more comprehensive set of gait parameters, while being less restrictive.

7.2 Impact of This Work

This thesis proposes a modular set of methods for non-restrictive magnetometer-free human motion analysis. The modularity of the proposed methods is the result of a novel approach of consistently separating inclination and heading information. In contrast to most existing work, the proposed methods limit the unknown quantity in magnetometer-free motion tracking to a scalar heading offset. In the IOE algorithm of Chapter 3, this scalar represents the heading offset with respect to the ENU reference frame. Similarly, the methods in Chapter 4 and Chapter 5 use this scalar to represent the estimated relative heading offset between the 6D reference frames of adjacent body segments. This separation of heading and inclination ensures that the highly accurate inclination estimates obtained by the proposed IOE algorithm cannot be affected by subsequent heading correction steps. It also reduces complexity and enables the introspection of intermediate estimation results, e.g., by plotting the estimated heading offsets over time. Furthermore, this separation facilitates fusing multiple sources of heading information and integrating custom application-specific algorithms. As an example for the former, one could average the magnetometer-based heading estimates of multiple sensors, obtained via the proposed IOE algorithm, to obtain an overall heading estimate while only relying on the more trusted relative heading offsets from the constraint-based methods of Chapter 5 for adjacent body segments. This enables drift-free 3D visualization while ensuring that joint angles are not affected by magnetic disturbances. As an example of an application-specific algorithm that is facilitated by the proposed separation of heading and inclination, the foot progression angle method introduced in Section 6.3.12 estimates a scalar heading offset to align the 6D reference frame with the walking direction.

The proposed set of methods can be employed in various combinations in a wide range of applications. In the following, this will be illustrated based on three exemplary scenarios.

As the first example, consider the assessment of a subject's elbow range of motion, which is relevant, e.g., for patients in post-stroke rehabilitation [235] or patients with cerebral palsy [18]. In this setting, the IOE algorithm from Chapter 3 could be integrated directly into the IMU firmware, which then wirelessly transmits 6D quaternions to a computer or smartphone. The methods for automatic anatomical calibration proposed in Chapter 4 can be used to estimate joint axes, followed by the heading tracking methods from Chapter 5 to obtain joint angles. In comparison to conventional approaches, the proposed methods are less restrictive: Magnetometers are not used, which eliminates the need to carefully prepare a lab environment free from potential magnetic disturbances and makes it possible for the subject to interact with electronics or objects containing ferromagnetic material. Furthermore, the subject does not need to perform calibration motions or repeatedly assume a known pose. Note that the modularity of the proposed methods makes it easy to adapt the combination of methods to the requirements of the specific use case. For example, it is easily possible to skip the anatomical calibration step and instead rely on a known sensor attachment.

As a second example in a different application area, consider workplace ergonomics. The proposed methods can be combined in a similar manner as in the first example to enable automatic work assessment. Such an assessment tool could, among other metrics, automatically evaluate phases during which the joint angles indicate unhealthy motions and postures [236]. In this setup, the automatic anatomical calibration methods reduce the risk of operating errors in unsupervised use. Additionally, they could be used to automatically detect and compensate accidental repositioning of the IMUs during the workday. By not relying on magnetometer measurements, this approach is suitable for both industrial and office environments, which are both prone to strong magnetic disturbances due to ferromagnetic material and electronics.

The gait analysis methods introduced in Chapter 6 provide a third example of the versatility of the proposed methods. The minimal two-sensor setup makes the methods suitable for unsupervised use in home environments to facilitate long-term daily-life assessment. For scenarios that require more elaborate motion analysis, the gait analysis methods can easily be combined with the anatomical calibration methods from Chapter 4 and the magnetometer-free motion tracking methods from Chapter 5 to realize full lower-body motion tracking with seven IMUs on feet, shanks, thighs, and hip.

As illustrated by these examples, the proposed modular set of methods facilitates non-restrictive motion analysis that works in indoor environments, does not require the IMUs to be attached in a precise orientation, and does not require the subject to perform tedious and error-prone calibration movements. The proposed methods are therefore important building blocks for achieving plug-and-play motion analysis with IMUs and are expected to help realize the full potential of body-worn IMUs in many application domains.

7.3 Outlook and Future Work

Several aspects of future work were mentioned at the end of the respective chapters. Here they are summarized, and the potential for future work in the context of the global topic of this thesis is discussed.

The IOE benchmark dataset could be broadened further by adding data recorded with different hardware and data from human motion trials. The next step in improving the IOE algorithm should be the integration of continuous and automatic magnetometer calibration. For the anatomical calibration methods, combining both kinematic constraints is the most promising path to increase robustness. The next steps needed for achieving robust plug-and-play motion tracking are the development of methods for assessing the estimation uncertainty, the automatic triggering of the calibration, and the combination of the anatomical calibration with the heading tracking methods. In order to extend the applicability to all joint types, a method based on the connection constraint should be integrated into the heading tracking framework. Research on the gait analysis methods should focus on the estimation of additional parameters, the validation on stairs and slopes, and the automatic segmentation of walking and non-walking phases.

In a broader context, many recent developments in IMU-based motion analysis complement the work pursued in this thesis.

The observability analysis of kinematic constraints for joint axis and heading offset estimation is a novel field with limited but promising results [129, 140, 237, 238]. Insight obtained from observability analysis can contribute to the development of more robust methods and better detection of phases in which the kinematic constraints do not yield information.

In an effort to increase the practicability of full-body motion tracking, methods for sparse motion tracking have recently gained traction. While this can be achieved via constraint-based methods [239, 240, 241], many of the recent achievements are based on machine learning [110, 242, 243, 244, 245]. In general, like in many fields in science and engineering, the advance of machine learning is prominent inertial motion tracking, ranging from IOE [57] and gait analysis [184] to sparse motion tracking and other novel approaches, e.g., to facilitate motion tracking with IMUs attached to loose clothing [246].

With microcontrollers found on IMUs becoming more powerful, an increasing number of algorithms can be implemented directly on-chip. While this is already common for IOE, many processing steps, such as gait event detection, have the potential to run directly on the sensor hardware. Even complex methods for analyzing kinematic chains could potentially be implemented in a distributed manner directly on the sensors. This on-chip data processing can be combined with emerging intelligent sampling and data transmission strategies [247, 248, 249] to reduce the communication load and power consumption of wireless IMU networks.

In summary, the recent progress in accuracy, miniaturization, and power efficiency of MEMS-based IMUs goes hand in hand with the recent progress in methods for inertial sensor fusion to which this thesis contributed. Still, to realize the vision of robust plug-and-play long-term motion assessment in unsupervised daily living scenarios, further work is required to increase robustness and to design intelligent systems that are aware of their current accuracy and automatically detect anomalies.

References

[1] M. Iosa, P. Picerno, S. Paolucci, and G. Morone. “Wearable Inertial Sensors for Human Movement Analysis”. In: *Expert Review of Medical Devices* 13.7 (July 2, 2016), pp. 641–659. ISSN: 1743-4440. DOI: 10.1080/17434440.2016.1198694 (cited on pp. 1, 2).

[2] P. Picerno, M. Iosa, C. D’Souza, M. G. Benedetti, S. Paolucci, and G. Morone. “Wearable Inertial Sensors for Human Movement Analysis: A Five-Year Update”. In: *Expert Review of Medical Devices* 18 (sup1 Dec. 3, 2021), pp. 79–94. ISSN: 1743-4440. DOI: 10.1080/17434440.2021.1988849 (cited on pp. 1, 2).

[3] E. van der Kruk and M. M. Reijne. “Accuracy of Human Motion Capture Systems for Sport Applications; State-of-the-Art Review”. In: *European Journal of Sport Science* 18.6 (July 3, 2018), pp. 806–819. ISSN: 1746-1391. DOI: 10.1080/17461391.2018.1463397 (cited on p. 1).

[4] C. Anthes, R. J. García-Hernández, M. Wiedemann, and D. Kranzlmüller. “State of the Art of Virtual Reality Technology”. In: *2016 IEEE Aerospace Conference*. Big Sky, MT, USA, Mar. 5–12, 2016, pp. 1–19. DOI: 10.1109/AERO.2016.7500674 (cited on pp. 1, 2).

[5] I. Weygers, M. Kok, M. Konings, H. Hallez, H. De Vroey, and K. Claeys. “Inertial Sensor-Based Lower Limb Joint Kinematics: A Methodological Systematic Review”. In: *Sensors* 20.3 (Jan. 2020), Article 673. DOI: 10.3390/s20030673 (cited on pp. 1, 2).

[6] P. Picerno. “25 Years of Lower Limb Joint Kinematics by Using Inertial and Magnetic Sensors: A Review of Methodological Approaches”. In: *Gait & Posture* 51 (Jan. 1, 2017), pp. 239–246. ISSN: 0966-6362. DOI: 10.1016/j.gaitpost.2016.11.008 (cited on pp. 1, 2).

[7] D. K. Shaeffer. “MEMS Inertial Sensors: A Tutorial Overview”. In: *IEEE Communications Magazine* 51.4 (Apr. 2013), pp. 100–109. ISSN: 1558-1896. DOI: 10.1109/MCOM.2013.6495768 (cited on pp. 1, 10, 11).

[8] M. Perlmutter and S. Breit. “The Future of the MEMS Inertial Sensor Performance, Design and Manufacturing”. In: *2016 DGON Inertial Sensors and Systems (ISS)*. Karlsruhe, Germany, Sept. 20–21, 2016, pp. 1–12. DOI: 10.1109/InertialSensors.2016.7745671 (cited on p. 1).

[9] M. Kok, J. D. Hol, and T. B. Schön. “Using Inertial Sensors for Position and Orientation Estimation”. In: *Foundations and Trends in Signal Processing* 11.1-2 (2017), pp. 1–153. ISSN: 1932-8346, 1932-8354. DOI: 10.1561/2000000094 (cited on pp. 1, 10–12, 21, 24).

[10] O. J. Woodman. *An Introduction to Inertial Navigation*. Technical report UCAM-CL-TR-696. University of Cambridge, Computer Laboratory, 2007. DOI: 10.48456/tr-696 (cited on pp. 1, 12, 24).

[11] Q. Wang, P. Markopoulos, B. Yu, W. Chen, and A. Timmermans. "Interactive Wearable Systems for Upper Body Rehabilitation: A Systematic Review". In: *Journal of NeuroEngineering and Rehabilitation* 14.1 (Mar. 11, 2017), Article 20. ISSN: 1743-0003. DOI: 10.1186/s12984-017-0229-y (cited on p. 2).

[12] C. D. Hayden, B. P. Murphy, O. Hardiman, and D. Murray. "Measurement of Upper Limb Function in ALS: A Structure Review of Current Methods and Future Directions". In: *Journal of Neurology* (May 25, 2022). ISSN: 1432-1459. DOI: 10.1007/s00415-022-11179-8 (cited on p. 2).

[13] M. Molnar, M. Kok, T. Engel, H. Kaplick, F. Mayer, and T. Seel. "A Method for Lower Back Motion Assessment Using Wearable 6D Inertial Sensors". In: *2018 21st International Conference on Information Fusion (FUSION)*. Cambridge, UK, July 10–13, 2018, pp. 799–806. DOI: 10.23919/ICIF.2018.8455828 (cited on p. 2).

[14] M. Dechenaud, D. Laidig, T. Seel, H. B. Gilbert, and N. A. Kuznetsov. "Development of Adapted Guitar to Improve Motor Function after Stroke: Feasibility Study in Young Adults". In: *2019 41st Annual International Conference of the IEEE Engineering in Medicine and Biology Society (EMBC)*. Berlin, Germany, July 23–27, 2019, pp. 5488–5493. DOI: 10.1109/EMBC.2019.8856651 (cited on p. 2).

[15] H. Nguyen, K. Lebel, S. Bogard, E. Goubault, P. Boissy, and C. Duval. "Using Inertial Sensors to Automatically Detect and Segment Activities of Daily Living in People with Parkinson's Disease". In: *IEEE Transactions on Neural Systems and Rehabilitation Engineering* 26.1 (Jan. 2018), pp. 197–204. ISSN: 1558-0210. DOI: 10.1109/TNSRE.2017.2745418 (cited on p. 2).

[16] B. Mariani, H. Rouhani, X. Crevoisier, and K. Aminian. "Quantitative Estimation of Foot-Flat and Stance Phase of Gait Using Foot-Worn Inertial Sensors". In: *Gait & Posture* 37.2 (Feb. 1, 2013), pp. 229–234. ISSN: 0966-6362. DOI: 10.1016/j.gaitpost.2012.07.012 (cited on pp. 2, 129–132, 135).

[17] C. Werner, S. Schneider, R. Gassert, A. Curt, and L. Demkó. "Complementing Clinical Gait Assessments of Spinal Cord Injured Individuals Using Wearable Movement Sensors". In: *2020 42nd Annual International Conference of the IEEE Engineering in Medicine Biology Society (EMBC)*. Montreal, QC, Canada, July 20–24, 2020, pp. 3142–3145. DOI: 10.1109/EMBC44109.2020.9175703 (cited on p. 2).

[18] C. Mittag, R. Leiss, K. Lorenz, and T. Seel. "Development of a home-based wrist range-of-motion training system for children with cerebral palsy". In: *at - Automatisierungstechnik* 68.11 (Nov. 26, 2020), pp. 967–977. ISSN: 2196-677X. DOI: 10.1515/auto-2020-0085 (cited on pp. 2, 165).

[19] A. Passon, T. Schauer, and T. Seel. "Inertial-Robotic Motion Tracking in End-Effector-Based Rehabilitation Robots". In: *Frontiers in Robotics and AI* 7 (2020), Article 554639. ISSN: 2296-9144. DOI: 10.3389/frobt.2020.554639 (cited on p. 2).

[20] T. Seel, D. Laidig, M. Valtin, C. Werner, J. Raisch, and T. Schauer. "Feedback Control of Foot Eversion in the Adaptive Peroneal Stimulator". In: *22nd Mediterranean Conference on Control and Automation*. Palermo, Italy, June 16–19, 2014, pp. 1482–1487. DOI: 10.1109/MED.2014.6961585 (cited on pp. 2, 131).

[21] C. Wiesener, T. Seel, L. Spieker, A. Niedeggen, and T. Schauer. "Inertial-Sensor-Controlled Functional Electrical Stimulation for Swimming in Paraplegics: Enabling a Novel Hybrid Exercise Modality". In: *IEEE Control Systems Magazine* 40.6 (Dec. 2020), pp. 117–135. ISSN: 1941-000X. DOI: 10.1109/MCS.2020.3019152 (cited on p. 2).

[22] R. S. McGinnis and N. C. Perkins. "A Highly Miniaturized, Wireless Inertial Measurement Unit for Characterizing the Dynamics of Pitched Baseballs and Softballs". In: *Sensors* 12.9 (9 Sept. 2012), pp. 11933–11945. DOI: 10.3390/s120911933 (cited on p. 2).

[23] L. Liu, H.-H. Wang, S. Qiu, Y.-C. Zhang, and Z.-D. Hao. "Paddle Stroke Analysis for Kayakers Using Wearable Technologies". In: *Sensors* 21.3 (3 Jan. 2021), Article 914. DOI: 10.3390/s21030914 (cited on p. 2).

[24] S. Schleitzer, S. Wirtz, R. Julian, and E. Eils. "Development and Evaluation of an Inertial Measurement Unit (IMU) System for Jump Detection and Jump Height Estimation in Beach Volleyball". In: *German Journal of Exercise and Sport Research* 52 (May 3, 2022), pp. 228–236. ISSN: 2509-3150. DOI: 10.1007/s12662-022-00822-1 (cited on p. 2).

[25] Y. Wu, H.-B. Zhu, Q.-X. Du, and S.-M. Tang. "A Survey of the Research Status of Pedestrian Dead Reckoning Systems Based on Inertial Sensors". In: *International Journal of Automation and Computing* 16.1 (Feb. 1, 2019), pp. 65–83. ISSN: 1751-8520. DOI: 10.1007/s11633-018-1150-y (cited on p. 2).

[26] V. Rodrigo Marco, J. Kalkkuhl, J. Raisch, W. J. Scholte, H. Nijmeijer, and T. Seel. "Multi-Modal Sensor Fusion for Highly Accurate Vehicle Motion State Estimation". In: *Control Engineering Practice* 100 (July 1, 2020), Article 104409. ISSN: 0967-0661. DOI: 10.1016/j.conengprac.2020.104409 (cited on p. 2).

[27] H. Chao, Y. Cao, and Y. Chen. "Autopilots for Small Unmanned Aerial Vehicles: A Survey". In: *International Journal of Control, Automation and Systems* 8.1 (Feb. 1, 2010), pp. 36–44. ISSN: 2005-4092. DOI: 10.1007/s12555-010-0105-z (cited on p. 2).

[28] J. H. Freter, T. Seel, C. Elfert, and D. Göhlich. "Motion Estimation for Tethered Airfoils with Tether Sag". In: *2020 IEEE International Conference on Multisensor Fusion and Integration for Intelligent Systems (MFI)*. Karlsruhe, Germany, Sept. 14–16, 2020, pp. 114–120. DOI: 10.1109/MFI49285.2020.9235235 (cited on p. 2).

[29] A. Filippeschi, N. Schmitz, M. Miezal, G. Bleser, E. Ruffaldi, and D. Stricker. "Survey of Motion Tracking Methods Based on Inertial Sensors: A Focus on Upper Limb Human Motion". In: *Sensors* 17.6 (June 2017), Article 1257. DOI: 10.3390/s17061257 (cited on p. 2).

[30] T. Seel, M. Kok, and R. S. McGinnis. "Inertial Sensors—Applications and Challenges in a Nutshell". In: *Sensors* 20.21 (21 Jan. 2020), Article 6221. DOI: 10.3390/s20216221 (cited on p. 3).

[31] J. Lenz and S. Edelstein. "Magnetic Sensors and Their Applications". In: *IEEE Sensors Journal* 6.3 (June 2006), pp. 631–649. ISSN: 1558-1748. DOI: 10.1109/JSEN.2006.874493 (cited on pp. 11, 12).

[32] N. El-Sheimy, H. Hou, and X. Niu. "Analysis and Modeling of Inertial Sensors Using Allan Variance". In: *IEEE Transactions on Instrumentation and Measurement* 57.1 (Jan. 2008), pp. 140–149. ISSN: 1557-9662. DOI: 10.1109/TIM.2007.908635 (cited on p. 12).

[33] *World Magnetic Model (WMM) – Maps of Magnetic Elements from the WMM2020*. National Centers for Environmental Information (NCEI). URL: https://www.ncei.noaa.gov/products/world-magnetic-model#tab-952 (visited on 01/17/2023) (cited on p. 13).

[34] National Centers for Environmental Information. *NCEI Geomagnetic Calculators*. URL: https://www.ngdc.noaa.gov/geomag/calculators/magcalc.shtml#igrfwmm (visited on 08/23/2022) (cited on p. 13).

[35] M. Kok and T. B. Schön. "Magnetometer Calibration Using Inertial Sensors". In: *IEEE Sensors Journal* 16.14 (July 2016), pp. 5679–5689. ISSN: 1558-1748. DOI: 10.1109/JSEN.2016.2569160 (cited on p. 13).

[36] A. Solin, M. Kok, N. Wahlström, T. B. Schön, and S. Särkkä. "Modeling and Interpolation of the Ambient Magnetic Field by Gaussian Processes". In: *IEEE Transactions on Robotics* 34.4 (Aug. 2018), pp. 1112–1127. ISSN: 1941-0468. DOI: 10.1109/TRO.2018.2830326 (cited on pp. 13, 14).

[37] K. P. Subbu, B. Gozick, and R. Dantu. "LocateMe: Magnetic-Fields-Based Indoor Localization Using Smartphones". In: *ACM Transactions on Intelligent Systems and Technology* 4.4 (Oct. 2013), 73:1–73:27. ISSN: 2157-6904. DOI: 10.1145/2508037.2508054 (cited on pp. 13, 98).

[38] W. H. K. de Vries, H. E. J. Veeger, C. T. M. Baten, and F. C. T. van der Helm. "Magnetic Distortion in Motion Labs, Implications for Validating Inertial Magnetic Sensors". In: *Gait & Posture* 29.4 (June 1, 2009), pp. 535–541. ISSN: 0966-6362. DOI: 10.1016/j.gaitpost.2008.12.004 (cited on pp. 13, 27, 74, 78, 98, 129).

[39] Y. Shu, C. Bo, G. Shen, C. Zhao, L. Li, and F. Zhao. "Magicol: Indoor Localization Using Pervasive Magnetic Field and Opportunistic WiFi Sensing". In: *IEEE Journal on Selected Areas in Communications* 33.7 (July 2015), pp. 1443–1457. ISSN: 0733-8716. DOI: 10.1109/JSAC.2015.2430274 (cited on pp. 13, 98).

[40] E. L. Grand and S. Thrun. "3-Axis Magnetic Field Mapping and Fusion for Indoor Localization". In: *2012 IEEE International Conference on Multisensor Fusion and Integration for Intelligent Systems (MFI)*. Hamburg, Germany, Sept. 13–15, 2012, pp. 358–364. DOI: 10.1109/MFI.2012.6343024 (cited on pp. 13, 98).

[41] J. B. Kuipers. "Quaternions and Rotation Sequences". In: *Proceedings of the International Conference on Geometry, Integrability and Quantization*. Varna, Bulgaria: Coral Press Scientific Publishing, Sept. 1–10, 1999, pp. 127–143. DOI: 10.7546/giq-1-2000-127-143 (cited on p. 15).

[42] E. B. Dam, M. Koch, and M. Lillholm. *Quaternions, Interpolation and Animation*. Vol. 2. Datalogisk Institut, Københavns Universitet Copenhagen, 1998. URL: https://archive.org/details/Erik_B_Dam_Martin_Koch_and_Martin_Lillholm___Quaternions_Interpolation_and_Animation (cited on pp. 15, 201).

[43] J. Diebel. *Representing Attitude: Euler Angles, Unit Quaternions, and Rotation Vectors*. Technical report 94301–9010. Stanford, California: Stanford University, 2006, pp. 1–35. URL: https://web.archive.org/web/20070417133253/http://ai.stanford.edu/~diebel/attitude/attitude.pdf (cited on pp. 15, 17).

[44] G. Wahba. "A Least Squares Estimate of Satellite Attitude". In: *SIAM Review* 7.3 (July 1, 1965), pp. 409–409. ISSN: 0036-1445. DOI: 10.1137/1007077 (cited on p. 17).

[45] M. D. Shuster and S. D. Oh. "Three-Axis Attitude Determination from Vector Observations". In: *Journal of Guidance and Control* 4.1 (1981), pp. 70–77. ISSN: 0162-3192. DOI: 10.2514/3.19717 (cited on p. 17).

[46] G. Wu et al. "ISB Recommendation on Definitions of Joint Coordinate System of Various Joints for the Reporting of Human Joint Motion—Part I: Ankle, Hip, and Spine". In: *Journal of Biomechanics* 35.4 (Apr. 1, 2002), pp. 543–548. ISSN: 1873-2380. DOI: 10.1016/S0021-9290(01)00222-6 (cited on p. 20).

[47] G. Wu et al. "ISB Recommendation on Definitions of Joint Coordinate Systems of Various Joints for the Reporting of Human Joint Motion—Part II: Shoulder, Elbow, Wrist and Hand". In: *Journal of Biomechanics* 38.5 (May 1, 2005), pp. 981–992. ISSN: 1873-2380. DOI: 10.1016/j.jbiomech.2004.05.042 (cited on pp. 20, 75, 76, 82–84, 90, 91, 104, 110, 112, 199, 200).

[48] P. Dobrowolski. *Swing-Twist Decomposition in Clifford Algebra*. June 17, 2015. DOI: 10.48550/arXiv.1506.05481. preprint (cited on p. 20).

[49] E. Bergamini, G. Ligorio, A. Summa, G. Vannozzi, A. Cappozzo, and A. M. Sabatini. "Estimating Orientation Using Magnetic and Inertial Sensors and Different Sensor Fusion Approaches: Accuracy Assessment in Manual and Locomotion Tasks". In: *Sensors* 14.10 (Oct. 2014), pp. 18625–18649. DOI: 10.3390/s141018625 (cited on p. 21).

[50] D. Laidig, M. Caruso, A. Cereatti, and T. Seel. "BROAD—A Benchmark for Robust Inertial Orientation Estimation". In: *Data* 6.7 (7 July 2021), Article 72. DOI: 10.3390/data6070072 (cited on p. 23).

[51] D. Laidig, I. Weygers, S. Bachhuber, and T. Seel. "VQF: A Milestone in Accuracy and Versatility of 6D and 9D Inertial Orientation Estimation". In: *2022 25th International Conference on Information Fusion (FUSION)*. Linköping, Sweden, July 4–7, 2022, pp. 1–6. DOI: 10.23919/FUSION49751.2022.9841356 (cited on p. 23).

[52] D. Laidig and T. Seel. “VQF: Highly Accurate IMU Orientation Estimation with Bias Estimation and Magnetic Disturbance Rejection”. In: *Information Fusion* 91 (Mar. 1, 2023), pp. 187–204. ISSN: 1566-2535. DOI: 10.1016/j.inffus.2022.10.014 (cited on p. 23).

[53] M. Caruso, A. M. Sabatini, M. Knaflitz, M. Gazzoni, U. D. Croce, and A. Cereatti. “Orientation Estimation through Magneto-Inertial Sensor Fusion: A Heuristic Approach for Suboptimal Parameters Tuning”. In: *IEEE Sensors Journal* 21.3 (Feb. 2021), pp. 3408–3419. ISSN: 1558-1748. DOI: 10.1109/JSEN.2020.3024806 (cited on pp. 24, 25, 30, 31, 33, 44, 59).

[54] M. Caruso, A. M. Sabatini, D. Laidig, T. Seel, M. Knaflitz, U. Della Croce, and A. Cereatti. “Analysis of the Accuracy of Ten Algorithms for Orientation Estimation Using Inertial and Magnetic Sensing under Optimal Conditions: One Size Does Not Fit All”. In: *Sensors* 21.7 (7 Jan. 2021), Article 2543. DOI: 10.3390/s21072543 (cited on pp. 24, 26, 27, 44).

[55] B. Fan, Q. Li, and T. Liu. “How Magnetic Disturbance Influences the Attitude and Heading in Magnetic and Inertial Sensor-Based Orientation Estimation”. In: *Sensors* 18.1 (1 Jan. 2018), Article 76. DOI: 10.3390/s18010076 (cited on p. 24).

[56] M. Nazarahari and H. Rouhani. “40 Years of Sensor Fusion for Orientation Tracking via Magnetic and Inertial Measurement Units: Methods, Lessons Learned, and Future Challenges”. In: *Information Fusion* 68 (Nov. 2, 2020), pp. 67–84. ISSN: 1566-2535. DOI: 10.1016/j.inffus.2020.10.018 (cited on pp. 25, 27).

[57] D. Weber, C. Gühmann, and T. Seel. “RIANN—A Robust Neural Network Outperforms Attitude Estimation Filters”. In: *AI* 2.3 (3 Sept. 2021), pp. 444–463. DOI: 10.3390/ai2030028 (cited on pp. 27–29, 61, 63, 166).

[58] D. Weber, C. Gühmann, and T. Seel. “Neural Networks versus Conventional Filters for Inertial-Sensor-Based Attitude Estimation”. In: *2020 IEEE 23rd International Conference on Information Fusion (FUSION)*. Rustenburg, South Africa, July 6–9, 2020, pp. 1–8. DOI: 10.23919/FUSION45008.2020.9190634 (cited on p. 27).

[59] R. E. Kalman. “A New Approach to Linear Filtering and Prediction Problems”. In: *Journal of Basic Engineering* 82.1 (Mar. 1, 1960), pp. 35–45. ISSN: 0021-9223. DOI: 10.1115/1.3662552 (cited on pp. 27, 54).

[60] G. Welch and G. Bishop. *An Introduction to the Kalman Filter*. Technical report 95-041. University of North Carolina at Chapel Hill, 2006, pp. 1–16. URL: https://www.cs.unc.edu/~welch/media/pdf/kalman_intro.pdf (cited on pp. 27, 54).

[61] A. Sabatini. “Quaternion-Based Extended Kalman Filter for Determining Orientation by Inertial and Magnetic Sensing”. In: *IEEE Transactions on Biomedical Engineering* 53.7 (July 2006), pp. 1346–1356. ISSN: 1558-2531. DOI: 10.1109/TBME.2006.875664 (cited on p. 27).

[62] A. M. Sabatini. “Estimating Three-Dimensional Orientation of Human Body Parts by Inertial/Magnetic Sensing”. In: *Sensors* 11.2 (2 Feb. 2011), pp. 1489–1525. DOI: 10.3390/s110201489 (cited on p. 27).

[63] A. M. Sabatini. "Kalman-Filter-Based Orientation Determination Using Inertial/Magnetic Sensors: Observability Analysis and Performance Evaluation". In: *Sensors* 11.10 (10 Oct. 2011), pp. 9182–9206. DOI: 10.3390/s111009182 (cited on pp. 27, 33).

[64] M. Ghobadi, P. Singla, and E. T. Esfahani. "Robust Attitude Estimation from Uncertain Observations of Inertial Sensors Using Covariance Inflated Multiplicative Extended Kalman Filter". In: *IEEE Transactions on Instrumentation and Measurement* 67.1 (Jan. 2018), pp. 209–217. ISSN: 1557-9662. DOI: 10.1109/TIM.2017.2761230 (cited on p. 27).

[65] D. Roetenberg, H. J. Luinge, C. T. M. Baten, and P. H. Veltink. "Compensation of Magnetic Disturbances Improves Inertial and Magnetic Sensing of Human Body Segment Orientation". In: *IEEE Transactions on Neural Systems and Rehabilitation Engineering* 13.3 (Sept. 2005), pp. 395–405. ISSN: 1534-4320. DOI: 10.1109/TNSRE.2005.847353 (cited on p. 27).

[66] W. Ding and Y. Gao. "Attitude Estimation Using Low-Cost MARG Sensors with Disturbances Reduction". In: *IEEE Transactions on Instrumentation and Measurement* 70 (2021), pp. 1–11. ISSN: 1557-9662. DOI: 10.1109/TIM.2021.3104395 (cited on p. 27).

[67] R. V. Vitali, R. S. McGinnis, and N. C. Perkins. "Robust Error-State Kalman Filter for Estimating IMU Orientation". In: *IEEE Sensors Journal* 21.3 (Feb. 2021), pp. 3561–3569. ISSN: 1558-1748. DOI: 10.1109/JSEN.2020.3026895 (cited on p. 27).

[68] J. K. Lee, E. J. Park, and S. N. Robinovitch. "Estimation of Attitude and External Acceleration Using Inertial Sensor Measurement during Various Dynamic Conditions". In: *IEEE Transactions on Instrumentation and Measurement* 61.8 (Aug. 2012), pp. 2262–2273. ISSN: 1557-9662. DOI: 10.1109/TIM.2012.2187245 (cited on p. 27).

[69] G. Ligorio and A. M. Sabatini. "A Novel Kalman Filter for Human Motion Tracking with an Inertial-Based Dynamic Inclinometer". In: *IEEE Transactions on Biomedical Engineering* 62.8 (Aug. 2015), pp. 2033–2043. ISSN: 1558-2531. DOI: 10.1109/TBME.2015.2411431 (cited on pp. 27, 44).

[70] R. G. Valenti, I. Dryanovski, and J. Xiao. "A Linear Kalman Filter for MARG Orientation Estimation Using the Algebraic Quaternion Algorithm". In: *IEEE Transactions on Instrumentation and Measurement* 65.2 (Feb. 2016), pp. 467–481. ISSN: 1557-9662. DOI: 10.1109/TIM.2015.2498998 (cited on p. 27).

[71] S. Guo, J. Wu, Z. Wang, and J. Qian. "Novel MARG-Sensor Orientation Estimation Algorithm Using Fast Kalman Filter". In: *Journal of Sensors* 2017 (Sept. 24, 2017), Article e8542153. ISSN: 1687-725X. DOI: 10.1155/2017/8542153 (cited on pp. 27, 28, 44, 61).

[72] Á. Deibe, J. A. Antón Nacimiento, J. Cardenal, and F. López Peña. "A Kalman Filter for Nonlinear Attitude Estimation Using Time Variable Matrices and Quaternions". In: *Sensors* 20.23 (23 Jan. 2020), Article 6731. DOI: 10.3390/s20236731 (cited on p. 27).

[73] R. Mahony, T. Hamel, and J.-M. Pflimlin. "Nonlinear Complementary Filters on the Special Orthogonal Group". In: *IEEE Transactions on Automatic Control* 53.5 (June 2008), pp. 1203–1218. ISSN: 1558-2523. DOI: 10.1109/TAC.2008.923738 (cited on pp. 27, 28, 41–44, 49, 52, 61).

[74] S. O. H. Madgwick. *An Efficient Orientation Filter for Inertial and Inertial/Magnetic Sensor Arrays*. Technical report. UK: University of Bristol, Apr. 30, 2010, pp. 1–32. URL: https://x-io.co.uk/downloads/madgwick_internal_report.pdf (cited on pp. 27, 28, 42, 49, 52, 61).

[75] R. G. Valenti, I. Dryanovski, and J. Xiao. "Keeping a Good Attitude: A Quaternion-Based Orientation Filter for IMUs and MARGs". In: *Sensors* 15.8 (8 Aug. 2015), pp. 19302–19330. DOI: 10.3390/s150819302 (cited on pp. 27, 28, 46, 61).

[76] T. Seel and S. Ruppin. "Eliminating the Effect of Magnetic Disturbances on the Inclination Estimates of Inertial Sensors". In: *IFAC-PapersOnLine*. 20th IFAC World Congress 50.1 (July 1, 2017), pp. 8798–8803. ISSN: 2405-8963. DOI: 10.1016/j.ifacol.2017.08.1534 (cited on pp. 27–29, 46, 49, 52, 61, 102).

[77] M. Caruso, A. M. Sabatini, M. Knaflitz, M. Gazzoni, U. D. Croce, and A. Cereatti. "Accuracy of the Orientation Estimate Obtained Using Four Sensor Fusion Filters Applied to Recordings of Magneto-Inertial Sensors Moving at Three Rotation Rates". In: *2019 41st Annual International Conference of the IEEE Engineering in Medicine and Biology Society (EMBC)*. Berlin, Germany, July 23–27, 2019, pp. 2053–2058. DOI: 10.1109/EMBC.2019.8857655 (cited on p. 27).

[78] B. Fan, Q. Li, and T. Liu. "Improving the Accuracy of Wearable Sensor Orientation Using a Two-Step Complementary Filter with State Machine-Based Adaptive Strategy". In: *Measurement Science and Technology* 29.11 (Oct. 2018), Article 115104. ISSN: 0957-0233. DOI: 10.1088/1361-6501/aae125 (cited on p. 27).

[79] B. Fan, Q. Li, C. Wang, and T. Liu. "An Adaptive Orientation Estimation Method for Magnetic and Inertial Sensors in the Presence of Magnetic Disturbances". In: *Sensors* 17 (May 19, 2017), Article 1161. DOI: 10.3390/s17051161 (cited on p. 27).

[80] G. Ligorio and A. M. Sabatini. "Dealing with Magnetic Disturbances in Human Motion Capture: A Survey of Techniques". In: *Micromachines* 7.3 (Mar. 2016), Article 43. DOI: 10.3390/mi7030043 (cited on p. 28).

[81] M. Kok and T. B. Schön. "A Fast and Robust Algorithm for Orientation Estimation Using Inertial Sensors". In: *IEEE Signal Processing Letters* 26.11 (Nov. 2019), pp. 1673–1677. ISSN: 1558-2361. DOI: 10.1109/LSP.2019.2943995 (cited on pp. 28, 29, 61).

[82] S. O. H. Madgwick, A. J. L. Harrison, and R. Vaidyanathan. "Estimation of IMU and MARG Orientation Using a Gradient Descent Algorithm". In: *2011 IEEE International Conference on Rehabilitation Robotics*. Zurich, Switzerland, June 29–July 1, 2011, pp. 1–7. DOI: 10.1109/ICORR.2011.5975346 (cited on pp. 28, 33, 41–44).

[83] A. Szczęsna, P. Skurowski, P. Pruszowski, D. Pęszor, M. Paszkuta, and K. Wojciechowski. "Reference Data Set for Accuracy Evaluation of Orientation Estimation Algorithms for Inertial Motion Capture Systems". In: *Computer Vision and Graphics*. Ed. by L. J. Chmielewski, A. Datta, R. Kozera, and K. Wojciechowski. Lecture Notes in Computer Science. Cham: Springer International Publishing, 2016, pp. 509–520. DOI: 10.1007/978-3-319-46418-3_45 (cited on pp. 30, 33, 59).

[84] K. Jędrasiak, K. Daniec, and A. Nawrat. "The Low Cost Micro Inertial Measurement Unit". In: *2013 IEEE 8th Conference on Industrial Electronics and Applications (ICIEA)*. Melbourne, Australia, June 19–21, 2013, pp. 403–408. DOI: 10.1109/ICIEA.2013.6566403 (cited on p. 30).

[85] C. Chen, P. Zhao, C. X. Lu, W. Wang, A. Markham, and N. Trigoni. "OxIOD: The Dataset for Deep Inertial Odometry". Sept. 20, 2018. arXiv: 1809.07491 [cs] (cited on pp. 30, 32, 33, 59).

[86] M. Burri, J. Nikolic, P. Gohl, T. Schneider, J. Rehder, S. Omari, M. W. Achtelik, and R. Siegwart. "The EuRoC Micro Aerial Vehicle Datasets". In: *The International Journal of Robotics Research* 35.10 (Sept. 1, 2016), pp. 1157–1163. ISSN: 0278-3649. DOI: 10.1177/0278364915620033 (cited on pp. 30, 32, 33, 59).

[87] D. Schubert, T. Goll, N. Demmel, V. Usenko, J. Stückler, and D. Cremers. "The TUM VI Benchmark for Evaluating Visual-Inertial Odometry". In: *2018 IEEE/RSJ International Conference on Intelligent Robots and Systems (IROS)*. Madrid, Spain, Oct. 1–5, 2018, pp. 1680–1687. DOI: 10.1109/IROS.2018.8593419 (cited on pp. 30, 32, 33, 59).

[88] G. H. Lee, M. Achtelik, F. Fraundorfer, M. Pollefeys, and R. Siegwart. "A Benchmarking Tool for MAV Visual Pose Estimation". In: *2010 11th International Conference on Control Automation Robotics Vision*. Singapore, Dec. 7–10, 2010, pp. 1541–1546. DOI: 10.1109/ICARCV.2010.5707339 (cited on p. 32).

[89] J. D. Hol. "Sensor Fusion and Calibration of Inertial Sensors, Vision, Ultra-Wideband and GPS". PhD thesis. Linköping, Sweden: Linköping University, 2011. URL: https://urn.kb.se/resolve?urn=urn:nbn:se:liu:diva-66184 (cited on p. 37).

[90] F. Gustafsson. "Determining the Initial States in Forward-Backward Filtering". In: *IEEE Transactions on Signal Processing* 44.4 (Apr. 1996), pp. 988–992. ISSN: 1941-0476. DOI: 10.1109/78.492552 (cited on p. 58).

[91] D. Laidig, P. Müller, and T. Seel. "Automatic Anatomical Calibration for IMU-based Elbow Angle Measurement in Disturbed Magnetic Fields". In: *Current Directions in Biomedical Engineering* 3.2 (2017), pp. 167–170. DOI: 10.1515/cdbme-2017-0035 (cited on pp. 71, 78).

[92] D. Laidig, I. Weygers, and T. Seel. "Self-Calibrating Magnetometer-Free Inertial Motion Tracking of 2-DoF Joints". In: *Sensors* 22.24 (24 Dec. 2022), Article 9850. ISSN: 1424-8220. DOI: 10.3390/s22249850 (cited on p. 71).

[93] R. V. Vitali and N. C. Perkins. “Determining Anatomical Frames via Inertial Motion Capture: A Survey of Methods”. In: *Journal of Biomechanics* 106 (June 9, 2020), Article 109832. ISSN: 0021-9290. DOI: 10.1016/j.jbiomech.2020.109832 (cited on pp. 72, 73).

[94] T. Seel, J. Raisch, and T. Schauer. “IMU-based Joint Angle Measurement for Gait Analysis”. In: *Sensors* 14.4 (Apr. 16, 2014), pp. 6891–6909. DOI: 10.3390/s140406891 (cited on pp. 72, 74, 77, 98, 101, 109, 161).

[95] F. Olsson, M. Kok, T. Seel, and K. Halvorsen. “Robust Plug-and-Play Joint Axis Estimation Using Inertial Sensors”. In: *Sensors* 20.12 (12 Jan. 2020), Article 3534. DOI: 10.3390/s20123534 (cited on pp. 72, 74, 112).

[96] D. Graurock, T. Schauer, and T. Seel. “Automatic Pairing of Inertial Sensors to Lower Limb Segments – a Plug-and-Play Approach”. In: *Current Directions in Biomedical Engineering* 2.1 (Sept. 1, 2016), pp. 715–718. DOI: 10.1515/cdbme-2016-0155 (cited on p. 73).

[97] T. Zimmermann, B. Taetz, and G. Bleser. “IMU-to-segment Assignment and Orientation Alignment for the Lower Body Using Deep Learning”. In: *Sensors* 18.1 (Jan. 2018), Article 302. DOI: 10.3390/s18010302 (cited on pp. 73, 74).

[98] S. J. Piazza, N. Okita, and P. R. Cavanagh. “Accuracy of the Functional Method of Hip Joint Center Location: Effects of Limited Motion and Varied Implementation”. In: *Journal of Biomechanics* 34.7 (July 1, 2001), pp. 967–973. ISSN: 0021-9290. DOI: 10.1016/S0021-9290(01)00052-5 (cited on p. 73).

[99] T. Seel, T. Schauer, and J. Raisch. “Joint Axis and Position Estimation from Inertial Measurement Data by Exploiting Kinematic Constraints”. In: *2012 IEEE International Conference on Control Applications*. Dubrovnik, Croatia, Oct. 3–5, 2012, pp. 45–49. DOI: 10.1109/CCA.2012.6402423 (cited on pp. 73, 74, 101).

[100] M. Crabolu, D. Pani, L. Raffo, and A. Cereatti. “Estimation of the Center of Rotation Using Wearable Magneto-Inertial Sensors”. In: *Journal of Biomechanics* 49.16 (Dec. 8, 2016), pp. 3928–3933. ISSN: 0021-9290. DOI: 10.1016/j.jbiomech.2016.11.046 (cited on p. 73).

[101] F. Olsson and K. Halvorsen. “Experimental Evaluation of Joint Position Estimation Using Inertial Sensors”. In: *2017 20th International Conference on Information Fusion (Fusion)*. Xi’an, China, July 10–13, 2017, pp. 1–8. DOI: 10.23919/ICIF.2017.8009669 (cited on p. 73).

[102] A. Brennan, K. Deluzio, and Q. Li. “Assessment of Anatomical Frame Variation Effect on Joint Angles: A Linear Perturbation Approach”. In: *Journal of Biomechanics* 44.16 (Nov. 10, 2011), pp. 2838–2842. ISSN: 0021-9290. DOI: 10.1016/j.jbiomech.2011.09.006 (cited on p. 73).

[103] B. Fan, Q. Li, T. Tan, P. Kang, and P. B. Shull. “Effects of IMU Sensor-to-Segment Misalignment and Orientation Error on 3-D Knee Joint Angle Estimation”. In: *IEEE Sensors Journal* 22.3 (Feb. 2022), pp. 2543–2552. ISSN: 1558-1748. DOI: 10.1109/JSEN.2021.3137305 (cited on p. 73).

[104] M. Miezal, B. Taetz, and G. Bleser. “On Inertial Body Tracking in the Presence of Model Calibration Errors”. In: *Sensors* 16.7 (July 2016), Article 1132. DOI: 10.3390/s16071132 (cited on p. 73).

[105] B. Bouvier, S. Duprey, L. Claudon, R. Dumas, and A. Savescu. “Upper Limb Kinematics Using Inertial and Magnetic Sensors: Comparison of Sensor-to-Segment Calibrations”. In: *Sensors* 15.8 (Aug. 2015), pp. 18813–18833. DOI: 10.3390/s150818813 (cited on pp. 73, 74).

[106] P. Picerno, A. Cereatti, and A. Cappozzo. “Joint Kinematics Estimate Using Wearable Inertial and Magnetic Sensing Modules”. In: *Gait & Posture* 28.4 (Nov. 1, 2008), pp. 588–595. ISSN: 0966-6362. DOI: 10.1016/j.gaitpost.2008.04.003 (cited on p. 73).

[107] P. Picerno et al. “Upper Limb Joint Kinematics Using Wearable Magnetic and Inertial Measurement Units: An Anatomical Calibration Procedure Based on Bony Landmark Identification”. In: *Scientific Reports* 9.1 (1 Oct. 8, 2019), Article 14449. ISSN: 2045-2322. DOI: 10.1038/s41598-019-50759-z (cited on p. 73).

[108] L. S. Vargas-Valencia, A. Elias, E. Rocon, T. Bastos-Filho, and A. Frizera. “An IMU-to-body Alignment Method Applied to Human Gait Analysis”. In: *Sensors* 16.12 (Dec. 2016), Article 2090. DOI: 10.3390/s16122090 (cited on p. 73).

[109] X. Robert-Lachaine, H. Mecheri, C. Larue, and A. Plamondon. “Accuracy and Repeatability of Single-Pose Calibration of Inertial Measurement Units for Whole-Body Motion Analysis”. In: *Gait & Posture* 54 (May 1, 2017), pp. 80–86. ISSN: 0966-6362. DOI: 10.1016/j.gaitpost.2017.02.029 (cited on p. 73).

[110] H. T. Butt, B. Taetz, M. Musahl, M. A. Sanchez, P. Murthy, and D. Stricker. “Magnetometer Robust Deep Human Pose Regression with Uncertainty Prediction Using Sparse Body Worn Magnetic Inertial Measurement Units”. In: *IEEE Access* 9 (2021), pp. 36657–36673. ISSN: 2169-3536. DOI: 10.1109/ACCESS.2021.3062545 (cited on pp. 73, 101, 166).

[111] R. van der Straaten et al. “Discriminant Validity of 3D Joint Kinematics and Centre of Mass Displacement Measured by Inertial Sensor Technology during the Unipodal Stance Task”. In: *PLOS ONE* 15.5 (May 14, 2020), Article e0232513. ISSN: 1932-6203. DOI: 10.1371/journal.pone.0232513 (cited on p. 73).

[112] E. Palermo, S. Rossi, F. Marini, F. Patanè, and P. Cappa. “Experimental Evaluation of Accuracy and Repeatability of a Novel Body-to-Sensor Calibration Procedure for Inertial Sensor-Based Gait Analysis”. In: *Measurement* 52 (June 1, 2014), pp. 145–155. ISSN: 0263-2241. DOI: 10.1016/j.measurement.2014.03.004 (cited on p. 73).

[113] J. Favre, R. Aissaoui, B. M. Jolles, J. A. de Guise, and K. Aminian. “Functional Calibration Procedure for 3D Knee Joint Angle Description Using Inertial Sensors”. In: *Journal of Biomechanics* 42.14 (Oct. 16, 2009), pp. 2330–2335. ISSN: 0021-9290. DOI: 10.1016/j.jbiomech.2009.06.025 (cited on p. 73).

[114] W. H. K. de Vries, H. E. J. Veeger, A. G. Cutti, C. Baten, and F. C. T. van der Helm. “Functionally Interpretable Local Coordinate Systems for the Upper Extremity Using Inertial & Magnetic Measurement Systems”. In: *Journal of Biomechanics* 43.10 (July 20, 2010), pp. 1983–1988. ISSN: 0021-9290. DOI: 10.1016/j.jbiomech.2010.03.007 (cited on p. 73).

[115] H. J. Luinge, P. H. Veltink, and C. T. M. Baten. “Ambulatory Measurement of Arm Orientation”. In: *Journal of Biomechanics* 40.1 (Jan. 1, 2007), pp. 78–85. ISSN: 1873-2380. DOI: 10.1016/j.jbiomech.2005.11.011 (cited on pp. 73, 101).

[116] A. G. Cutti, A. Giovanardi, L. Rocchi, A. Davalli, and R. Sacchetti. “Ambulatory Measurement of Shoulder and Elbow Kinematics through Inertial and Magnetic Sensors”. In: *Medical & Biological Engineering & Computing* 46.2 (Feb. 1, 2008), pp. 169–178. ISSN: 1741-0444. DOI: 10.1007/s11517-007-0296-5 (cited on p. 74).

[117] G. Ligorio, E. Bergamini, L. Truppa, M. Guaitolini, M. Raggi, A. Mannini, A. M. Sabatini, G. Vannozzi, and P. Garofalo. “A Wearable Magnetometer-Free Motion Capture System: Innovative Solutions for Real-World Applications”. In: *IEEE Sensors Journal* 20.15 (Aug. 2020), pp. 8844–8857. ISSN: 1558-1748. DOI: 10.1109/JSEN.2020.2983695 (cited on pp. 74, 100).

[118] J. Favre, B. M. Jolles, R. Aissaoui, and K. Aminian. “Ambulatory Measurement of 3D Knee Joint Angle”. In: *Journal of Biomechanics* 41.5 (Jan. 1, 2008), pp. 1029–1035. ISSN: 0021-9290. DOI: 10.1016/j.jbiomech.2007.12.003 (cited on p. 74).

[119] J. Lebleu, T. Gosseye, C. Detrembleur, P. Mahaudens, O. Cartiaux, and M. Penta. “Lower Limb Kinematics Using Inertial Sensors during Locomotion: Accuracy and Reproducibility of Joint Angle Calculations with Different Sensor-to-Segment Calibrations”. In: *Sensors* 20.3 (Jan. 2020), Article 715. DOI: 10.3390/s20030715 (cited on p. 74).

[120] G. Mascia, P. Brasiliano, P. Di Feo, A. Cereatti, and V. Camomilla. “A Functional Calibration Protocol for Ankle Plantar-Dorsiflexion Estimate Using Magnetic and Inertial Measurement Units: Repeatability and Reliability Assessment”. In: *Journal of Biomechanics* (June 20, 2022), Article 111202. ISSN: 0021-9290. DOI: 10.1016/j.jbiomech.2022.111202 (cited on p. 74).

[121] D. S. Cottam, A. C. Campbell, P. C. Davey, P. Kent, B. C. Elliott, and J. A. Alderson. “Functional Calibration Does Not Improve the Concurrent Validity of Magneto-Inertial Wearable Sensor-Based Thorax and Lumbar Angle Measurements When Compared with Retro-Reflective Motion Capture”. In: *Medical & Biological Engineering & Computing* 59 (Sept. 16, 2021), pp. 2253–2262. ISSN: 1741-0444. DOI: 10.1007/s11517-021-02440-9 (cited on p. 74).

[122] S. Cordillet, N. Bideau, B. Bideau, and G. Nicolas. “Estimation of 3D Knee Joint Angles during Cycling Using Inertial Sensors: Accuracy of a Novel Sensor-to-Segment Calibration Procedure Based on Pedaling Motion”. In: *Sensors* 19 (May 30, 2019), Article 2474. DOI: 10.3390/s19112474 (cited on p. 74).

[123] L. Carcreff, G. Payen, G. Grouvel, F. Massé, and S. Armand. "Three-Dimensional Lower-Limb Kinematics from Accelerometers and Gyroscopes with Simple and Minimal Functional Calibration Tasks: Validation on Asymptomatic Participants". In: *Sensors* 22.15 (15 Jan. 2022), Article 5657. ISSN: 1424-8220. DOI: 10.3390/s22155657 (cited on p. 74).

[124] S. Salehi, G. Bleser, A. Reiss, and D. Stricker. "Body-IMU Autocalibration for Inertial Hip and Knee Joint Tracking". In: *Proceedings of the 10th EAI International Conference on Body Area Networks*. Brussels, Belgium: ICST, 2015, pp. 51–57. DOI: 10.4108/eai.28-9-2015.2261522 (cited on p. 74).

[125] T. McGrath, R. Fineman, and L. Stirling. "An Auto-Calibrating Knee Flexion-Extension Axis Estimator Using Principal Component Analysis with Inertial Sensors". In: *Sensors* 18 (June 8, 2018), Article 1882. DOI: 10.3390/s18061882 (cited on p. 74).

[126] T. McGrath and L. Stirling. "Body-Worn IMU Human Skeletal Pose Estimation Using a Factor Graph-Based Optimization Framework". In: *Sensors* 20 (Dec. 2, 2020), Article 6887. DOI: 10.3390/s20236887 (cited on pp. 74, 100).

[127] T. McGrath and L. Stirling. "Body-Worn IMU-based Human Hip and Knee Kinematics Estimation during Treadmill Walking". In: *Sensors* 22.7 (7 Jan. 2022), Article 2544. ISSN: 1424-8220. DOI: 10.3390/s22072544 (cited on pp. 74, 100).

[128] F. Olsson, T. Seel, D. Lehmann, and K. Halvorsen. "Joint Axis Estimation for Fast and Slow Movements Using Weighted Gyroscope and Acceleration Constraints". In: *2019 22th International Conference on Information Fusion (FUSION)*. Ottawa, ON, Canada, July 2–5, 2019, pp. 1–8. DOI: 10.23919/FUSION43075.2019.9011409 (cited on p. 74).

[129] D. Nowka, M. Kok, and T. Seel. "On Motions That Allow for Identification of Hinge Joint Axes from Kinematic Constraints and 6D IMU Data". In: *2019 18th European Control Conference (ECC)*. Naples, Italy, June 25–28, 2019. DOI: 10.23919/ECC.2019.8795846 (cited on pp. 74, 166).

[130] B. Taetz, G. Bleser, and M. Miezal. "Towards Self-Calibrating Inertial Body Motion Capture". In: *2016 19th International Conference on Information Fusion (FUSION)*. Heidelberg, Germany, July 5–8, 2016, pp. 1751–1759. URL: https://ieeexplore.ieee.org/document/7528095 (cited on pp. 74, 100, 101).

[131] P. Müller, M. A. Bégin, T. Schauer, and T. Seel. "Alignment-Free, Self-Calibrating Elbow Angles Measurement Using Inertial Sensors". In: *IEEE Journal of Biomedical and Health Informatics* 21.2 (Mar. 2017), pp. 312–319. ISSN: 2168-2194. DOI: 10.1109/JBHI.2016.2639537 (cited on p. 74).

[132] M. Norden, P. Müller, and T. Schauer. "Real-Time Joint Axes Estimation of the Hip and Knee Joint during Gait Using Inertial Sensors". In: *Proceedings of the 5th International Workshop on Sensor-based Activity Recognition and Interaction*. New York, NY, USA: Association for Computing Machinery, Sept. 20, 2018, pp. 1–6. DOI: 10.1145/3266157.3266213 (cited on p. 74).

[133] J. Nocedal and S. Wright. *Numerical Optimization*. Springer New York, NY, 1999. URL: https://link.springer.com/book/10.1007/b98874 (cited on p. 81).

[134] I. Weygers, M. Kok, T. Seel, D. Shah, O. Taylan, L. Scheys, H. Hallez, and K. Claeys. "In-Vitro Validation of Inertial-Sensor-to-Bone Alignment". In: *Journal of Biomechanics* (Oct. 2, 2021), Article 110781. ISSN: 0021-9290. DOI: 10.1016/j.jbiomech.2021.110781 (cited on p. 94).

[135] D. Laidig, T. Schauer, and T. Seel. "Exploiting Kinematic Constraints to Compensate Magnetic Disturbances When Calculating Joint Angles of Approximate Hinge Joints from Orientation Estimates of Inertial Sensors". In: *2017 International Conference on Rehabilitation Robotics (ICORR)*. London, UK, July 17–20, 2017, pp. 971–976. DOI: 10.1109/ICORR.2017.8009375 (cited on pp. 97, 98, 106).

[136] D. Lehmann, D. Laidig, and T. Seel. "Magnetometer-Free Motion Tracking of One-Dimensional Joints by Exploiting Kinematic Constraints". In: *Proceedings on Automation in Medical Engineering* 1.1 (Feb. 16, 2020), Article 027. URL: https://www.journals.infinite-science.de/index.php/automed/article/view/335 (cited on pp. 97, 98).

[137] D. Laidig, D. Lehmann, M.-A. Bégin, and T. Seel. "Magnetometer-Free Realtime Inertial Motion Tracking by Exploitation of Kinematic Constraints in 2-DoF Joints". In: *2019 41st Annual International Conference of the IEEE Engineering in Medicine and Biology Society (EMBC)*. Berlin, Germany, July 23–27, 2019, pp. 1233–1238. DOI: 10.1109/EMBC.2019.8857535 (cited on pp. 97, 98).

[138] C. Salchow-Hömmen, L. Callies, D. Laidig, M. Valtin, T. Schauer, and T. Seel. "A Tangible Solution for Hand Motion Tracking in Clinical Applications". In: *Sensors* 19.1 (Jan. 2019), Article 208. DOI: 10.3390/s19010208 (cited on pp. 98–100, 118, 120, 124).

[139] D. Laidig and T. Seel. "Deriving Kinematic Quantities from Accelerometer Readings for Assessment of Functional Upper Limb Motions". In: *Current Directions in Biomedical Engineering* 3.2 (2017), pp. 573–576. DOI: 10.1515/cdbme-2017-0119 (cited on p. 100).

[140] M. Kok, K. Eckhoff, I. Weygers, and T. Seel. "Observability of the Relative Motion from Inertial Data in Kinematic Chains". In: *Control Engineering Practice* 125 (Aug. 1, 2022), Article 105206. ISSN: 0967-0661. DOI: 10.1016/j.conengprac.2022.105206 (cited on pp. 100, 101, 166).

[141] M. Kok, J. D. Hol, and T. B. Schön. "An Optimization-Based Approach to Human Body Motion Capture Using Inertial Sensors". In: *IFAC Proceedings Volumes*. 19th IFAC World Congress 47.3 (Jan. 1, 2014), pp. 79–85. ISSN: 1474-6670. DOI: 10.3182/20140824-6-ZA-1003.02252 (cited on pp. 100, 101).

[142] W. Teufl, M. Miezal, B. Taetz, M. Fröhlich, and G. Bleser. "Validity, Test-Retest Reliability and Long-Term Stability of Magnetometer Free Inertial Sensor Based 3D Joint Kinematics". In: *Sensors* 18.7 (July 2018), Article 1980. DOI: 10.3390/s18071980 (cited on pp. 100, 101).

[143] M. Lorenz, G. Bleser, D. Stricker, and B. Taetz. "Towards Inertial Human Motion Tracking with Drift-Free Absolute Orientations Using Only Sparse Sources of Heading Information". In: *2022 25th International Conference on Information Fusion (FUSION)*.

Linköping, Sweden, July 4–7, 2022, pp. 1–8. DOI: 10.23919/FUSION49751.2022.9841280 (cited on p. 100).

[144] F. Wenk and U. Frese. "Posture from Motion". In: *2015 IEEE/RSJ International Conference on Intelligent Robots and Systems (IROS)*. Hamburg, Germany, Sept. 28–Oct. 2, 2015, pp. 280–285. DOI: 10.1109/IROS.2015.7353386 (cited on pp. 100, 101).

[145] B. Fasel, J. Spörri, J. Chardonnens, J. Kröll, E. Müller, and K. Aminian. "Joint Inertial Sensor Orientation Drift Reduction for Highly Dynamic Movements". In: *IEEE Journal of Biomedical and Health Informatics* 22.1 (Jan. 2018), pp. 77–86. ISSN: 2168-2208. DOI: 10.1109/JBHI.2017.2659758 (cited on pp. 100, 101).

[146] J. K. Lee and T. H. Jeon. "IMU-based but Magnetometer-Free Joint Angle Estimation of Constrained Links". In: *2018 IEEE SENSORS*. New Delhi, India, Oct. 28–31, 2018, pp. 1–4. DOI: 10.1109/ICSENS.2018.8589825 (cited on pp. 100, 101).

[147] J. K. Lee and T. H. Jeon. "Magnetic Condition-Independent 3D Joint Angle Estimation Using Inertial Sensors and Kinematic Constraints". In: *Sensors* 19.24 (Jan. 2019), Article 5522. DOI: 10.3390/s19245522 (cited on pp. 100, 101).

[148] J. K. Lee, T. H. Jeon, and W. C. Jung. "Constraint-Augmented Kalman Filter for Magnetometer-Free 3D Joint Angle Determination". In: *International Journal of Control, Automation and Systems* 18 (June 24, 2020), pp. 2929–2942. ISSN: 2005-4092. DOI: 10.1007/s12555-019-0948-x (cited on pp. 100, 101).

[149] I. Weygers, M. Kok, H. De Vroey, T. Verbeerst, M. Versteyhe, H. Hallez, and K. Claeys. "Drift-Free Inertial Sensor-Based Joint Kinematics for Long-Term Arbitrary Movements". In: *IEEE Sensors Journal* 20.14 (2020), pp. 7969–7979. ISSN: 1558-1748. DOI: 10.1109/JSEN.2020.2982459 (cited on pp. 100, 101).

[150] E. Remmerswaal, I. Weygers, G. Smit, and M. Kok. "Fast Relative Sensor Orientation Estimation in the Presence of Real-World Disturbances". In: *2021 European Control Conference (ECC)*. Delft, Netherlands, June 29–July 2, 2021, pp. 411–416. DOI: 10.23919/ECC54610.2021.9654849 (cited on pp. 100, 101).

[151] G. Cooper, I. Sheret, L. McMillian, K. Siliverdis, N. Sha, D. Hodgins, L. Kenney, and D. Howard. "Inertial Sensor-Based Knee Flexion/Extension Angle Estimation". In: *Journal of Biomechanics* 42.16 (Dec. 11, 2009), pp. 2678–2685. ISSN: 0021-9290. DOI: 10.1016/j.jbiomech.2009.08.004 (cited on p. 101).

[152] R. V. Vitali, S. M. Cain, R. S. McGinnis, A. M. Zaferiou, L. V. Ojeda, S. P. Davidson, and N. C. Perkins. "Method for Estimating Three-Dimensional Knee Rotations Using Two Inertial Measurement Units: Validation with a Coordinate Measurement Machine". In: *Sensors* 17.9 (Sept. 2017), Article 1970. DOI: 10.3390/s17091970 (cited on p. 101).

[153] H. G. Kortier, V. I. Sluiter, D. Roetenberg, and P. H. Veltink. "Assessment of Hand Kinematics Using Inertial and Magnetic Sensors". In: *Journal of NeuroEngineering and Rehabilitation* 11.1 (Apr. 21, 2014), Article 70. ISSN: 1743-0003. DOI: 10.1186/1743-0003-11-70 (cited on p. 101).

[154] M. Caruso, L. Gastaldi, S. Pastorelli, A. Cereatti, and E. Digo. "An ISB-consistent Denavit-Hartenberg Model of the Human Upper Limb for Joint Kinematics Optimization: Validation on Synthetic and Robot Data during a Typical Rehabilitation Gesture". In: *2022 44th Annual International Conference of the IEEE Engineering in Medicine & Biology Society (EMBC)*. Glasgow, Scotland, United Kingdom, July 11–15, 2022, pp. 1805–1808. DOI: 10.1109/EMBC48229.2022.9871201 (cited on p. 101).

[155] J. F. S. Lin and D. Kulić. "Human Pose Recovery Using Wireless Inertial Measurement Units". In: *Physiological Measurement* 33.12 (Nov. 2012), pp. 2099–2115. ISSN: 0967-3334. DOI: 10.1088/0967-3334/33/12/2099 (cited on p. 101).

[156] M. El-Gohary and J. McNames. "Human Joint Angle Estimation with Inertial Sensors and Validation with a Robot Arm". In: *IEEE Transactions on Biomedical Engineering* 62.7 (July 2015), pp. 1759–1767. ISSN: 0018-9294. DOI: 10.1109/TBME.2015.2403368 (cited on p. 101).

[157] D. Lehmann, D. Laidig, R. Deimel, and T. Seel. "Magnetometer-Free Inertial Motion Tracking of Arbitrary Joints with Range of Motion Constraints". In: *IFAC-PapersOnLine*. 21st IFAC World Congress 53.2 (Jan. 1, 2020), pp. 16016–16022. ISSN: 2405-8963. DOI: 10.1016/j.ifacol.2020.12.401 (cited on p. 101).

[158] M. Valtin, C. Salchow, T. Seel, D. Laidig, and T. Schauer. "Modular Finger and Hand Motion Capturing System Based on Inertial and Magnetic Sensors". In: *Current Directions in Biomedical Engineering* 3.1 (2017), pp. 19–23. DOI: 10.1515/cdbme-2017-0005 (cited on p. 118).

[159] D. Laidig, A. J. Jocham, B. Guggenberger, K. Adamer, M. Fischer, and T. Seel. "Calibration-Free Gait Assessment by Foot-Worn Inertial Sensors". In: *Frontiers in Digital Health* 3 (2021), Article 147. ISSN: 2673-253X. DOI: 10.3389/fdgth.2021.736418 (cited on pp. 127, 141).

[160] A. J. Jocham, D. Laidig, B. Guggenberger, and T. Seel. "Measuring Highly Accurate Foot Position and Angle Trajectories with Foot-Mounted IMUs in Clinical Practice". [Manuscript submitted for publication]. 2023 (cited on p. 127).

[161] C. J. Hass, P. Malczak, J. Nocera, E. L. Stegemöller, A. Shukala, I. Malaty, C. E. Jacobson, M. S. Okun, and N. McFarland. "Quantitative Normative Gait Data in a Large Cohort of Ambulatory Persons with Parkinson's Disease". In: *PLoS ONE* 7.8 (Aug. 3, 2012), Article e42337. ISSN: 1932-6203. DOI: 10.1371/journal.pone.0042337 (cited on p. 128).

[162] J. Park and T.-H. Kim. "The Effects of Balance and Gait Function on Quality of Life of Stroke Patients". In: *NeuroRehabilitation* 44.1 (Jan. 1, 2019), pp. 37–41. ISSN: 1053-8135. DOI: 10.3233/NRE-182467 (cited on p. 128).

[163] Z. O. Abu-Faraj, G. F. Harris, P. A. Smith, and S. Hassani. "Human Gait and Clinical Movement Analysis". In: *Wiley Encyclopedia of Electrical and Electronics Engineering*. American Cancer Society, 2015, pp. 1–34. ISBN: 978-0-471-34608-1. DOI: 10.1002/047134608X.W6606.pub2 (cited on p. 128).

[164] R. Baker. "Gait Analysis Methods in Rehabilitation". In: *Journal of NeuroEngineering and Rehabilitation* 3.1 (Mar. 2, 2006), Article 4. ISSN: 1743-0003. DOI: 10.1186/1743-0003-3-4 (cited on p. 128).

[165] R. W. Baker. *Measuring Walking: A Handbook of Clinical Gait Analysis*. 1st edition. London: Mac Keith Press, May 28, 2013. ISBN: 978-1-908316-66-0 (cited on pp. 128, 130).

[166] S. Chen, J. Lach, B. Lo, and G.-Z. Yang. "Toward Pervasive Gait Analysis with Wearable Sensors: A Systematic Review". In: *IEEE Journal of Biomedical and Health Informatics* 20.6 (Nov. 2016), pp. 1521–1537. ISSN: 2168-2208. DOI: 10.1109/JBHI.2016.2608720 (cited on pp. 128, 131).

[167] S. A. Bridenbaugh and R. W. Kressig. "Laboratory Review: The Role of Gait Analysis in Seniors' Mobility and Fall Prevention". In: *Gerontology* 57.3 (2011), pp. 256–264. ISSN: 1423-0003. DOI: 10.1159/000322194 (cited on p. 128).

[168] U. Givon, G. Zeilig, and A. Achiron. "Gait Analysis in Multiple Sclerosis: Characterization of Temporal–Spatial Parameters Using GAITRite Functional Ambulation System". In: *Gait & Posture* 29.1 (Jan. 1, 2009), pp. 138–142. ISSN: 0966-6362. DOI: 10.1016/j.gaitpost.2008.07.011 (cited on p. 128).

[169] T. A. L. Wren, C. A. Tucker, S. A. Rethlefsen, G. E. Gorton, and S. Õunpuu. "Clinical Efficacy of Instrumented Gait Analysis: Systematic Review 2020 Update". In: *Gait & Posture* 80 (July 1, 2020), pp. 274–279. ISSN: 0966-6362. DOI: 10.1016/j.gaitpost.2020.05.031 (cited on p. 128).

[170] J. Riis, S. M. Byrgesen, K. H. Kragholm, M. M. Mørch, and D. Melgaard. "Validity of the GAITRite Walkway Compared to Functional Balance Tests for Fall Risk Assessment in Geriatric Outpatients". In: *Geriatrics* 5.4 (Oct. 17, 2020), Article 77. ISSN: 2308-3417. DOI: 10.3390/geriatrics5040077 (cited on p. 128).

[171] T. Schmitz-Hübsch, A. U. Brandt, C. Pfueller, L. Zange, A. Seidel, A. A. Kühn, F. Paul, M. Minnerop, and S. Doss. "Accuracy and Repeatability of Two Methods of Gait Analysis – GaitRite™ Und Mobility Lab™ – in Subjects with Cerebellar Ataxia". In: *Gait & Posture* 48 (July 1, 2016), pp. 194–201. ISSN: 0966-6362. DOI: 10.1016/j.gaitpost.2016.05.014 (cited on p. 128).

[172] S. C. Wearing, L. F. Reed, and S. R. Urry. "Agreement between Temporal and Spatial Gait Parameters from an Instrumented Walkway and Treadmill System at Matched Walking Speed". In: *Gait & Posture* 38.3 (July 1, 2013), pp. 380–384. ISSN: 0966-6362. DOI: 10.1016/j.gaitpost.2012.12.017 (cited on pp. 128, 139, 160).

[173] D. Kotiadis, H. J. Hermens, and P. H. Veltink. "Inertial Gait Phase Detection for Control of a Drop Foot Stimulator: Inertial Sensing for Gait Phase Detection". In: *Medical Engineering & Physics* 32.4 (May 1, 2010), pp. 287–297. ISSN: 1350-4533. DOI: 10.1016/j.medengphy.2009.10.014 (cited on pp. 129–131).

[174] A. Dvorani, C. Wiesener, M. Valtin, H. Voigt, A. Kühn, N. Wenger, and T. Schauer. "Mobil4Park: Development of a Sensor-Stimulator Network for the Therapy of Freezing of Gait in Parkinson Patients". In: *Current Directions in Biomedical Engineering* 6.2 (Oct. 19, 2020), Article 20202013. DOI: 10.1515/cdbme-2020-2013 (cited on p. 129).

[175] D. Trojaniello, A. Cereatti, E. Pelosin, L. Avanzino, A. Mirelman, J. M. Hausdorff, and U. Della Croce. "Estimation of Step-by-Step Spatio-Temporal Parameters of Normal and Impaired Gait Using Shank-Mounted Magneto-Inertial Sensors: Application to Elderly, Hemiparetic, Parkinsonian and Choreic Gait". In: *Journal of NeuroEngineering and Rehabilitation* 11.1 (Nov. 11, 2014), Article 152. ISSN: 1743-0003. DOI: 10.1186/1743-0003-11-152 (cited on pp. 129–132).

[176] A. Rampp, J. Barth, S. Schülein, K.-G. Gaßmann, J. Klucken, and B. M. Eskofier. "Inertial Sensor-Based Stride Parameter Calculation from Gait Sequences in Geriatric Patients". In: *IEEE Transactions on Biomedical Engineering* 62.4 (Apr. 2015), pp. 1089–1097. ISSN: 1558-2531. DOI: 10.1109/TBME.2014.2368211 (cited on pp. 129–132).

[177] A. M. Sabatini, G. Ligorio, and A. Mannini. "Fourier-Based Integration of Quasi-Periodic Gait Accelerations for Drift-Free Displacement Estimation Using Inertial Sensors". In: *BioMedical Engineering OnLine* 14.1 (Nov. 23, 2015), Article 106. ISSN: 1475-925X. DOI: 10.1186/s12938-015-0103-8 (cited on pp. 129–131).

[178] A. Mannini, D. Trojaniello, U. Della Croce, and A. M. Sabatini. "Hidden Markov Model-Based Strategy for Gait Segmentation Using Inertial Sensors: Application to Elderly, Hemiparetic Patients and Huntington's Disease Patients". In: *2015 37th Annual International Conference of the IEEE Engineering in Medicine and Biology Society (EMBC)*. Milan, Italy, Aug. 25–29, 2015, pp. 5179–5182. DOI: 10.1109/EMBC.2015.7319558 (cited on pp. 129–131).

[179] E. Sejdić, K. A. Lowry, J. Bellanca, S. Perera, M. S. Redfern, and J. S. Brach. "Extraction of Stride Events from Gait Accelerometry during Treadmill Walking". In: *IEEE Journal of Translational Engineering in Health and Medicine* 4 (2016), pp. 1–11. ISSN: 2168-2372. DOI: 10.1109/JTEHM.2015.2504961 (cited on p. 129).

[180] W. Teufl, M. Lorenz, M. Miezal, B. Taetz, M. Fröhlich, and G. Bleser. "Towards Inertial Sensor Based Mobile Gait Analysis: Event-Detection and Spatio-Temporal Parameters". In: *Sensors* 19.1 (Jan. 2019), Article 38. DOI: 10.3390/s19010038 (cited on pp. 129–131).

[181] J. Marín, T. Blanco, J. de la Torre, and J. J. Marín. "Gait Analysis in a Box: A System Based on Magnetometer-Free IMUs or Clusters of Optical Markers with Automatic Event Detection". In: *Sensors* 20.12 (12 Jan. 2020), Article 3338. DOI: 10.3390/s20123338 (cited on pp. 129–131).

[182] T. N. Hung and Y. S. Suh. "Inertial Sensor-Based Two Feet Motion Tracking for Gait Analysis". In: *Sensors* 13.5 (May 2013), pp. 5614–5629. DOI: 10.3390/s130505614 (cited on p. 129).

[183] A. Sabatini, C. Martelloni, S. Scapellato, and F. Cavallo. “Assessment of Walking Features from Foot Inertial Sensing”. In: *IEEE Transactions on Biomedical Engineering* 52.3 (Mar. 2005), pp. 486–494. ISSN: 1558-2531. DOI: 10.1109/TBME.2004.840727 (cited on pp. 130, 131).

[184] J. Hannink, T. Kautz, C. F. Pasluosta, K.-G. Gaßmann, J. Klucken, and B. M. Eskofier. “Sensor-Based Gait Parameter Extraction with Deep Convolutional Neural Networks”. In: *IEEE Journal of Biomedical and Health Informatics* 21.1 (Jan. 2017), pp. 85–93. ISSN: 2168-2208. DOI: 10.1109/JBHI.2016.2636456 (cited on pp. 130–132, 166).

[185] A. Mannini, V. Genovese, and A. Maria Sabatini. “Online Decoding of Hidden Markov Models for Gait Event Detection Using Foot-Mounted Gyroscopes”. In: *IEEE Journal of Biomedical and Health Informatics* 18.4 (July 2014), pp. 1122–1130. ISSN: 2168-2208. DOI: 10.1109/JBHI.2013.2293887 (cited on pp. 130, 131).

[186] A. Mannini and A. M. Sabatini. “Gait Phase Detection and Discrimination between Walking–Jogging Activities Using Hidden Markov Models Applied to Foot Motion Data from a Gyroscope”. In: *Gait & Posture* 36.4 (Sept. 1, 2012), pp. 657–661. ISSN: 0966-6362. DOI: 10.1016/j.gaitpost.2012.06.017 (cited on pp. 130, 131, 135).

[187] J. M. Jasiewicz, J. H. J. Allum, J. W. Middleton, A. Barriskill, P. Condie, B. Purcell, and R. C. T. Li. “Gait Event Detection Using Linear Accelerometers or Angular Velocity Transducers in Able-Bodied and Spinal-Cord Injured Individuals”. In: *Gait & Posture* 24.4 (Dec. 1, 2006), pp. 502–509. ISSN: 0966-6362. DOI: 10.1016/j.gaitpost.2005.12.017 (cited on p. 130).

[188] B. Mariani, M. C. Jiménez, F. J. G. Vingerhoets, and K. Aminian. “On-Shoe Wearable Sensors for Gait and Turning Assessment of Patients with Parkinson’s Disease”. In: *IEEE Transactions on Biomedical Engineering* 60.1 (Jan. 2013), pp. 155–158. ISSN: 1558-2531. DOI: 10.1109/TBME.2012.2227317 (cited on pp. 130, 131).

[189] M. Bertoli et al. “Estimation of Spatio-Temporal Parameters of Gait from Magneto-Inertial Measurement Units: Multicenter Validation among Parkinson, Mildly Cognitively Impaired and Healthy Older Adults”. In: *BioMedical Engineering OnLine* 17 (May 9, 2018), Article 58. ISSN: 1475-925X. DOI: 10.1186/s12938-018-0488-2 (cited on pp. 130–132).

[190] N. Chia Bejarano, E. Ambrosini, A. Pedrocchi, G. Ferrigno, M. Monticone, and S. Ferrante. “A Novel Adaptive, Real-Time Algorithm to Detect Gait Events from Wearable Sensors”. In: *IEEE Transactions on Neural Systems and Rehabilitation Engineering* 23.3 (May 2015), pp. 413–422. ISSN: 1558-0210. DOI: 10.1109/TNSRE.2014.2337914 (cited on pp. 130, 131).

[191] T. Seel, L. Landgraf, V. Cermeño Escobar, J. Raisch, and T. Schauer. “Online Gait Phase Detection with Automatic Adaption to Gait Velocity Changes Using Accelerometers and Gyroscopes”. In: *Biomedical Engineering / Biomedizinische Technik* (Jan. 1, 2014). DOI: 10.1515/bmt-2014-5011 (cited on pp. 130, 131, 135, 137–139).

[192] P. Müller, T. Seel, and T. Schauer. "Experimental Evaluation of a Novel Inertial Sensor Based Realtime Gait Phase Detection Algorithm". In: *Proceedings of the Technically Assisted Rehabilitation Conference*. 2015 (cited on pp. 130, 131, 138).

[193] A. Schicketmueller, G. Rose, and M. Hofmann. "Feasibility of a Sensor-Based Gait Event Detection Algorithm for Triggering Functional Electrical Stimulation during Robot-Assisted Gait Training". In: *Sensors* 19.21 (21 Jan. 2019), Article 4804. DOI: 10.3390/s19214804 (cited on pp. 130, 131, 135, 137).

[194] L. Donath, O. Faude, E. Lichtenstein, C. Nüesch, and A. Mündermann. "Validity and Reliability of a Portable Gait Analysis System for Measuring Spatiotemporal Gait Characteristics: Comparison to an Instrumented Treadmill". In: *Journal of NeuroEngineering and Rehabilitation* 13.1 (Jan. 20, 2016), Article 6. ISSN: 1743-0003. DOI: 10.1186/s12984-016-0115-z (cited on p. 130).

[195] E. P. Washabaugh, T. Kalyanaraman, P. G. Adamczyk, E. S. Claflin, and C. Krishnan. "Validity and Repeatability of Inertial Measurement Units for Measuring Gait Parameters". In: *Gait & Posture* 55 (June 1, 2017), pp. 87–93. ISSN: 0966-6362. DOI: 10.1016/j.gaitpost.2017.04.013 (cited on pp. 130, 131).

[196] B. Mariani, C. Hoskovec, S. Rochat, C. Büla, J. Penders, and K. Aminian. "3D Gait Assessment in Young and Elderly Subjects Using Foot-Worn Inertial Sensors". In: *Journal of Biomechanics* 43.15 (Nov. 16, 2010), pp. 2999–3006. ISSN: 0021-9290. DOI: 10.1016/j.jbiomech.2010.07.003 (cited on pp. 130–132, 154, 159, 161).

[197] N. Lefeber, M. Degelaen, C. Truyers, I. Safin, and D. Beckwée. "Validity and Reproducibility of Inertial Physilog Sensors for Spatiotemporal Gait Analysis in Patients with Stroke". In: *IEEE Transactions on Neural Systems and Rehabilitation Engineering* 27.9 (Sept. 2019), pp. 1865–1874. ISSN: 1558-0210. DOI: 10.1109/TNSRE.2019.2930751 (cited on pp. 130–132, 159).

[198] J. Perry and J. M. Burnfield, eds. *Gait Analysis: Normal and Pathological Function*. 2. ed. Thorofare, NJ: SLACK, 2010. ISBN: 978-1-55642-766-4 (cited on pp. 130, 134–137, 160).

[199] R. Caldas, M. Mundt, W. Potthast, F. Buarque de Lima Neto, and B. Markert. "A Systematic Review of Gait Analysis Methods Based on Inertial Sensors and Adaptive Algorithms". In: *Gait & Posture* 57 (Sept. 1, 2017), pp. 204–210. ISSN: 0966-6362. DOI: 10.1016/j.gaitpost.2017.06.019 (cited on pp. 131, 159).

[200] S. Yang and Q. Li. "Inertial Sensor-Based Methods in Walking Speed Estimation: A Systematic Review". In: *Sensors* 12.5 (5 May 2012), pp. 6102–6116. DOI: 10.3390/s120506102 (cited on p. 131).

[201] D. Laidig, T. Seel, and T. Schauer. "Entwicklung einer inertialsensorbasierten Eversionswinkelregelung für einen Peroneus-Stimulator [Development of an Inertial Sensor-Based Eversion Angle Control System for a Peroneal Stimulator]". In: *7th International Symposium on Automatic Control*. Wismar, Germany, 2014, pp. 1–12 (cited on p. 131).

[202] B. Mariani, S. Rochat, C. J. Büla, and K. Aminian. “Heel and Toe Clearance Estimation for Gait Analysis Using Wireless Inertial Sensors”. In: *IEEE Transactions on Biomedical Engineering* 59.11 (Nov. 2012), pp. 3162–3168. ISSN: 1558-2531. DOI: 10.1109/TBME.2012.2216263 (cited on pp. 132, 154, 159, 161).

[203] M. Benoussaad, B. Sijobert, K. Mombaur, and C. Azevedo Coste. “Robust Foot Clearance Estimation Based on the Integration of Foot-Mounted IMU Acceleration Data”. In: *Sensors* 16.1 (1 Jan. 2016), Article 12. ISSN: 1424-8220. DOI: 10.3390/s16010012 (cited on pp. 132, 154, 159, 161).

[204] N. Kitagawa and N. Ogihara. “Estimation of Foot Trajectory during Human Walking by a Wearable Inertial Measurement Unit Mounted to the Foot”. In: *Gait & Posture* 45 (Mar. 1, 2016), pp. 110–114. ISSN: 0966-6362. DOI: 10.1016/j.gaitpost.2016.01.014 (cited on pp. 132, 154, 159, 161).

[205] Y. Huang, W. Jirattigalachote, M. R. Cutkosky, X. Zhu, and P. B. Shull. “Novel Foot Progression Angle Algorithm Estimation via Foot-Worn, Magneto-Inertial Sensing”. In: *IEEE Transactions on Biomedical Engineering* 63.11 (Nov. 2016), pp. 2278–2285. ISSN: 1558-2531. DOI: 10.1109/TBME.2016.2523512 (cited on pp. 132, 154, 159, 161).

[206] F. J. Wouda, S. L. J. O. Jaspar, J. Harlaar, B.-J. F. van Beijnum, and P. H. Veltink. “Foot Progression Angle Estimation Using a Single Foot-Worn Inertial Sensor”. In: *Journal of NeuroEngineering and Rehabilitation* 18.1 (Feb. 17, 2021), Article 37. ISSN: 1743-0003. DOI: 10.1186/s12984-021-00816-4 (cited on pp. 132, 154, 159, 161).

[207] A. Brégou Bourgeois, B. Mariani, K. Aminian, P. Y. Zambelli, and C. J. Newman. “Spatio-Temporal Gait Analysis in Children with Cerebral Palsy Using, Foot-Worn Inertial Sensors”. In: *Gait & Posture* 39.1 (Jan. 1, 2014), pp. 436–442. ISSN: 0966-6362. DOI: 10.1016/j.gaitpost.2013.08.029 (cited on pp. 132, 154, 159, 161).

[208] E. Chalmers, J. Le, D. Sukhdeep, J. Watt, J. Andersen, and E. Lou. “Inertial Sensing Algorithms for Long-Term Foot Angle Monitoring for Assessment of Idiopathic Toe-Walking”. In: *Gait & Posture* 39.1 (Jan. 1, 2014), pp. 485–489. ISSN: 0966-6362. DOI: 10.1016/j.gaitpost.2013.08.021 (cited on pp. 132, 154, 159, 161).

[209] H. Schwameder, M. Andress, E. Graf, and G. Strutzenberger. “Validation of an IMU-System (Gait-Up) to Identify Gait Parameters in Normal and Induced Limping Walking Conditions”. In: *33rd International Conference on Biomechanics in Sports*. Poitiers, France, June 29–July 3, 2015. URL: https://ojs.ub.uni-konstanz.de/cpa/article/view/6495 (cited on pp. 132, 154, 159, 161).

[210] T. Seel, D. Graurock, and T. Schauer. “Realtime Assessment of Foot Orientation by Accelerometers and Gyroscopes”. In: *Current Directions in Biomedical Engineering* 1.1 (2015), pp. 446–469. DOI: 10.1515/cdbme-2015-0112 (cited on pp. 132, 154, 159, 161).

[211] J. Hannink, M. Ollenschläger, F. Kluge, N. Roth, J. Klucken, and B. M. Eskofier. “Benchmarking Foot Trajectory Estimation Methods for Mobile Gait Analysis”. In: *Sensors* 17.9 (9 Sept. 2017), Article 1940. DOI: 10.3390/s17091940 (cited on pp. 132, 154, 159, 161).

[212] T. W. Ridler and S. Calvard. "Picture Thresholding Using an Iterative Selection Method". In: *IEEE Transactions on Systems, Man, and Cybernetics* 8.8 (Aug. 1978), pp. 630–632. DOI: 10.1109/TSMC.1978.4310039 (cited on p. 138).

[213] D. Giavarina. "Understanding Bland Altman Analysis". In: *Biochemia Medica* 25.2 (June 5, 2015), pp. 141–151. ISSN: 1330-0962. DOI: 10.11613/BM.2015.015 (cited on p. 149).

[214] Y. H. Chan. "Biostatistics 104: Correlational Analysis". In: *Singapore Medical Journal* 44.12 (Dec. 2003), pp. 614–619. ISSN: 0037-5675. URL: https://pubmed.ncbi.nlm.nih.gov/14770254/ (cited on p. 158).

[215] T. d. A. Busch, Y. A. Duarte, D. Pires Nunes, M. L. Lebrão, M. Satya Naslavsky, A. dos Santos Rodrigues, and E. Amaro. "Factors Associated with Lower Gait Speed among the Elderly Living in a Developing Country: A Cross-Sectional Population-Based Study". In: *BMC Geriatrics* 15.1 (Apr. 1, 2015), Article 35. ISSN: 1471-2318. DOI: 10.1186/s12877-015-0031-2 (cited on p. 159).

[216] L. J. Dommershuijsen, B. M. Isik, S. K. L. Darweesh, J. N. van der Geest, M. K. Ikram, and M. A. Ikram. "Unraveling the Association between Gait and Mortality—One Step at a Time". In: *The Journals of Gerontology: Series A* 75.6 (May 22, 2020), pp. 1184–1190. ISSN: 1079-5006. DOI: 10.1093/gerona/glz282 (cited on p. 159).

[217] D. K. White et al. "Trajectories of Gait Speed Predict Mortality in Well-Functioning Older Adults: The Health, Aging and Body Composition Study". In: *The Journals of Gerontology: Series A* 68.4 (Apr. 1, 2013), pp. 456–464. ISSN: 1079-5006. DOI: 10.1093/gerona/gls197 (cited on p. 159).

[218] G. J. Jerome, S.-u. Ko, D. Kauffman, S. A. Studenski, L. Ferrucci, and E. M. Simonsick. "Gait Characteristics Associated with Walking Speed Decline in Older Adults: Results from the Baltimore Longitudinal Study of Aging". In: *Archives of Gerontology and Geriatrics* 60.2 (Mar. 1, 2015), pp. 239–243. ISSN: 0167-4943. DOI: 10.1016/j.archger.2015.01.007 (cited on p. 159).

[219] G. Abellan Van Kan et al. "Gait Speed at Usual Pace as a Predictor of Adverse Outcomes in Community-Dwelling Older People an International Academy on Nutrition and Aging (IANA) Task Force". In: *The Journal of Nutrition, Health & Aging* 13.10 (Dec. 1, 2009), pp. 881–889. ISSN: 1760-4788. DOI: 10.1007/s12603-009-0246-z (cited on p. 159).

[220] S. Studenski et al. "Gait Speed and Survival in Older Adults". In: *JAMA* 305.1 (Jan. 5, 2011), pp. 50–58. ISSN: 1538-3598. DOI: 10.1001/jama.2010.1923 (cited on p. 159).

[221] S. Studenski, S. Perera, D. Wallace, J. M. Chandler, P. W. Duncan, E. Rooney, M. Fox, and J. M. Guralnik. "Physical Performance Measures in the Clinical Setting". In: *Journal of the American Geriatrics Society* 51.3 (2003), pp. 314–322. ISSN: 1532-5415. DOI: 10.1046/j.1532-5415.2003.51104.x (cited on p. 159).

[222] A. J. J. Smith and E. D. Lemaire. "Temporal-Spatial Gait Parameter Models of Very Slow Walking". In: *Gait & Posture* 61 (Mar. 1, 2018), pp. 125–129. ISSN: 0966-6362. DOI: 10.1016/j.gaitpost.2018.01.003 (cited on p. 159).

[223] J. Verghese, R. Holtzer, R. B. Lipton, and C. Wang. “Quantitative Gait Markers and Incident Fall Risk in Older Adults”. In: *The Journals of Gerontology: Series A* 64A.8 (Aug. 1, 2009), pp. 896–901. ISSN: 1079-5006. DOI: 10.1093/gerona/glp033 (cited on p. 159).

[224] B. E. Maki. “Gait Changes in Older Adults: Predictors of Falls or Indicators of Fear?” In: *Journal of the American Geriatrics Society* 45.3 (1997), pp. 313–320. ISSN: 1532-5415. DOI: 10.1111/j.1532-5415.1997.tb00946.x (cited on p. 159).

[225] R. W. Bohannon and S. S. Glenney. “Minimal Clinically Important Difference for Change in Comfortable Gait Speed of Adults with Pathology: A Systematic Review”. In: *Journal of Evaluation in Clinical Practice* 20.4 (2014), pp. 295–300. ISSN: 1365-2753. DOI: 10.1111/jep.12158 (cited on p. 159).

[226] J. K. Tilson, K. J. Sullivan, S. Y. Cen, D. K. Rose, C. H. Koradia, S. P. Azen, P. W. Duncan, and for the Locomotor Experience Applied Post Stroke (LEAPS) Investigative Team. “Meaningful Gait Speed Improvement during the First 60 Days Poststroke: Minimal Clinically Important Difference”. In: *Physical Therapy* 90.2 (Feb. 1, 2010), pp. 196–208. ISSN: 0031-9023. DOI: 10.2522/ptj.20090079 (cited on p. 159).

[227] K. M. Palombaro, R. L. Craik, K. K. Mangione, and J. D. Tomlinson. “Determining Meaningful Changes in Gait Speed after Hip Fracture”. In: *Physical Therapy* 86.6 (June 1, 2006), pp. 809–816. ISSN: 0031-9023. DOI: 10.1093/ptj/86.6.809 (cited on p. 159).

[228] J. C. Brown, M. O. Harhay, and M. N. Harhay. “Walking Cadence and Mortality among Community-Dwelling Older Adults”. In: *Journal of General Internal Medicine* 29.9 (Sept. 2014), pp. 1263–1269. ISSN: 0884-8734. DOI: 10.1007/s11606-014-2926-6 (cited on p. 159).

[229] J. Hannink, T. Kautz, C. F. Pasluosta, J. Barth, S. Schülein, K.-G. Gaßmann, J. Klucken, and B. M. Eskofier. “Mobile Stride Length Estimation with Deep Convolutional Neural Networks”. In: *IEEE Journal of Biomedical and Health Informatics* 22.2 (Mar. 2018), pp. 354–362. ISSN: 2168-2208. DOI: 10.1109/JBHI.2017.2679486 (cited on p. 159).

[230] C. Nüesch, J.-A. Overberg, H. Schwameder, G. Pagenstert, and A. Mündermann. “Repeatability of Spatiotemporal, Plantar Pressure and Force Parameters during Treadmill Walking and Running”. In: *Gait & Posture* 62 (May 1, 2018), pp. 117–123. ISSN: 0966-6362. DOI: 10.1016/j.gaitpost.2018.03.017 (cited on p. 160).

[231] S. J. Lee and J. Hidler. “Biomechanics of Overground vs. Treadmill Walking in Healthy Individuals”. In: *Journal of Applied Physiology* 104.3 (Mar. 1, 2008), pp. 747–755. ISSN: 8750-7587. DOI: 10.1152/japplphysiol.01380.2006 (cited on p. 161).

[232] J. R. Watt, J. R. Franz, K. Jackson, J. Dicharry, P. O. Riley, and D. C. Kerrigan. “A Three-Dimensional Kinematic and Kinetic Comparison of Overground and Treadmill Walking in Healthy Elderly Subjects”. In: *Clinical Biomechanics (Bristol, Avon)* 25.5 (June 2010), pp. 444–449. ISSN: 1879-1271. DOI: 10.1016/j.clinbiomech.2009.09.002 (cited on p. 161).

[233] C. Meyer, T. Killeen, C. S. Easthope, A. Curt, M. Bolliger, M. Linnebank, B. Zörner, and L. Filli. "Familiarization with Treadmill Walking: How Much Is Enough?" In: *Scientific Reports* 9.1 (1 Mar. 26, 2019), Article 5232. ISSN: 2045-2322. DOI: 10.1038/s41598-019-41721-0 (cited on p. 161).

[234] A. Kalron, Z. Dvir, L. Frid, and A. Achiron. "Quantifying Gait Impairment Using an Instrumented Treadmill in People with Multiple Sclerosis". In: *ISRN Neurology* 2013 (June 25, 2013), Article 867575. ISSN: 2090-5505. DOI: 10.1155/2013/867575 (cited on p. 161).

[235] T. Ro, T. Ota, T. Saito, and O. Oikawa. "Spasticity and Range of Motion over Time in Stroke Patients Who Received Multiple-Dose Botulinum Toxin Therapy". In: *Journal of Stroke and Cerebrovascular Diseases* 29.1 (Jan. 1, 2020), Article 104481. ISSN: 1052-3057. DOI: 10.1016/j.jstrokecerebrovasdis.2019.104481 (cited on p. 165).

[236] B. R. da Costa and E. R. Vieira. "Risk Factors for Work-Related Musculoskeletal Disorders: A Systematic Review of Recent Longitudinal Studies". In: *American Journal of Industrial Medicine* 53.3 (2010), pp. 285–323. ISSN: 1097-0274. DOI: 10.1002/ajim.20750 (cited on p. 165).

[237] K. Eckhoff, M. Kok, S. Lucia, and T. Seel. "Sparse Magnetometer-Free Inertial Motion Tracking – a Condition for Observability in Double Hinge Joint Systems". In: *IFAC-PapersOnLine*. 21th IFAC World Congress 53.2 (Jan. 1, 2020), pp. 16023–16030. ISSN: 2405-8963. DOI: 10.1016/j.ifacol.2020.12.403 (cited on p. 166).

[238] S. Bachhuber, D. Weber, I. Weygers, and T. Seel. "RNN-based Observability Analysis for Magnetometer-Free Sparse Inertial Motion Tracking". In: *2022 25th International Conference on Information Fusion (FUSION)*. Linköping, Sweden, July 4–7, 2022, pp. 1–8. DOI: 10.23919/FUSION49751.2022.9841375 (cited on p. 166).

[239] T. von Marcard, B. Rosenhahn, M. J. Black, and G. Pons-Moll. "Sparse Inertial Poser: Automatic 3D Human Pose Estimation from Sparse IMUs". In: *Computer Graphics Forum* 36.2 (May 1, 2017), pp. 349–360. ISSN: 0167-7055. DOI: 10.1111/cgf.13131 (cited on p. 166).

[240] A. Grapentin, D. Lehmann, A. Zhupa, and T. Seel. "Sparse Magnetometer-Free Real-Time Inertial Hand Motion Tracking". In: *2020 IEEE International Conference on Multisensor Fusion and Integration for Intelligent Systems (MFI)*. Karlsruhe, Germany, Sept. 14–16, 2020, pp. 94–100. DOI: 10.1109/MFI49285.2020.9235262 (cited on p. 166).

[241] L. Sy, M. Raitor, M. D. Rosario, H. Khamis, L. Kark, N. H. Lovell, and S. J. Redmond. "Estimating Lower Limb Kinematics Using a Reduced Wearable Sensor Count". In: *IEEE Transactions on Biomedical Engineering* 68.4 (Apr. 2021), pp. 1293–1304. ISSN: 1558-2531. DOI: 10.1109/TBME.2020.3026464 (cited on p. 166).

[242] Y. Huang, M. Kaufmann, E. Aksan, M. J. Black, O. Hilliges, and G. Pons-Moll. "Deep Inertial Poser: Learning to Reconstruct Human Pose from Sparse Inertial Measurements in Real Time". In: *ACM Transactions on Graphics* 37.6 (Dec. 4, 2018), 185:1–185:15. ISSN: 0730-0301. DOI: 10.1145/3272127.3275108 (cited on p. 166).

[243] J. H. Geissinger and A. T. Asbeck. "Motion Inference Using Sparse Inertial Sensors, Self-Supervised Learning, and a New Dataset of Unscripted Human Motion". In: *Sensors* 20.21 (21 Jan. 2020), Article 6330. DOI: 10.3390/s20216330 (cited on p. 166).

[244] M. Mundt, A. Koeppe, F. Bamer, S. David, and B. Markert. "Artificial Neural Networks in Motion Analysis—Applications of Unsupervised and Heuristic Feature Selection Techniques". In: *Sensors* 20.16 (16 Jan. 2020), Article 4581. DOI: 10.3390/s20164581 (cited on p. 166).

[245] Y. Jiang, Y. Ye, D. Gopinath, J. Won, A. W. Winkler, and C. K. Liu. *Transformer Inertial Poser: Attention-Based Real-Time Human Motion Reconstruction from Sparse IMUs*. Mar. 29, 2022. DOI: 10.48550/arXiv.2203.15720. preprint (cited on p. 166).

[246] M. Lorenz, G. Bleser, T. Akiyama, T. Niikura, D. Stricker, and B. Taetz. "Towards Artefact Aware Human Motion Capture Using Inertial Sensors Integrated into Loose Clothing". In: *2022 International Conference on Robotics and Automation (ICRA)*. Philadelphia, PA, USA, May 23–27, 2022, pp. 1682–1688. DOI: 10.1109/ICRA46639.2022.9811933 (cited on p. 166).

[247] D. Laidig, S. Trimpe, and T. Seel. "Event-Based Sampling for Reducing Communication Load in Realtime Human Motion Analysis by Wireless Inertial Sensor Networks". In: *Current Directions in Biomedical Engineering* 2.1 (2016), pp. 711–714. DOI: 10.1515/cdbme-2016-0154 (cited on p. 166).

[248] T. Zhang, D. Laidig, and T. Seel. "Stop Repeating Yourself: Exploitation of Repetitive Signal Patterns to Reduce Communication Load in Sensor Networks". In: *2019 18th European Control Conference (ECC)*. Naples, Italy, June 25–28, 2019, pp. 2893–2898. DOI: 10.23919/ECC.2019.8796022 (cited on p. 166).

[249] J. Beuchert, F. Solowjow, S. Trimpe, and T. Seel. "Overcoming Bandwidth Limitations in Wireless Sensor Networks by Exploitation of Cyclic Signal Patterns: An Event-Triggered Learning Approach". In: *Sensors* 20.1 (Jan. 2020), Article 260. DOI: 10.3390/s20010260 (cited on p. 166).

A

Details on the Inertial Orientation Estimation Method

A.1 Effect of Gyroscope Integration Errors

Every gyroscope prediction step causes a small error, due to gyroscope bias, noise, and other measurement errors. Without correction by accelerometers and magnetometers, those errors will add up and lead to drift in the orientation estimates. We can show that this error can be regarded as a small drift in the $\mathcal{I}_i$ frame, i.e., all rotation that happens in the gyroscope prediction and that is not the true change of sensor orientation can mathematically be expressed as a rotation ${}^{\mathcal{I}_i(t_{k-1})}_{\mathcal{I}_i(t_k)}\mathbf{q}$.

The gyroscope prediction step consists of multiplication of the previous estimate with an update quaternion based on the measured angular rate:

$$ {}^{\mathcal{S}_i(t_k)}_{\mathcal{I}_i(t_k)}\mathbf{q} = {}^{\mathcal{S}_i(t_{k-1})}_{\mathcal{I}_i(t_{k-1})}\mathbf{q} \otimes \left(T_\mathrm{s}\|\boldsymbol{\omega}\| \,@\, \boldsymbol{\omega}\right). \tag{A.1} $$

This update quaternion can be expressed as the true change in sensor orientation multiplied with an error quaternion $\mathbf{q}_\mathrm{e}$, i.e.,

$$ \left(T_\mathrm{s}\|\boldsymbol{\omega}\| \,@\, \boldsymbol{\omega}\right) = {}^{\mathcal{S}_i(t_k)}_{\mathcal{S}_i(t_{k-1})}\mathbf{q} \otimes \mathbf{q}_\mathrm{e}. \tag{A.2} $$

We can transform the error rotation $\mathbf{q}_\mathrm{e}$ into any frame, here $\mathcal{I}_i(t_{k-1})$:

$$ \mathbf{q}_\mathrm{e} = {}^{\mathcal{I}_i(t_{k-1})}_{\mathcal{S}_i(t_k)}\mathbf{q} \otimes [\mathbf{q}_\mathrm{e}]_{\mathcal{I}_i(t_{k-1})} \otimes {}^{\mathcal{I}_i(t_{k-1})}_{\mathcal{S}_i(t_k)}\mathbf{q}^{-1}. \tag{A.3} $$

When putting this into the prediction step, we obtain

$$\begin{aligned}
{}^{\mathcal{S}_i(t_k)}_{\mathcal{I}_i(t_k)}\mathbf{q} &= {}^{\mathcal{S}_i(t_{k-1})}_{\mathcal{I}_i(t_{k-1})}\mathbf{q} \otimes (T_\mathrm{s}\|\boldsymbol{\omega}\| \mathbin{@} \boldsymbol{\omega}) \\
&= {}^{\mathcal{S}_i(t_{k-1})}_{\mathcal{I}_i(t_{k-1})}\mathbf{q} \otimes {}^{\mathcal{S}_i(t_k)}_{\mathcal{S}_i(t_{k-1})}\mathbf{q} \otimes \mathbf{q}_\mathrm{e} \\
&= {}^{\mathcal{S}_i(t_k)}_{\mathcal{I}_i(t_{k-1})}\mathbf{q} \otimes {}^{\mathcal{I}_i(t_{k-1})}_{\mathcal{S}_i(t_k)}\mathbf{q} \otimes [\mathbf{q}_\mathrm{e}]_{\mathcal{I}_i(t_{k-1})} \otimes {}^{\mathcal{I}_i(t_{k-1})}_{\mathcal{S}_i(t_k)}\mathbf{q}^{-1} \\
&= \underbrace{[\mathbf{q}_\mathrm{e}]_{\mathcal{I}_i(t_{k-1})}}_{{}^{\mathcal{I}_i(t_{k-1})}_{\mathcal{I}_i(t_k)}\mathbf{q}} \otimes {}^{\mathcal{S}_i(t_k)}_{\mathcal{I}_i(t_{k-1})}\mathbf{q}.
\end{aligned} \tag{A.4}$$

Therefore, expressed in the almost-inertial frame $\mathcal{I}_i(t_{k-1})$, the gyroscope prediction error quaternion $\mathbf{q}_\mathrm{e}$ corresponds to the drift rotation ${}^{\mathcal{I}_i(t_{k-1})}_{\mathcal{I}_i(t_k)}\mathbf{q}$ of the almost-inertial frame $\mathcal{I}_i$.

A.2 Measurement for Motion Bias Estimation

The approach for gyroscope bias estimation during motion, as shown in Figure 3.19, is based on the assumption that the current inclination correction step corresponds to the gyroscope bias that is transformed into the global frame using the current sensor orientation. This works well if the sensor orientation does not change much. In reality, due to the low-pass filter used for the acceleration, the inclination correction corresponds to the bias-induced rotations from the last few seconds, taking the respective sensor orientations into account. In the following, we show that this effect is well-described by applying the same low-pass filter to the elements of the rotation matrices $\mathbf{R}$ corresponding to ${}^{\mathcal{S}_i}_{\mathcal{I}_i}\mathbf{q}$, and also to the rotated bias estimates $\mathbf{R}\hat{\mathbf{b}}$.

To simplify the notation, we introduce the rotation operator

$$\operatorname{rot}(\mathbf{q}, \mathbf{v}) := \mathbf{q} \otimes \mathbf{v} \otimes \mathbf{q}^{-1}. \tag{A.5}$$

Assume that the accelerometer measurements are always a perfect vertical vector ($[\mathbf{a}(t_k)]_{\mathcal{E}_\mathrm{true}} = [\mathbf{v}]_{\mathcal{E}_\mathrm{true}} = [0\ 0\ 1]^\intercal$), i.e., there are no disturbances or measurement errors (unit length is only used to simplify the notation). In the accelerometer update step, those measurements are transformed into the $\mathcal{I}_i(t_k)$ frame and then low-pass filtered with an infinite impulse response (IIR) filter with impulse response b_n, i.e.,

$$\begin{aligned}
[\mathbf{a}_\mathrm{LP}(t_k)]_{\mathcal{I}_i(t_k)} &= \sum_{n=0}^{\infty} b_n \left[\operatorname{rot}\left({}^{\mathcal{E}_\mathrm{true}}_{\mathcal{I}_i(t_{k-n})}\mathbf{q}, [\mathbf{v}]_{\mathcal{E}_\mathrm{true}}\right)\right] \\
&= \sum_{n=0}^{\infty} b_n \, [\mathbf{v}]_{\mathcal{I}_i(t_{k-n})} .
\end{aligned} \tag{A.6}$$

One time step earlier, the filter output is

$$\begin{aligned}
[\mathbf{a}_\mathrm{LP}(t_{k-1})]_{\mathcal{I}_i(t_{k-1})} &= \sum_{n=0}^{\infty} b_n \, [\mathbf{v}]_{\mathcal{I}_i(t_{k-1-n})} \\
&= \sum_{n=0}^{\infty} b_n \operatorname{rot}\left({}^{\mathcal{I}_i(t_{k-n})}_{\mathcal{I}_i(t_{k-1-n})}\mathbf{q}, [\mathbf{v}]_{\mathcal{I}_i(t_{k-n})}\right) .
\end{aligned} \tag{A.7}$$

From Rodrigues' rotation formula follows that for a small rotation θ around axis $\mathbf{k}$,

$$\mathbf{p}_{\text{rot}} \approx \mathbf{p} + \theta\mathbf{k} \times \mathbf{p}. \tag{A.8}$$

We use this approximation for the rotation of the $\mathcal{I}_i$ frame due to gyroscope bias in one sample step ${}^{\mathcal{I}_i(t_{k-1-n})}_{\mathcal{I}_i(t_{k-n})}\mathbf{q}$ (cf. Appendix A.1). Note that this rotation is only caused by the uncorrected part of the gyroscope bias, i.e., by $\mathbf{b}'(t_k) := \mathbf{b} - \hat{\mathbf{b}}(t_k)$. Therefore, we obtain

$$[\mathbf{a}_{\text{LP}}(t_{k-1})]_{\mathcal{I}_i(t_{k-1})} \approx \sum_{n=0}^{\infty} b_n \left([\mathbf{v}]_{\mathcal{I}_i(t_{k-n})} - T_{\text{s}} \left[\mathbf{b}'(t_{k-n})\right]_{\mathcal{I}_i(t_{k-n})} \times [\mathbf{v}]_{\mathcal{I}_i(t_{k-n})}\right). \tag{A.9}$$

The difference between two consecutive filtered accelerations is then

$$\begin{aligned}
&[\mathbf{a}_{\text{LP}}(t_k)]_{\mathcal{I}_i(t_k)} - [\mathbf{a}_{\text{LP}}(t_{k-1})]_{\mathcal{I}_i(t_{k-1})} \\
&\approx T_{\text{s}} \sum_{n=0}^{\infty} b_n \left(\left[\mathbf{b}'(t_{k-n})\right]_{\mathcal{I}_i(t_{k-n})} \times [\mathbf{v}]_{\mathcal{I}_i(t_{k-n})}\right) \\
&= T_{\text{s}} \sum_{n=0}^{\infty} b_n \left(\operatorname{rot}\left({}^{\mathcal{S}_i(t_{k-n})}_{\mathcal{I}_i(t_{k-n})}\mathbf{q}, \mathbf{b}'(t_{k-n})\right) \times [\mathbf{v}]_{\mathcal{I}_i(t_{k-n})}\right).
\end{aligned} \tag{A.10}$$

Now, we express this difference in the frame $\mathcal{E}_i(t_{k-1})$ that is used to perform the inclination correction step, assuming that $\mathcal{E}_i$ and $\mathcal{I}_i$ do not change much over the duration that is relevant for the filter (since the influence of bias and the inclination correction is limited during short time spans), and assuming that the true vertical axis is approximately $[0\ \ 0\ \ 1]^\intercal$ in the $\mathcal{E}_i(t_{k-1})$ frame.

$$\begin{aligned}
&[\mathbf{a}_{\text{LP}}(t_k)]_{\mathcal{E}_i(t_{k-1})} - [\mathbf{a}_{\text{LP}}(t_{k-1})]_{\mathcal{E}_i(t_{k-1})} \\
&\approx T_{\text{s}} \sum_{n=0}^{\infty} b_n \left[\operatorname{rot}\left({}^{\mathcal{S}_i(t_{k-n})}_{\mathcal{E}_i(t_{k-1-n})}\mathbf{q}, \mathbf{b}'(t_{k-n})\right) \times \begin{bmatrix}0 & 0 & 1\end{bmatrix}^\intercal\right] \\
&= T_{\text{s}} \left[\sum_{n=0}^{\infty} b_n \operatorname{rot}\left({}^{\mathcal{S}_i(t_{k-n})}_{\mathcal{E}_i(t_{k-1-n})}\mathbf{q}, \mathbf{b}'(t_{k-n})\right)\right] \times \begin{bmatrix}0 & 0 & 1\end{bmatrix}^\intercal.
\end{aligned} \tag{A.11}$$

Expressing the rotation by ${}^{\mathcal{S}_i(t_{k-n})}_{\mathcal{E}_i(t_{k-n-1})}\mathbf{q}$ with a rotation matrix $\mathbf{R}(t_{k-n})$ and introducing the LPF operator to simplify the notation of the low-pass filter yields

$$\begin{aligned}
&[\mathbf{a}_{\text{LP}}(t_k)]_{\mathcal{E}_i(t_{k-1})} - [\mathbf{a}_{\text{LP}}(t_{k-1})]_{\mathcal{E}_i(t_{k-1})} \\
&= T_{\text{s}} \left[\sum_{n=0}^{\infty} b_n \left(\mathbf{R}(t_{k-n})\mathbf{b}'(t_{k-n})\right)\right] \times \begin{bmatrix}0 & 0 & 1\end{bmatrix}^\intercal \\
&= T_{\text{s}} \operatorname{LPF}\left(\mathbf{R}(t_k)\mathbf{b}'(t_k)\right) \times \begin{bmatrix}0 & 0 & 1\end{bmatrix}^\intercal.
\end{aligned} \tag{A.12}$$

Since $[\mathbf{a}_{\text{LP}}(t_{k-1})]_{\mathcal{E}_i(t_{k-1})}$ is always $[0\ \ 0\ \ 1]^\intercal$ as the result of the previous inclination correction step, we get

$$[\mathbf{a}_{\text{LP}}(t_k)]_{\mathcal{E}_i(t_{k-1})} = \begin{bmatrix}0 & 0 & 1\end{bmatrix}^\intercal + T_{\text{s}} \operatorname{LPF}\left(\mathbf{R}(t_k)\mathbf{b}'(t_k)\right) \times \begin{bmatrix}0 & 0 & 1\end{bmatrix}^\intercal. \tag{A.13}$$

The inclination correction rotation vector $\mathbf{c}(t_k)$, i.e., expressing the correction quaternion $\mathbf{q}_{\text{corr}}$ from (3.16) as a rotation vector, is (neglecting the small change of the norm of $[\mathbf{a}_{\text{LP}}(t_k)]_{\mathcal{E}_i(t_{k-1})}$)

$$\begin{aligned}
\mathbf{c}(t_k) &= [\mathbf{a}_{\text{LP}}(t_{k-1})]_{\mathcal{E}_i(t_k)} \times \begin{bmatrix}0 & 0 & 1\end{bmatrix}^\intercal \\
&= \left(\begin{bmatrix}0 & 0 & 1\end{bmatrix}^\intercal + T_\text{s} \,\text{LPF}\left(\mathbf{R}(t_k)\mathbf{b}'(t_k)\right) \times \begin{bmatrix}0 & 0 & 1\end{bmatrix}^\intercal\right) \times \begin{bmatrix}0 & 0 & 1\end{bmatrix}^\intercal \\
&= -\operatorname{diag}(1,1,0) T_\text{s} \,\text{LPF}\left(\mathbf{R}(t_k)\mathbf{b}'(t_k)\right) \\
&= -\operatorname{diag}(1,1,0) T_\text{s} \left(\text{LPF}(\mathbf{R}(t_k))\mathbf{b} - \text{LPF}(\mathbf{R}(t_k)\hat{\mathbf{b}}(t_k))\right).
\end{aligned} \tag{A.14}$$

Therefore, when choosing the system output matrix as $\mathbf{C}(t_k) = \text{LPF}(\mathbf{R}(t_k))$, we obtain the following measurement in the horizontal plane:

$$\operatorname{diag}(1,1,0)\mathbf{y}(t_k) = -\frac{1}{T_\text{s}}\mathbf{c}(t_k) + \operatorname{diag}(1,1,0)\,\text{LPF}(\mathbf{R}(t_k)\hat{\mathbf{b}}(t_k)). \tag{A.15}$$

A.3 Parametrization of the Bias Estimation Method

Gyroscope bias is estimated using the system model

$$\mathbf{b}_k = \mathbf{b}_{k-1} + \mathbf{v}_k, \qquad \mathbf{v}_k \sim \mathcal{N}(0, \mathbf{V}), \tag{A.16}$$

$$\mathbf{y}_k = \mathbf{C}_k\mathbf{b}_k + \mathbf{w}_k, \qquad \mathbf{w}_k \sim \mathcal{N}(0, \mathbf{W}_k), \tag{A.17}$$

where the index k denotes sampling at t_k, and the standard Kalman filter update equations for the estimated state $\hat{\mathbf{b}}_k$:

$$\mathbf{P}_k^- = \mathbf{P}_{k-1}^+ + \mathbf{V}, \tag{A.18}$$

$$\mathbf{K}_k = \mathbf{P}_k^-\mathbf{C}_k^\intercal(\mathbf{W}_k + \mathbf{C}_k\mathbf{P}_k^-\mathbf{C}_k^\intercal)^{-1}, \tag{A.19}$$

$$\hat{\mathbf{b}}_k = \hat{\mathbf{b}}_{k-1} + \mathbf{K}_k(\mathbf{y}_k - \mathbf{C}_k\hat{\mathbf{b}}_{k-1}), \tag{A.20}$$

$$\mathbf{P}_k^+ = \mathbf{P}_k^- - \mathbf{K}_k\mathbf{C}_k\mathbf{P}_k^-. \tag{A.21}$$

The tuning parameters are the initial covariance $\mathbf{P}_0^+$, the variance of the process noise $\mathbf{V}$, and the variance of measurement noise $\mathbf{W}(t_k)$. In the following, we derive an intuitive parametrization for those values that is independent of the sampling frequency. Note that scaling all parameters of the Kalman filter with the same value will not change the system behavior. For heuristically determined parameters, the actual quantities are therefore arbitrary. However, a good parametrization still helps to make the behavior of the algorithm understandable and facilitates tuning.

A fixed amount of variance, the variance of the process noise $\mathbf{V}$, is added to the covariance matrix in every update step. To be independent of the sampling frequency, scaling with the sampling time T_s is necessary. To facilitate interpretation of the value as a *forgetting time*, we parametrize the process noise by the time needed for the standard deviation of the estimation uncertainty to increase from 0 to 0.1 °/s in the absence of measurements, i.e.,

$$\mathbf{V} = (0.1\,°/\text{s})^2 \frac{T_\text{s}}{t_\text{forget}} \mathbf{I}_{3\times 3}. \tag{A.22}$$

We use the initial estimation uncertainty, i.e., the standard deviation σ_{init}, to initialize the covariance matrix, i.e.,

$$\mathbf{P}_0^+ = \sigma_{\text{init}}^2 \mathbf{I}_{3\times 3}. \tag{A.23}$$

For the rest and motion updates, instead of directly specifying the variance of the motion and rest update measurements, we provide the uncertainties σ_{rest} and σ_{motion} to which the estimate will eventually converge when the respective filter update is active. This ensures independence of the sampling rates and makes it easy to compare the parameters to the initial estimation uncertainty. The relation to the measurement variance $w_{\text{rest/motion}}$ is given by

$$w_{\text{rest/motion}} = \frac{\sigma_{\text{rest/motion}}^4}{v} + \sigma_{\text{rest/motion}}^2, \tag{A.24}$$

with v being the process noise variance.

To derive this, consider the update equations for a simplified case of a Kalman filter for a system with one constant state ($x_k = x_{k-1}$) and direct measurement of the state ($C = 1$):

$$p_k^- = p_{k-1}^+ + v, \tag{A.25}$$

$$k_k = \frac{p_k^-}{w + p_k^-}, \tag{A.26}$$

$$\hat{x}_k = \hat{x}_{k-1} + k_k(y_k - \hat{x}_{k-1}), \tag{A.27}$$

$$p_k^+ = p_k^- - k_k p_k^-. \tag{A.28}$$

In the converged state, $k_k = k_{k-1}$ and $p_k^+ = p_{k-1}^+$. From (A.28) follows

$$p_k^+ = p_k^+ + v - \frac{p_k^+ + v}{p_k^+ + v + w}(p_k^+ + v), \tag{A.29}$$

$$v = \frac{(p_k^+ + v)^2}{p_k^+ + v + w}, \tag{A.30}$$

$$w = \frac{(p_k^+ + v)^2}{v} - p_k^+ - v = \frac{(p_k^+)^2}{v} + p_k^+. \tag{A.31}$$

The relation given in (A.24) is then obtained by replacing the variance p_k with σ^2.

Note that, for the 3-dimensional bias estimate, the 3×3 covariance matrix might not be close to a diagonal matrix, especially if the same sensor axis is vertical for a long time. The uncertainty σ of the bias estimate (in the worst-case direction) can be derived from the largest eigenvalue of the covariance matrix $\mathbf{P}$. In order to avoid calculating eigenvalues, we can leverage the Gershgorin circle theorem to obtain an upper bound estimate via the largest absolute row sum of $\mathbf{P}$.

B

Details on the Anatomical Calibration Methods

B.1 General 2D Joint Model to Euler Angles

The methods for automatic anatomical calibration in Chapter 4 use z-y'-x'' Euler angles to decompose the relative segment orientation into joint angles. This decomposition was chosen because it is recommended by the ISB for the elbow [47]. However, this choice is not restrictive in any way. In the following, we show that any joint model with two degrees of freedom can be transformed to fit the chosen Euler angle representation. For example, instead of using regular Euler angles, we could consider modeling a 2-DoF joint with axes that are all potentially non-orthogonal (including the carrying angle axis), i.e.,

$$^{\mathcal{B}_2'}_{\mathcal{B}_1'}\mathbf{q} = (\alpha'(t) \mathbin{@} \mathbf{j}_1') \otimes \left(\beta_0' \mathbin{@} \mathbf{j}_\beta'\right) \otimes (\gamma'(t) \mathbin{@} \mathbf{j}_2') \,, \tag{B.1}$$

or assume that the relative segment orientation is a sequence of two non-orthogonal rotations (which is a special case of the above model with $\beta_0' = 0$). Furthermore, the joint model might include additional fixed rotations, similar to the carrying angle, at the beginning or at the end of the rotation sequence.

To capture all those possibilities, we start with a very general model of a joint with two degrees of freedom, described as the following decomposition of the relative body segment orientation quaternion:

$$^{\mathcal{B}_2'}_{\mathcal{B}_1'}\mathbf{q} = \mathbf{q}_1 \otimes (\alpha \mathbin{@} \mathbf{j}_1) \otimes \mathbf{q}_2 \otimes (\gamma \mathbin{@} \mathbf{j}_2) \otimes \mathbf{q}_3. \tag{B.2}$$

The 3D vectors $\mathbf{j}_1$ and $\mathbf{j}_2$ are arbitrary but constant joint rotation axes, $\alpha(t)$ and $\gamma(t)$ are the two time-varying joint angles, and $\mathbf{q}_1$, $\mathbf{q}_2$ and $\mathbf{q}_3$ are arbitrary but constant rotations.

Without loss of generality, we can write $(\alpha \mathbin{@} \mathbf{j}_1) = \mathbf{q}_4 \otimes (\alpha \mathbin{@} [\,0\;\;0\;\;1\,]^\intercal) \otimes \mathbf{q}_4^{-1}$ and $(\gamma \mathbin{@} \mathbf{j}_2) = \mathbf{q}_5 \otimes (\alpha \mathbin{@} [\,0\;\;1\;\;0\,]^\intercal) \otimes \mathbf{q}_5^{-1}$, with some constant rotations $\mathbf{q}_4$, $\mathbf{q}_5$ that rotate between the given joint axes and the z-axis and y-axis, respectively. Inserting this into (B.2) gives

$$ {}^{\mathcal{B}_2'}_{\mathcal{B}_1'}\mathbf{q} = \mathbf{q}_1 \otimes \mathbf{q}_4 \otimes (\alpha \,@\, [\,0\;\;0\;\;1\,]^\intercal) \otimes \mathbf{q}_4^{-1} \otimes \mathbf{q}_2 \otimes \mathbf{q}_5 \otimes (\gamma \,@\, [\,0\;\;1\;\;0\,]^\intercal) \otimes \mathbf{q}_5^{-1} \otimes \mathbf{q}_3. \tag{B.3}$$

Since we can decompose any quaternion into Euler angles, we can write

$$ \mathbf{q}_4^{-1} \otimes \mathbf{q}_2 \otimes \mathbf{q}_5 = (\alpha_0 \,@\, [\,0\;\;0\;\;1\,]^\intercal) \otimes (\beta_0 \,@\, [\,1\;\;0\;\;0\,]^\intercal) \otimes (\gamma_0 \,@\, [\,0\;\;1\;\;0\,]^\intercal)\,. \tag{B.4}$$

Furthermore, we can define new body segment coordinate systems $\mathcal{B}_1$ and $\mathcal{B}_2$:

$$ {}^{\mathcal{B}_1}_{\mathcal{B}_1'}\mathbf{q} = \mathbf{q}_1 \otimes \mathbf{q}_4, \tag{B.5}$$

$$ {}^{\mathcal{B}_2'}_{\mathcal{B}_2}\mathbf{q} = \mathbf{q}_5^{-1} \otimes \mathbf{q}_3. \tag{B.6}$$

Putting (B.4), (B.5), and (B.5) into (B.3) yields

$$ \begin{aligned} {}^{\mathcal{B}_2}_{\mathcal{B}_1}\mathbf{q} &= (\alpha \,@\, [\,0\;\;0\;\;1\,]^\intercal) \otimes \mathbf{q}_4^{-1} \otimes \mathbf{q}_2 \otimes \mathbf{q}_5 \otimes (\gamma \,@\, [\,0\;\;1\;\;0\,]^\intercal) \\ &= (\alpha + \alpha_0 \,@\, [\,0\;\;0\;\;1\,]^\intercal) \otimes (\beta_0 \,@\, [\,1\;\;0\;\;0\,]^\intercal) \otimes (\gamma + \gamma_0 \,@\, [\,0\;\;1\;\;0\,]^\intercal)\,. \end{aligned} \tag{B.7}$$

This represents z-x'-y'' Euler angles as recommended for the elbow by [47], with a constant carrying angle β_0. The time-varying joint angles in the generic model (B.2) and in the Euler angle model (B.7) are only shifted by constant offsets α_0 and γ_0. Therefore, all joints that can be represented with two sequential rotations around arbitrary but constant axes can be described using z-x'-y'' Euler angles.

B.2 Gradient of Rotation-Based Cost Function

For efficient optimization using the rotation-based joint constraint introduced in Section 4.4.2, we need to calculate the elements of the Jacobian $\mathbf{J} \in \mathbb{R}^{M\times 5}$, i.e.,

$$ [\mathbf{J}]_{ij} = \frac{\partial e_i}{\partial \Phi_j} = \boldsymbol{\omega}_{\mathrm{rel}} \cdot \frac{\partial}{\partial \Phi_j}\frac{\mathbf{j}_\mathrm{n}}{\|\mathbf{j}_\mathrm{n}\|} + \frac{\mathbf{j}_\mathrm{n}}{\|\mathbf{j}_\mathrm{n}\|} \cdot \frac{\partial}{\partial \Phi_j}\boldsymbol{\omega}_{\mathrm{rel}}. \tag{B.8}$$

The derivative of the normalized axis is

$$ \frac{\partial}{\partial \Phi_j}\frac{\mathbf{j}_\mathrm{n}}{\|\mathbf{j}_\mathrm{n}\|} = \frac{\frac{\partial}{\partial \Phi_j}\mathbf{j}_\mathrm{n}}{\|\mathbf{j}_\mathrm{n}\|} - \mathbf{j}_\mathrm{n}\frac{\mathbf{j}_\mathrm{n} \cdot \frac{\partial}{\partial \Phi_j}\mathbf{j}_\mathrm{n}}{\|\mathbf{j}_\mathrm{n}\|^3}. \tag{B.9}$$

All necessary subsequent derivatives are detailed in the following. Note that while $\mathbf{j}_\mathrm{n}$ depends on all parameters in $\boldsymbol{\Phi}$, the relative angular rate $\boldsymbol{\omega}_{\mathrm{rel}}$ only depends on δ.

B.2.1 Derivative with Respect to the Joint Axes

We exploit the fact that the product rule holds for quaternion multiplication [42].[1]

$$\frac{\partial \mathbf{j}_{\mathrm{n}}}{\partial \theta_1, \varphi_1} = \left({}^{\mathcal{S}_1}_{\mathcal{E}_1}\mathbf{q} \otimes \frac{\partial}{\partial \theta_1, \varphi_1} \mathbf{j}_1 \otimes {}^{\mathcal{S}_1}_{\mathcal{E}_1}\mathbf{q}^{-1} \right) \times [\mathbf{j}_2]_{\mathcal{E}_1}, \tag{B.10}$$

$$\frac{\partial \mathbf{j}_{\mathrm{n}}}{\partial \theta_2, \varphi_2} = [\mathbf{j}_1]_{\mathcal{E}_1} \times \left({}^{\mathcal{S}_2}_{\mathcal{E}_1}\mathbf{q} \otimes \frac{\partial}{\partial \theta_2, \varphi_2} \mathbf{j}_2 \otimes {}^{\mathcal{S}_2}_{\mathcal{E}_1}\mathbf{q}^{-1} \right). \tag{B.11}$$

Deriving the axes in local sensor coordinates with respect to θ and φ as defined in (4.16) is straightforward:

$$\frac{\partial \mathbf{j}_{\mathrm{i}}}{\partial \theta_i} = [\, \cos\theta_i \cos\varphi_i \quad \cos\theta_i \sin\varphi_i \quad -\sin\theta_i \,]^{\intercal}, \tag{B.12}$$

$$\frac{\partial \mathbf{j}_{\mathrm{i}}}{\partial \varphi_i} = [\, -\sin\theta_i \sin\varphi_i \quad \sin\theta_i \cos\varphi_i \quad 0 \,]^{\intercal}, \quad i = 1, 2. \tag{B.13}$$

The same is possible for the alternative joint axis parametrization.

B.2.2 Derivative with Respect to the Heading Offset

Instead of quaternion multiplication, we can make use of Rodrigues' rotation formula to express the transformation of a vector $\mathbf{v} \in \mathbb{R}^3$ from $\mathcal{E}_2$ into $\mathcal{E}_1$, i.e.,

$$\begin{aligned} [\mathbf{v}]_{\mathcal{E}_1} &= {}^{\mathcal{E}_2}_{\mathcal{E}_1}\mathbf{q} \otimes [\mathbf{v}]_{\mathcal{E}_2} \otimes {}^{\mathcal{E}_2}_{\mathcal{E}_1}\mathbf{q}^{-1} \\ &= [\mathbf{v}]_{\mathcal{E}_2} \cos(\delta) + \left([0 \;\; 0 \;\; 1]^{\intercal} \times [\mathbf{v}]_{\mathcal{E}_2} \right) \sin(\delta) \\ &\quad + [0 \;\; 0 \;\; 1]^{\intercal} \left([0 \;\; 0 \;\; 1]^{\intercal} \cdot [\mathbf{v}]_{\mathcal{E}_2} \right) (1 - \cos(\delta)). \end{aligned} \tag{B.14}$$

This allows us to calculate the derivatives

$$\begin{aligned} \frac{\partial \boldsymbol{\omega}_{\mathrm{rel}}}{\partial \delta} &= -\frac{\partial}{\partial \delta} [\boldsymbol{\omega}_2]_{\mathcal{E}_1} \\ &= [\boldsymbol{\omega}_2]_{\mathcal{E}_2} \sin(\delta) - \left([0 \;\; 0 \;\; 1]^{\intercal} \times [\boldsymbol{\omega}_2]_{\mathcal{E}_2} \right) \cos(\delta) \\ &\quad - [0 \;\; 0 \;\; 1]^{\intercal} \left([0 \;\; 0 \;\; 1]^{\intercal} \cdot [\boldsymbol{\omega}_2]_{\mathcal{E}_2} \right) \sin(\delta) \end{aligned} \tag{B.15}$$

and

$$\frac{\partial \mathbf{j}_{\mathrm{n}}}{\partial \delta} = [\mathbf{j}_1]_{\mathcal{E}_1} \times \frac{\partial}{\partial \delta} [\mathbf{j}_2]_{\mathcal{E}_1} \text{ with} \tag{B.16}$$

$$\begin{aligned} \frac{\partial}{\partial \delta} [\mathbf{j}_2]_{\mathcal{E}_1} &= -[\mathbf{j}_2]_{\mathcal{E}_2} \sin(\delta) + \left([0 \;\; 0 \;\; 1]^{\intercal} \times [\mathbf{j}_2]_{\mathcal{E}_2} \right) \cos(\delta) \\ &\quad + [0 \;\; 0 \;\; 1]^{\intercal} \left([0 \;\; 0 \;\; 1]^{\intercal} \cdot [\mathbf{j}_2]_{\mathcal{E}_2} \right) \sin(\delta). \end{aligned} \tag{B.17}$$

[1] Similarly, we could argue that the rotation can be expressed using a rotation matrix and make use of the product rule for matrix multiplication.

B.3 Gradient of Orientation-Based Cost Function

Analogously to the derivation in Appendix B.2, we now show how to calculate the elements of the Jacobian $\mathbf{J} \in \mathbb{R}^{M\times 6}$ for the orientation-based constraint introduced in Section 4.4.2, i.e.,

$$[\mathbf{J}]_{ij} = \frac{\partial e_i}{\partial \Phi_j} = \frac{\partial}{\partial \Phi_j}\Big(\arcsin \underbrace{(2q_w q_x + 2q_y q_z)}_{=:\, s(\theta_1,\varphi_1,\theta_2,\varphi_2,\delta)} - \beta_0\Big), \tag{B.18}$$

with ${}^{\mathcal{B}_2}_{\mathcal{B}_1}\mathbf{q} =: [\, q_w \;\; q_x \;\; q_y \;\; q_z \,]^\intercal$.

Trivially, the derivative with respect to the fixed carrying angle β_0 is

$$\frac{\partial e_i}{\partial \beta_0} = -1. \tag{B.19}$$

For the derivatives with respect to the other parameters, we make use of the fact that

$$\frac{\partial}{\partial \Phi_j} \arcsin s(\Phi_j) = \frac{\frac{\partial}{\partial \Phi_j} s(\Phi_j)}{\sqrt{1 - s(\Phi_j)^2}} \tag{B.20}$$

and that

$$\frac{\partial}{\partial \Phi_j} s(\Phi_j) = 2\left(\frac{\partial q_x}{\partial \Phi_j} q_w + q_x \frac{\partial q_w}{\partial \Phi_j} + \frac{\partial q_y}{\partial \Phi_j} q_z + q_y \frac{\partial q_z}{\partial \Phi_j}\right). \tag{B.21}$$

To determine the derivative of the quaternion components q_w, q_x, q_y, and q_z, remember that the relative segment orientation ${}^{\mathcal{B}_2}_{\mathcal{B}_1}\mathbf{q}$, as defined in (4.13), is the multiplicative concatenation of five quaternions:

$${}^{\mathcal{B}_2}_{\mathcal{B}_1}\mathbf{q} = {}^{\mathcal{S}_1}_{\mathcal{B}_1}\mathbf{q}(\theta_1, \varphi_1) \otimes {}^{\mathcal{E}_1}_{\mathcal{S}_1}\mathbf{q} \otimes {}^{\mathcal{E}_2}_{\mathcal{E}_1}\mathbf{q}(\delta) \otimes {}^{\mathcal{S}_2}_{\mathcal{E}_2}\mathbf{q} \otimes {}^{\mathcal{B}_2}_{\mathcal{S}_2}\mathbf{q}(\theta_2, \varphi_2). \tag{B.22}$$

Since for each parameter, only a single of those five quaternions depends on the respective parameter, the other four quaternions are constant factors, i.e.,

$$\frac{\partial}{\partial \theta_1, \varphi_1} {}^{\mathcal{B}_2}_{\mathcal{B}_1}\mathbf{q} = \left(\frac{\partial}{\partial \theta_1, \varphi_1} {}^{\mathcal{S}_1}_{\mathcal{B}_1}\mathbf{q}\right) \otimes {}^{\mathcal{E}_1}_{\mathcal{S}_1}\mathbf{q} \otimes {}^{\mathcal{E}_2}_{\mathcal{E}_1}\mathbf{q} \otimes {}^{\mathcal{S}_2}_{\mathcal{E}_2}\mathbf{q} \otimes {}^{\mathcal{B}_2}_{\mathcal{S}_2}\mathbf{q}, \tag{B.23}$$

$$\frac{\partial}{\partial \delta} {}^{\mathcal{B}_2}_{\mathcal{B}_1}\mathbf{q} = {}^{\mathcal{S}_1}_{\mathcal{B}_1}\mathbf{q} \otimes {}^{\mathcal{E}_1}_{\mathcal{S}_1}\mathbf{q} \otimes \left(\frac{\partial}{\partial \delta} {}^{\mathcal{E}_2}_{\mathcal{E}_1}\mathbf{q}\right) \otimes {}^{\mathcal{S}_2}_{\mathcal{E}_2}\mathbf{q} \otimes {}^{\mathcal{B}_2}_{\mathcal{S}_2}\mathbf{q}, \tag{B.24}$$

$$\frac{\partial}{\partial \theta_2, \varphi_2} {}^{\mathcal{B}_2}_{\mathcal{B}_1}\mathbf{q} = {}^{\mathcal{S}_1}_{\mathcal{B}_1}\mathbf{q} \otimes {}^{\mathcal{E}_1}_{\mathcal{S}_1}\mathbf{q} \otimes {}^{\mathcal{E}_2}_{\mathcal{E}_1}\mathbf{q} \otimes {}^{\mathcal{S}_2}_{\mathcal{E}_2}\mathbf{q} \otimes \left(\frac{\partial}{\partial \theta_2, \varphi_2} {}^{\mathcal{B}_2}_{\mathcal{S}_2}\mathbf{q}\right). \tag{B.25}$$

B.3.1 Derivative with Respect to the Joint Axes

The sensor-to-segment orientation for the first segment can be expressed as

$${}^{\mathcal{S}_1}_{\mathcal{B}_1}\mathbf{q} = \begin{bmatrix} \cos(\frac{\psi}{2}) \\ \sin(\frac{\psi}{2}) \frac{\mathbf{v}}{\|\mathbf{v}\|} \end{bmatrix}, \text{ with } \psi = \arccos(j_{1,z}) \text{ and } \mathbf{v} = \mathbf{j}_1 \times \begin{bmatrix} 0 \\ 0 \\ 1 \end{bmatrix} = \begin{bmatrix} j_{1,y} \\ -j_{1,x} \\ 0 \end{bmatrix}. \tag{B.26}$$

For the scalar part of the quaternion,

$$\frac{\partial}{\partial \theta_1, \varphi_1} \cos\left(\frac{\psi}{2}\right) = -\frac{1}{2} \sin\left(\frac{\psi}{2}\right) \frac{\partial \psi}{\partial \theta_1, \varphi_1} \tag{B.27}$$

and

$$\frac{\partial}{\partial \theta_1, \varphi_1} \psi = -\frac{\frac{\partial j_{1,z}}{\partial \theta_1, \varphi_1}}{\sqrt{1 - j_{1,z}^2}}. \tag{B.28}$$

The derivative of the vector part of the quaternion is

$$\frac{\partial}{\partial \theta_1, \varphi_1} \sin\left(\frac{\psi}{2}\right) \frac{\mathbf{v}}{\|\mathbf{v}\|} = \frac{1}{\|\mathbf{v}\|^2} \left(\mathbf{v} \|\mathbf{v}\| \frac{\partial \sin(\frac{\psi}{2})}{\partial \theta_1, \varphi_1} + \sin\left(\frac{\psi}{2}\right) \|\mathbf{v}\| \frac{\partial \mathbf{v}}{\partial \theta_1, \varphi_1} - \sin\left(\frac{\psi}{2}\right) \mathbf{v} \frac{\partial \|\mathbf{v}\|}{\partial \theta_1, \varphi_1}\right), \tag{B.29}$$

with

$$\frac{\partial}{\partial \theta_1, \varphi_1} \sin\left(\frac{\psi}{2}\right) = \frac{1}{2} \cos\left(\frac{\psi}{2}\right) \frac{\partial \psi}{\partial \theta_1, \varphi_1} \tag{B.30}$$

and

$$\frac{\partial}{\partial \theta_1, \varphi_1} \|\mathbf{v}\| = \frac{1}{\|\mathbf{v}\|} \left(j_{1,y} \frac{\partial j_{1,y}}{\partial \theta_1, \varphi_1} - j_{1,x} \frac{\partial j_{1,x}}{\partial \theta_1, \varphi_1}\right). \tag{B.31}$$

For the derivatives of the Cartesian joint axis vector $\mathbf{j}_1$ with respect to θ_1 and φ_1, refer to Appendix B.2.

The derivative with respect to θ_2 and φ_2 follows analogously for the second sensor-to-segment orientation

$${}^{\mathcal{B}_2}_{\mathcal{S}_2}\mathbf{q} = \begin{bmatrix} \cos(\frac{\psi}{2}) \\ \sin(\frac{\psi}{2}) \frac{\mathbf{v}}{\|\mathbf{v}\|} \end{bmatrix}, \text{ with } \psi = \arccos(j_{2,x}) \text{ and } \mathbf{v} = \begin{bmatrix} 0 \\ 1 \\ 0 \end{bmatrix} \times \mathbf{j}_2 = \begin{bmatrix} j_{1,z} \\ 0 \\ -j_{1,x} \end{bmatrix}. \tag{B.32}$$

B.3.2 Derivative with Respect to the Heading Offset

The derivative of the heading offset quaternion

$${}^{\mathcal{E}_2}_{\mathcal{E}_1}\mathbf{q} = \begin{bmatrix} \cos(\frac{\delta}{2}) & 0 & 0 & \sin(\frac{\delta}{2}) \end{bmatrix}^\intercal \tag{B.33}$$

with respect to the heading offset δ is

$$\frac{\partial}{\partial \delta} {}^{\mathcal{E}_2}_{\mathcal{E}_1}\mathbf{q} = \begin{bmatrix} -\frac{1}{2}\sin(\frac{\delta}{2}) & 0 & 0 & \frac{1}{2}\cos(\frac{\delta}{2}) \end{bmatrix}^\intercal. \tag{B.34}$$